Title
Experimental and Theoretical Studies on Mechanical Properties of Complex Oxides in Concrete

Author
Moon, Juhyuk

Publication Date
2013

Peer reviewed|Thesis/dissertation

Experimental and Theoretical Studies on Mechanical Properties of Complex Oxides in Concrete

By

Juhyuk Moon

A dissertation submitted in partial satisfaction of the

requirements for the degree of

Doctor of Philosophy

in

Engineering – Civil and Environmental Engineering

in the

Graduate Division

of the

University of California, Berkeley

Committee in charge:

Professor Paulo J.M. Monteiro, Chair
Professor Shaofan Li
Professor Hans-Rudolf Wenk

Spring 2013

Abstract

Experimental and Theoretical Studies on Mechanical Properties of Complex Oxides in Concrete

by

Juhyuk Moon

Doctor of Philosophy in Engineering-Civil and Environmental Engineering

University of California, Berkeley

Professor Paulo J.M. Monteiro, Chair

Despite the enormous amount of concrete consumed, fundamental understanding on the structural properties of hydrated oxides in concrete is still an open question. Due to the structural hierarchies and heterogeneous characteristics of concrete, accurate experimental and theoretical studies have not been well-developed for measuring mechanical properties of crystalline and amorphous materials in concrete. Lack of the information makes the development of constitutive relation of them to the macroscopic concrete properties difficult.

The objective of this thesis is to compute mechanical properties of various phases in concrete. Unconventional methods of high pressure x-ray diffraction, absorption, and first-principles calculation are applied to calcium silicate hydrates (tobermorite 14 Å, 11 Å, 9 Å, and jennite), calcium aluminate hydrates (hemi-carboaluminate, monocarboaluminate, strätlingite, and hydrogarnet), tricalcium aluminate, and alkali-silica reaction gel. From the systematic comparison of both experiment and simulation, a comprehensive understanding of structural mechanism is achieved.

For tobermorites, interlayer thickness which is related to the number of interlayer water molecules determines its compressibility. Hemicarboaluminate and strätlingite shows a pressure-induced dehydration while monocarboaluminate with the full occupancy of carbon oxide group behaves stable and incompressible under pressure. In the cases of tobermorite 14 Å and monocarboaluminate, linear density approximation in the first-principles calculation predicts the experimentally measured bulk modulus with high accuracy. Based on the excellent agreement of bulk moduli between experiment and simulation, it can be concluded that computed elastic properties of shear and Young's modulus,

Poisson's ratio, and elastic tensor coefficients are highly reliable. In addition, combining x-ray diffraction and absorption methods allows accurate measurement of density variation under pressure which is used to compute the bulk modulus of alkali-silica reaction gel.

The fundamental structural properties obtained in both experiments and simulations given in this thesis will pave a path toward not just to increase our knowledge of the structural mechanism of concrete but also to optimize concrete design for better structural performance.

TABLE OF CONTENTS

1. Introduction..……1
1.1 Research Motivation……..1
1.2 Outline of Thesis…… ……5

2. Overview of Experimental and Theoretical Techniques……..6
2.1 Introduction to Synchrotron based x-ray experiments……6
2.2 First-Principles Calculation……..11
2.3 Review on equations of state and micromechanics……..17

3. High Pressure X-ray Diffraction and First-Principles Calculation Studies on Calcium Silicate Hydrates…… ……..22
3.1 Calcium Silicate Hydrates in Concrete…….22
3.2 High Pressure X-ray Diffraction Experiments on Calcium Silicate Hydrates.....28
3.2.1 Normal tobermorite 11Å……28
3.2.2 Anomalous tobermorite 11 Å……..……36
3.2.3 Tobermorite 9 Å…….…….40
3.2.4 Jennite……43
3.3 First-Principles Calculations on Calcium Silicate Hydrates…….…….51
3.3.1 Tobermorite 14 Å……...51
3.3.2 Tobermorite 9 Å…….58
3.3.3 Jennite……62
3.4 Discussion on Structural Mechanism of Calcium Silicate Hydrates…68
3.5 Chapter Summary…….….81

4. High Pressure X-ray Diffraction and First-Principles Calculation Studies on Calcium Aluminate Oxides…….83
4.1 Calcium Aluminate Hydrates in Concrete…….……83
4.2 High Pressure X-ray Diffraction Experiments on Calcium Aluminate Oxides…….……....86
4.2.1 Strätlingite…….……..86
4.2.2 Hemicarboaluminate……..……..89
4.2.3 Monocarboaluminate……..…….95
4.2.4 Tricalcium aluminate……..……...100
4.3 First-principles Calculations on Calcium Aluminate Oxides…….….104
4.3.1 Monocarboaluminate……...104
4.3.2 Tricalcium aluminate……..……...115
4.4 Discussion on Elastic Properties of Calcium Aluminate Oxides and Calcium Aluminate Hydrated Oxides…….119
4.5 Chapter Summary…….……...128

5. X-ray Absorption Experiments to Measure Pressure-induced Density Variation of Alkali-Silica Reaction Gel……130
5.1 Alkali-Silica Reaction Gel…….……..130
5.2 High Pressure X-ray Absorption Experiment on Alkali-Silica Reaction Gel…….…….131
5.2.1 Chemical Compositions and Density of Alkali-Silica Reaction Gel……..…….....……...131
5.2.2 Application of X-ray Absorption Method…….133
5.3 Discussion on Measured Bulk Modulus of Alkali-Silica Reaction Gel…….…….140
5.4 Chapter Summary……..……...143

6. Conclusions……...144

References…….147

Appendix: Geometrically optimized atomic coordinates of crystals in concrete.162

LIST OF FIGURES

Figure 1.1 Structural hierarchies in concrete. The images in nano and micro scales are from Richardson [2]. The concrete image in macro scale is from Mehta and Monteiro [1]. The atomic structure in a red box is tobermorite 14Å, reproduced from [3]……..…….....2

Figure 2.1 Raw synchrotron x-ray powder diffraction patterns collected on (a) tobermorite 14 Å (Plombierite), (b) After heating the plombierite at 135 ºC for 1 day, (c) Pressurized at 6 GPa after the heating, and (d) synthesized C-S-H at ambient condition……8

Figure 2.2 Integrated synchrotron x-ray powder diffraction patterns of tobermorite 14 Å (Plombierite) at ambient condition, after heating at 135 ºC for 1 day, and pressurized at 6 GPa after the heating……..…8

Figure 3.1 The analogy of x-ray diffraction patterns between synthesized C-S-H (red, bottom) and crystalline calcium silicate hydrates (normal tobermorite 11 Å and jennite)…….……22

Figure 3.2 Schematic diagram showing the relative stability of part of the C-S-H compounds prepared under hydrothermal conditions [123]……...24

Figure 3.3 (a) The single dreierketten silicate structure in Hamid tobermorite 11 Å [129] (b) double (condensed) dreierketten silicate structure in Merlino tobermorite 11 Å [55]…….....25

Figure 3.4 (a) Silicate chains in tilleyite ribbon projected along [100] in jennite crystal structure. (b) Tilleyite ribbon projected along [010]. The silicate tetrahedra and calcium oxide octahedra are denoted in dark blue and light blue, respectively [118].....25

Figure 3.5 Molecular model of C-S-H proposed by Pellenq et al. [142]. Silicon, calcium, oxygen, water molecules and hydroxyl groups are denoted with dark blue, light blue, red, white spheres, and black sticks, respectively.....26

Figure 3.6 Crystal structure of tobermorite 11 Å projected along (a) [110] and (b) [010] proposed by Hamid [129]. Silicate chains, calcium octahedral, and oxygen atoms are shown as dark blue, light blue tetrahedra, and red spheres, respectively…….29

Figure 3.7 Crystal structure of tobermorite 11 Å projected along (a) [110] and (b) [010] proposed by Merlino et al. [55]. Same graphical notation in Fig. 3.1 is used.....29

Figure 3.8 Variation of basal spacing of tobermorite 14 Å under heating…….32

Figure 3.9 Measured x-ray diffraction patterns of normal tobermorite 11 Å (λ = 0.6199 Å) with alcohol mixture (Methanol:ethanol=4:1). Bottom peaks indicate reference peak positions from [129]……..…….33

Figure 3.10 (a) Variation of axial lattice parameters of normal tobermorite 11 Å under pressure. (b) Refined unit cell volumes of normal tobermorite 11 Å under pressure. The 2nd and 3rd order BM EoS fittings give the bulk modulus of 71(4) GPa and 62(4) GPa…….34

Figure 3.11 F-f plot of normal tobermorite 11 Å……35

Figure 3.12 Crystal structure of anomalous tobermorite 11 Å from Wessels mine, South Africa (a) and normal tobermorite 11 Å from Bashenov, Urals (b). The structures are projected along [010] and proposed by Merlino et al. [55, 116]. Same graphical notation in Fig. 3.1 is used……...36

Figure 3.13 Measured x-ray diffraction patterns of anomalous tobermorite 11 Å (λ = 0.6199 Å) with alcohol mixture (Methanol:ethanol=4:1). Bottom peaks indicate reference peak positions from [129]……..…38

Figure 3.14 (a) Variation of axial lattice parameters of anomalous tobermorite 11 Å under pressure. (b) Refined unit cell volumes of anomalous tobermorite 11 Å under pressure. The 2nd and 3rd order BM EoS fittings give the bulk modulus of 63(2) GPa and 67(2) GPa……39

Figure 3.15 (a) F-f plot of anomalous tobermorite 11Å. (b) Pressure dependent behavior of normal and anomalous tobermorite 11 Å. First-principles calculations result is reproduced from RVH bulk modulus of Shahsavari et al. [155]……..39

Figure 3.16 (a) A unit cell structure of tobermorite 9 Å projected along [010]. (b) Crystal structure of tobermorite 9 Å projected along [100] proposed by Merlino et al.[116]. Same graphical notation in Fig. 3.1 is used.....40

Figure 3.17 Measured x-ray diffraction patterns of tobermorite 9 Å (λ = 0.4959Å) with alcohol mixture (Methanol:ethanol=4:1). Bottom peaks indicate reference peak positions from [116].....41

Figure 3.18 (a) Variation of axial lattice parameters of tobermorite 9 Å under pressure. (b) Refined unit cell volumes of tobermorite 9 Å under pressure. The 2nd and 3rd order BM EoS fittings give the bulk modulus of 115(14) GPa and 86(6) GPa……..…42

Figure 3.19 F-f plot of tobermorite 9 Å……..….42

Figure 3.20 (a) A unit cell structure of jennite projected along [010]. (b) Crystal structure of jennite projected along [010] proposed by Bonaccorsi et al.[118]. Same graphical notation in Fig. 3.1 is used……....43

Figure 3.21 Jennite collected from Zeilberg, Bavaria, Germany. The crystal was purchased from http://minernet.it.....44

Figure 3.22 Measured x-ray diffraction patterns of jennite (λ = 0.6199 Å) with alcohol mixture (Methanol:ethanol=4:1). Bottom peaks indicate reference peak positions from [118].....44

Figure 3.23 Measured x-ray diffraction patterns of jennite (λ = 0.4959 Å) with silicone oil. Bottom peaks indicate reference peak positions from [118]……..45

Figure 3.24 Variation of (a) axial and (b) angular lattice parameters of jennite under pressure. Closed and open symbols correspond to refined parameters measured with alcohol mixture (Methanol:ethanol=4:1) and silicone oil, respectively…….49

Figure 3.25 (a) Refined unit cell volumes of jennite under pressure. (b) F-f plot of jennite. The 2nd order BM EoS fittings give the bulk modulus of 68(5) GPa and 64(2) GPa with alcohol mixture and silicone oil, respectively……...49

Figure 3.26 Geometrically optimized tobermorite 14 Å projected along (a) [010] and (b) [110]. Silicate chains, calcium octahedral, and oxygen atoms are shown as dark blue, light blue tetrahedra, and red spheres, respectively. Hydroxyl groups and hydrogen atoms in water molecules are denoted with black sticks…….51

Figure 3.27 Comparison of (a) axial and (b) volumetric compressibilities of tobermorite 14 Å from high pressure experiment and LDA (red line) and GGA (black line) simulation. First-principles calculations result is reproduced from RVH bulk modulus of Shahsavari et al. [155]……53

Figure 3.28 Directional Young's modulus of tobermorite 14 Å using (a) LDA and (b) GGA functionals. Scale bars indicate Young's modulus in GPa……..57

Figure 3.29 Geometrically optimized tobermorite 9 Å projected along (a) [010] and (b) [100]. Silicate chains, calcium octahedral, hydrogen atoms, and oxygen atoms are shown as dark blue, light blue tetrahedral, black spheres, and red spheres, respectively.....58

Figure 3.30 Comparison of (a) axial and (b) volumetric compressibilities of tobermorite 9 Å from high pressure experiment and LDA (red line) and GGA (black line) simulation. First-principles calculations result is reproduced from RVH bulk modulus of Shahsavari et al. [155]……59

Figure 3.31 Directional Young's modulus of tobermorite 14 Å computed from (a) LDA and (b) GGA functionals. Elastic constants calculated in the coordinate system of ($\vec{X}\|\vec{a}$, $\vec{Z}\|\vec{a}\times\vec{b}$, and $\vec{Y}\|\vec{Z}\times\vec{X}$) are used. Scale bars indicate Young's modulus in GPa……..61

Figure 3.32 Geometrically optimized jennite projected along [010]. Silicate chains, calcium octahedra, and oxygen atoms are shown as dark blue, light blue tetrahedra, and red spheres, respectively. Hydroxyl groups and hydrogen atoms in water molecules are denoted with black sticks……....62

Figure 3.33 Comparison of (a) axial and (b) angular compressibilities of jennite from high pressure experiment and LDA and GGA simulation…….63

Figure 3.34 Comparison of volumetric compressibilities of jennite from high pressure experiment, LDA (red line), and GGA (black line) simulations. First-principles calculations result is reproduced from RVH bulk modulus of Shahsavari et al. [155]……...64

Figure 3.35 Directional Young's modulus of jennite computed from (a) LDA and (b) GGA functionals. Elastic constants calculated in the conventional orthogonal coordinate system ($\vec{Z}\|\vec{c}$, $\vec{Y}\|\vec{c}\times\vec{a}$, and $\vec{X}\|\vec{Y}\times\vec{Z}$) are used. Scale bars indicate Young's modulus in GPa……65

Figure 3.36 X-ray diffraction patterns of calcium silicate hydrates and hydrated Portland cement. In hydrated cement, ▬, ■, and ● indicate C-S-H gel, AFm, and AFt phase, respectively……...68

Figure 3.37 (Fig.3.10(b)) Pressure dependent behavior of normal and anomalous tobermorite 11 Å. First principles calculations result is reproduced from RVH bulk modulus of Shahsavari et al. [155]…….....71

Figure 3.38 Comparison of experimentally measured pressure-volume (a) and pressure-layer thickness (b) behaviors of tobermorite series. Rectangular symbols indicate identical tobermorite source from Crestmore, CA with different thermal treatments……72

Figure 3.39 Volumetric compressibilities of tobermorite 14 Å (a) and 9 Å (b) from high pressure experiment and LDA (red line) and GGA (black line) simulation. First principles calculations result is reproduced from RVH bulk modulus of Shahsavari et al. [155]……75

Figure 3.40 X-ray diffraction patterns of tobermorite 9 Å. Reference profile (red line) was reproduced from [116]. Tobermorite 9 Å was made from heating the tobermorite 14Å at 360 ºC for 24 hours. Black and dotted lines represent the x-ray profile at ambient condition and mixed with alcohol mixture in DAC, respectively…….77

Figure 3.41 (Fig. 29) Comparison of volumetric compressibilities of jennite from high pressure experiment, LDA (red line), and GGA (black line) simulations. First-principles calculations result is reproduced from RVH bulk modulus of Shahsavari et al. [155]……79

Figure 3.42 Standard directions of elastic constants in triclinic crystal system of jennite…….80

Figure 4.1 Crystal structure of (a) strätlingite [191] (b) monocarboaluminate [187]. Calcium-aluminate ions are shown as dark blue octahedral, silicate/aluminate ions in interlayers are shown as light blue tetrahedra, and oxygen ions are represented as red spheres. Water and hydroxyl groups in monocarboaluminate are denoted with red spheres and black sticks for oxygen and hydrogen atoms, respectively..84

Figure 4.2 Measured x-ray diffraction patterns of strätlingite (λ = 0.6199Å). Bottom peaks indicate reference peak positions from [191]. The numbers indicate measured pressure (GPa) corresponding to each x-ray pattern……..86

Figure 4.3 (a) Variation of lattice parameters of strätlingite under pressure. (b) Refined unit cell volume of strätlingite under pressure. 2nd order BM EoS fitting gives the bulk modulus of 23(2) GPa at low pressure range and 100(3) GPa at higher pressure range……..87

Figure 4.4 Measured x-ray diffraction patterns of hemicarboaluminate (λ = 0.4133 Å) with alcohol mixture (Methanol:ethanol=4:1). Hydrogarnet peaks are denoted as (*). Bottom peaks indicate reference peak positions from [196]. The numbers indicate measured pressure (GPa) corresponding to each x-ray pattern. The (D) means data collected in decompression……..….90

Figure 4.5 Measured x-ray diffraction patterns of hemicarboaluminate (λ = 0.4959 Å) with silicone oil. Hydrogarnet peaks are denoted as (*). Bottom peaks indicate reference peak positions from [196]. The numbers indicate measured pressure (GPa) corresponding to each x-ray pattern. The (D) means data collected in decompression.....90

Figure 4.6 Variation of basal peak of hemicarboaluminate (λ = 0.4133 Å) with alcohol mixture (Methanol:ethanol=4:1). The numbers indicate measured pressure (GPa) corresponding to each x-ray pattern. The (D) means data collected in decompression……91

Figure 4.7 (a) Variation of lattice parameters of hemicarboaluminate under pressure. (b) The refined unit cell volumes of hemicarboaluminate under pressure. Closed and open symbols correspond to pressure medium of alcohol mixture and silicone oil, respectively. Black and gray lines indicate BM EoS fitting results of alcohol mixture and silicone oil, respectively……92

Figure 4.8 The refined unit cell volumes of hydrogarnet under pressure. Closed and open symbols correspond to pressure medium of alcohol mixture and silicone oil, respectively. Black and gray line indicate BM EoS fitting results of alcohol mixture and silicone oil, respectively…….93

Figure 4.9 Crystal structure of monocarboaluminate [187]. Same graphical notation in Fig. 4.1 is used. Brown sphere indicates a carbon atom……..96

Figure 4.10 Measured x-ray diffraction patterns of monocarboaluminate (λ = 0.4965Å) with silicone oil. Bottom peaks indicate reference peak positions from [187]. The numbers indicate measured pressure (GPa) corresponding to each x-ray pattern. The (D) means data collected in decompression……...97

Figure 4.11 Variation of (a) axial and (b) angular lattice parameters of mono-carboaluminate under pressure. Closed and open symbols correspond to refined parameters measured during compression and decompression, respectively…….98

Figure 4.12 (a) Refined unit cell volumes of monocarboaluminate under pressure. (b) F-f plot of monocarboaluminate. The 2nd and 3rd order BM EoS fittings give the bulk modulus of 54(4) GPa and 53(5) GPa……..99

Figure 4.13 Crystal structure of tricalcium aluminate [213]. Light blue tetrahedra, dark blue spheres and red spheres indicate aluminates, calcium and oxygen atoms…….100

Figure 4.14 Measured x-ray diffraction patterns of tricalcium aluminate (λ = 0.6199Å) with silicone oil. Bottom peaks indicate reference peak positions from [213]. The numbers indicate measured pressure (GPa) corresponding to each x-ray pattern. The (D) means data collected in decompression…….101

Figure 4.15 (a) Refined unit cell volumes of tricalcium aluminate under pressure. (b) F-f plot of tricalcium aluminate. The 2nd and 3rd order BM EoS fittings give the bulk modulus of 110(3) GPa and 102(6) GPa……..103

Figure 4.16 (a) Geometrically optimized 5 water monocarboaluminate projected along [100]. (b) Water and hydroxyl group distribution in calcium aluminate principal layer. Calcium-aluminate ions are shown as dark blue octahedral, silicate/aluminate ions in interlayers are shown as light blue tetrahedra, and oxygen ions are represented as red spheres. Water and hydroxyl groups are denoted with red spheres and black sticks for oxygen and hydrogen atoms, respectively…….....105

Figure 4.17 (a) Geometrically optimized 2 water monocarboaluminate projected along [100]. (b) Water and hydroxyl group distribution in calcium aluminate principal layer. Same graphical notation in Fig. 4.15 is used……..105

Figure 4.18 X-ray diffraction patterns of optimized monocarboaluminates and from the single-crystal x-ray experiment [218]. Weak (010) peak is overlapped with strong (011) peak in the reference x-ray profile of [218]…….106

Figure 4.19 Comparison between high pressure x-ray diffraction patterns of monocarboaluminates and simulated patterns from first principles calculations. Hydrogen or water disorder makes experimental x-ray profile more diffuse…...107

Figure 4.20 Comparison of (a) axial and (b) angular compressibilities of 5 water monocarboaluminate from high pressure experiment and LDA and GGA simulation……..109

Figure 4.21 Variation of unit cell volume of 5 water monocarboaluminate from high pressure x-ray diffraction experiment and LDA and GGA calculation……109

Figure 4.22 Directional Young's modulus of monocarboaluminates in conventional orthogonal coordinate system ($\vec{Z}\|\vec{c}$, $\vec{Y}\|\vec{c}\times\vec{a}$ and $\vec{X}\|\vec{Y}\times\vec{Z}$) : results for 5 water MC using (a) LDA and (b) GGA functionals and for 2 water MC using (c) LDA and (d) GGA functionals. Scale bars indicate Young's modulus in GPa. Anisotropy decreases by addition of water molecules in the interlayer region……....113

Figure 4.23 (a) Geometrically optimized tricalcium aluminate projected along [100]. (b) Geometrically optimized structure of Al_6O_{18} ring. Light blue tetrahedra, dark blue spheres and red spheres indicate aluminates, calcium and oxygen atoms…….115

Figure 4.24 Variation of unit cell volume of tricalcium aluminate from high pressure x-ray diffraction experiment and GGA calculation. RVH bulk modulus from [225] is used for pressure-volume relation……..….118

Figure 4.25 Pressure-volume behavior of monocarboaluminate and hemicarboaluminate. The lines show 2nd order BM EoS fitting results……...122

Figure 4.26 Variation of unit cell volume of 5 water and 2 water monocarboaluminates from LDA and GGA calculation……..125

Figure 5.1 (a) ASR gel fragment collected from the Furnas dam. (b) Measured x-ray diffraction patterns of ASR gel at ambient condition (λ = 0.6199 Å). The broad hump of 8-14° indicates disordered crystal structure……...131

Figure 5.2 Transmitted x-ray contour profile measured by a diode with a monochromatic x-ray beam of 20 keV. The profile was measured by scanning in a step of 40 μm and 40 μm in x and y direction with x-ray beam size of 10 × 10 μm…….133

Figure 5.3 Measured x-ray diffraction patterns of ASR gel (λ = 0.6199 Å). The pressures were determined by x-ray diffraction peaks of Re at ASR gel sample hole. The wide range of hump was shifting as pressure increases. Top three patterns (D) were measured during decompression…….….134

Figure 5.4 Measured volumes of NaCl (a) and rhenium (b). Corresponding pressures are computed from the equation of state of NaCl [99] and rhenium [251]……..135

Figure 5.5 Total attenuation with coherent scattering of ASR gel as a function of phonon energy. Data was reproduced from NIST standard reference database [252]……..136

Figure 5.6 (a) Thickness variation of the gasket as a function of pressure. (b) Applied pressures in two holes in DAC. The pressure was determined from Re and NaCl peaks of each holder……136

Figure 5.7 (a) Pressure dependence of the density of ASR gel. (b) Molar volume ratio of ASR gel as a function of pressure. The 2^{nd} and 3^{rd} BM EoS fitting results are shown in solid and dash line, respectively……..138

Figure 5.8 Normalized pressure F as a function of Eulerian strain f with 3^{rd} and 2^{nd} order BM EoS fitting results…….140

.

LIST OF TABLES

Table 3.1 Crystallographic data of calcium silicate hydrates……..…23

Table 3.2 Crystallographic data of tobermorite 11 Å…….30

Table 3.3 Chemical composition of normal tobermorite 11 Å (Major oxide weight %)……31

Table 3.4 High pressure x-ray diffraction results of normal tobermorite 11 Å..…33

Table 3.5 Chemical composition of anomalous tobermorite 11 Å (Major oxide weight %)……37

Table 3.6 High pressure x-ray diffraction results of anomalous tobermorite 11 Å……..……38

Table 3.7 High pressure x-ray diffraction results of tobermorite 9 Å……41

Table 3.8 Measured peak positions (Å) of jennite at ambient and under pressure (Methanol:Ethanol = 4:1)……46

Table 3.9 Measured peak positions (Å) of jennite at ambient and under pressure (Silicone oil)……...47

Table 3.10 High pressure x-ray diffraction results of jennite (Methanol:Ethanol = 4:1)……..47

Table 3.11 High pressure x-ray diffraction results of jennite (Silicone oil)……...48

Table 3.12 Bulk modulus, its first derivative and ambient volume of calcium silicate hydrates according to the Birch-Murnaghan equation of state. The high pressure experimental data of tobermorite 14Å is reproduced from Oh. et al. [148]……...…….50

Table 3.13 First-principles calculation results of tobermorite 14 Å (LDA)…...…53

Table 3.14 First-principles calculation results of tobermorite 14 Å (GGA)……...53

Table 3.15 Calculated elastic coefficients of tobermorite 14 Å…….56

Table 3.16 First-principles calculation results of tobermorite 9 Å (LDA)…….59

Table 3.17 First-principles calculation results of tobermorite 9 Å (GGA)…….59

Table 3.18 Calculated elastic coefficients of tobermorite 9 Å……...60

Table 3.19 First-principles calculation results of jennite (LDA)……63

Table 3.20 First-principles calculation results of jennite (GGA)……...63

Table 3.21 Calculated elastic coefficients of jennite……..65

Table 3.22 Computed elasticity of calcium silicate hydrates from first-principle calculations…….67

Table 3.23 Summary of nanomechanical properties of tobermorite 14 Å……..74

Table 3.24 Summary of nanomechanical properties of tobermorite 11 Å…….....75

Table 3.25 Summary of nanomechanical properties of tobermorite 9 Å……78

Table 3.26 Summary of nanomechanical properties of jennite……..79

Table 4.1 Crystallographic data of calcium aluminate hydrates…….85

Table 4.2 High pressure x-ray diffraction results of strätlingite (Silicone oil)…...87

Table 4.3 High pressure x-ray diffraction results of hemicarboaluminate (Methanol:ethanol=4:1 and silicone oil)…….92

Table 4.4 Measured lattice parameters of hydrogarnet in hemicarboaluminate (Methanol:ethanol=4:1 and silicone oil)…….93

Table 4.5 High pressure x-ray diffraction results of monocarboaluminate (Silicone oil)……...98

Table 4.6 High pressure x-ray diffraction results of tricalcium aluminate (Silicone oil)…….102

Table 4.7 First-principles calculation results of monocarboaluminate containing 5 water molecules (LDA, GGA).....107

Table 4.8 First-principles calculation results of monocarboaluminate containing 2 water molecules (LDA, GGA).....108

Table 4.9 Calculated elastic coefficients of monocarboaluminate……...112

Table 4.10 Calculated elastic coefficients of tricalcium aluminate……..117

Table 4.11 Bulk modulus, its first derivative and ambient volume of calcium aluminate hydrates according to the Birch-Murnaghan equation of state……119

Table 4.12 The summary of high pressure x-ray diffraction and atomistic simulation results of hydrogarnet……121

Table 4.13 Computed elasticity of monocarboaluminate hydrates and tricalcium aluminate from first-principle calculations……...124

Table 5.1 Chemical composition of ASR gel (Major oxide weight %)……132

Table 5.2 High pressure x-ray absorption results of ASR gel. The data of last five rows were collected during decompression……..137

Table A1. Relaxed atomic coordinates of tobermorite 14 Å……162

Table A2. Relaxed atomic coordinates of tobermorite 9 Å.....165

Table A3. Relaxed atomic coordinates of Jennite……167

Table A4. Relaxed atomic coordinates of monocarboaluminate containing 5 water.....169

Table A5. Relaxed atomic coordinates of monocarboaluminate containing 2 water……..171

Table A6. Relaxed atomic coordinates of tricalcium aluminate……...172

Acknowledgements

My deepest gratitude goes to my advisor, Prof. Paulo Monteiro, not only for giving me the huge opportunity to enter into the research area of construction materials, but for his continuous guidance, invaluable support and warm encouragement throughout my doctoral journey.

I wish to express my thanks to the members of my committee of dissertation and qualifying exam. I am highly thankful to Prof. Rudy Wenk and Prof. Shaofan Li for their valuable discussions on my research. In particular, without Prof. Simon Clark, this thesis would have not been possible. I would like to appreciate for sharing beamline facility and his insightful advices with regard to my research.

I also wish to express my appreciation to all my current and former colleagues in the Monteiro group.

The financial supports from KAUST, NIST, and SinBerBest are gratefully acknowledged. Experimental work and theoretical calculation in this thesis are supported by the Advanced Light Source and the UC Berkeley Molecular Graphics and Computation Facility.

I am indebted to my beloved families for their endless supports throughout the completion of my thesis. Finally, I would like to express special thanks to my wife for her unending love and being beside me.

1. Introduction

1.1 Research Motivation

Concrete is the most widely used building material in the world. Global concrete production is around 18 billion tons, enough to produce more than one cubic meter of concrete per person per year and it is expected to grow [1]. The main ingredients in concrete are water, aggregates, and cement. Due to the abundance of raw materials, this very common combination of materials has provided a space for people to live for over 100 years. Nevertheless, microstructure of concrete and its mechanical characteristic have not been fully understood due to its complexity. The research in this thesis aims to investigate the fundamental mechanical properties of various hydration products and clinker in concrete, for better understanding its structural performance.

Ordinary portland cement is the most commonly used cement for usual construction condition. It is produced by heating clays and limestone up to 1550 ºC, which involves a series of chemical transformations to form a coarse clinker. The resulting cement clinker contains alite (C_3S), belite (C_2S), aluminate (C_3A), and ferrite (C_4AF) crystalline phases. Note that cement chemistry, such as that given in parenthesis, is used to simplify chemical equations; $S=SiO_2$, $C=CaO$, $A=Al_2O_3$, and $F=Fe_2O_3$. When finely milled cement powder and gypsum are mixed with water, chemical reactions and thermodynamic processes take place to form numerous phases, which combined make a hardened cement paste [1].

Cement paste is a porous and hierarchical material consisting of various components. It plays a key role of binding the ingredients of concrete together such as aggregates, unhydrated cement, and crystalline phases in the cement paste. The main components of cement paste are poorly crystalline calcium silicate hydrate (C-S-H gel) and crystalline phases of portlandite, ettringite, and Al_2O_3-Fe_2O_3-mono (AFm) phases such as monosulfate and monocarboaluminate. Because of the intrinsic heterogeneity and compositional variance, cement paste has various levels of structures across different length scales. Each scale has a different characteristic size and accordingly different structural properties, which yield the concrete a highly complex material. The concrete can thus be interpreted as a hierarchy of distinct levels as shown in Fig. 1.1.

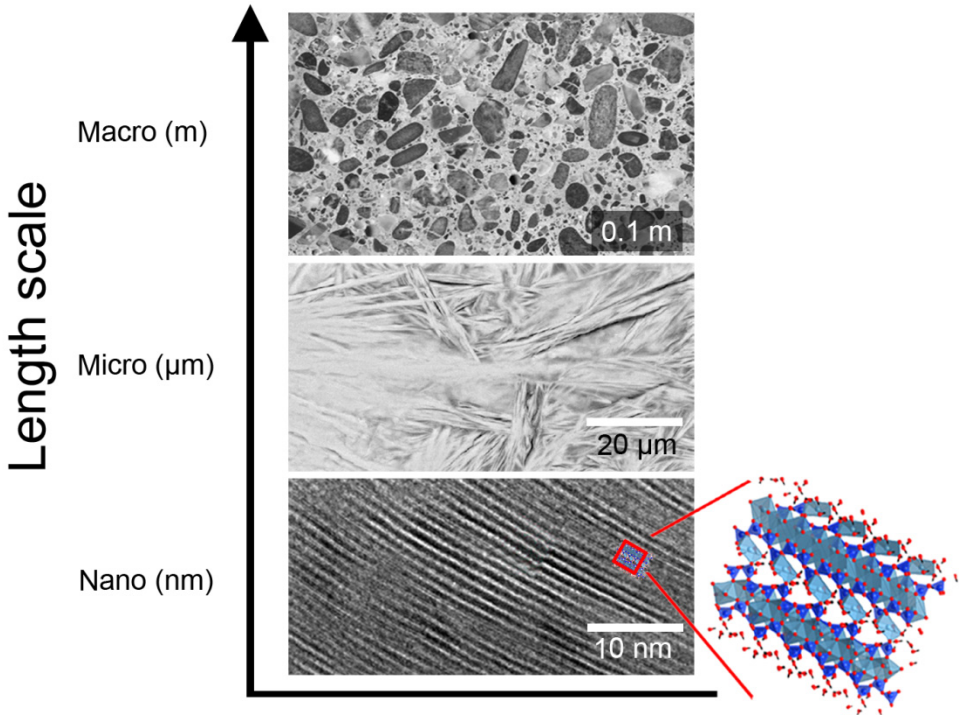

Figure 1.1 Structural hierarchies in concrete. The images in nano and micro scales are from Richardson [2]. The concrete image in macro scale is from Mehta and Monteiro [1]. The atomic structure in a red box is tobermorite 14Å, reproduced from [3].

At a scale of meters, concrete is set with preinstalled reinforcing steel bars to compensate its weak tensile mechanical properties. Several macroscopic material properties such as compressive strength, elastic modulus, and thermal expansion coefficient are considered for the design of concrete for a building and civil infrastructure. At this macro scale, cement hydrates can be represented as homogeneous, with bulk physical and chemical properties. In fact, the concrete is a composite of coarse and fine aggregates that are randomly dispersed in a matrix of hardened cement paste as shown in Fig. 1.1. Various millimeters sized pores also co-exist with hydration products and unreacted clinker particles which yield heterogeneous appearance of concrete. At a macro scale for engineering purpose, it can be assumed that concrete has homogeneous bulk properties. However, heterogeneously distributed pores from admixtures or hydration process at the micro-scale, can lower the density of concrete and affect the mechanical performance of concrete [1].

The hardened cement paste is a heterogeneous composite of cement grains interspersed with hydration products of portlandite, AFm phases, and a poorly crystalline C-S-H at a scale of micrometers. Among the different cement hydration products, the C-S-H gel constitutes more than 60 % of the volume and encompasses all the other phases. Several morphologies are attempted to describe the C-S-H structure including: sheaf of wheat, needles, foils, fibril, and flakes [4-

6]. These morphologies differ based on parameters such as water to cement ratio (w/c), hydration stage, and types of accelerators [7-9].

At a scale of nanometers, the structure of C-S-H gel is similar with that of disordered layered silicates, while other embedded hydration products are perfectly crystalline structures [2, 4, 10, 11] which form large crystals, typically 1 μm maximum. The complex structure consisting of hydration products and voids at this scale level are referred to as the nanostructure of concrete. The capillary voids exist when the spaces originally occupied with water do not get completely filled with the hydration products. The size of capillary voids ranges from 10 nm to 1 μm, but in well-cured pastes with low w/c, they can be less than 100 nm [1, 12, 13]. Although concrete has been in widespread use for over 100 years, many of nano-structural properties such as interaction between the components and physical and thermodynamical characteristics are unexplored.

The C-S-H gel is the most important component in concrete. Not only because it constitutes large volume of cement paste, but because it is responsible for numerous important properties of concrete including setting, hardening, shrinkage, and creep [1]. In spite of its role in concrete, not much known about the structural mechanism of the C-S-H gel. The disordered nature, compositional and density variance makes research on the C-S-H gel difficult [2, 8, 14]. Therefore, the structural manipulation of C-S-H gel is absent from actual concrete design practice. In addition, structural repair related to the behavior of C-S-H gel is of huge cost, due to the ignorance of the nanostructure of the C-S-H gel. For instance, the prevention methods for cracking in concrete or unexpected asymmetric strain induced by creep and shrinkage are still under development. Various advanced experimental techniques have been studied to characterize C-S-H gel at the nano-scale including: Small Angle x-ray Spectroscopy (SAXS) [5, 14]; Nuclear Magnetic Resonance (NMR) [15-19]; Scanning Electron Microscopy (SEM) [4, 20-22]; and x-ray Pair-Distribution Function (PDF) [23, 24]. The reaction of Ca_3SiO_5 (C_3S) or β-Ca_2SiO_4 (C_2S) with water produces C-S-H gel and $Ca(OH)_2$ (CH). C-S-H gel in cement paste is less ordered than synthetic C-S-H(I) or C-S-H(II) which have x-ray diffraction patterns of a broad band at 2.6-3.2 Å and a sharp peak at 1.82 Å. It has been proposed that C-S-H(I) and C-S-H(II) are semi-crystalline versions of crystalline calcium silicate hydrate minerals, tobermorite 14 Å and jennite, respectively [25-27]. Alternatively, it has also been suggested that C-S-H gel is initially a mixture of tobermorite- and jennite-like structures. The jennite-like structure becomes dominant with age [2, 5, 8, 13, 14]. However, the accurate atomic arrangement and the structural mechanism of C-S-H gel is a still open question. More detail description of the structure will be introduced in section 3.1.

Compared to poorly crystalline material, the perfectly crystalline materials of portlandite, $Ca(OH)_2$, AFm (Al_2O_3-Fe_2O_3-mono), and AFt (Al_2O_3-Fe_2O_3-tri) phases are also formed during the hydration of Portland cement. The principal nanostructure of AFm and AFt phases is originated from portlandite. Although the volumetric amount of those mineral phases is small (up to 15 % in concrete), they play a critical role in durability of the concrete [1]. In addition, these minerals are potential candidates for the retention of anionic species [28, 29] because of the positively charged surfaces of AFm and AFt phases. For instance, they can be utilized as a cementitous repository for disposal of radioactive waste [30]. Given the huge amount of concrete used in the world, it also has a huge potential as a carbon sequestrator. Two types of carbon containing AFm phases: monocarboaluminate and hemicarboalumiante will be discussed in more detail in chapter 4.

This complexity of research on structural mechanism of concrete is from the lack of experimental data at a fundamental level. The main objective of this thesis is to provide experimental and theoretical data for the mechanical characteristic of cementitous materials. The understanding of mechanical properties of structural materials is crucial because the nano- and micro-scale of properties of any structural materials will govern the macro-scale and as such the overall behavior of them [1]. Relying on accurate experimental and theoretical data from this study, the microstructural properties of materials in concrete will provide a better understanding of the macro-properties for large-scale civil engineering application. Last, the research on stability and mechanics of cementitous crystals will give us an insight on developing a next generation of concrete including investigating mechanical influence of carbon sequestration on concrete or optimization of the nanostructure of C-S-H gel for developing a high performance concrete.

1.2 Outline of Thesis

This thesis is divided into six chapters. The first chapter summarizes a review of nanostructure of concrete and general description of this thesis.

Chapter 2 reviews experimental and theoretical techniques used in this thesis. Section 2.1 introduces the general application of various synchrotron based x-ray techniques to concrete. Section 2.2 presents an overview of first-principle calculation. Section 2.3 summarizes a theoretical background of thermodynamics and micromechanics which will be used for calculating elastic properties in Chapters 3, 4, and 5.

Chapter 3 discusses crystalline calcium silicate hydrates minerals. Section 3.1 introduces several mineral analogs of C-S-H gel and compares the crystal structures. Section 3.2 presents the direct measurements of bulk modulus of crystalline calcium silicate hydrates of normal and anomalous tobermorite 11 Å, tobermorite 9 Å, and jennite by high pressure x-ray diffraction experiments. Section 3.3 focuses on the application of first-principles calculation on tobermorite 14 Å and 9 Å, and Jennite. Section 3.4 discusses the structural mechanism of the calcium silicate hydrates crystals based on the experimentally and theoretically obtained mechanical properties. Section 3.5 summaries the main findings in chapter 3.

Chapter 4 focuses on structural behavior of calcium aluminate oxides in concrete. Section 4.1 introduces calcium aluminate hydrate phases in concrete. Similarly to in chapter 3, sections 4.2 and 4.3 discuss the high pressure x-ray diffraction measurements and first-principles calculations on the AFm phases, respectively. Also a similar study on clinker material of tricalcium aluminate will be discussed. Section 4.4 discusses the mechanical characteristics of the calcium aluminate hydrates and tricalcium aluminate. Section 4.5 outlines key results in chapter 4.

Chapter 5 deals with amorphous material, alkali-silica reaction (ASR) gel and x-ray absorption experiment. Section 5.1 introduces ASR gel and its atomistic characteristics. Section 5.2 introduces the x-ray absorption experiment and its application to the ASR gel. Section 5.3 presents the measured bulk modulus from the experiment and compares with that of amorphous silica to understand its expansion mechanism in concrete. Section 5.4 is a summary of the outcomes drawn in chapter 5.

Chapter 6 summarizes the major conclusions achieved in this work and proposes future research work.

2. Overview of Experimental and Theoretical Techniques

2.1 Introduction to Synchrotron based x-ray experiments

A significant number of x-ray diffraction studies on concrete provided fundamental information on the crystal structure of many phases of the cement paste in concrete. However, deeper understanding on poorly crystalline phases or measuring mechanical and thermodynamical properties of crystals require advanced techniques. Especially for highly complex heterogeneous materials like concrete, the conventional laboratory facilities such as laboratory based x-ray diffraction, nuclear magnetic resonance (NMR) or x-ray fluorescence (XRF) are not enough to give detail short-range information on concrete due to its hierarchical and heterogeneous structure [31, 32]. On the other hand, electron microscopy in the scanning electron microscope (SEM) and transmission electron microscope (TEM) have been useful in understanding the morphology of C-S-H as well as of other hydration products [2, 8, 33] in various scales with high spatial resolution. In addition, synchrotron-based microscopy [6, 9, 34] and/or x-ray spectroscopy such as scanning-transmission x-ray microscopy led to detailed information on the morphology and composition of polymer-modified and carbonated C-S-H [35-37]. In this section, synchrotron based x-ray diffraction method will be discussed with recent applications to concrete.

The experimental work described in this dissertation has been performed at the Advanced Light Source (ALS), Lawrence Berkeley National Laboratory. This synchrotron radiation facility benefits from the hard x-ray radiation generated by a 6T superconducting bending magnet [38]. The radiation is transferred from the superbend to the experimental enclosure by the brightness-preserving optics of beamlines. To reduce possible correlated uncertainties, the x-ray energy is calibrated by absorption edge of standard materials such as Cu, Zn, Pd, Sn, Ag and Mo. Then, some specific x-ray energies can be accurately calibrated by the derivative intensity attenuation, and the target energy can be achieved by driving the monochromator using a tuning program [38]. Due to the high intensity and tunabilitly, this synchrotron radiation facility has been widely used for powder x-ray diffraction technique to characterize complex materials [39, 40]. For instance, the poorly crystalline features of C-S-H gel in concrete or geopolymeric gel could be detected using the synchrotron based x-ray diffraction [39, 41]. This allows differentiating the poorly crystalline binding materials of C-S-H gel and geopolymeric gel in green concrete. Combining with diamond anvil cell (DAC), hydrostatic pressure can be generated up to 100 GPa. X-ray diffraction, Extended x-ray Absorption Fine Structure (EXAPS), and x-ray imaging through the DAC can be obtained through the DAC [38]. Clark et al. was the first to measure the bulk modulus of cement hydration product, ettringite (one of AFt phases in

concrete) by the high pressure x-ray diffraction technique [42]. Later Oh et al. successfully observed the volume variations of C-S-H(I) and zeolites such as hydroxycancrinite and basic sodalite under loading and unloading conditions [40, 43, 44]. In addition to the pressure, combined with double-sided laser heating, synchrotron radiation has become a unique method for high pressure and high temperature studies. The experimental melting temperature of Ni, Mo, Pt, and W were recently measured using the laser heating system in the Beamline [45].

Although the x-ray diffraction allows to obtain detailed information of the crystalline material, it is still an experimental challenge to apply the diffraction method to amorphous materials under various conditions due to the limited information (i.e., small number of diffraction peaks) for amorphous materials. Eggert et al. established a new method of combining x-ray absorption and diffraction to study fluids and non-crystalline solids [46-49]. According to the absorption law, the density of a sample under various conditions can be determined by comparing transmitted x-ray absorption intensity of the sample with that of reference material. Again, combined with the DAC and laser heating technique, density variation under extreme pressure and/or temperature condition can be measured. Detail method and application to alkali-silica reaction (ASR) gel will be discussed in chapter 5.

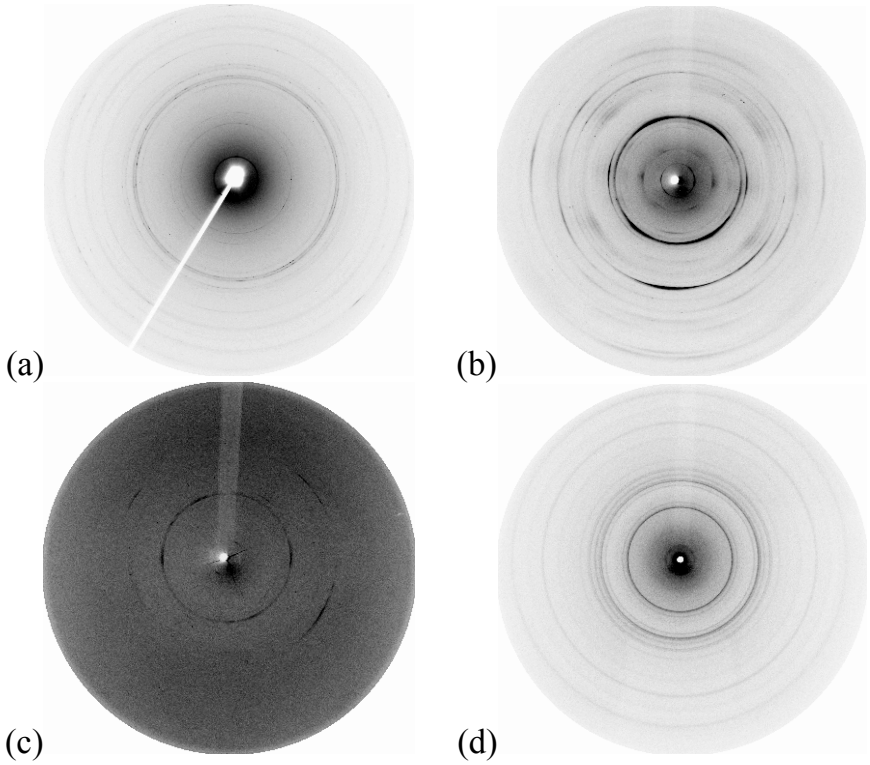

Figure 2.1 Raw synchrotron x-ray powder diffraction patterns collected on (a) tobermorite 14 Å (Plombierite), (b) After heating the plombierite at 135 ºC for 1 day, (c) Pressurized at 6 GPa after the heating, and (d) synthesized C-S-H at ambient condition.

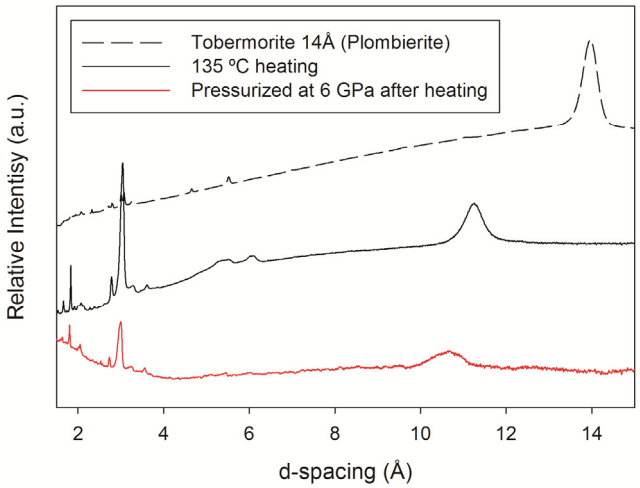

Figure 2.2 Integrated synchrotron x-ray powder diffraction patterns of tobermorite 14 Å (Plombierite) at ambient condition, after heating at 135 ºC for 1 day, and pressurized at 6 GPa after the heating.

Figures 2.1 and 2.2 show some cases of synchrotron x-ray diffraction. Pure crystalline material of tobermorite 14 Å from Crestmore, CA, US was measured at

ambient, after heating 135 ºC, and under 6 GPa of hydrostatic pressure using the DAC. Mar3450 image detector shows perfectly radial x-ray diffraction patterns of each sample. The white line in each Fig. 2.1(a) is from the shadow of a beam stopper which is to protect the detector. Then, the overall experimental detail of the x-ray was refined by lattice parameter of standard materials. Standard reference material of lanthanum hexaboride 660 (From National Institute of Standard and Technology (NIST)) was selected due to its low strain broadening and distinct x-ray diffraction positions [45]. Integrating the 2D radial images in Fig. 2.1 yields regular powder diffraction patterns shown in Fig. 2.2. From refining the high-resolution powder diffraction patterns, lattice parameters and detail atomic positions can be obtained. As shown in Fig. 2.2, the lattice parameters are shifting under heating and pressing. Its analysis will be discussed in more detail in chapters 3 and 4. In addition, a preferred orientation in sample can be detected using the Mar3450 detector. For instance, the density variation of a ring in Fig. 2.1(b) shows the preferred orientation at certain direction. The orientation distribution of ettringite crystals was analyzed by Wenk et al. using micro-diffraction technique [50] and they provides elastic anisotropy of ettringite aggregates in concrete. This phenomenon is especially important in earth and planetary science to determine seismic velocity in deep in the earth [51, 52].

The x-ray source can be applied to two different types of materials; the first is based on the structure factor, which relates the diffraction pattern to lattice planes in the long-range ordered crystal [53]. Combining with Rietveld refinement, both lattice parameters and detail atomic position can be determined. The second method is to determine the distribution of atom pairs which yields radial-distribution function (RDF) or pair-distribution function (PDF). This method is mainly applied to amorphous materials without long-range order or highly disordered structure [54]. The C-S-H gel, main binding material in cement is poorly crystalline material. It does have few diffraction peaks but has long-range disorder which makes the x-ray analysis on C-S-H gel difficult. However, synchrotron x-ray diffraction has a potential to overcome the difficulty. Recently Skinner et al. [23] suggests that the nanostructure of C-S-H resembled the crystal structure of tobermorite 11 Å by using reverse Monte Carlo simulation starting from the structure proposed by Merlino [55]. The conclusion was obtained by simulating the diffuse x-ray scattering due to the nanostructured features of the material by a Gaussian shape broadening of the structure factor of tobermorite family. Also they proposed that the loss of coherent scattering on the C-S-H sample above about 3.5 nm reflects the maximum crystallite size of the material. Based on the results, Battocchio et al. [56] could refine nanostructure of C-S-H (Ca/Si=1.0 and 1.5, 4 months) by using high energy x-ray diffraction and the tobermorite phases as starting refining materials as well. Similarly, the nanostructure of geopolymeric gel (main binding material in new green cement

made of fly ash and/or slag) were recently studied by total scattering measurement using synchrotron facilities [57-61]. In those works, they considered not only geometrical distribution of atoms but the electrical connectivity were also considered by combining a first-principle calculation. In section 3.1, more detailed discussion on the analog of nanostructure between C-S-H gel and tobermorite family will be found.

2.2 First-Principles Calculation

In this section, theoretical background on first-principles calculation will be introduced. Atomistic modeling of materials has become an essential research tool to study various problems in physics, chemistry, material science engineering [62-75]. First-principles or *ab initio* calculation refers to a method that is independent of any empirical input data and is only based on the electronic properties of a material. Therefore, the first-principles calculation can be the most accurate as a bottom-up simulation approach, but also can be the most expensive calculation compared to other atomistic calculations including Molecular Dynamics (MD) or Monte-Carlo (MC) simulations [76]. The Schrödinger equation can theoretically describe the statics and dynamics of materials within the scale of molecules and atoms. The ground-state energy E of an N-electron system can be found from the lowest-energy solution of the Schrödinger equation:

$$\hat{H}\Psi = E\Psi \qquad \text{- (2.1)}$$

where $\hat{H}$ is the Hamiltonian operator and E is the total energy of the system. For a given system of n electrons and N nuclei, in the absence of external fields, the Hamiltonian can be written as below [77]:

$$\hat{H} = \hat{T}_e + \hat{T}_n + \hat{V}_{en} + \hat{V}_{ee} + \hat{V}_{nn} \qquad \text{- (2.2)}$$

where $\hat{T}$ and $\hat{V}$ stand for the kinetic and potential energy of the system and the subscribe e and n refers to electron and nuclei, respectively. For example, $\hat{T}_e$ shows the kinetic energy of electrons and $\hat{V}_{en}$ total potential energy of the all interacting electrons with nuclei, and so on. These energy operator terms can be expressed as,

$$\hat{T}_e = -\frac{\hbar^2}{2m_e}\sum_{i=1}^{n}\nabla_i^2 \qquad \text{- (2.3)}$$

$$\hat{T}_n = -\frac{\hbar^2}{2M_I}\sum_{I=1}^{N}\nabla_I^2 \qquad \text{- (2.4)}$$

$$\hat{V}_{en} = -\sum_{i=1}^{n}\sum_{I=1}^{N}\frac{Z_I e^2}{\left|\vec{R}_i - \vec{r}_I\right|} \qquad \text{- (2.5)}$$

$$\hat{V}_{ee} = \frac{1}{2}\sum_{i=1}^{n}\sum_{\substack{j=i \\ i\neq j}}^{n}\frac{e^2}{\left|\vec{r}_i - \vec{r}_j\right|} \qquad \text{- (2.6)}$$

$$\hat{V}_{nn} = \frac{1}{2}\sum_{I=1}^{N}\sum_{\substack{J=1 \\ J\neq I}}^{N}\frac{Z_I Z_J e^2}{\left|\vec{R}_I - \vec{R}_J\right|} \qquad \text{- (2.7)}$$

In above equations, Z_i is the atomic number of the nucleus i. $\vec{R}$ and $\vec{r}$ are the vector distance of nuclei and electron, respectively. m_e and M_I are mass of electron of e and nuclei of I, respectively. The wavefunction $\Psi_i(\vec{r})$ is not an observable, hence it doesn't have a physical meaning, but its square specifies the probability distribution of finding electrons at a certain determinate state, $\vec{r}$.

$$n(\vec{r}) = N\int d^3r_2 ... d^3r_N \left|\psi(\vec{r},\vec{r}_2,...,\vec{r}_n)\right|^2 \qquad \text{- (2.8)}$$

$n(\vec{r})d^3r$ is the average number of electrons in volume element d^3r at position $\vec{r}$, and also the probability to find one electron in this volume element. However, as a consequence of the electron-electron pair interaction in the Hamiltonian operator H, Eqn. (2.1) is not so easy to solve for many-body system, N>1. Thus, except for a few simple systems, the analytical solution of the Schrödinger equation is impossible [78, 79].

However, the variational approach provides a convenient way to solve this many body problem. It said that for any given trial wave function $\Psi_{trial}(\vec{r})$, E_{trial} will only be minimal, (i.e. ground state energy) if $\Psi_{trial}(\vec{r})$ is the ground state wave function. Thus the foundation of constructing a wave function is minimizing the system energy (i.e., to find wave function of ground state) to get close as much as possible to the ground state energy. The main difficulty is how to solve the Schrödinger equation of Eqn. (2.1) for the total wave functions for a large system of interacting electrons in a periodic potential set given by the positions of the nuclei. Density functional theory (DFT) is a powerful theory to deal with this problem [80]. The DFT begins with the Born-Oppenheimer approximation [81]. It provides a separation of electronic and nuclear motions, and allows one to treat the electrons with frozen nuclei positions. Because the nuclei are thousands of times heavier than the electrons, it can be made that the Born-Oppenheimer approximation in which the electrons are in their ground state for each set of nuclear positions ($\vec{R}_1$, $\vec{R}_2$,…). Then the electronic ground-state energy $E(\vec{R}_1,\vec{R}_2,\ldots)$ serves as a potential energy surface for the nuclei. Minimizing this function yields the equilibrium structure [82]. According to this approximation,

the wave function of a system can be separated into electronic (Φ_e) and nuclear (Φ_n) functions, hence Eqn. (3.1) simplifies to

$$\hat{H}\Phi_e(\vec{r})\Phi_n(\vec{r}) = E_{total}\Phi_e(\vec{r})\Phi_n(\vec{r}) \qquad \text{- (2.9)}$$

In Eqn. (2.9), nuclei are first assumed to be frozen with respect to the motion of electrons. In other words, the key of Born-Oppenheimer approximation is that electrons can instantaneously adjust to the nuclei positions for any movement of nuclei.

In DFT, the electronic energy equals the sum of the electron-nuclear attraction, Coulomb energy, and a universal functional. The universal functional consists of electronic kinetic energy and exchange-correlation energy. The main point in DFT is the Coulomb energy and exchange-correlation energy can be described as functional forms of the electron densities with a great accuracy. In other word, the central quantity is the electron probability density, $\rho(\vec{r})$, itself which is a function of the position $\vec{r}$. Thus the energy, E, is a functional of $\rho(\vec{r})$ and is written as E[ρ]. This simply means that there is a single energy, E, corresponding to the entire function $\rho(\vec{r})$. The exact ground state energy functional of an n-electron system can be expressed as

$$E_{total}[\rho] = E_{KE}[\rho] + E_{NE}[\rho] + E_{E_H}[\rho] + E_{XC}[\rho] \qquad \text{- (2.10)}$$

The square brackets denote a functional dependence. In Eqn. (2.10), the first term is the kinetic energy of the electrons and its functional form is not known explicitly. However, the concept of wave function by [80] Kohn and Sham can express the kinetic energy of electrons as

$$E_{KE}[\rho] = \frac{\hbar^2}{2m_e}\sum_{i=1}^{n}\int \psi_i^*(\vec{r})\nabla^2\psi_i(\vec{r})d\vec{r} \qquad \text{- (2.11)}$$

In above, the one-electron orbital, $\psi_i(\vec{r})$, are the Kohn-Sham molecular orbitals. They are related to, but different from, the ground state charge density, $\Psi_i(\vec{r})$. The $\psi_i(\vec{r})$ orbitals are the solutions to the Kohn-Sham Equations discussed below. The ground state charge density can be obtained from

$$\rho(\vec{r}) = \sum_{i=1}^{n}\left|\psi_i(\vec{r})\right|^2 \qquad \text{- (2.12)}$$

The second term in Eqn. (2.10) is the electron-nuclei interactions

$$E_{NE}[\rho] = -\sum_{I=1}^{N} \int \frac{Z_I e^2}{4\pi\varepsilon_0 \left|\vec{r} - \vec{R}_I\right|} \rho(\vec{r}) d\vec{r} \qquad \text{- (2.13)}$$

where the summation is over all *i* nuclei; the $\left|\vec{r} - \vec{r}_i\right|$ is the separation of point $\vec{r}$ and nucleus *i*; ε_0 is the dielectric constant in vacuum and *e* is the charge of an electron. The third term is the classical coulombic energy between the electron densities at point $\vec{r}_a$ and point $\vec{r}_b$;

$$E_{E_H}[\rho] = \frac{1}{2} \int \frac{\rho(\vec{r}_a)\rho(\vec{r}_b)e^2}{4\pi\varepsilon_0 \left|\vec{r}_a - \vec{r}_b\right|} d\vec{r}_a \vec{r}_b \qquad \text{- (2.14)}$$

This term is referred to as the Hatree energy, because it corresponds to the coulombic interactions between average electron densities at $\vec{r}_a$ and $\vec{r}_b$. The last term is Eqn. (2.10), $E_{XC}[\rho]$, is the exchange-correlation energy, which cannot be explicitly defined. This term modifies the energy to take account for the fact that the motion of each electron is influenced by the motions of all the other electrons. $E_{XC}[\rho]$ can also be assumed as a function of the electron density. It will be introduced below with two different approximations.

It was mentioned above that the kinetic energy of the electrons is given in terms of the Kohn-Sham orbitals, $\psi_i(\vec{r})$, which are found by solving the Kohn-Sham equations:

$$\left(-\frac{\hbar^2}{2m_e}\nabla^2 - \sum_{I=1}^{N} \frac{Z_I e^2}{4\pi\varepsilon_0 \left|\vec{r} - \vec{r}_I\right|} + \int \frac{\rho(\vec{r}_a)e^2}{4\pi\varepsilon_0 \left|\vec{r}_a - \vec{r}_b\right|} + V_{XC} \right) \psi_i(\vec{r}) = \varepsilon_i \psi_i(\vec{r}) \quad \text{- (2.15)}$$

where the ε_i are the orbital energies and the exchange-correlation potential, V_{XC} is

$$V_{XC}[\rho] = \frac{\delta E_{XC}[\rho]}{\delta\rho} \qquad \text{- (2.16)}$$

Although the DFT is an exact method to deal with the ground state properties of systems, it depends on the exchange-correlation energy, E_{XC} in Eqn. (2.16) that is unknown and can only be approximated as a functional of electron densities. Commonly used exchange-correlation potentials are the local density approximation (LDA, [83, 84]) and generalized gradient approximation (GGA, [85]). The LDA is based upon exact exchange energy for a uniform electron gas,

which can be obtained from the local values of the electron density at that point, or from the correlation energy of a uniform electron gas [86, 87].

$$E_{XC}^{LDA}[\rho] = \int d^3r\, n(\vec{r})\, \varepsilon_{xc}^{unif}\left(\rho(\vec{r})\right) \qquad \text{- (2.17)}$$

where $\varepsilon_{xc}^{unif}\left(\rho(\vec{r})\right)$ is the exchange-correlation energy per electron for an electron gas of uniform spin densities, ρ. The functional derivative gives the first-order change of the functional with density. However, for a molecule the electronic density is obviously not uniform. For example, the LDA correctly predicts the mechanical behavior of silicates and oxides but tends to overbind structures [88]. Hence, as the alteration of LDA, the General Gradient Approximation (GGA), uses functional forms that are dependent on both the local electron density and its gradient at that point. For an electron density that varies slowly over space, the exchange-correlation energy has an expansion in powers of the density gradients [89, 90]. The generalized gradient approximation is [85, 91-95]

$$E_{XC}^{GGA}[\rho] = \int d^3r\, n(\vec{r})\, \varepsilon_{xc}^{GGA}\left(\rho(\vec{r}), \nabla\rho(\vec{r})\right) \qquad \text{- (2.18)}$$

GGA predicts much more accurate atomization energies compared to that from LDA calculation. Thus the GGA and its extensions are extensively used in chemistry. This, however, is likely to underbind structures and overestimate mechanical properties. For example, the equations of state for MgO from the LDA and GGA lie below and above experimental data, respectively [96]. Ultimately, the appropriateness of the LDA and GGA should be evaluated by comparing its predictions to experiments.

Another approximation is a pseudopotential approximation. It substitutes the strong potential from the nucleus and core electrons for a slowly varying potential with the same scattering properties. This allows one to apply plane-waves to the basis functions to represent the electronic wave functions. In chapters 3 and 4, ultrasoft pseudopotentials were applied where the projector augmented wave method is used to model the interactions between valence electrons and the core [97].

The Kohn-Sham equations are solved iteratively and self-consistently because the solution, $\rho(\vec{r})$, itself is a part of the Hamiltonian (i.e., electron density, ρ) on the left hand side of Eqn. (2.15). The self-consistent calculation starts from making a guess of the charge densities by superimposing the atomic densities. Then, assuming a functional form is available for E_{XC}, the electron density can be used to solve Eqn. (2.15) to give an initial set of Kohn-Sham orbital $\psi_i(\vec{r})$. From

these orbitals, an improved electron density can be found via Eqn. (2.12), which can be re-inserted into the Kohn-Sham equations of Eqn. (2.15). This iterative process can be continued until the electron density and E_{XC} have converged. Then, the total energy can be obtained from Eqn. (2.10) [80]. Finally the equilibrium geometry of the system is determined by the condition that the forces acting on individual nuclei vanish.

$$F_I = -\frac{\delta E_{total}[\rho]}{\delta R_I} \qquad \text{- (2.19)}$$

where R_I is the coordinate of the I-th nucleus. During the self-consistent solutions, two main convergence criteria should be decided: the size of the basis and special integration points over reciprocal space. In the pseudopotential method, the size of the basis is determined by the maximum kinetic energy of the plane waves. Sampling of the Brillouin zone is treated with the special integration points, which has been proved to yield rapid convergence [98]. With the appropriate convergence criteria, the optimized atomic system can be found by iterating the self-consistent calculation until the forces between atoms in Eqn. (2.19) vanishes. This first-principles technique based on DFT have demonstrated remarkable accuracy for materials in both ambient and external conditions [88]. In chapters 3 and 4, application of the first-principles calculation and detail simulation criteria will be shown. In addition, the performance of LDA and GGA pseudopotentials for calcium silicate hydrates and calcium aluminate hydrates will be evaluated by high-pressure x-ray experiments.

2.3 Review on equations of state and micromechanics

In this section, thermodynamical equation of states and micromechanics will be reviewed. To get macroscopic properties from micro-scale experiment and/or simulation, thermodynamics and micromechanics are prerequisite. From high pressure x-ray diffraction, unit cell volume variation under pressure can be directly measured. The equation of state allows computation of a bulk modulus, fundamental mechanical constant of a material. In isothermal equation of state, a crystal is treated as a homogeneous, anisotropic medium. Large finite strain is the frame invariant Eulerian strain f:

$$E_{ij} = \frac{1}{2}(f_{ii} + f_{ii} - f_{ik} f_{ik}) \qquad \text{- (2.20)}$$

$$f_{ii} \equiv 1 - \frac{a_i}{X_i} = 1 - \left(\frac{V_0}{V}\right)^{1/3} \qquad \text{- (2.21)}$$

with

$$X_i - a_i = f_{ij} X_j \qquad \text{- (2.22)}$$

where a_i is the position vector of a point in a material in the unstrained state and X_i is the position vector of the same point after the material is compressed. V_0 and V are unstrained volume and strained volume in assumption of cubic crystal structure of a material. Therefore E_{ij} in Eqn. (2.20) is invariably assumed to be isotropic in finite strain expansions of a free energy used to derive equation of state.

$$E_{ij} = -f\delta_{ij} \qquad \text{- (2.23)}$$

Substituting Eqn. (2.21) into Eqn. (2.20) yields the invariant Eulerian strain:

$$f = \frac{1}{2}\left[\left(\frac{V_0}{V}\right)^{2/3} - 1\right] \qquad \text{- (2.24)}$$

Then the Helmholtz free energy of a compressed state can be expanded in a Taylor series in terms of the Eulerian strains.

$$F(f) = a + bf + cf^2 + df^3 + \ldots \qquad \text{- (2.25)}$$

Under isothermal state, thermodynamic pressure can be expressed as below.

$$P = -\left(\frac{\partial F}{\partial V}\right)_T \qquad \text{- (2.26)}$$

Since the reference state V_0 is the zero pressure state, b term in Eqn. (2.25) vanishes.

$$P = -\left(\frac{\partial f}{\partial V}\right)\left(\frac{\partial F}{\partial f}\right)_T = -\left(\frac{\partial f}{\partial V}\right)\left(2cf + 3df^2\right) \qquad \text{- (2.27)}$$

In addition, the isothermal bulk modulus K is a partial derivative of pressure with volume.

$$K = -V\left(\frac{\partial P}{\partial V}\right) = -V\left(\frac{\partial P}{\partial f}\right)\left(\frac{\partial f}{\partial V}\right) \qquad \text{- (2.28)}$$

Then, from Eqn. (2.24) and (2.27), the bulk modulus can be expressed in terms of volume and Eulerian strain.

$$K = \frac{1}{9}V_0^{-\frac{1}{3}}V^{-\frac{2}{3}}\left(1+2f\right)^{3/2}\left\{5\left(2cf+3df^2\right)+\left(1+2f\right)\left(2c+6df\right)\right\} \text{- (2.29)}$$

If we define isothermal bulk modulus at zero pressure as $K_0 \equiv \lim_{\substack{f\to 0 \\ V\to V_0}} K$, the constant c in Eqn. (2.29) can be expressed in terms of K_0 and V_0.

$$c = \frac{9}{2}K_0V_0 \qquad \text{- (2.30)}$$

Then, the 2nd order Birch-Murnaghan equation of state can be derived as below [99].

$$P(V) = \frac{3}{2}K_0\left\{\left(\frac{V}{V_0}\right)^{-\frac{7}{3}} - \left(\frac{V}{V_0}\right)^{-\frac{5}{3}}\right\} \qquad \text{- (2.31)}$$

Similarly, additional definition of $K_0' \equiv \lim_{\substack{f\to 0 \\ V\to V_0}} \frac{\partial K}{\partial P}$ yields the 3rd order Birch-Murnaghan equation of state [99].

$$P(V)=\frac{3}{2}K_0\left\{\left(\frac{V}{V_0}\right)^{-\frac{7}{3}}-\left(\frac{V}{V_0}\right)^{-\frac{5}{3}}\right\}\left[1+\frac{3}{4}\left(K_0^{'}-4\right)\left\{\left(\frac{V}{V_0}\right)^{-\frac{2}{3}}-1\right\}\right] \quad \text{- (2.32)}$$

At absolute zero temperature, the Helmholtz free energy, F is same with internal energy, E (F=E-TS). This is important for theoretical calculation of isothermal bulk modulus, K_0 and its derivative, K_0'. Then integrating pressure (in Eqn. 2.32) with volume gives below equation of state in terms of energy instead of pressure.

$$E(V)=E_0+\frac{9V_0K_0}{16}\left\{\left[\left(\frac{V}{V_0}\right)^{-\frac{2}{3}}-1\right]^3K_0^{'}+\left[\left(\frac{V}{V_0}\right)^{-\frac{2}{3}}-1\right]^2\left[6-4\left(\frac{V}{V_0}\right)^{-\frac{2}{3}}\right]\right\} \quad \text{- (2.33)}$$

The 2nd order Birch-Murnaghan equation of state (Eqn. 2.31) is identical with 3rd order Birch-Murnaghan equation of state with $K_0'= 4$ (Eqn. 2.32). From curve fitting of Eqn. 2.31 and 2.32, isothermal bulk modulus and its pressure derivative can be obtained through high pressure x-ray diffraction experiment. Detail application will be shown in chapters 3 and 4.

In addition to the large strain finite strain, elastic constants of a crystal structure could be experimentally or theoretically computed from applying infinitesimal strains to the structure [100]. The elastic tensor coefficients are calculated from a simple stress-strain relationship,

$$\sigma_i=\sum_{j=1}^{6}C_{ij}\varepsilon_j \quad \text{- (2.34)}$$

where the tensor has 3 to 21 independent constants depending on the type of crystal systems. Below 4 crystal systems are common in concrete system.

Triclinic crystal system:

$$C_{ij}=\begin{bmatrix} C_{11} & C_{12} & C_{13} & C_{14} & C_{15} & C_{16} \\ & C_{22} & C_{23} & C_{24} & C_{25} & C_{26} \\ & & C_{33} & C_{34} & C_{35} & C_{36} \\ & & & C_{44} & C_{45} & C_{46} \\ & & & & C_{55} & C_{56} \\ sym. & & & & & C_{66} \end{bmatrix} \quad \text{- (2.35)}$$

Monoclinic crystal system:

$$C_{ij} = \begin{bmatrix} C_{11} & C_{12} & C_{13} & \cdot & C_{15} & \cdot \\ & C_{22} & C_{23} & \cdot & C_{25} & \cdot \\ & & C_{33} & \cdot & C_{35} & \cdot \\ & & & C_{44} & \cdot & C_{46} \\ & & & & C_{55} & \cdot \\ sym. & & & & & C_{66} \end{bmatrix} \qquad \text{- (2.36)}$$

Orthorhombic crystal system:

$$C_{ij} = \begin{bmatrix} C_{11} & C_{12} & C_{13} & \cdot & \cdot & \cdot \\ & C_{22} & C_{23} & \cdot & \cdot & \cdot \\ & & C_{33} & \cdot & \cdot & \cdot \\ & & & C_{44} & \cdot & \cdot \\ & & & & C_{55} & \cdot \\ sym. & & & & & C_{66} \end{bmatrix} \qquad \text{- (2.37)}$$

Cubic crystal system:

$$C_{ij} = \begin{bmatrix} C_{11} & C_{12} & C_{12} & \cdot & \cdot & \cdot \\ & C_{11} & C_{12} & \cdot & \cdot & \cdot \\ & & C_{11} & \cdot & \cdot & \cdot \\ & & & C_{44} & \cdot & \cdot \\ & & & & C_{44} & \cdot \\ sym. & & & & & C_{44} \end{bmatrix} \qquad \text{- (2.38)}$$

where $C_{44}=1/2(C_{11}-C_{12})$ in isotropic cubic case. The connection between the averaged elastic properties of an aggregate and a single crystal is studied by [101, 102]. As a method for calculating the elastic moduli of an aggregate of crystals, Voigt (1928) proposed an equation of averaging over all possible lattice orientations with expressing the stress in a single crystal in terms of the given strain [103]. Reuss (1929) proposed, on the other hand, an averaging method of expressing the strain in terms of the given stress [104]. In the first Voigt model, it is assumed that the strain is uniform throughout an aggregate. Thus, the forces between grains cannot be in equilibrium. On the other hand, Reuss assumes that the stress is uniform so the distorted grains cannot fit together. It was assumed by Voigt that

$$K_V = \frac{(C_{11} + C_{22} + C_{33}) + 2(C_{12} + C_{23} + C_{31})}{9} \qquad \text{- (2.39)}$$

$$G_V = \frac{(C_{11}+C_{22}+C_{33})-(C_{12}+C_{23}+C_{31})+3(C_{44}+C_{55}+C_{66})}{15} \quad \text{- (2.40)}$$

And by Reuss that

$$K_R = \frac{1}{(S_{11}+S_{22}+S_{33})+2(S_{12}+S_{23}+S_{31})} \quad \text{- (2.41)}$$

$$G_R = \frac{15}{4(S_{11}+S_{22}+S_{33})-4(S_{12}+S_{23}+S_{31})+4(C_{44}+C_{55}+C_{66})} \quad \text{- (2.42)}$$

where the compliance tensor, S, is the inverse of the elasticity tensor, $S = C^{-1}$. It is interesting to note that only nine of the 21 independent elastic constants for the single crystal are considered in these equations for the macroscopic moduli. Finally, it is found that the measured moduli for the aggregate lie between the Reuss and Voigt values.

$$K_R \le K \le K_V, \; K_{VRH} = \frac{K_V + K_R}{2} \quad \text{- (2.43)}$$

$$G_R \le G \le G_V, \; G_{VRH} = \frac{G_V + G_R}{2} \quad \text{- (2.44)}$$

The corresponding estimates of Poisson's ratio **v** and Young's modulus E can be obtained by substituting the values of K and G in Eqns (2.43 and 2.44).

.

$$\eta = \frac{(3K-2G)}{2(3K+G)} \quad \text{- (2.45)}$$

$$E = \frac{9KG}{(3K+G)} \quad \text{- (2.46)}$$

In chapters 3 and 4, the presented tensor coefficients and averaged mechanical properties of various crystals will be calculated and compared with experiments.

3. High Pressure X-ray Diffraction and First-Principles Calculation Studies on Calcium Silicate Hydrates

3.1 Calcium Silicate Hydrates in Concrete

By mixing water and portland cement, calcium silicate hydrates (C-S-H) precipitates as the principal binding phase of concrete [1, 13, 105-107]. C-S-H is a nonstoichiometric compound and the hyphen refers to different arrangement of CaO, SiO_2 and H_2O. While C-S-H in ordinary portland cement paste is called C-S-H gel, synthesized C-S-H in laboratory refers to C-S-H(I) or C-S-H(II) depending on calcium silicon ratio.

C-S-H(I) has a Ca/Si ratio around 1. When CaO and SiO_2, or C_3S is reacted in dilute aqueous system, the C-S-H(I) [108] can be produced which results a broad basal reflection of x-ray powder diffraction. That indicates that the material has roughly two-dimensional order. Like C-S-H gel, C-S-H(I) can accommodate a considerable concentration of defects such as the omission of bridging tetrahedra [25], or variations in the contents of interlayer. These changes allow variations in Ca/Si ratio and the silicate chain length. On the other hand, C-S-H(II), first proposed by Taylor [108], is produced from a reaction of C_3S or C_2S with excess water [109]. X-ray diffraction, electron diffraction, infrared spectroscopy, and compositional analysis suggest that C-S-H(II) is an imperfect version of jennite, while C-S-H(I) is more similar to tobermorite phases [27, 110].

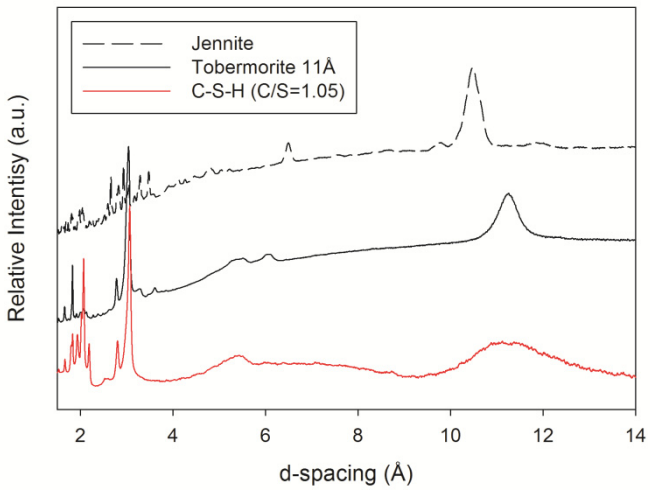

Figure 3.1 The analogy of x-ray diffraction patterns between synthesized C-S-H (red, bottom) and crystalline calcium silicate hydrates (normal tobermorite 11 Å and jennite).

In 1952, Taylor first suggested that C-S-H(I) and C-S-H(II) are semi-crystalline versions of crystalline calcium silicate hydrates: tobermorite 14 Å and jennite, respectively [25, 26]. His hypothesis is still recognized as the primary models for the nanostructure of C-S-H gel [107]. As described in chapter 2, due to its complexity, the precise structure of C-S-H gel is still unresolved at the nanoscale. Even though C-S-H gel is poorly crystalline but it has some short-range order at sub-nanometer scales. Much of the findings at this level are obtained through comparison with fully crystalline calcium silicate hydrate minerals [108, 110-114]. For instance, Figure 3.1 shows the analog of x-ray diffraction patterns of C-S-H(I), tobermorite 11 Å, and jennite. The tobermorite 11 Å crystal was obtained from heating tobermorite 14 Å mineral from Crestmore, California, US. The jennite mineral is from Zeilberg, Germany. While the C-S-H(I) has broad hump peak around 10-12 Å, tobermorite 11Å and jennite have distinct basal diffraction peaks. It shows the similarity of nanostructure among the calcium silicate phases but more variation of layer thickness in C-S-H(I). Detail argument on the analog of x-ray diffraction pattern will be discussed in section 3.4.

Table 3.1 Crystallographic data of calcium silicate hydrates.

Chemical formula	Mineral name	Crystal system	Space group	a (Å)	b (Å)	C (Å)	α (º)	β (º)	γ (º)	Ref.
$Ca_5Si_6O_{16}(OH)_2 \cdot 7(H_2O)$	Tobermorite 14 Å (Plombierite)	Mono.	B11b	6.74	7.43	27.99	90	90	123	[3]
$Ca_5Si_6O_{16}(OH)_2$	Tobermorite 14 Å (Plombierite)	Ortho.	I2mm	5.63	3.71	27.99	90	90	90	[115]
	Tobermorite 9Å (Natural)	Tri.	C-1	11.2	7.30	9.57	101	93	90	[116]
	Clinotobermorite 9Å	Mono	A2/m	5.58	3.65	18.78	90	92.8	90	[115]
	Tobermorite 9Å (riverseideite)	Ortho.	Pnmm	5.58	3.65	18.78	90	90	90	[115]
$Ca_5Si_6O_{17} \cdot 2.5(H_2O)$	Tobermorite 9Å (syn.)	Ortho.	-	11.1	7.32	19.2	90	90	90	[117]
$Ca_9Si_6O_{18}(OH)_6 \cdot 8(H_2O)$	Jennite	Tri.	P-1	10.9	7.27	10.93	101	97	110	[118]
$Ca_9Si_6O_{16}(OH)_{10} \cdot 2(H_2O)$	Metajennite	Tri.	P-1	10.6	7.28	9.51	101	106	110	[118]
$Ca_6Si_6O_{17}(OH)_2$	Xonotlite	Mono.	P-1	8.71	7.36	7.01	90	90	102	[119]
$Ca_3Si_2O_6(OH)_2 \cdot 2(H_2O)$	Awfillite	Mono.	C1c1	16.3	5.63	13.23	90	135	90	[120]
$Ca_4Si_6O_{15}(OH)_2 \cdot 3(H_2O)$	Gyrolite	Hexa.	P61	9.74	9.74	22.40	96	92	120	[121]

Besides tobermorite and jennite, over 30 crystalline calcium silicate hydrate phases which have similar structure with the C-S-H gel have been proposed [122]. Among many calcium silicate hydrate phases, the crystallographic data of several important minerals is summarized in Table 3.1. The crystalline calcium silicate hydrates are still quite complex because of the large ionic radius and electropositive character of calcium, which allow a number of different types of coordination with oxygen [26]. The various coordination of oxygen can explain important characteristics of the calcium silicate hydrate phases such as variation in composition and degree of polymerization. Figure 3.2 presents a schematic

stability diagram, in the Ca/Si ratio 0.6 to 1.0, and temperature range up to 300 ºC, presenting the relative stabilities of C-S-H phases [123]. This stability diagram also indicates C-S-H(I) is tobermorite-like structure and C-S-H(II) is jennite-like structure [4, 124].

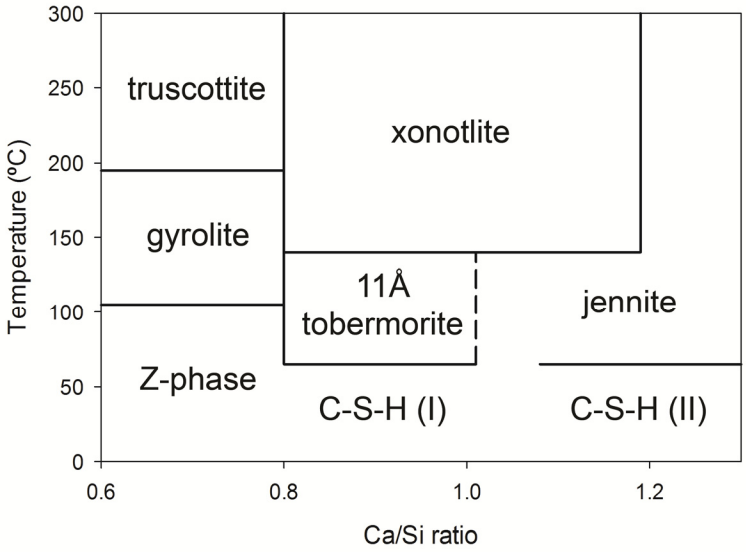

Figure 3.2 Schematic diagram showing the relative stability of part of the C-S-H compounds prepared under hydrothermal conditions [123].

The particular interest in the crystalline calcium silicate hydrates is stemmed not only from their analogous with C-S-H gel, but also from their properties as cation exchangers. It indicates that the materials can be used in potential applications of nuclear and hazardous waste disposal. That has motivated deep studies over few decades to understand the structural aspects of these minerals, especially in case of tobermorite 11 Å due to its ambiguous behavior under thermal treatment. As described earlier, the interlayer space between Ca-O layers in tobermorite can accommodate a significant amount of water molecules and cause hydration of tobermorite. Thus tobermorites can exist in several hydration states which can be characterized by basal spacings of 14.0, 11.3, and 9.3 Å [25, 26, 125, 126]. McConnell [117] found natural tobermorite compounds of 11 Å-14 Å hydrates transform to tobermorite 11 Å upon heating at 80-100 ºC; then transform to tobermorite 9 Å upon heating at 300 ºC. The notations 9 Å, 11 Å, and 14 Å refer to the size of basal spacings of 9.3, 11.3, and 14 Å. In addition, he designated the tobermorite 9 Å as riverseideite and tobermorite 14 Å as plombierite [117]. Recently clinotobermorite found at Fuka, Japan [127, 128] which has a basal spacing of 11 Å and shrinks to 9 Å spacing upon heating at 300 ºC [127, 128]. Their crystallographic data is summarized in Table 3.1.

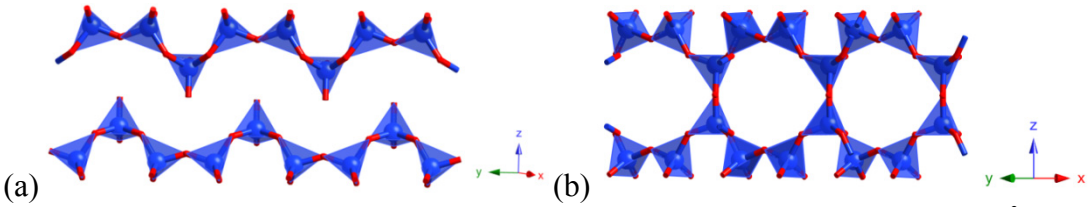

Figure 3.3 (a) The single dreierketten silicate structure in Hamid tobermorite 11 Å [129] (b) double (condensed) dreierketten silicate structure in Merlino tobermorite 11 Å [55].

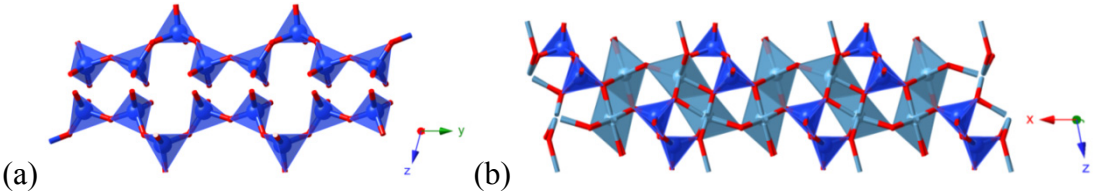

Figure 3.4 (a) Silicate chains in tilleyite ribbon projected along [100] in jennite crystal structure. (b) Tilleyite ribbon projected along [010]. The silicate tetrahedra and calcium oxide octahedra are denoted in dark blue and light blue, respectively [118].

The crystal structure of the tobermorite 11 Å was determined by Hamid [129] and Merlino [55]. Si tetrahedron chains attached to Ca-O layers are covalently connected each other in Merlino structure and exist as an independent chain in the Hamid structure. Various experimental techniques such as NMR were deployed to characterize the chains in tobermorite [130-134]. These chains are Wollastonite type or Dreierketten with finite lengths of 2, 5, 8, 3n-1, where n is an integer. The minimum length of the repeating silicate oxide unit contains three tetrahedra (Fig. 3.3). Two connected tetrahedra share an oxygen are called paired tetrahedra while the third tetrahedron, which is in a different chemical site and its vortex points out of the Ca-O layer, is called bridging tetrahedron shown in Fig. 3.3 (b) [4, 8, 135]. In Merlino's structure, two dreierketten silicate chains attached on the separate Ca-O layers are linked by chemical bonding (i.e., Si-O-Si bond), whereas in the Hamid model, no chemical bond exists between two silicate chains (i.e., independent layers). The proposed chain types are visualized in Fig. 3.3. In addition, Merlino et al. could explain their diffuse diffraction patterns and unusual systematic absences by order-disorder (OD) character [136-140]. In addition, there are some specimens of tobermorite 11 Å that do not shrink to 9 Å upon heating and are called anomalous tobermorite to distinguish them from normal tobermorite which shrink to 9 Å. A possible reason for such strange behavior has been hypothesized by Merlino et al. [55, 116, 141]. Based on their hypothesis, additional Ca ions in interlayers make interlayer unstable under heating which causes collapse of the interlayer. On the other hand, the crystal structures of jennite and its dehydrated phase (i.e. metajennite) have been recently resolved [118]. The silicate chain in jennite so called tilleyite ribbon is shown in Fig. 3.4.

The cell parameters and space groups of the various calcium silicate hydrates are collected in Table 3.1 and Table 3.2.

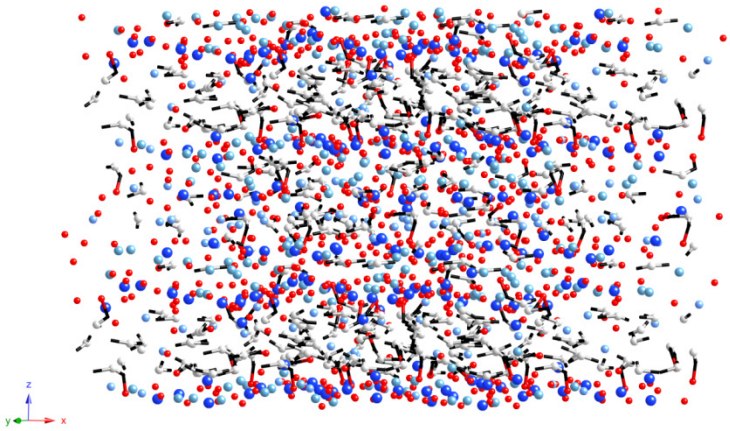

Figure 3.5 Molecular model of C-S-H proposed by Pellenq et al. [142]. Silicon, calcium, oxygen, water molecules and hydroxyl groups are denoted with dark blue, light blue, red, white spheres, and black sticks, respectively.

Structural models for C-S-H have been developed along with the structural determination of tobermorite family and jennite. At first, Taylor proposed nanophasic model as a disordered layered structure consisting of a mixture of tobermorite 14 Å and jennite for C-S-H model [4]. In this model, two different sub-crystalline phases are sandwiched with small fragments of Ca-O layers and separated from each other on a nanometer length scale. The compositional variations of Ca/Si and structural disorders can be explained in terms of the omission of silicate tetrahedra from dreierketten silicate chains [143]. The solid solution model was first proposed by Fujii and Kondo [144], and also other authors have explained the structure of C-S-H using two-component solid solution systems [15, 135, 143, 145]. This model describes C-S-H as a solid solution of a calcium silicate hydrate of tobermorite 14 Å or jennite with a low Ca/Si ratio and $Ca(OH)_2$. Recently, Pellenq et al. developed a molecular model of C-S-H particle. Given the Ca/Si ratio of 1.7 and density of 2.6 g/cm^3 from small-angle neutron scattering measurement [14], a molecular model of C-S-H is computationally constructed from grand canonical Monte Carlo simulation [142]. The model is reproduced in Fig. 3.5.

With increasing interests in mineral analogs of C-S-H at the nanoscale, their mechanical properties are undoubtedly an important part of the understanding of mechanical characteristics of C-S-H. Section 3.2 reports the structural and mechanical properties of several C-S-H crystals from high-pressure x-ray diffraction experiments. Section 3.3 presents first-principles calculations of the

structural and mechanical properties of tobermorite family and jennite minerals. Section 3.4 compares the experimental and theoretical results.

3.2 High Pressure X-ray Diffraction Experiments on Calcium Silicate Hydrates

3.2.1 Normal tobermorite 11Å

Section 3.2 presents the high pressure x-ray diffraction experiments on C-S-H minerals (normal and anomalous tobermorite 11 Å, tobermorite 9 Å, and jennite). Early x-ray diffraction studies of tobermorite 11 Å suggested single dreierketten (i.e., Hamid model), then later ^{29}Si NMR data suggested double dreierketten which corresponds to Merlino model [114, 129]. Figures 3.6 and 3.7 show the proposed crystal structure of tobermorite 11 Å by Hamid [129] and Merlino et al. [55, 116], respectively.

The whole compositional range for tobermorite 11 Å, without considering substitution of silicon by aluminum in the tetrahedra, spans between $Ca_4Si_6O_{15}(OH)_2 \cdot 5(H_2O)$ and $Ca_5Si_6O_{17} \cdot 5(H_2O)$ as summarized in Table 3.2. If there is a Al substitution with Si, the charge imbalance is compensated by a higher Ca content or higher hydroxide substitution [146]. That has been confirmed by the structural determination on a synthetic specimen of tobermorite 11 Å of composition of $Ca_5Si_{5.5}Al_{0.5}O_{16}(OH) \cdot 5(H_2O)$, through Rietveld refinement of synchrotron radiation powder diffraction data [147]. Taylor and McConnell found the lattice parameters of $\boldsymbol{a}$ = 11.3 Å, $\boldsymbol{b}$ = 7.3 Å, and $\boldsymbol{c}$ = 22.6 Å as orthorhombic structure [117, 125]. Starting from the 'average' structure of orthorhombic structure, various crystallographic determinations have been conducted (Summarized in Table 3.2). One of ordered tobermorite 11 Å is monoclinic, space group P21, with the unit cell dimensions of $\boldsymbol{a}$ = 6.69 Å, $\boldsymbol{b}$ = 7.39 Å, $\boldsymbol{c}$ = 22.779 Å, and $\boldsymbol{\gamma}$ = 123.49 º [129].

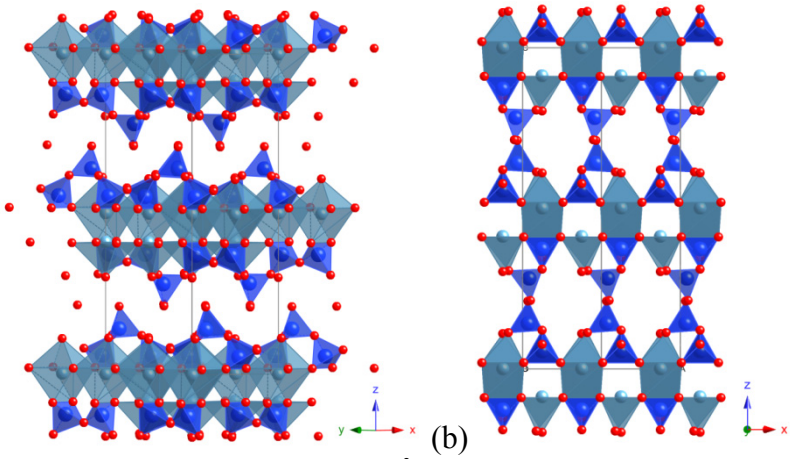

(a) (b)

Figure 3.6 Crystal structure of tobermorite 11 Å projected along (a) [110] and (b) [010] proposed by Hamid [129]. Silicate chains, calcium octahedral, and oxygen atoms are shown as dark blue, light blue tetrahedra, and red spheres, respectively.

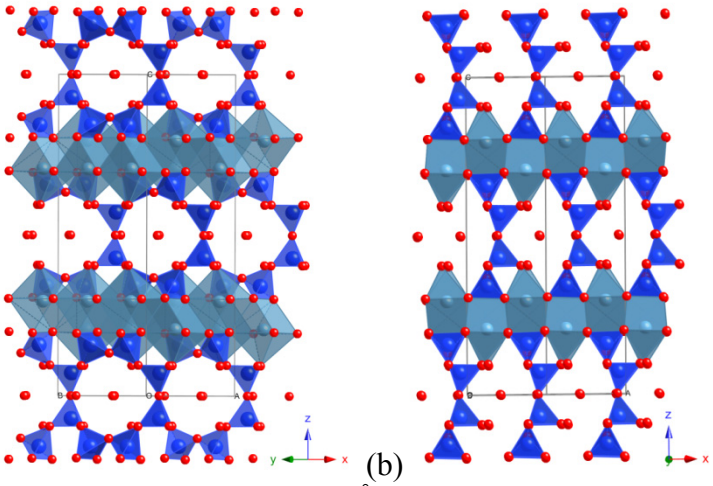

(a) (b)

Figure 3.7 Crystal structure of tobermorite 11 Å projected along (a) [110] and (b) [010] proposed by Merlino et al. [55]. Same graphical notation in Fig. 3.1 is used.

As described in previous section, some tobermorite 11 Å, often referred as normal tobermorite, shrink to tobermorite 9Å form upon heating at 300 ºC, while others, called anomalous tobermorite, do not [126]. The mechanism of the formation of the 9 Å phase in the dehydration process is not cleared yet. This phenomenon had been previously explained with the existence of interlayer Si-O-Si linkage: (double chains) in anomalous tobermorites and their absence (single chains) in normal tobermorite. But, Merlino et al. proposed another hypothesis based on zeolitic calcium cations in the cavities of the structure considering NMR experimental data [55, 115, 116]. They referred the case of clinotobermorite, $Ca_5Si_6O_{17}\cdot 5H_2O$ which has the zeolitic calcium cations in the cavities and double silicate chains. Upon heating at 300 ºC, the water molecules are lost and a wide rearrangement occurs around the Ca cations involving decondensation. Based on

the hypothesis, they resolved several normal and anomalous tobermorite 11 Å with different calcium occupancy using Order-Disorder (OD) theory. The resulting crystal chemical formula of the normal tobermorite from Urals is $Ca_{4.5}Si_6O_{16}(OH)\cdot 5(H_2O)$. The crystal structures of the Hamid model and anomalous tobermorite 11 Å models are summarized in Table 3.2.

Table 3.2 Crystallographic data of tobermorite 11 Å.

Chemical formula	Mineral name	Crystal System	Space group	a (Å)	b (Å)	c (Å)	α (º)	β (º)	γ (º)	Ref.
$Ca_{2.25}Si_3O_{7.5}(OH)_{1.5}\cdot H_2O$	Hamid model	Mono.	P1121	6.69	7.39	22.77	90	90	123	[129]
	Hamid model	Ortho.	Imm2	5.59	3.70	22.78	90	90	90	[129]
$Ca_4Si_6O_{15}(OH)_2\cdot 5(H_2O)$	Anomalous-Merlino	Mono.	B11m	6.74	7.39	22.49	90	90	123	[55]
	Anomalous-Merlino	Ortho.	F2dd	11.3	7.39	44.97	90	90	90	[55]
$Ca_5Si_6O_{17}\cdot 5(H_2O)$	Clinotobermorite	Mono.	A2/m	5.64	3.67	22.64	90	97	90	[115]
	Merlino model	Ortho.	I2mm	5.63	3.69	22.49	90	90	90	[115]
$Ca_{4.5}Si_6O_{16}(OH)\cdot 5(H_2O)$	Normal-Merlino	Mono.	B11m	6.73	7.37	22.68	90	90	123	[55]
$Ca_{4.9}Si_{5.5}Al_{0.5}O_{16.3}(OH)_{0.7}\cdot 5(H_2O)$	Normal-Yamazaki	Mono.	B11m	6.73	7.35	22.61	90	90	123	[147]

In the present study, tobermorite 14 Å from Crestmore, California, US which is identical sample with Bonaccorsi et al. ($Ca_5Si_6O_{16}(OH)_2\cdot 7H_2O$)[3] was examined for high pressure x-ray diffraction measurements of normal tobermorite 11 Å and tobermorite 9 Å. Previously, Oh et al. [148] conducted high pressure x-ray diffraction experiment on the tobermorite 14 Å. The major element composition analysis was performed in the UC Berkeley Electron Microprobe Laboratory on a SX-51 electron microprobe equipped with five tunable wavelength dispersive spectrometers using the software, Probe for EPMA. Operating conditions were 40 degrees takeoff angle, a beam energy of 15 keV, beam current of 10 nA, and the beam diameter of 1 micron. Oxygen was calculated by cation stoichiometry and included in the matrix correction. The obtained chemical composition is summarized in Table 3.3. Although there is a 4 % Al substitution, main Ca/Si ratio of 0.77 is similar with that of Bonaccorsi et al. ($Ca_5Si_6O_{16}(OH)_2\cdot 7H_2O$, Ca/Si=0.83) [3].

Table 3.3 Chemical composition of normal tobermorite 11 Å (Major oxide weight %).

	SiO_2	Al_2O_3	TiO_2	FeO	MnO	MgO	CaO	Na_2O	K_2O	BaO	TOTAL
Tobermorite 14 Å (Crestmore, California, US)	28.39	4.15	-0.01	0.00	-0.09	-0.01	21.97	0.19	1.23	0.07	55.79
	33.65	4.13	-0.01	-0.17	0.10	-0.01	28.36	0.19	1.93	0.12	68.25
	41.52	6.05	0.01	0.03	-0.08	0.00	28.37	0.23	1.72	0.20	77.94
	36.76	5.26	0.00	0.01	0.13	-0.02	27.86	0.20	1.61	0.05	71.77
	25.46	3.63	-0.01	-0.01	-0.03	-0.01	20.25	0.28	2.07	0.06	51.63
	26.26	3.30	-0.02	-0.08	-0.15	0.02	19.57	0.33	2.00	0.03	51.23
	21.40	3.34	0.01	-0.03	0.23	0.02	19.49	0.30	1.75	0.16	46.60
	25.24	2.67	-0.01	-0.06	-0.04	0.00	16.54	0.24	2.05	0.04	46.67
	40.78	5.24	0.01	0.05	-0.04	-0.02	30.29	0.26	1.57	0.14	78.24
	32.63	4.40	0.00	0.05	0.02	-0.01	28.44	0.42	2.29	0.16	68.37
Average	**31.21**	**4.22**	**0.00**	**-0.02**	**0.01**	**0.00**	**24.11**	**0.26**	**1.82**	**0.10**	**61.71**

The thermal study carried on the tobermorite 14 Å in Advanced Light Source. The sample was vacuum-heated at targeting temperature (125, 135, 150, 180, 300, 330, and 400 ºC) for 24 hours then x-ray of 0.6199 Å wavelength was exposed. The variation of basal spacing is shown in Fig. 3.9. A first collapse of basal peak occurs at 125 ºC, when the tobermorite 11 Å phase forms [149]. A broad x-ray diffraction peak around 11.3 Å indicates some variations of layer thickness. As temperature increases, the broad peak becomes sharper until 180 ºC then diffuse at higher temperature. At 300 ºC, 9.3 Å peak which indicates the formation of tobermorite 9 Å was observed with coexistence of broad peak around 11 Å. At 400 ºC, the 11Å peak was totally disappeared and only 9.3 Å peak has survived. It is interesting to note that unexpected basal peak at 10 Å was observed at 180 ºC which indicates a meta-stable phase between tobermorite 11 Å and 9 Å. For high pressure x-ray diffraction, a sample should be pure as much as possible to reduce any factors affecting the experiment. Thus tobermorite 14 Å heated at 150 ºC and 400 ºC for 24 hours were selected for high pressure x-ray diffraction experiments of tobermorite 11 Å and 9 Å, respectively.

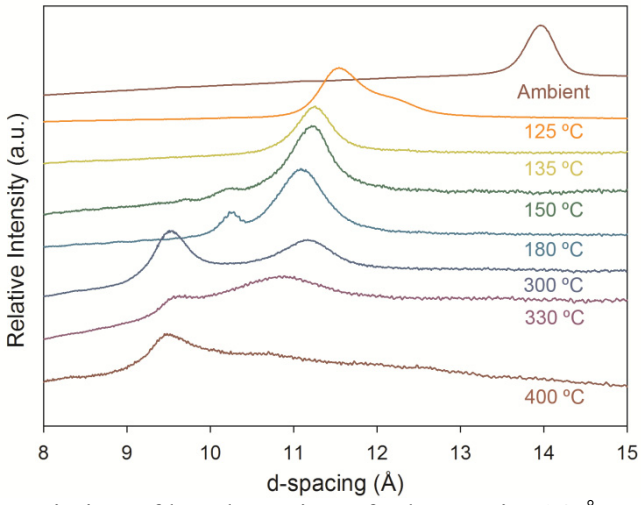

Figure 3.8 Variation of basal spacing of tobermorite 14 Å under heating.

Ambient condition phase identification and the high pressure powder x-ray diffraction experiment of normal tobermorite 11 Å were carried out at beamline 12.2.2 of the Advanced Light Source [38], using a synchrotron monochromatic x-ray beam. The wavelength of the beam was 0.6199 Å. The National Bureau of Standards LaB_6 powder diffraction standard was used to calibrate the distance between the sample and detector (i.e. 280.6 mm). High pressures were generated using a diamond anvil cell (DAC). The mineral was finely ground and mixed with a pressure medium and a few chips of ruby. Samples were placed into a sample chamber within a gasketed diamond anvil cell. The sample chamber size was 180-µm diameter, with 75 µm thickness. The sample was equilibrated for about 20 min at each pressure. Exposure times of 600 sec were chosen to collect powder diffraction patterns. A 4:1 mixture of methanol:ethanol was used as a pressure-transmitting medium. The pressure was measured at off-line using the ruby fluorescence technique [150].

All two-dimensional x-ray data were radially integrated to give powder diffraction patterns using the fit2d program [151]. The integrated x-ray diffractions at different pressures are compared in Fig. 3.10 with arbitrary peak intensity. Diffraction peak positions of (002), (110), (017), (0010), (127), (130), and (217) were used to calculate the orthorhombic unit cell volume of normal tobermorite 11 Å [115, 129]. Changes in lattice parameters and a unit cell volume of the samples were computed using the XFit [152] and Celref program [153] (Fig. 3.10 and Table 3.4). Accurate volume (around 1% error) was refined up to 6 hydrostatic pressure. However, the basal spacing became significantly diffuse around the 6 GPa and totally disappeared at 6.3 GPa. Repeated measurement at 6.3 GPa confirmed the collapse of layer structure of normal tobermorite 11 Å as shown in Fig. 3.10.

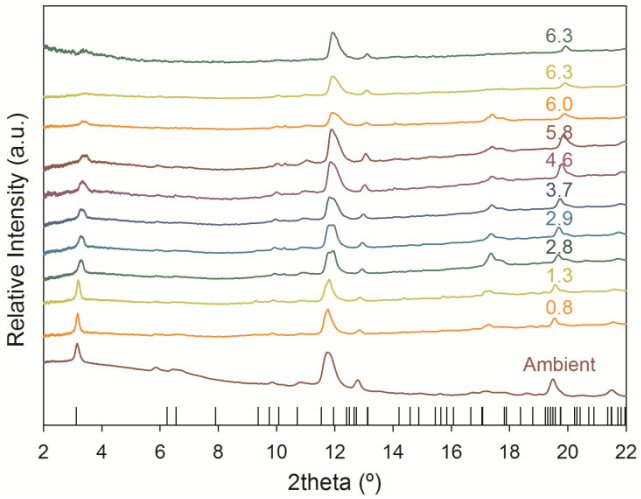

Figure 3.9 Measured x-ray diffraction patterns of normal tobermorite 11 Å (λ = 0.6199 Å) with alcohol mixture (Methanol:ethanol=4:1). Bottom peaks indicate reference peak positions from [129].

Table 3.4 High pressure x-ray diffraction results of normal tobermorite 11 Å.

Normal tobermorite 11 Å experiment (M:E=4:1)				
P (GPa)	**a (Å)**	**b (Å)**	**c (Å)**	**V (Å^3)**
ambient	5.59(2)	3.64(1)	22.71(9)	462(3)
0.8(1)	5.57(2)	3.62(1)	22.62(8)	457(3)
1.3(1)	5.57(2)	3.61(1)	22.58(9)	455(3)
2.8(2)	5.54(3)	3.60(2)	22.2(1)	445(5)
2.9(2)	5.54(3)	3.60(2)	22.2(1)	444(5)
3.7(3)	5.52(3)	3.60(2)	22.1(1)	441(5)
4.6(3)	5.51(3)	3.58(2)	22.0(1)	436(5)
5.8(4)	5.48(3)	3.58(2)	22.0(2)	433(6)
6.0(4)	5.48(3)	3.58(2)	21.9(2)	431(5)

At ambient pressure with the lattice parameter ***a*** = 5.59(2) Å , ***b*** = 3.64(1) Å, ***c*** = 22.71(9) Å, and unit-cell volume V=462(3) Å^3 that agree well with a previous study by Bonaccorsi et al. [115], which found ***a*** = 5.63 Å , ***b*** = 3.69 Å, ***c*** = 22.49 Å, and unit-cell volume V=467 Å^3 within I2mm orthorhombic crystal structure. The error ranges of lattice parameters contained in Table 3.4 and shown in Fig. 3.11(a) are seen to increase at high pressure. This is due to a peak broadening effect in the DAC. A weighted linear least-squares fit was applied to the data to assess both pressure and volume errors [154]. The pressure normalized volume data were fitted by a second- and third- order finite strain equation of state (i.e., Murnaghan and Birch-Murnaghan equation of state) [99]. The below Birch-Murnaghan equation of state (BM EoS) is driven in section 2.3.

$$P(V)=\frac{3}{2}K_0\left\{\left(\frac{V}{V_0}\right)^{-\frac{7}{3}}-\left(\frac{V}{V_0}\right)^{-\frac{5}{3}}\right\}\left[1+\frac{3}{4}\left(K_0^{'}-4\right)\left\{\left(\frac{V}{V_0}\right)^{-\frac{2}{3}}-1\right\}\right] \quad \text{- (3.1)}$$

where V is volume of the unit cell, V_0 is initial volume of the unit cell at ambient pressure, P is the pressure applied to a material, K_0 is the bulk modulus at zero pressure, and K_0' is the derivative of the bulk modulus at zero pressure. By defining the normalized pressure, F and the Eulerian strain, f, the third order BM EoS is reorganized into the linear form:

$$F(f)=K_0-1.5K_0(4-K_0^{'})f \quad \text{- (3.2)}$$

$$\text{and } f=\frac{1}{2}\left[\left(\frac{V}{V_0}\right)^{-2/3}-1\right] \quad \text{- (3.3)}$$

In a plot of *F* versus *f*, the y-intercept and slope of graph gives the bulk modulus K_0 and its derivative K_0' by the weighted linear least-squares fitting. The 3rd BM EoS determines a bulk modulus of 62(4) GPa, a derivative of 9.7 and ambient volume of 463(3) Å^3 with a goodness of fit of $R^2 = 0.995$. In addition, the 2nd BM EoS fit gives a bulk modulus of 71(4) GPa and same initial volume with $R^2 = 0.989$. The 2nd and 3rd BM EoS fitting results are shown in Fig. 3.10 (b) and 3.11.

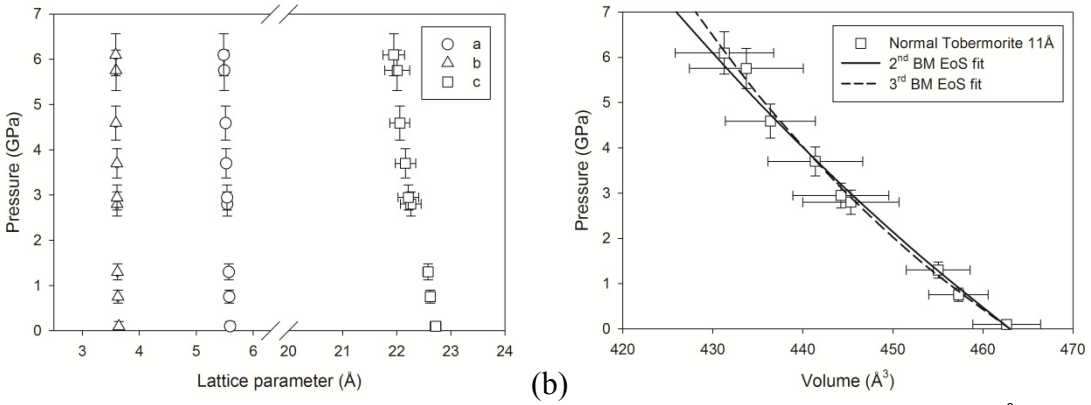

Figure 3.10 (a) Variation of axial lattice parameters of normal tobermorite 11 Å under pressure. (b) Refined unit cell volumes of normal tobermorite 11 Å under pressure. The 2nd and 3rd order BM EoS fittings give the bulk modulus of 71(4) GPa and 62(4) GPa.

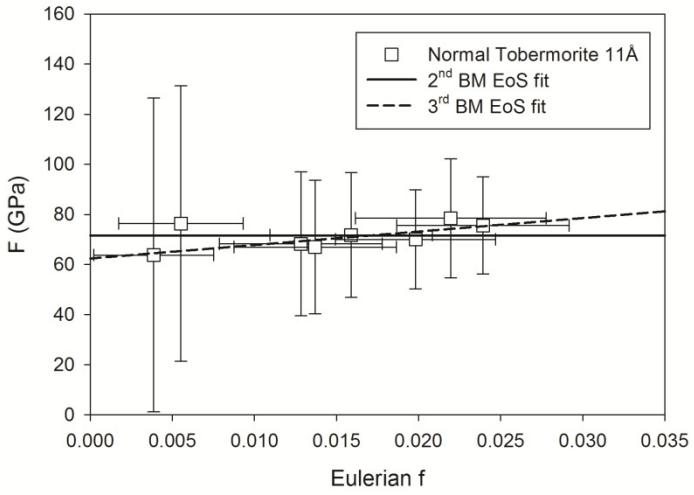

Figure 3.11 F-f plot of normal tobermorite 11 Å.

3.2.2 Anomalous tobermorite 11 Å

As discussed in section 3.2.1, the thermal mechanism of anomalous tobermorite 11 Å was recently proposed by Merlino et al. [55, 115, 116]. Based on the hypothesis, while the substantial zeolitic calcium causes the collapse of basal spacing, few zeolitic calcium cations reside in the cavities of anomalous tobermorite 11 Å. Therefore, no requirement of proper calcium coordination is caused by the dehydration and the specimen preserves the basal spacing of 11.3 Å. Due to the absence of the zeolitic cation and the weakness of the hydrogen bonding of the water molecules with the oxygen atoms of the framework, it was concluded that the crystal chemical formula of the anomalous tobermorite from Wessels Mine is $Ca_4Si_6O_{15}(OH)_2 \cdot 5H_2O$. Similarly, the crystal structure of anomalous tobermorite 11 Å was resolved by OD theory and its crystal system can be monoclinic with B11m and orthorhombic with F2dd. Lattice parameters with the two systems are summarized in Table 3.2. Figure 3.12 compares the crystal structure of anomalous and normal tobermorite 11 Å proposed by Merlino et al. [55, 115, 116] .

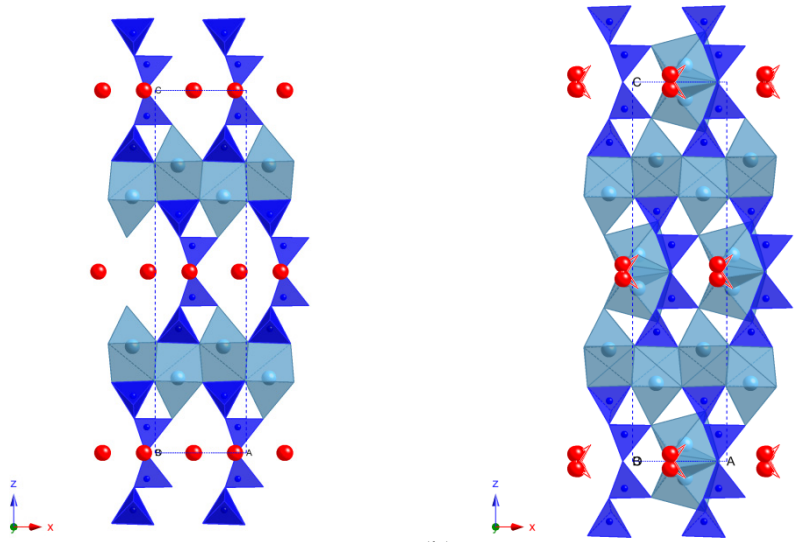

(a) (b)

Figure 3.12 Crystal structure of anomalous tobermorite 11 Å from Wessels mine, South Africa (a) and normal tobermorite 11 Å from Bashenov, Urals (b). The structures are projected along [010] and proposed by Merlino et al. [55, 116]. Same graphical notation in Fig. 3.1 is used.

In this study, anomalous tobermorite 11 Å was found from Mine Lac D'Amiante, Quebec, Canada. Ambient x-ray diffraction experiments show it did not shrink under heating over 300 ºC for 24 hours. Electron microprobe analysis (i.e., identical procedure described in section 3.2.1) indicates it does not have any

Al while tobermorite 14 Å from Crestmore, CA contains 4 % Al. The microprobe result is summarized in Table 3.5. It is interesting to note that the measured Ca/Si ratio is 1.1 which has almost 40 % more calcium contents compared to another anomalous tobermorite 11 Å from Wessels mine (Ca/Si = 0.67) [55]. More detailed discussion on chemical composition and compressibility of normal and anomalous tobermorite will be presented in section 3.4.

Table 3.5 Chemical composition of anomalous tobermorite 11 Å (Major oxide weight %).

	SiO_2	Al_2O_3	TiO_2	FeO	MnO	MgO	CaO	Na_2O	K_2O	BaO	TOTAL
Anomalous Tobermorite 11 Å (Lac D'Amiante Mine, Quebec, Canada)	34.91	0.00	0.00	0.02	0.10	0.02	38.06	0.06	0.01	-0.04	73.13
	35.18	0.07	-0.01	0.04	-0.08	-0.01	38.22	0.05	-0.01	0.00	73.38
	36.18	0.09	-0.05	0.17	0.02	0.03	39.03	0.02	0.03	0.08	75.52
	36.26	0.21	0.04	0.09	0.03	0.03	38.56	0.04	0.04	-0.11	75.11
	35.67	0.22	-0.03	0.14	0.02	0.22	38.52	0.05	-0.01	-0.06	74.70
	35.47	0.02	-0.02	-0.04	-0.11	-0.01	37.80	0.04	0.04	0.01	73.17
	36.49	0.00	0.02	0.11	-0.12	0.03	37.52	0.12	0.02	0.01	74.18
	35.97	0.00	0.00	-0.05	-0.01	0.01	37.76	0.06	0.03	-0.03	73.63
	36.52	-0.01	0.00	0.05	-0.15	0.00	39.02	0.05	0.00	0.03	75.44
	36.02	0.01	0.00	-0.12	-0.10	0.07	37.49	0.08	0.01	-0.06	73.37
Average	**35.87**	**0.06**	**0.00**	**0.04**	**-0.04**	**0.04**	**38.20**	**0.06**	**0.02**	**-0.02**	**74.22**

Ambient condition phase identification and the high pressure powder x-ray diffraction experiments were carried out at beamline 12.2.2 of the Advanced Light Source [38], using a synchrotron monochromatic x-ray beam of λ=0.6199 Å and sample-to-detector distance of 221.9 mm. The same pressure-transmitting medium of 4:1 methanol:ethanol was selected. Identical DAC used for normal tobermorite 11 Å was chosen for generating hydrostatic pressure. Integrated x-ray diffraction patterns are shown in Fig. 3.13. Peak positions based on orthorhombic unit cell with I2mm space group shows excellent agreement with a previously refined by Bonaccorsi et al. [115].

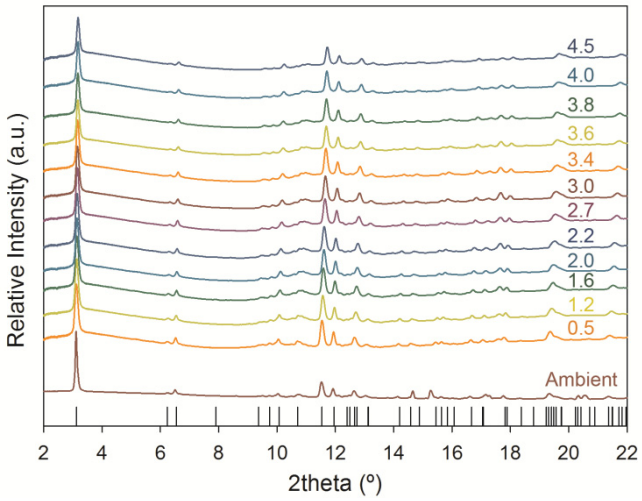

Figure 3.13 Measured x-ray diffraction patterns of anomalous tobermorite 11 Å (λ = 0.6199 Å) with alcohol mixture (Methanol:ethanol=4:1). Bottom peaks indicate reference peak positions from [129].

Table 3.6 High pressure x-ray diffraction results of anomalous tobermorite 11 Å.

Anomalous tobermorite 11 Å experiment (M:E=4:1)				
P (GPa)	**a (Å)**	**b (Å)**	**c (Å)**	**V (Å^3)**
ambient	5.621(2)	3.696(2)	22.795(9)	473.6(4)
0.5(1)	5.604(2)	3.694(2)	22.775(8)	471.5(3)
1.2(1)	5.592(2)	3.687(1)	22.699(7)	468.0(3)
1.6(1)	5.579(1)	3.680(1)	22.639(6)	464.9(2)
2.0(2)	5.571(2)	3.674(2)	22.59(1)	462.4(4)
2.2(2)	5.564(2)	3.670(1)	22.571(8)	461.0(3)
2.7(2)	5.553(1)	3.662(1)	22.487(7)	457.3(2)
3.0(2)	5.545(2)	3.656(1)	22.461(8)	455.4(3)
3.4(3)	5.536(2)	3.653(1)	22.408(8)	453.1(3)
3.6(3)	5.529(2)	3.649(2)	22.384(9)	451.6(3)
3.8(3)	5.528(2)	3.647(2)	22.34(1)	450.5(4)
4.0(3)	5.521(1)	3.641(1)	22.309(8)	448.5(2)
4.5(3)	5.514(2)	3.638(2)	22.299(9)	447.4(3)

Diffraction peak positions of (002), (004), (011), (101), (015), (110), (112), (017), (022), (024), (107), (019), (0010), (123), (118), (125), (200), (130), and (217) were used to calculate the orthorhombic unit cell volume of tobermorite 11 Å [115]. More diffraction peaks survived in the DAC compared with normal tobermorite 11 Å which would increase the accuracy of high pressure experiment. At ambient pressure, the refined lattice parameters are ***a*** = 5.621(2) Å, ***b*** = 3.696(2) Å, ***c*** = 22.795(9) Å, and unit-cell volume V=473.6(4) Å^3. As expected, smaller range of error (less than 0.1% of volume error) was achieved while

ambient volume refinement of normal tobermorite 11 Å shows 1% volume error. The ranges of lattice parameters and applied pressure are shown in Table 3.6 and Fig. 3.14. Same fitting procedure described in section 3.2.1 was applied to pressure-volume data of anomalous tobermorite 11 Å. The 3rd BM EoS determines a bulk modulus of 67(2) GPa, a pressure derivative of 1.8 and ambient volume of 475.9(4) $Å^3$ with a goodness of fit of $R^2 = 0.996$. In addition, the 2nd BM EoS fit gives a bulk modulus of 63(2) GPa and same initial volume with $R^2 = 0.997$. The 2nd and 3rd BM EoS fitting results are shown in Fig. 3.14 (b) and 3.15 (a). Figure 3.15 (b) shows the comparison of compressibility of different types of tobermorite 11 Å. While the compressibility (i.e., slope of pressure-volume plot) looks similar among high pressure experiments and first-principles calculation by Shahsavari et al. [155], the ambient volumes and its error ranges from experiments differ. Section 3.4 will cover systematic discussion on this observation.

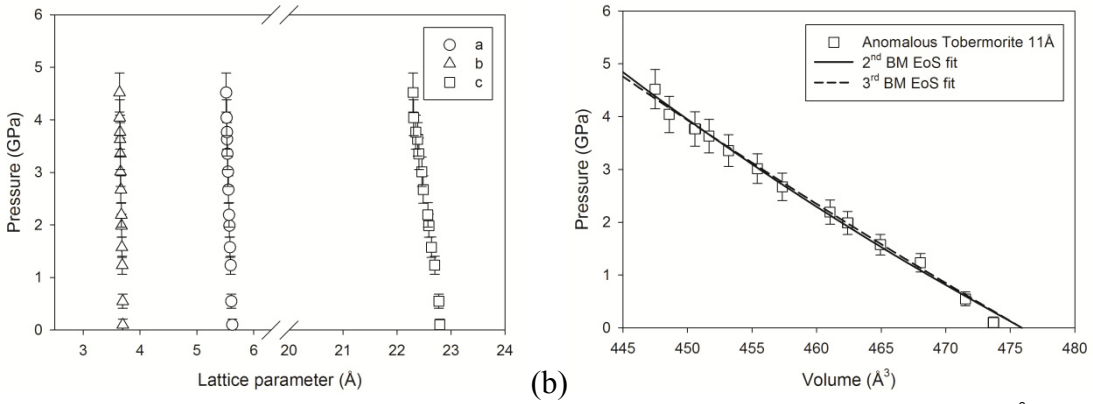

(a) (b)

Figure 3.14 (a) Variation of axial lattice parameters of anomalous tobermorite 11 Å under pressure. (b) Refined unit cell volumes of anomalous tobermorite 11 Å under pressure. The 2nd and 3rd order BM EoS fittings give the bulk modulus of 63(2) GPa and 67(2) GPa.

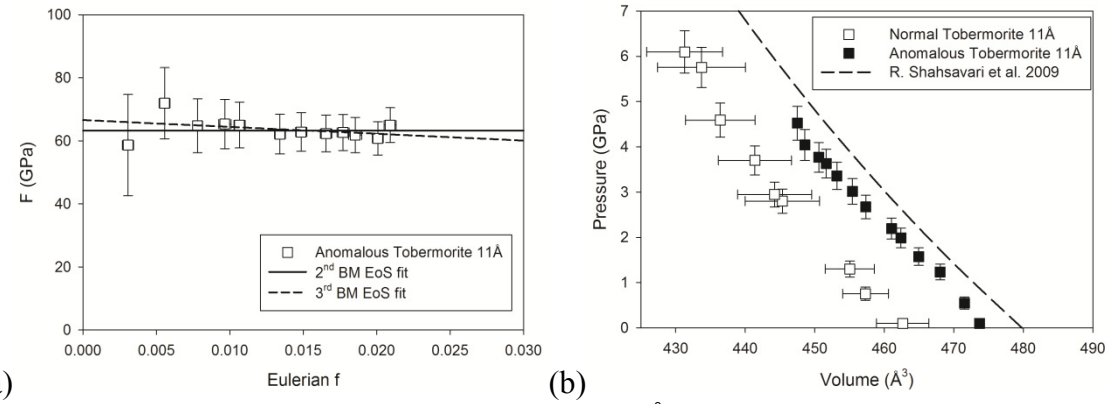

(a) (b)

Figure 3.15 (a) F-f plot of anomalous tobermorite 11Å. (b) Pressure dependent behavior of normal and anomalous tobermorite 11 Å. First-principles calculations result is reproduced from RVH bulk modulus of Shahsavari et al. [155].

3.2.3 Tobermorite 9 Å

It was found that clinotobermorite 9 Å and tobermorite 9 Å (riverseideite) can be obtained by heating of clinotobermorite and tobermorite 11 Å at 300 ºC, respectively [116]. The unit cell parameters of clinotobermorite 9 Å and natural/synthetic tobermorite 9 Å are summarized in Table 3.1. The crystal chemical formula is resolved as $Ca_5Si_6O_{16}(OH)_2$ [116]. The structure of tobermorite 11 Å is built up by complex modules and after the decondensation of the double chains, the complex layers will face each other. An ordered rearrangement occurring on both sides of each complex layer gives rise to the structure of tobermorite 9 Å. The crystal structure resolved by Merlino et al. [116] is visualized in Fig. 3.16.

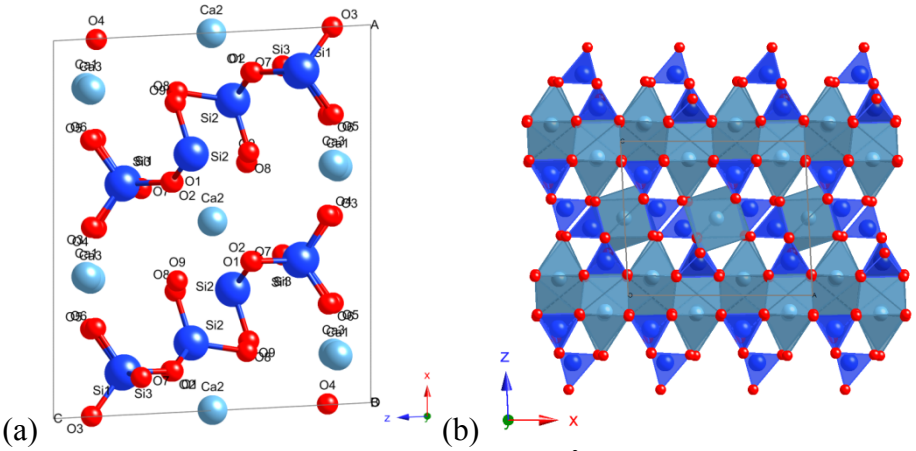

Figure 3.16 (a) A unit cell structure of tobermorite 9 Å projected along [010]. (b) Crystal structure of tobermorite 9 Å projected along [100] proposed by Merlino et al.[116]. Same graphical notation in Fig. 3.1 is used.

Tobermorite 9 Å was prepared by heating tobermorite 14 Å from Crestmore, California, US at 400 ºC for 24 hours. The x-ray diffraction in Fig. 3.8 shows sharp 9 Å basal peak without any other basal peaks which indicates an appropriate purity for high pressure x-ray diffraction experiment. The ambient condition phase identification and the high pressure x-ray diffraction experiment were performed with a synchrotron monochromatic x-ray beam of $\lambda = 0.4959$ Å and sample-to-detector distance of 235.3 mm. Identical DAC preparation described in section 3.2.1 was applied to generate pressure with a 4:1 mixture of methanol:ethanol. The integrated x-ray diffractions at different pressures are compared in Fig. 3.17 with arbitrary peak intensity. Diffraction peak positions of (105), (123), (108), (503), (430), (3110), (246), and (837) were used to calculate the orthorhombic unit cell volume of tobermorite 9 Å [117]. Although the basal peak of (101) was disappeared with the pressure-transmitting medium in DAC, the remaining peaks were survived at rather high pressure of 8.5 GPa.

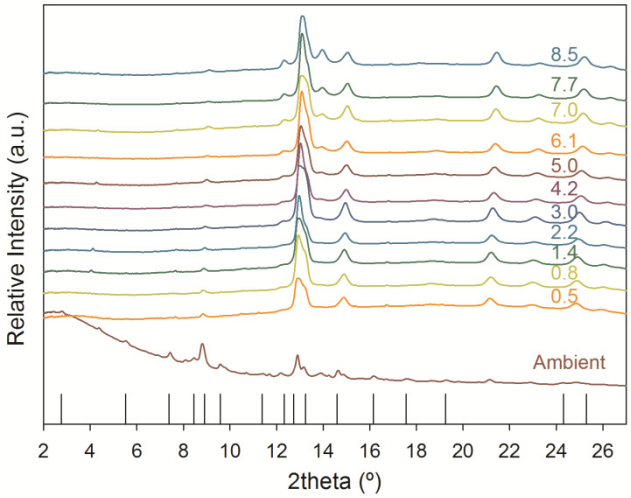

Figure 3.17 Measured x-ray diffraction patterns of tobermorite 9 Å (λ = 0.4959Å) with alcohol mixture (Methanol:ethanol=4:1). Bottom peaks indicate reference peak positions from [116].

The refined ambient lattice parameters agree well with the results of McConnell [117] with less than 1.5 % error (Table 3.1 and 3.7). Refined orthorhombic unit-cell volume is 2 % smaller than that of [117]. The identical fitting procedure described in section 3.2.1 was applied to the tobermorite. The 3rd BM EoS determines a bulk modulus of 86(6) GPa, a derivative of 20.9 and ambient volume of 1471(1) $Å^3$ with a goodness of fit of R^2 = 0.991. Next, the 2nd BM EoS fit gives a bulk modulus of 115(14) GPa and same initial volume with R^2 = 0.989. The 2nd and 3rd BM EoS fitting results are shown in Fig. 3.18 and 19.

Table 3.7 High pressure x-ray diffraction results of tobermorite 9 Å.

Tobermorite 9 Å experiment (M:E=4:1)				
P (GPa)	**a (Å)**	**b (Å)**	**c (Å)**	**V ($Å^3$)**
ambient	10.95(6)	7.25(7)	19.18(9)	1472(1)
0.5(1)	10.93(3)	7.29(5)	18.39(6)	1467.0(8)
0.8(1)	10.90(4)	7.26(7)	18.40(8)	1457(1)
1.4(1)	10.90(3)	7.25(6)	18.36(7)	1452.5(9)
2.2(2)	10.90(2)	7.21(3)	18.32(4)	1441.6(5)
3.0(2)	10.87(4)	7.18(6)	18.33(8)	1432(1)
4.2(3)	10.85(3)	7.13(5)	18.34(7)	1420.1(9)
5.0(4)	10.84(2)	7.13(3)	18.30(4)	1416.9(5)
6.1(4)	10.84(1)	7.11(1)	18.24(2)	1407.2(2)
7.0(5)	10.828(6)	7.073(9)	18.24(1)	1397.8(1)
7.7(5)	10.81(1)	7.05(2)	18.24(3)	1391.9(4)
8.5(6)	10.82(1)	7.02(2)	18.24(2)	1387.6(3)

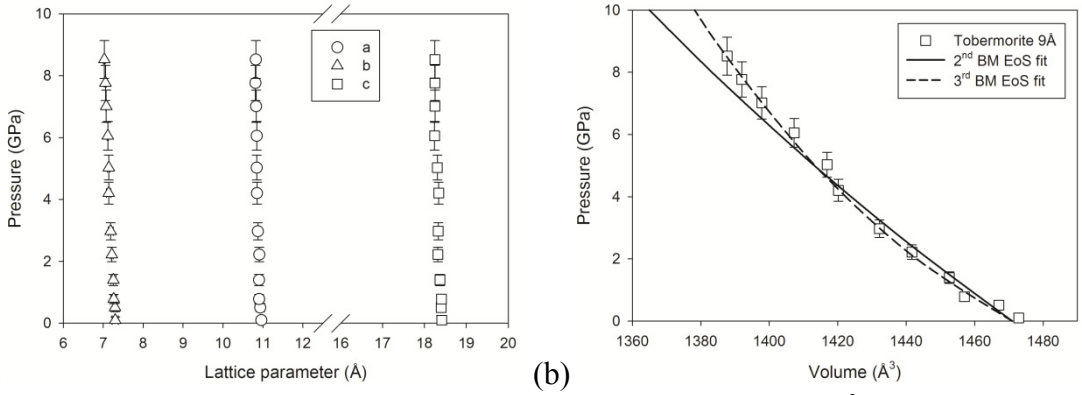

(a) (b)

Figure 3.18 (a) Variation of axial lattice parameters of tobermorite 9 Å under pressure. (b) Refined unit cell volumes of tobermorite 9 Å under pressure. The 2nd and 3rd order BM EoS fittings give the bulk modulus of 115(14) GPa and 86(6) GPa.

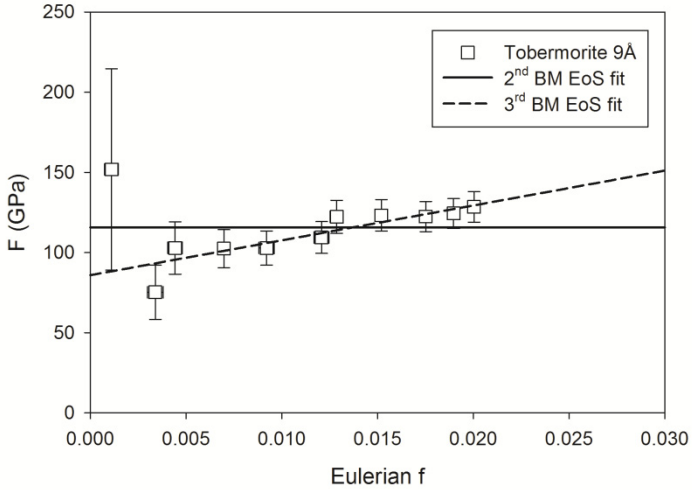

Figure 3.19 F-f plot of tobermorite 9 Å.

3.2.4 Jennite

Jennite, $Ca_9(Si_6O_{18})(OH)_6 \cdot 8H_2O$, also occurs as a natural mineral, usually in contact with tobermorite 14 Å [156]. The large amount of research on structural determination has performed on the natural and synthetic samples of jennite suggested structural similarities with tobermorite 14 Å. The atomic structure of jennite is based on a central Ca-O corrugated sheet flanked by rows of dreierketten and OH groups [15, 132, 157, 158]. It can be synthesized in suspensions of $Ca(OH)_2$ and hydrous silica at 60-100 ºC [159] and has an ideal Ca/Si ratio of 1.5. The ratio is significantly higher than that of tobermorite 14Å which only forms to Ca/Si ratios of 1.1-1.2 [160]. As discussed in section 3.1, the structure of jennite is a suitable model for C-S-H at high Ca/Si ratios, especially that formed in Ca_3SiO_5 pastes.

The crystal structure of jennite has recently been determined by direct method [118]. The structure of jennite is built up with three main characters of (1) the tilleyite ribbons of edge-sharing calcium octahedral; (2) the Si-O dreierketten chains running along [010]; and (3) the additional calcium octahedral sitting on inversion centers, which are shown as Ca5 in Fig. 3.20 (a). Dehydration also occurs as tobermorite 14 Å. Upon dehydration at 70-90 ºC, water molecules are lost which creates a deficiency of atomic coordinate of interlayer Ca. To be a stable configuration, the structure shrinks in the ***c*** direction and it leads to metajennite, $Ca_9[Si_6O_{16}(OH)_2](OH)_8 \cdot 2H_2O$. Above 350 ºC, the Ca-OH groups of metajennite are eliminated, forming an amorphous phase, which finally transforms to wollastonite and larnite (β-Ca_2SiO_4) above 800 ºC [20]. The resolved crystal structure of jennite is shown in Fig. 3.20. The unit cell parameters of jennite and metajennite are summarized in Table 3.1.

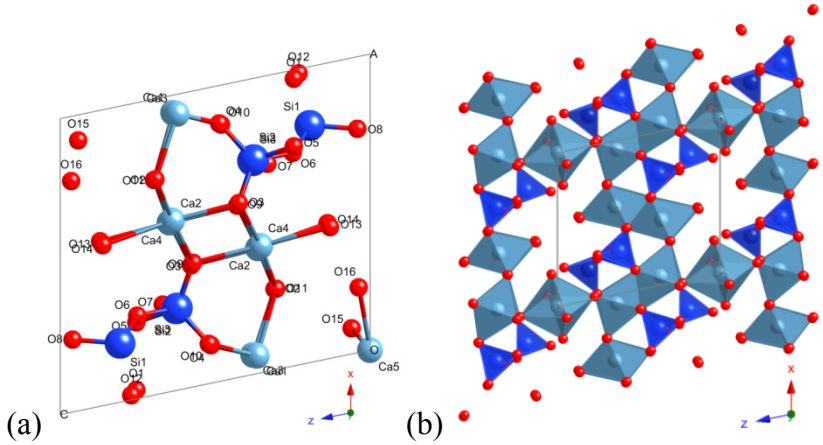

Figure 3.20 (a) A unit cell structure of jennite projected along [010]. (b) Crystal structure of jennite projected along [010] proposed by Bonaccorsi et al.[118]. Same graphical notation in Fig. 3.1 is used.

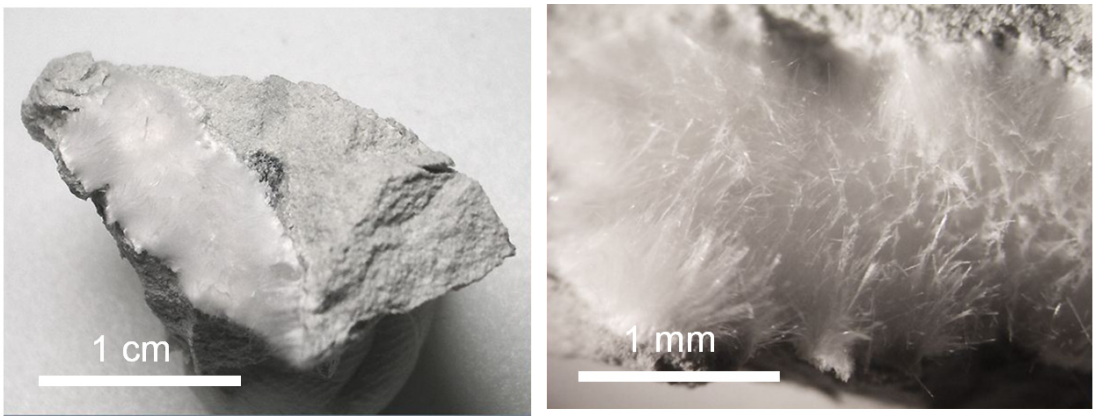

Figure 3.21 Jennite collected from Zeilberg, Bavaria, Germany. The crystal was purchased from http://minernet.it.

Pure jennite from Zeilberg, Bavaria, Germany (Fig. 3.21) was studied. Ambient and high pressure x-ray diffraction experiments were also carried out at beamline 12.2.2 of the Advanced Light Source [38], using a synchrotron monochromatic x-ray beam. Experimental detail is given in section 3.2.1. For high pressure test, a 4:1 mixture of methanol:ethanol was used in the first run and silicone oil for the second run. For the alcohol mixture, x-ray wavelength of λ=0.6199 Å and sample-to-detector distance of 221.4 mm was selected. For silicone oil, different setting of λ=0.4959 Å and 387.5 mm were chosen. The ambient and high pressure x-ray diffraction patterns of jennite are shown in Fig. 3.22 and 3.23 measureing with alcohol mixture and silicone oil, respectively. The position and relative intensities of ambient x-ray reflections agree with the data of [22].

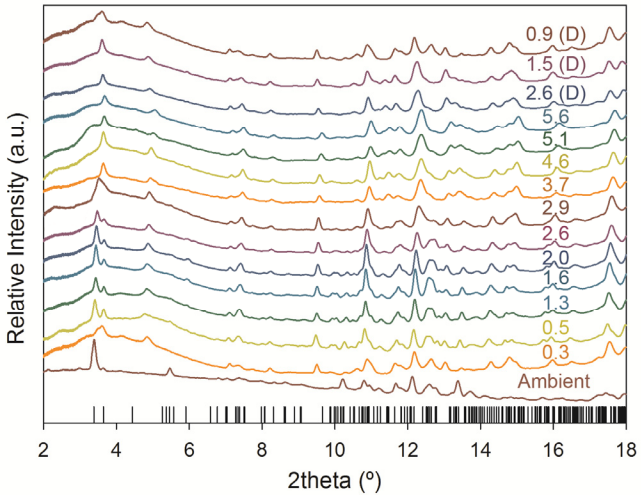

Figure 3.22 Measured x-ray diffraction patterns of jennite (λ = 0.6199 Å) with alcohol mixture (Methanol:ethanol=4:1). Bottom peaks indicate reference peak positions from [118].

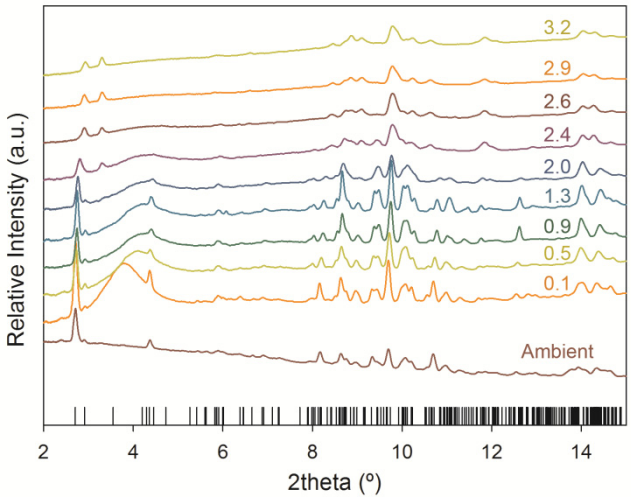

Figure 3.23 Measured x-ray diffraction patterns of jennite (λ = 0.4959 Å) with silicone oil. Bottom peaks indicate reference peak positions from [118].

Selected peak positions were summarized in Table 3.8 and 3.9. Due to its low symmetry crystal structure, it is quite complex to refine the lattice parameters of jennite. The relation between d-spacings and Miller indices in triclinic symmetry is,

$$\frac{1}{d^2} = \frac{1}{V^2}\left(S_{11}h^2 + S_{22}k^2 + S_{33}l^2 + 2S_{12}hk + 2S_{23}kl + 2S_{13}hl\right) \quad \text{- (3.4)}$$

where $S_{11} = b^2c^2\sin^2\alpha$

$S_{22} = a^2c^2\sin^2\beta$

$S_{33} = a^2b^2\sin^2\gamma$

$S_{12} = abc^2\left(\cos\alpha\cos\beta - \cos\gamma\right)$

$S_{23} = a^2bc\left(\cos\beta\cos\gamma - \cos\alpha\right)$

$S_{13} = ab^2c\left(\cos\gamma\cos\alpha - \cos\beta\right)$.

Unit cell volume of triclinic system is,

$$V = abc\sqrt{1 - \cos^2\alpha - \cos^2\beta - \cos^2\gamma + 2\cos\alpha\cos\beta\cos\gamma}\,. \quad \text{- (3.5)}$$

Least squares estimation in nonlinear regression method was used to calculate the lattice parameters of jennite [161]. X-ray diffraction peaks given in Table 3.8 and 3.9 were selected for the nonlinear regression method. Given the d-spacing and hkl information, lattice parameters of ***a***, ***b***, ***c***, ***α***, ***β,*** and ***γ*** were successfully refined by iteratively solving the Eqn. (3.4). However, at higher

pressure above 2.9 GPa, x-ray diffraction peaks overlapped too much so refinement of unit cell was unsuccessful over the pressure range regardless of the type of pressure-transmitting medium. The refined lattice parameters with alcohol mixture and silicone oil are summarized in Table 3.10 and 3.11, respectively.

Table 3.8 Measured peak positions (Å) of jennite at ambient and under pressure (Methanol:Ethanol = 4:1).

			[118]	This study	Methanol:Ethanol = 4:1					
h	k	l	ambient	ambient	0.3(1) GPa	0.5(1) GPa	1.3(1) GPa	1.6(1) GPa	2.0(2) GPa	2.6(2) GPa
0	0	1	10.4961	10.4835	10.4629	10.4183	10.3529	10.3262	10.2888	10.2193
0	1	0	9.7528	9.7680	9.7478	9.7324	9.7158	9.7144	9.6994	9.6898
0	1	1	6.5156	6.4933	5.0321	5.0195	5.0002	4.9959	4.9899	4.9782
0	0	2	5.2480	5.2291	-	-	-	-	-	-
1	1	-1	4.8438	4.8212	4.8271	4.8374	4.8186	4.8078	4.7934	4.7848
1	0	-2	4.7378	4.7338	-	-	-	-	-	-
1	-2	1	4.4545	4.4619	4.4547	4.4415	4.4314	4.4233	4.4125	4.4083
0	1	2	4.2737	4.2699	-	-	-	-	-	-
1	1	-2	4.1312	4.1196	4.1198	4.1001	4.0977	4.0917	4.0828	4.0658
1	-1	2	3.9271	3.9224	-	-	-	-	-	-
0	0	3	3.4987	3.4794	3.4788	3.4650	3.4486	3.4459	3.4421	3.4396
0	3	-1	3.3005	3.2936	3.2938	3.2879	3.2813	3.2779	3.2725	3.2675
0	2	2	3.2578	3.2508	-	-	-	-	-	-
2	-1	1	3.1847	3.1729	3.1760	3.1687	3.1568	3.1533	3.1420	3.1329
0	3	-2	3.0551	3.0481	3.0502	3.0418	3.0326	3.0294	3.0229	3.0181
0	3	1	2.9413	2.9340	2.9306	2.9257	2.9181	2.9152	2.9090	2.9034
2	-3	-1	2.8451	2.8244	-	-	-	-	-	-
0	3	-3	2.6666	2.6600	2.6578	2.6511	2.6402	2.6373	2.6314	2.6279
2	-2	-3	2.5886	2.5930	-	-	-	-	-	-
2	0	2	2.5255	2.5252	2.5084	2.5019	2.4956	2.4927	2.4904	2.4845
-4	1	-2	2.2438	-	2.2413	2.2356	2.2282	2.2286	2.2247	2.2210
2	2	1	2.1780	-	2.1676	2.1638	2.1552	2.1525	2.1476	2.1441
-5	2	0	2.0433	-	2.0425	2.0382	2.0338	2.0330	2.0293	2.0259
-5	2	-1	1.9848	-	1.9845	1.9836	1.9774	1.9765	1.9737	1.9730
4	-2	-1	1.8154	1.8100	1.8113	1.8101	1.8048	1.8010	1.7999	1.7966

Table 3.9 Measured peak positions (Å) of jennite at ambient and under pressure (Silicone oil).

			[118]	This study	Silicone oil				
h	k	l	ambient	ambient	0.1(1) GPa	0.5(1) GPa	0.9(1) GPa	1.3(1) GPa	2.0(1) GPa
0	0	1	10.4961	10.4835	10.4610	10.4020	10.3514	10.3261	10.2587
0	1	0	9.7528	9.7680	9.7281	9.7161	9.7081	-	9.7041
0	1	1	6.5156	6.4933	6.5030	6.4921	6.4565	6.4483	6.3991
0	0	2	5.2480	5.2291	5.2245	5.2020	5.1846	5.1672	5.1398
1	1	-1	4.8438	4.8212	4.8212	4.8170	4.8058	4.8030	4.6881
1	0	-2	4.7378	4.7338	4.7326	4.7133	4.6937	4.6783	-
1	-2	1	4.4545	4.4619	4.4498	4.4476	4.4243	4.4215	-
0	1	2	4.2737	4.2699	4.2542	4.2475	-	-	-
1	1	-2	4.1312	4.1196	4.1220	4.1078	4.0980	4.0939	4.0772
1	-1	2	3.9271	3.9224	3.9295	3.9061	3.8858	-	-
0	0	3	3.4987	3.4794	3.4841	3.4673	3.4523	3.4449	3.4253
0	3	-1	3.3005	3.2936	3.2924	3.2892	3.2821	3.2821	3.2726
0	2	2	3.2578	3.2508	3.2496	-	-	-	-
2	-1	1	3.1847	3.1729	3.1721	3.1681	3.1539	3.1523	-
0	3	-2	3.0551	3.0481	3.0481	3.0391	3.0317	3.0280	-
0	3	1	2.9413	2.9340	2.9355	2.9271	2.9178	2.9141	2.9141
2	-3	-1	2.8451	2.8244	2.8244	2.8234	2.8206	2.8113	2.8123
0	3	-3	2.6666	2.6600	2.6590	2.6521	2.6410	2.6382	2.6234
2	-2	-3	2.5886	2.5930	2.5907	2.5910	2.5826	2.5734	2.5734
2	0	2	2.5255	2.5252	2.5206	2.5132	2.5012	2.4799	-
-4	1	-2	2.2438	-	-	-	-	-	-
2	2	1	2.1780	-	-	-	-	-	-
-5	2	0	2.0433	-	-	-	-	-	-
-5	2	-1	1.9848	-	-	-	-	-	-
4	-2	-1	1.8154	1.8100	1.8120	1.8107	1.8052	1.8066	1.8066

Table 3.10 High pressure x-ray diffraction results of jennite (Methanol:Ethanol = 4:1).

	Jennite experiment (M:E=4:1)						
P (GPa)	a (Å)	b (Å)	c (Å)	α (º)	β (º)	γ (º)	V (Å^3)
ambient	10.52(1)	7.25(1)	10.92(2)	101.4(1)	96.9(1)	109.4(1)	755(2)
0.3(1)	10.569(7)	7.248(4)	10.87(2)	101.4(1)	96.96(9)	109.80(9)	751(1)
0.5(1)	10.552(8)	7.244(5)	10.82(2)	101.5(1)	96.9(1)	109.8(1)	746(1)
1.3(1)	10.524(7)	7.222(4)	10.77(2)	101.4(1)	96.94(9)	109.85(9)	739(1)
1.6(1)	10.519(7)	7.207(4)	10.77(2)	101.4(1)	96.89(9)	109.90(8)	736(1)
2.0(2)	10.496(7)	7.202(4)	10.76(2)	101.5(1)	96.82(9)	109.95(9)	733(1)
2.6(2)	10.483(9)	7.189(6)	10.74(2)	101.5(1)	96.7(1)	109.9(1)	730(1)

Table 3.11 High pressure x-ray diffraction results of jennite (Silicone oil).

Jennite experiment (Silicone oil)							
P (GPa)	a (Å)	b (Å)	c (Å)	α (º)	β (º)	γ (º)	V (Å^3)
ambient	10.53(1)	7.245(5)	10.92(1)	101.4(1)	96.9(1)	109.4(1)	754(1)
0.1(1)	10.53(1)	7.251(4)	10.92(1)	101.5(1)	96.94(9)	109.4(1)	754(1)
0.5(1)	10.52(1)	7.247(5)	10.88(1)	101.6(1)	96.8(1)	109.5(1)	749(1)
0.9(1)	10.49(1)	7.241(4)	10.83(1)	101.7(1)	96.77(9)	109.5(1)	743(1)
1.3(1)	10.48(1)	7.237(4)	10.80(1)	101.7(1)	96.66(9)	109.6(2)	740(1)
2.0(2)	10.46(4)	7.22(1)	10.73(4)	101.7(5)	96.5(2)	109.6(4)	733(4)

The refined ambient lattice parameters agree well with the results of Bonaccorsi et al. [118] with less than 1 % error range except ***a*** lattice parameter (Table 3.1, 3.10 and 3.11). They found the reflections with odd ***k*** were systematically weak due to disorder in the sequence of the structural layers along **a** direction [118, 162, 163]. The existence of the disorder in crystal system makes it difficult to apply the Rietveld refinement method. The ***a*** parameter is 3 % smaller than that of [118]. However, it is an acceptable error range considering the complexity of crystal structure of jennite. The variation of lattice parameters is shown in Fig. 3.24. It shows almost identical results with different pressure-transmitting media. The same fitting procedure described in section 3.2.1 was applied to the jennite with two different pressure-transmitting media. In the case of alcohol mixture, the 3rd BM EoS determines a bulk modulus of 45(5) GPa, a derivative of 42.3, and ambient volume of 754(2) Å^3 with a goodness of fit of R^2 = 0.997. In addition, the 2nd BM EoS fit gives a bulk modulus of 68(5) GPa and same initial volume with R^2 = 0.970. In the case of silicone oil, the 3rd BM EoS determines a bulk modulus of 61(4) GPa, a derivative of 9.9, and ambient volume of 755(1) Å^3 with a goodness of fit of R^2 = 0.964. In addition, the 2nd BM EoS fit gives a bulk modulus of 64(2) GPa and same initial volume with R^2 = 0.956. The 2nd and 3rd BM EoS fitting results are shown in Fig. 3.25.

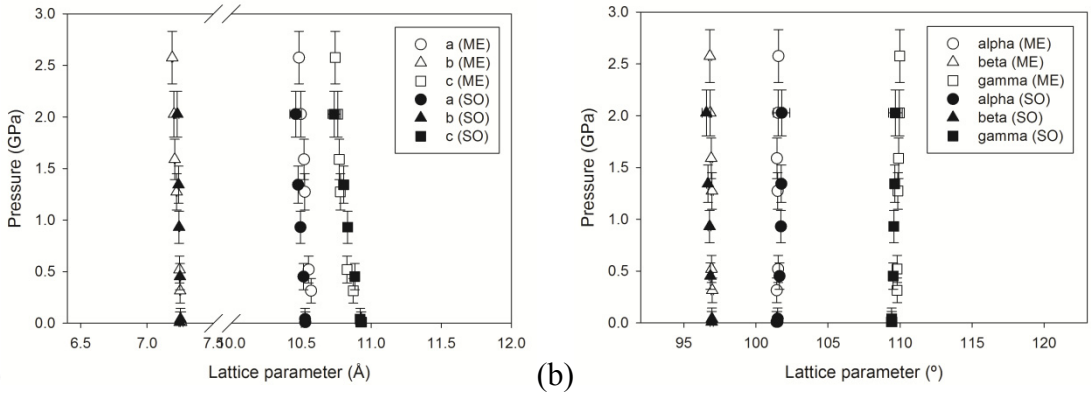

(a) (b)

Figure 3.24 Variation of (a) axial and (b) angular lattice parameters of jennite under pressure. Closed and open symbols correspond to refined parameters measured with alcohol mixture (Methanol:ethanol=4:1) and silicone oil, respectively.

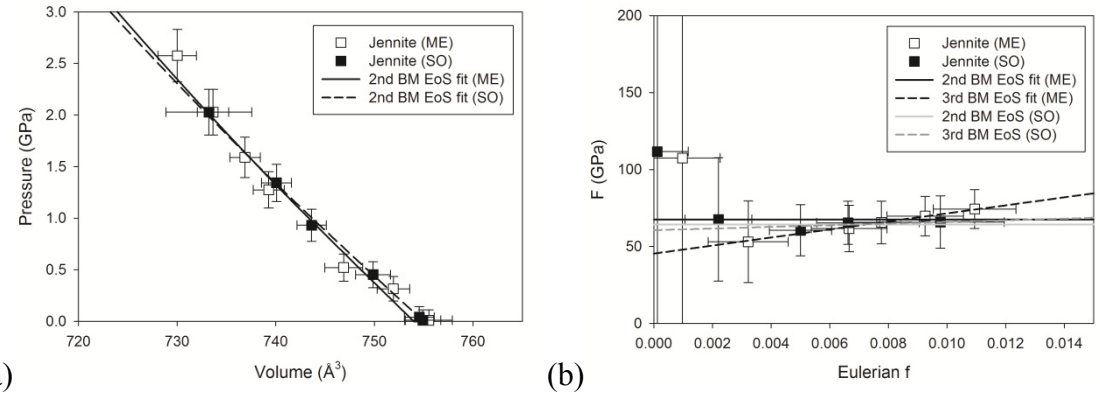

(a) (b)

Figure 3.25 (a) Refined unit cell volumes of jennite under pressure. (b) F-f plot of jennite. The 2nd order BM EoS fittings give the bulk modulus of 68(5) GPa and 64(2) GPa with alcohol mixture and silicone oil, respectively.

The measured bulk modulus, its first derivative, and ambient unit-cell volume according to the 2nd and 3rd BM EoS of calcium silicate hydrate minerals are summarized in Table. 3. The values of first pressure derivative might not be reliable due to the relatively small number of data points in *F-f* plots of Fig. 3.11, 3.15(a), 3.19, and 3.25(a). Jennite shows K_0 value of 64-68 GPa. In case of tobermorite family, layer spacing determines the compressibility of the crystals. More systematic comparison will be discussed in section 3.4.

Table 3.12 Bulk modulus, its first derivative and ambient volume of calcium silicate hydrates according to the Birch-Murnaghan equation of state. The high pressure experimental data of tobermorite 14Å is reproduced from Oh. et al. [148].

		Tob 14 Å M:E=4:1	Normal Tob 11 Å M:E=4:1	Anomalous Tob 11 Å M:E=4:1	Tob 9 Å M:E=4:1	Jennite M:E=4:1	Jennite Silicone oil
3rd EoS	K_0 (GPa)	53(2)	62(4)	67(2)	86(6)	45(5)	61(4)
	K_0'	0.8	9.7	1.8	20.9	42.3	9.9
	V_0 (Å^3)	577.9(4)	463(3)	475.9(4)	1471(1)	754(2)	755(1)
2nd EoS	K_0	47(4)	71(4)	63(2)	115(14)	68(5)	64(2)
	V_0 (Å^3)	577.9(4)	463(3)	475.9(4)	1471(1)	754(2)	755(1)

3.3 First-Principles Calculations on Calcium Silicate Hydrates

3.3.1 Tobermorite 14 Å

In this section, the structure, elasticity, and strength properties of several C-S-H crystals are comprehensively simulated based on the first-principles calculations. The crystal structure of tobermorite 14 Å (plombierite) was resolved by Bonaccorsi et al. in 2005 [3]. It is built up by the same complex module of tobermorite 11 Å whole crystal structure is explained in section 3.2.1. However, the wollastonite-type chains facing each other on adjacent layers are not condensed into double chains. Furthermore, they are shifted by *b*/2. The space in between contains calcium cations and a larger amount of water molecules compared to the 11 Å phase. Some water molecules in the interlayer region as well as a Ca cation have half occupancies, whereas the other waters are fully occupied. The monoclinic polytype of plombierite is represented in Fig. 3.26. The crystal chemical formula indicated by the structural study [3] is $Ca_5Si_6O_{16}(OH)_2 \cdot 7H_2O$ in agreement with chemical, thermal, and NMR data [15, 126, 130, 132, 149, 164].

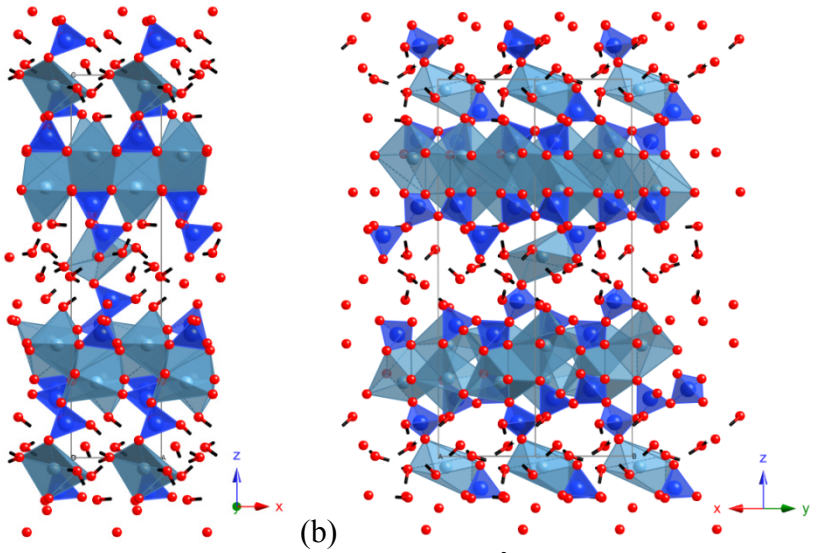

(a) (b)

Figure 3.26 Geometrically optimized tobermorite 14 Å projected along (a) [010] and (b) [110]. Silicate chains, calcium octahedral, and oxygen atoms are shown as dark blue, light blue tetrahedra, and red spheres, respectively. Hydroxyl groups and hydrogen atoms in water molecules are denoted with black sticks.

All calculations reported in this section are performed by the Density functional theory (DFT) to address the elasticity of calcium silicate hydrates. As a starting system, the monoclinic crystal structure with B11b resolved by Bonaccorsi et al.[3] was chosen (***a*** = 6.735Å, ***b*** = 7.425Å, ***c*** = 27.987Å, ***α*** = 90º, ***β***

= 90º, and γ = 123.25º). The crystal symmetry and lattice parameters are summarized in Table 3.1. The missing positions of hydrogen atoms were added adjacent to oxide atoms of water molecules and hydroxides with a distance of 1 Å. The half occupancy of Ca2, W2, W3, and W4 molecules was appropriately considered by removing the molecules in the unit cell. The computations were performed on Linux clusters in the Molecular Graphics and Computation Facility at the University of California, Berkeley. The DFT calculations were performed using Linear-Density-Approximation (LDA) and Perdew-Burke-Ernzerhof (PBE) GGA [85] exchange-correlation functionals and plane wave techniques implemented in the Quantum ESPRESSO distribution [165]. Ultrasoft type pseudopotentials [166] were used with a plane-wave energy cut-off of 1600 eV. The reference valence configurations and core radii for GGA and LDA pseudopotentials were chosen as $3s^2$, $3p^6$, $4s^2$, r_c = 1.2 Å for Ca, $3s^2$, $3p^2$, r_c = 1.2 Å for Si, $2s^2$, $2p^4$, r_c = 0.8 Å for O, and $1s^1$, for H. γ-points sampling [98] were selected due to large size of the system.

Before calculating structural and elastic properties, structural optimizations were performed at zero pressure. Atomic positions and lattice parameters were optimized until atomic forces were smaller than 10^{-4} eV/Å and total energy converged within 10^{-6} eV. The final residual stress components of the optimized structure were less than 0.1 kbar. The geometrically optimized crystal structure is shown in Fig. 3.26. Resulting lattice parameters and fractional atomic positions are summarized in appendix Table A1. Static equilibrium structures at arbitrary pressures were obtained using damped variable cell shape molecular dynamics [167] for predicting pressure-volume behavior. Computed lattice parameters at different pressures using LDA and GGA pseudopotentials are summarized in Table 3.13 and 3.14, respectively. Comparison with high pressure experiment on tobermorite 14 Å [148] is shown in Fig. 3.27. The LDA and GGA compression curves compare well with the experimental data, with the LDA giving a better agreement. GGA overestimates its volume at ambient by 4 % (i.e., 1220.12 $Å^3$ in GGA vs. 1170.43 $Å^3$ from [3]) while LDA underestimates the volume by 1% (i.e., 1154.7 $Å^3$ in LDA vs. 1170.43 $Å^3$ from [3]). The discrepancy is mainly due to ***c*** lattice parameter as shown in Fig. 3.27 (a). GGA predicted the ***c*** parameter to be 2 % larger but the monoclinic symmetry was slightly broken at relaxed and constrained structure. This causes large error of unit-cell volumes at zero and high pressure.

Table 3.13 First-principles calculation results of tobermorite 14 Å (LDA).

Tobermorite 14 Å LDA computation							
P (GPa)	a (Å)	b (Å)	c (Å)	α (º)	β (º)	γ (º)	V (Å^3)
-1.0	7.140	7.734	25.65	90.00	90.00	123.56	1180.57
0.0	7.115	7.703	25.28	90.00	90.00	123.56	1154.70
1.0	7.090	7.664	24.96	90.00	90.00	123.54	1130.69
2.0	7.071	7.623	24.61	90.00	90.00	123.53	1105.78
3.0	7.057	7.570	24.25	89.99	90.00	123.42	1081.47
4.0	7.034	7.543	24.13	90.00	90.01	123.45	1067.94
5.0	7.013	7.513	23.94	89.99	90.00	123.51	1051.77
6.0	7.000	7.475	23.77	90.00	90.00	123.51	1037.26
7.0	6.983	7.431	23.66	89.99	90.00	123.50	1023.98

Table 3.14 First-principles calculation results of tobermorite 14 Å (GGA).

Tobermorite 14 Å GGA computation							
P (GPa)	a (Å)	b (Å)	c (Å)	α (º)	β (º)	γ (º)	V (Å^3)
-1.0	6.818	7.528	29.038	90.03	89.80	122.91	1251.24
0.0	6.789	7.507	28.650	90.26	89.76	123.32	1220.12
0.9	6.690	7.423	28.297	90.71	89.27	122.59	1183.83
1.9	6.643	7.387	27.969	91.06	89.07	122.59	1156.26
3.0	6.606	7.365	27.675	91.25	88.81	122.64	1133.58
4.0	6.573	7.340	27.397	91.42	88.49	122.69	1111.98
5.0	6.541	7.310	27.125	91.63	88.10	122.68	1090.92
6.0	6.514	7.286	26.822	91.88	87.61	122.74	1069.68
7.0	6.490	7.265	26.517	92.13	87.07	122.84	1049.05

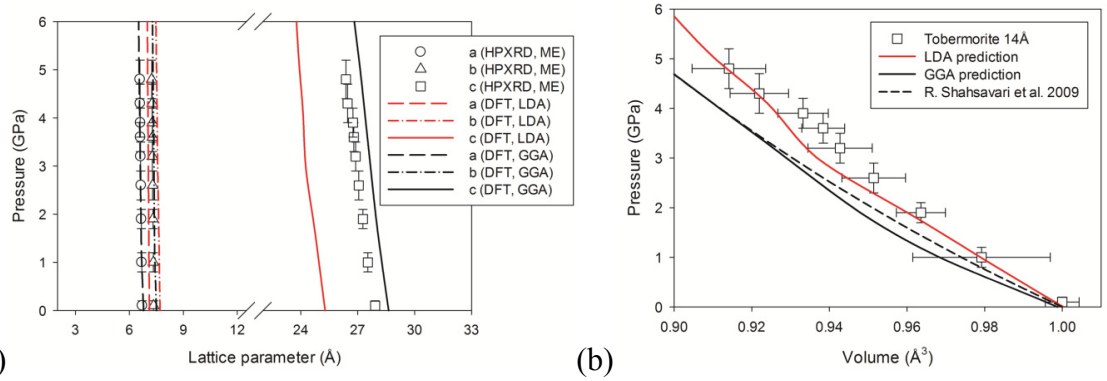

(a) (b)

Figure 3.27 Comparison of (a) axial and (b) volumetric compressibilities of tobermorite 14 Å from high pressure experiment and LDA (red line) and GGA (black line) simulation. First-principles calculations result is reproduced from RVH bulk modulus of Shahsavari et al. [155].

Elastic coefficients for these structures were calculated based on a stress-strain relation. For infinitesimal strains this relation is linear and at 0 GPa it is simply:

$$\sigma_i = \sum_{j=1}^{6} C_{ij}\varepsilon_j \qquad \text{- (3.6)}$$

Individual strains were applied to the equilibrium structure (i.e., structural optimization at 0 GPa). Next, internal structural degrees of freedom were re-optimized. Residual stress components for these optimized and re-optimized structures were less than 0.1 kbar. This allows computations of elastic coefficients with well constrained and small errors [100]. The elastic tensor of a monoclinic structure has thirteen independent constants as described in Eqn. (2.36) in chapter 2:

The elastic constants are defined in an orthogonal coordinate system, thus cell parameters are related to a Cartesian coordinate XYZ setting: $\vec{X} \| \vec{a}, \vec{Z} \| \vec{a} \times \vec{b}$ and $\vec{Y} \| \vec{Z} \times \vec{X}$. The Lagrangian strains in Cartesian coordinates:

$$\varepsilon_1 = \begin{pmatrix} \delta & 0 & 0 \\ 0 & 0 & 0 \\ 0 & 0 & 0 \end{pmatrix},$$

$$\varepsilon_2 = \begin{pmatrix} 0 & 0 & 0 \\ 0 & \delta & 0 \\ 0 & 0 & 0 \end{pmatrix},$$

$$\varepsilon_3 = \begin{pmatrix} 0 & 0 & 0 \\ 0 & 0 & 0 \\ 0 & 0 & \delta \end{pmatrix} \qquad \text{- (3.7)}$$

$$\varepsilon_4 = \begin{pmatrix} 0 & 0 & 0 \\ 0 & 0 & \delta/2 \\ 0 & \delta/2 & 0 \end{pmatrix},$$

$$\varepsilon_5 = \begin{pmatrix} 0 & 0 & \delta/2 \\ 0 & 0 & 0 \\ \delta/2 & 0 & 0 \end{pmatrix},$$

$$\varepsilon_6 = \begin{pmatrix} 0 & \delta/2 & 0 \\ \delta/2 & 0 & 0 \\ 0 & 0 & 0 \end{pmatrix} \qquad \text{- (3.8)}$$

where the indices are given in Voigt notation were applied to the relaxed crystal structure. Sufficiently small strains of $\delta = \pm 0.5$ % were applied and elastic coefficients were obtained by averaging stresses resulting from positive and negative strains. Table 3.15 summarizes the computed elastic coefficients of tobermorite 14 Å from LDA and GGA pseudopotentials.

Adiabatic mechanical constants can be derived from the computed elastic constants. Poly-crystalline averages are difficult to estimate since they involve statistical averages over grain sizes and orientations. But a scheme has been devised to give upper and lower bounds to the bulk modulus, K, and to the shear modulus, G, in terms of the elastic coefficients. This is the Reuss-Voigt-Hill (RVH) averaging method [101, 102]. The Voigt moduli correspond to a situation in which the aggregate is subjected to uniform strain. It provides the upper bounds for K and G. The Reuss moduli correspond to the situation of uniform stress and give the lower bounds. The RVH moduli are the average of Voigt and Reuss moduli and correspond roughly to the situation in which neither stress or strain are uniform [101, 102]. Detail derivations on RVH average are introduced in chapter 2. The bound values were computed using elastic coefficients, C, determined by first-principles from Eqn. (3.6). From the computed K_{RVH} and G_{RVH}, the Young's modulus (E) and Poisson ratio (η) could be also calculated. The computed LDA and GGA properties for tobermorite 14 Å structure are summarized in Table 3.15.

Table 3.15 Calculated elastic coefficients of tobermorite 14 Å.

Tobermorite 14 Å computation							
	LDA	**GGA**	**[155]**		**LDA**	**GGA**	**[155]**
c11	125.5	71.4	77.6	**K_Voigt**	59.4	30.8	42.1
c12	41.2	18.5	35.9	**K_Reuss**	55.0	29.8	29.7
c13	35.3	5.7	20.2	**K_RVH**	57.2	30.3	35.9
c14	0.0	2.9	0.0	**G_Voigt**	42.9	24.5	24.2
c15	0.0	1.6	0.0	**G_Reuss**	39.3	19.1	17.0
c16	-11.1	6.5	3.1	**G_RVH**	41.1	21.8	20.6
c22	121.7	53.0	104.5	**E_RVH**	99.5	52.8	51.9
c23	30.5	26.6	26.3	***v*_RVH**	0.2	0.2	0.3
c24	0.0	1.7	0.0				
c25	-0.1	3.6	0.0				
c26	-4.9	-6.1	-1.8				
c33	73.5	51.2	32.1				
c34	-0.1	2.6	0.0				
c35	0.0	1.2	0.0				
c36	2.3	-3.5	3.0				
c44	57.8	39.6	24.5				
c45	4.9	-7.5	-9.4				
c46	0.1	-1.2	0.0				
c55	46.7	16.6	14.7				
c56	0.0	-1.2	0.0				
c66	38.7	24.8	38.1				

The Young's modulus for uniaxial compression along arbitrary directions was computed. The general definition of the directional Young's modulus in terms of unit vectors, $\hat{n}$, along the compression axis is:

$$E_{ani} = \frac{1}{\hat{n}^T \cdot [C^{-1} : (\hat{n} \cdot \hat{n})] \cdot \hat{n}} \qquad \text{-(3.9)}$$

This expression was used to investigate the anisotropy of tobermorite 14 Å (Fig. 3.28). Magnitudes of the LDA and GGA Young's modulus are represented in colors on the surface a 'sphere' with unit radius. X, Y, and Z directions are defined by a setting of ($\vec{X} \| \vec{a}$, $\vec{Z} \| \vec{a} \times \vec{b}$, and $\vec{Y} \| \vec{Z} \times \vec{X}$). The large structural anisotropy of tobermorite 14 Å is evident in this figure. The softest direction of [001] was computed as the direction perpendicular to the principal layer. The GGA shows slightly different modulus profile because the monoclinic symmetry was not broken after relaxation.

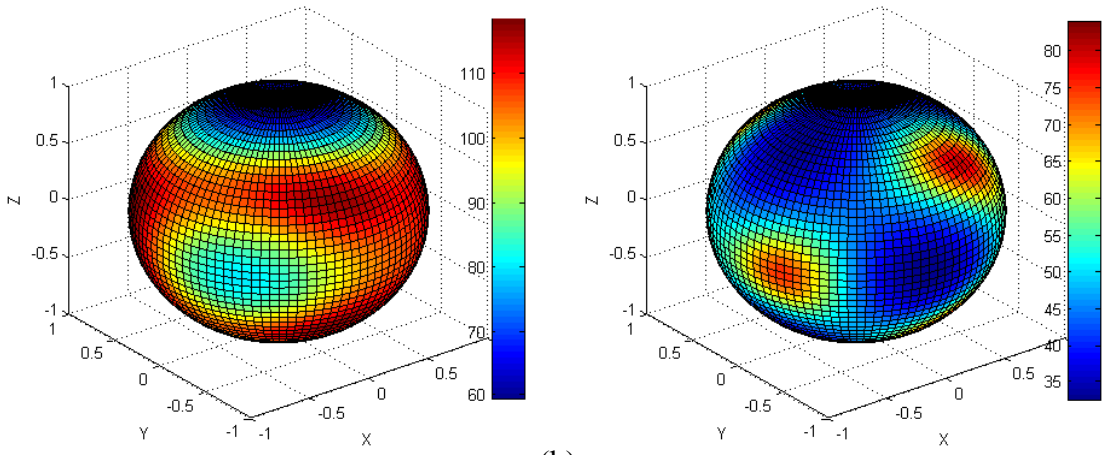

(a) (b)

Figure 3.28 Directional Young's modulus of tobermorite 14 Å using (a) LDA and (b) GGA functionals. Scale bars indicate Young's modulus in GPa.

3.3.2 Tobermorite 9 Å

Identical DFT calculation was performed to tobermorite 9 Å crystal structure. Triclinic crystal structure with $C\bar{1}$ was selected (***a*** = 11.156 Å, ***b*** = 7.303 Å, ***c*** = 9.566 Å, ***α*** = 101.08 º, ***β*** = 92.83 º, and ***γ*** = 89.98 º) for initial system. The four missing hydrogen atoms in [115] were added adjacent to oxide atoms of hydroxides with a distance of 1 Å. The DFT calculations were performed using LDA and GGA [85] exchange-correlation functionals and the Quantum ESPRESSO distribution [165]. Ultrasoft type pseudopotentials [166] were used with a plane-wave energy cut-off of 1600 eV. ***K***-points grid of 2 by 2 by 2 [98] was selected for convergence criterion.

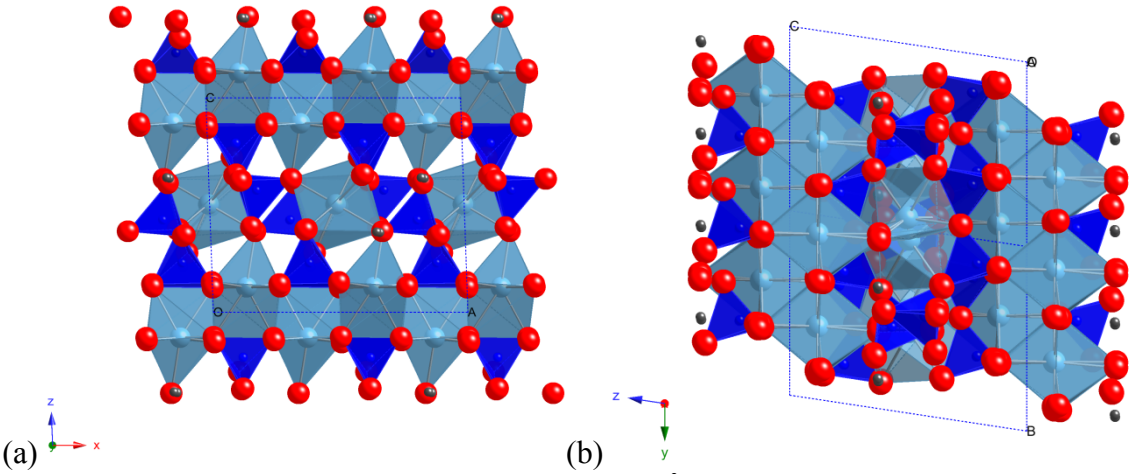

Figure 3.29 Geometrically optimized tobermorite 9 Å projected along (a) [010] and (b) [100]. Silicate chains, calcium octahedral, hydrogen atoms, and oxygen atoms are shown as dark blue, light blue tetrahedral, black spheres, and red spheres, respectively.

Same structural optimization procedure in section 3.3.1 was performed at zero and arbitrary pressures [167]. The geometrically optimized crystal structure is shown in Fig. 3.29. Resulting lattice parameters and fractional atomic positions of tobermorite 9 Å at zero pressure are summarized in appendix Table A2. Computed lattice parameters using LDA and GGA at different pressures are summarized in Table 3.16 and 3.17, respectively. Comparison with high pressure experiment on tobermorite 9Å is shown in Fig. 3.30. The LDA and GGA compression curves agree well with previous DFT-GGA study by [155] but there is a difference with high pressure experiment, especially over 2 GPa. At zero pressure, LDA and GGA overestimate the experimental volume by 12 % and 3 %, respectively. It is worth to note that triclinic crystal structure was used for DFT calculation while orthorhombic crystal system was used for the refinement of high pressure experiment. The possible reasons of the discrepancy are discussed in section 3.4.

Table 3.16 First-principles calculation results of tobermorite 9 Å (LDA).

Tobermorite 9 Å LDA computation

P (GPa)	a (Å)	b (Å)	c (Å)	α (º)	β (º)	γ (º)	V (Å^3)
0.0	11.901	7.544	9.668	97.03	91.33	90.93	861.19
1.0	11.862	7.519	9.607	97.14	91.40	91.02	849.81
2.0	11.824	7.494	9.562	97.17	91.43	91.04	840.29
3.0	11.786	7.474	9.518	97.23	91.46	91.06	830.40
4.0	11.798	7.394	9.473	98.29	91.36	91.38	817.14
5.0	11.771	7.359	9.445	98.62	91.40	91.51	808.34
6.0	11.732	7.340	9.413	98.65	91.46	91.60	800.74
7.0	11.691	7.323	9.383	98.62	91.49	91.65	793.58
8.0	11.646	7.311	9.353	98.58	91.52	91.69	786.71

Table 3.17 First-principles calculation results of tobermorite 9 Å (GGA).

Tobermorite 9 Å GGA computation

P (GPa)	a (Å)	b (Å)	c (Å)	α (º)	β (º)	γ (º)	V (Å^3)
0.0	11.247	7.364	9.620	98.54	91.87	90.52	787.55
1.0	11.209	7.336	9.522	98.73	92.16	90.67	773.06
2.0	11.174	7.308	9.465	98.85	92.18	90.68	763.02
3.0	11.139	7.280	9.408	98.96	92.27	90.75	752.90
4.0	11.102	7.253	9.359	99.06	92.34	90.83	743.47
5.0	11.069	7.225	9.316	99.14	92.40	90.89	734.80
6.0	11.038	7.197	9.274	99.27	92.45	90.97	726.25
7.0	11.007	7.171	9.239	99.34	92.48	91.03	718.69
8.0	10.976	7.145	9.209	99.43	92.49	91.11	711.61

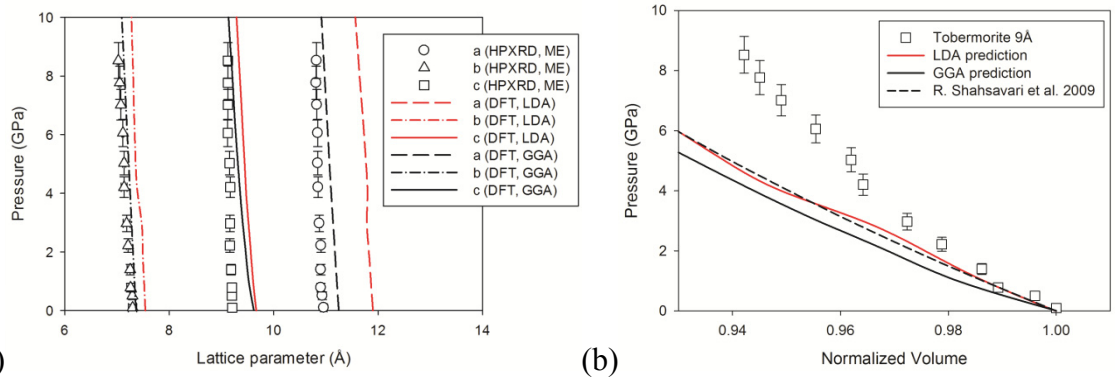

(a) (b)

Figure 3.30 Comparison of (a) axial and (b) volumetric compressibilities of tobermorite 9 Å from high pressure experiment and LDA (red line) and GGA (black line) simulation. First-principles calculations result is reproduced from RVH bulk modulus of Shahsavari et al. [155].

In addition, elastic coefficients for tobermorite 9 Å were calculated based on the stress-strain relation of Eqn. (3.6). Same procedure in section 3.3.1 was

applied with identical convergence criteria. The elastic tensor of a triclinic structure has twenty-one independent constants as described in Eqn. (2.35) in chapter 2:

In the cases of tobermorite 9 Å and jennite, elastic constants were computed in two crystallographic settings of ($\vec{Z}\|\vec{c}$, $\vec{Y}\|\vec{c}\times\vec{a}$, and $\vec{X}\|\vec{Y}\times\vec{Z}$) and ($\vec{X}\|\vec{a}$, $\vec{Z}\|\vec{a}\times\vec{b}$, and $\vec{Y}\|\vec{Z}\times\vec{X}$). The $\vec{Z}\|\vec{c}$ setting is conventional for triclinic system [168, 169] while the $\vec{X}\|\vec{a}$ setting is for systematic comparison of the elastic constants for different crystal systems. The six Lagrangian strains of ± 0.5 % of Eqn. (3.7 and 3.8) were applied to the relaxed crystal structure. Table 3.18 summarizes the computed elastic coefficients of tobermorite 9 Å from LDA and GGA pseudopotentials with two different crystallographic settings. In addition, averaged mechanical properties were computed and summarized in the Table 3.18.

Table 3.18 Calculated elastic coefficients of tobermorite 9 Å.

Tobermorite 9 Å computation											
	LDA		GGA		[155]		LDA		GGA		[155]
	Z//c	X//a	Z//c	X//a	X//a		Z//c	X//a	Z//c	X//a	X//a
c11	180.2	180.2	178.8	179.1	169.2	**K_Voigt**	88.1	85.7	78.7	78.0	76.4
c12	76.7	79.3	53.3	51.0	54.5	**K_Reuss**	82.5	77.5	69.8	69.6	66.4
c13	37.7	36.6	39.0	38.8	37.5	**K_RVH**	85.3	81.6	74.2	73.8	71.4
c14	-2.1	0.0	-1.7	-0.4	-1.1	**G_Voigt**	55.9	54.8	52.1	52.3	41.1
c15	-0.2	-0.3	-2.3	-2.1	-8.9	**G_Reuss**	52.2	50.8	48.0	48.2	33.3
c16	-6.2	-6.3	-2.9	-3.0	2.7	**G_RVH**	54.1	52.8	50.1	50.3	37.2
c22	171.2	174.4	164.6	168.5	170.0	**E_RVH**	134.0	130.3	122.6	122.9	95.1
c23	39.5	33.8	39.0	37.9	36.2	***v*_RVH**	0.2	0.2	0.2	0.2	0.3
c24	-17.7	-16.1	-14.6	-12.1	3.6						
c25	-9.8	-9.4	-13.9	-14.4	-11.8						
c26	-3.5	-1.8	-2.9	-0.1	-1.1						
c33	133.7	117.7	102.3	98.8	92.7						
c34	-6.6	-6.3	-14.5	-10.7	2.6						
c35	5.5	4.7	0.0	0.5	-3.5						
c36	-2.5	-3.8	0.7	-1.1	0.6						
c44	55.3	52.7	53.0	53.1	40.6						
c45	1.0	-0.7	1.5	-0.3	0.4						
c46	-9.8	-9.7	-10.8	-10.7	-5.5						
c55	44.2	44.0	42.3	42.3	17.9						
c56	0.8	2.7	1.3	2.8	-1.9						
c66	69.8	69.8	60.3	59.9	45.7						

The Young's modulus for uniaxial compression along arbitrary directions was computed based on the Eqn. (3.9). The visualized magnitude of the anisotropic Young's modulus is given in Fig. 3.31 which is computed based on the setting of ($\vec{X} \| \vec{a}$, $\vec{Z} \| \vec{a} \times \vec{b}$, and $\vec{Y} \| \vec{Z} \times \vec{X}$). Although the predicted volume from LDA calculation is larger than that from GGA, it shows mechanically stiffer structure as presented in Table 3.18 and Fig. 3.31. Like the case of tobermorite 14 Å, the layer direction of tobermorite 9 Å is the softest direction in terms of stiffness regardless of types of LDA and GGA pseudopotentials.

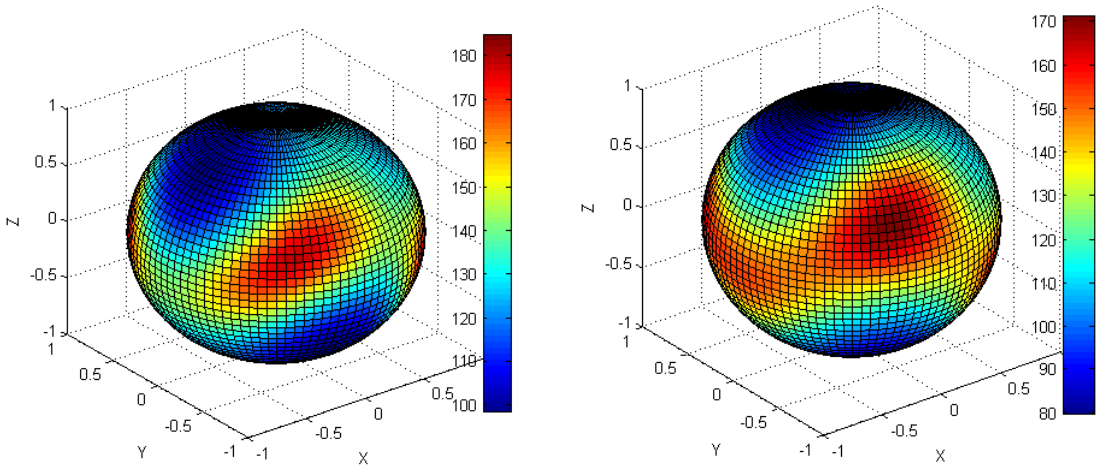

(a) (b)

Figure 3.31 Directional Young's modulus of tobermorite 14 Å computed from (a) LDA and (b) GGA functionals. Elastic constants calculated in the coordinate system of ($\vec{X} \| \vec{a}$, $\vec{Z} \| \vec{a} \times \vec{b}$, and $\vec{Y} \| \vec{Z} \times \vec{X}$) are used. Scale bars indicate Young's modulus in GPa.

3.3.3 Jennite

This section discusses the DFT calculation of jennite whose crystal structure is reported in section 3.2.4. It is built up by tilleyite ribbons of edge-sharing calcium octahedral, silicate chains of wollastonite-type, and additional calcium octahedral. The ribbons are firmly connected through the silicate chains running on both sides of it. The silicate chains present in jennite is close to those in tobermorite, (i.e., Dreierketten, Fig. 3.32). The crystal structure used for DFT simulation is triclinic system of $\boldsymbol{a}$ = 10.576 Å, $\boldsymbol{b}$ = 7.265 Å, $\boldsymbol{c}$ = 10.931 Å, $\boldsymbol{\alpha}$ = 101.3º, $\boldsymbol{\beta}$ = 96.98 º, and $\boldsymbol{\gamma}$ = 109.65 º. The missing hydrogen atoms from x-ray diffraction experiment were recently proposed through DFT calculation by Churakov in 2008 [170]. This hydrogen bonding scheme was chosen for investigating mechanical performance of jennite crystal in this study. The calculation procedures described in sections 3.3.1 and 3.3.2 were applied with a plane-wave energy cut-off of 1900 eV and 4 by 2 by 2 $\boldsymbol{k}$-points sampling [98].

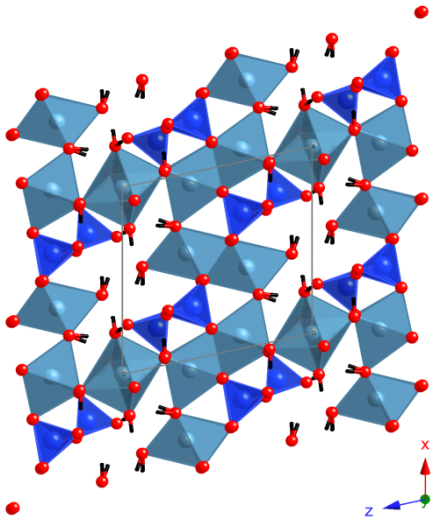

Figure 3.32 Geometrically optimized jennite projected along [010]. Silicate chains, calcium octahedra, and oxygen atoms are shown as dark blue, light blue tetrahedra, and red spheres, respectively. Hydroxyl groups and hydrogen atoms in water molecules are denoted with black sticks.

The result of geometrically optimization is shown in Fig. 3.32. The relaxed lattice parameters and fractional atomic positions of jennite at zero pressure are summarized in appendix Table A3. Computed lattice parameters at different pressures using LDA and GGA are summarized in Table 3.19 and 3.20, respectively. Fig. 3.33 and 3.34 show the comparison of pressure-volume behavior with the result of high pressure experiment in section 3.2.4. The DFT calculations predict the mechanical behavior quite accurately. Although LDA overestimates the initial volume as 6 %, GGA predicts the value precisely within

0.7 % difference. Overall, in terms of pressure-volume behavior, the LDA and GGA provide the upper and lower bounds of experimental results as shown in Fig. 3.34. Nevertheless, there is a significant difference with former GGA calculation by Shahsavari et al. [155]. It might be due to different initial hydrogen bonding scheme or poor convergence criteria.

Table 3.19 First-principles calculation results of jennite (LDA).

Jennite LDA computation							
P (GPa)	a (Å)	b (Å)	c (Å)	α (º)	β (º)	γ (º)	V (Å^3)
-1.0	10.894	7.664	11.184	102.25	96.26	109.82	841.65
0.0	10.762	7.584	11.046	102.14	96.38	109.94	811.99
1.0	10.746	7.564	10.940	102.29	96.48	110.00	799.61
2.0	10.730	7.544	10.834	102.45	96.58	110.06	787.23
3.0	10.663	7.510	10.807	102.42	96.62	110.04	776.93
4.0	10.627	7.491	10.766	102.45	96.75	110.04	768.90
5.0	10.619	7.485	10.663	102.60	97.23	110.07	758.07

Table 3.20 First-principles calculation results of jennite (GGA).

Jennite GGA computation							
P (GPa)	a (Å)	b (Å)	c (Å)	α (º)	β (º)	γ (º)	V (Å^3)
-1.0	10.673	7.327	11.006	100.90	97.76	109.33	779.20
0.0	10.626	7.292	10.912	100.98	97.71	109.35	765.22
1.0	10.579	7.261	10.826	101.00	97.81	109.34	752.22
2.0	10.535	7.234	10.742	101.03	97.85	109.36	740.12
3.0	10.506	7.210	10.628	101.05	97.95	109.32	727.70
4.0	10.472	7.187	10.542	101.08	98.02	109.31	716.95
5.0	10.440	7.166	10.462	101.14	98.00	109.33	707.04

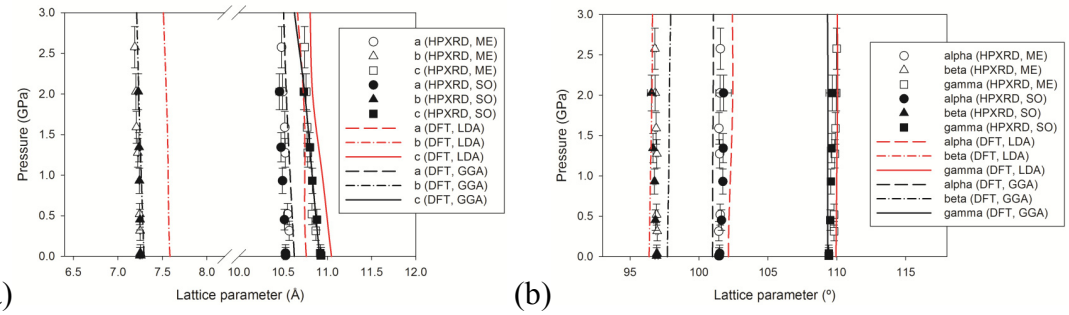

(a) (b)

Figure 3.33 Comparison of (a) axial and (b) angular compressibilities of jennite from high pressure experiment and LDA and GGA simulation.

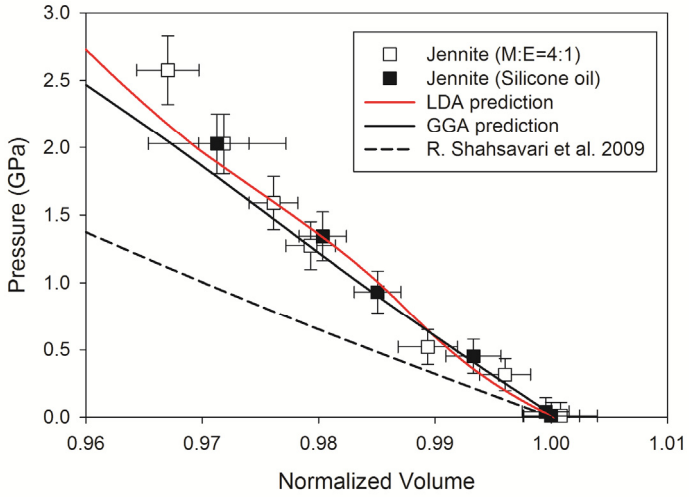

Figure 3.34 Comparison of volumetric compressibilities of jennite from high pressure experiment, LDA (red line), and GGA (black line) simulations. First-principles calculations result is reproduced from RVH bulk modulus of Shahsavari et al. [155].

Twenty-one independent elastic coefficients for jennite were calculated based on two different crystallographic settings of ($\vec{Z}\|\vec{c}$, $\vec{Y}\|\vec{c}\times\vec{a}$, and $\vec{X}\|\vec{Y}\times\vec{Z}$) and ($\vec{X}\|\vec{a}$, $\vec{Z}\|\vec{a}\times\vec{b}$, and $\vec{Y}\|\vec{Z}\times\vec{X}$) described in section 3.3.2. The results were summarized in Table 3.21. The former GGA calculation [155] used the setting of ($\vec{X}\|\vec{a}$, $\vec{Z}\|\vec{a}\times\vec{b}$, and $\vec{Y}\|\vec{Z}\times\vec{X}$). Similar with the pressure-volume behavior, there is a difference of elastic constants especially in the case of C_{22} and C_{33}. Detail investigation of this difference will be discussed in next section.

RVH mechanical properties were computed and summarized in the Table 3.18. In addition, the Young's modulus for uniaxial compression along arbitrary directions was computed. The visualized magnitude of the anisotropic Young's modulus is given in Fig. 3.35 which is computed based on the setting of ($\vec{Z}\|\vec{c}$, $\vec{Y}\|\vec{c}\times\vec{a}$, and $\vec{X}\|\vec{Y}\times\vec{Z}$). Although relaxed lattice volume from LDA calculation is 6 % larger than that from GGA, it shows quite similar range of the Young's modulus and tendency of variation depending on directions.

Table 3.21 Calculated elastic coefficients of jennite.

Jennite computation											
	LDA		GGA		[155]		LDA		GGA		[155]
	Z//c	X//a	Z//c	X//a	X//a		Z//c	X//a	Z//c	X//a	X//a
c11	99.9	100.0	111.7	110.4	100.1	**K_Voigt**	63.1	64.5	61.2	60.8	36.8
c12	44.5	49.0	41.6	40.9	26.9	**K_Reuss**	59.8	61.4	57.9	58.2	26.8
c13	45.9	46.6	39.2	41.1	32.0	**K_RVH**	61.5	63.0	59.6	59.5	31.8
c14	-8.4	-6.7	0.0	1.5	1.3	**G_Voigt**	30.1	29.6	33.8	33.9	23.3
c15	4.4	4.9	2.6	5.1	1.5	**G_Reuss**	26.8	26.2	31.5	31.9	20.6
c16	-1.9	-3.0	4.2	1.9	3.3	**G_RVH**	28.4	27.9	32.7	32.9	22.0
c22	128.2	127.5	130.1	126.9	45.7	**E_RVH**	73.9	72.9	82.8	83.3	53.6
c23	39.6	41.7	33.6	33.9	4.4	***v*_RVH**	0.3	0.3	0.3	0.3	0.2
c24	-4.2	3.0	-1.9	1.2	7.4						
c25	-3.1	-4.9	-2.3	-5.7	-6.2						
c26	-10.4	-6.9	-9.8	-9.6	-3.2						
c33	80.3	78.8	80.3	78.4	59.2						
c34	-0.5	0.3	-5.0	-2.6	-1.3						
c35	-8.2	-6.0	-6.4	-1.5	1.4						
c36	0.2	-1.4	3.5	3.1	0.1						
c44	24.0	23.3	32.0	32.5	22.0						
c45	-0.7	-3.2	0.5	-0.2	-1.7						
c46	-4.2	1.8	-1.5	-0.3	-1.6						
c55	31.7	27.0	27.7	30.3	21.0						
c56	-1.6	-0.6	1.7	1.2	2.7						
c66	35.1	41.1	40.2	40.2	26.6						

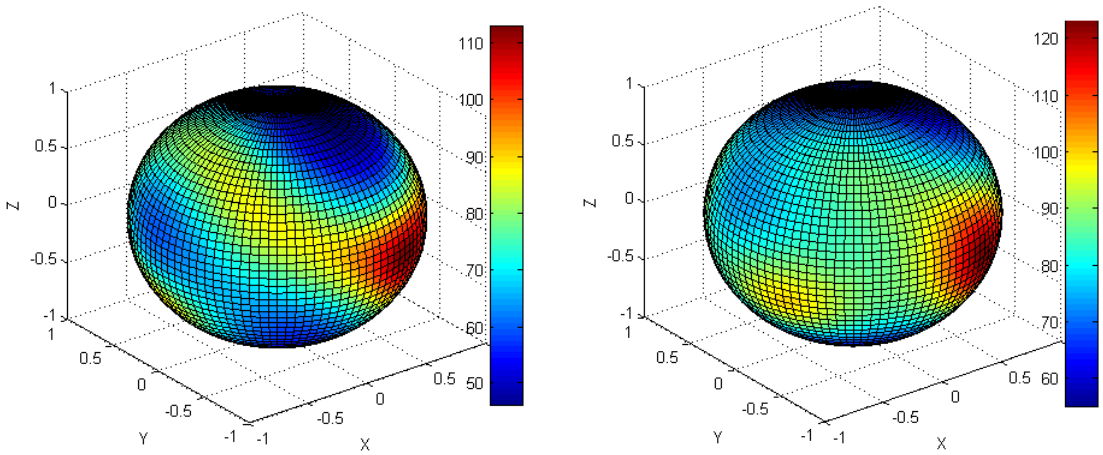

(a) (b)

Figure 3.35 Directional Young's modulus of jennite computed from (a) LDA and (b) GGA functionals. Elastic constants calculated in the conventional orthogonal coordinate system ($\vec{Z}\|\vec{c}$, $\vec{Y}\|\vec{c}\times\vec{a}$, and $\vec{X}\|\vec{Y}\times\vec{Z}$) are used. Scale bars indicate Young's modulus in GPa.

The (isothermal) bulk modulus can be obtained by fitting a finite strain expansion to the calculated free energy versus volume relation. For large compression, it is standard to expand the free energy in terms of an isotropically defined Eulerian strain, *f*:

$$f = \frac{1}{2}\left[\left(\frac{V_0}{V}\right)^{2/3} - 1\right] \qquad \text{- (3.9)}$$

where V_0 and V are a reference volume and compressed volume under pressure, respectively. Then the Helmholtz free energy versus volume relation is expanded in a power series in terms of the Eulerian strains. In all DFT calculations in this work, the Helmholtz free energy, *F*, is the same as the internal energy, E (F=E-TS) since T = 0 K. The Birch-Murnaghan equation of state corresponds to a finite strain expansion to third power in the strain [99].

$$E(V)=E_0+\frac{9V_0K_0}{16}\left\{\left[\left(\frac{V}{V_0}\right)^{-\frac{2}{3}}-1\right]^3 K_0'+\left[\left(\frac{V}{V_0}\right)^{-\frac{2}{3}}-1\right]^2\left[6-4\left(\frac{V}{V_0}\right)^{-\frac{2}{3}}\right]\right\} \qquad \text{- (3.10)}$$

This is the 3rd order Birch-Murnaghan equation of state in terms of energy instead of pressure. When the Eqn. (3.10) is differentiate with respect to volume, V, the same 3rd order BM EoS can be found as Eqn. (2.32) in chapter 2. The fitting gives the reference volume, isothermal bulk modulus at zero pressure, and its pressure derivative at 0 GPa. Results for the fitting to tobermorite 14 Å and 9 Å and jennite are summarized in Table 3.22. In the table, the fitting results of 2nd order BM EoS (i.e., Murnaghan equation of state) are also summarized. This equation results from a finite strain expansion of the free energy to second power in strain. It is equivalent to Eq. (2.32) but with fixed K_0' as 4.

Table 3.22 Computed elasticity of calcium silicate hydrates from first-principle calculations.

		Tobermorite 14 Å				Tobermorite 9 Å				Jennite			
		LDA	**GGA**	**[155]**	**[171]**	**LDA**	**GGA**	**[155]**	**[171]**	**LDA**	**GGA**	**[155]**	**[171]**
3rd EoS	**K_0 (GPa)**	39(1)	33(2)	-	-	70(3)	56(1)	-	-	62(7)	57(1)	-	-
	K_0'	6.6	4.7	-	-	4.6	6.8	-	-	5.1	2.4	-	-
	V_0 (Å^3)	1155	1220	-	-	861	787	-	-	812	765.2	-	-
2nd EoS	**K_0 (GPa)**	44(1)	34.9(9)	-	-	71(4)	63(1)	-	-	63(1)	54.2(8)	-	-
	V_0 (Å^3)	1155	1220	1213	-	861	787	784.0	-	812	765.2	775	-
RVH	**K (GPa)**	57(2)	30(1)	36(6)	46	82(4)	74(4)	71(5)	68	63(2)	60(1)	32(5)	43
	G (GPa)	41(2)	22(3)	21(4)	39	53(2)	50(2)	37(4)	67	28(2)	33(1)	22(1)	26
	E (GPa)	99.5	52.8	51.9	91	130.3	122.9	95.1	152	72.9	83.3	53.6	66
	v	0.2	0.2	0.3	0.2	0.2	0.2	0.3	0.1	0.3	0.3	0.2	0.2

3.4 Discussion on Structural Mechanism of Calcium Silicate Hydrates

Figure 3.36 shows x-ray diffraction analog of various calcium silicate hydrates. All calcium silicate hydrates give strong x-ray peaks in the 3 Å and 1.8 Å regions, indicating that the peaks correspond to important repeat distances in the Ca-O structures within individual layers. For a Bragg reflection to be observed, about 5-10 ordered lattices have to be repeated perpendicular to the diffracting plane. In the case of tobermorite peak at 3 Å, 5-10 repeat along the (200) direction means good atomic ordering parallel to the c-axis of 15-30 Å. Thus the analog of the peaks suggests the resembling presence of well-ordered Ca-O layers in these structures. However, C-S-H gel in hydrated portland cement does not have a strong basal peak while other calcium silicate hydrates show strong intensity of the basal peak over 10 Å. This indicates that, even though the C-S-H gel is a well-known 'layered' structure, the degree of ordering in the layer direction is not enough to make a Bragg reflection. That agrees with the recent experimental observation about the size of C-S-H. Skinner et al. suggests that C-S-H exists as a nano-particle whose size is less than 40Å [23]. The basal spacing of C-S-H (I) is around 10-12 Å as shown in Fig. 3.36. Thus the small size of C-S-H gel particle (50 Å < 70-120 Å) may result in missing the basal peak in x-ray diffraction experiment.

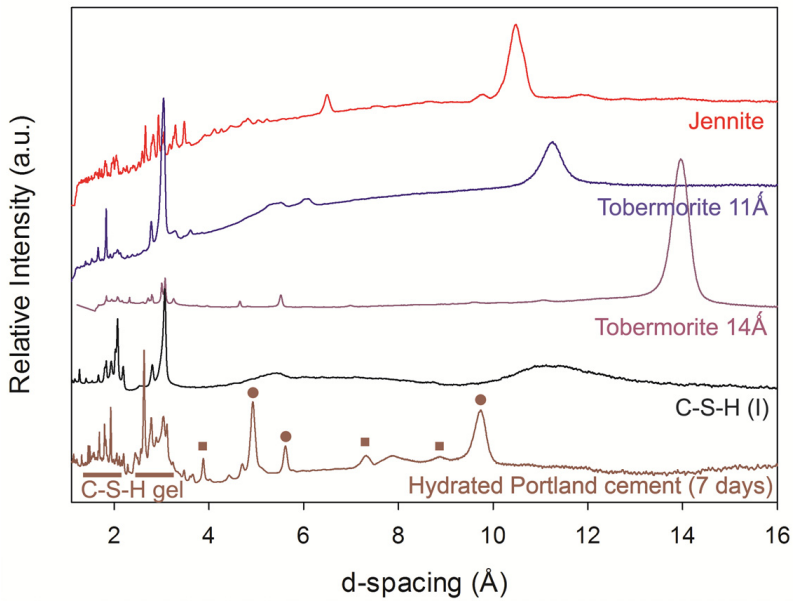

Figure 3.36 X-ray diffraction patterns of calcium silicate hydrates and hydrated Portland cement. In hydrated cement, ▬, ■, and ● indicate C-S-H gel, AFm, and AFt phase, respectively.

The tobermorite 11 Å structure is normally orthorhombic, although possible monoclinic forms have been proposed [55, 115, 129, 147]. A first structural model of tobermorite 11 Å was proposed by Megaw and Kelsey on the basis of single crystal data [114]. According to their description, the 'pseudo-orthorhombic' structure is based on layers parallel to (001), 11.3Å thick, built up by a central sheet of CaO_2 stoichiometry. Since Merlino et al. proposed the double chain of SiO_4 tetrahedra in the orthorhombic structure, which is well in accordance with ^{29}Si NMR experiment, the model is widely accepted [55, 116]. Moreover, they proposed the crystal structures of normal and anomalous tobermorite through x-ray diffraction based on OD theory. According to them, the most distinctive feature of the two tobermorites is the content of the structural cavities. While only water molecules were found in anomalous one, both 'zeolitic' calcium cations and water molecules were found in normal one [55]. The proposed chemical formula of normal and anomalous tobermorite 11 Å are $Ca_{4.5}Si_6O_{16}(OH)\cdot 5(H_2O)$ and $Ca_4Si_6O_{15}(OH)_2 \cdot 5(H_2O)$, respectively [55, 116]. Merlino et al. explain the thermal behavior by the existence of 'zeolitic' calcium cations in the cavities of tobermorite 11 Å. Upon heating at 300ºC, significant structural rearrangement occurs around the 'zeolitic' calcium which yields chain decondensation. However, it does not need to be contracted without the 'zeolitic' calcium cations.

According to the Merlino's hypothesis, the normal tobermorite should have more calcium ions in the structure. The average values of 10 measurements in the normal tobermorite 14 Å found in this study were 0.77 and 0.68 for Ca/Si and Ca/(Si+Al), respectively. The Ca/(Si+Al) of 0.68 is well in accordance with ratios (0.77-0.91) in previous reports regarding the hydrothermally formed Al-substituted tobermorites [126, 172, 173]. In addition, it agrees with the ratio proposed by Merlino et al. (i.e., 0.75). However, anomalous tobermorite 11 Å tested in this study had Ca/Si = 1.1. This high value of Ca/Si ratio in anomalous tobermorite might be due to short length of silicate chains in the system. Additional Nuclear Magnetic Resonance (NMR) studies could explain the high Ca/Si ratio in anomalous one. In addition, it is interesting to note that the d-spacing of 10 Å was observed with 9 and 11 Å at 150ºC heating (Fig. 3.8), which indicates instantaneously unstable structure of tobermorite 10 Å. Based on the hypothesis by Merlino et al. the partial occupancy of the 'zeolitic' calcium will determine the thermal shrinkage of normal tobermorite 11 Å. Then it may be possible to have a metastable tobermorite 10 Å depending on spatial distribution of the 'zeolitic' calcium cations.

Tobermorite 11 Å has two different types of SiO_4 tetrahedra. One is chain middle group SiO_4, and the other is bridging SiO_4. Komarneni and Tsuji suggested that Al atoms preferably substitute at the chain middle group SiO_4 by ^{29}Si NMR measurements [174]. In contrast, Sasaki et al. reported that the Al

substitution preferably occurs at the bridging SiO_4 [175]. The previous structural determination of tobermorite crystals did not consider the Al substitution due to the fact that it is difficult to distinguish Si and Al by x-ray experiment [55, 129]. Up to now, the accurate crystal structure of Al substituted tobermorite is still unknown. In case of partial substitution of silicon by aluminum in the bridging tetrahedra [176, 177], it was suggested that general and local charge balance is restored through additional OH^- for O^{2-} substitutions. These coupled substitutions may explain the results of the ionic content of tobermorite and the growth of silicate chains in hydrated cement paste. However, the lack of information on Al substituted tobermorite makes further discussion difficult in this study.

The other interesting observation is the stability under high pressure. The normal tobermorite 11 Å exhibits pressure-induced amorphization at high pressure (Fig. 3.9). The basal peak completely disappeared over 6 GPa. This amorphization might be associated with dehydration of the structure as observed during thermal process [178] or disruption of hydrogen bonding network. But anomalous tobermorite 11 Å shows stable behavior (Fig. 3.13). Furthermore it shows greater number of distinct diffraction peaks in ambient and under high pressure. Under hydrostatic pressure, variations of **a** and **b** lattice parameters in both tobermorite 11 Å were small compared to that of **c** lattice parameter (Fig. 3.10 and 3.10). That means the areas of the ***ab***-plane of a unit cell were almost equal but **c**-axis was mostly contracted under hydrostatic pressure. Figure 3.37 shows measured pressure-volume behavior of tobermorite 11 Å comparing with First-principles calculation by Shahsavari et al. [155]. The First-principles calculation result was reproduced from RVH based bulk modulus of Merlino's tobermorite 11 Å. The experimentally measured data agree quite well with the simulation. Smaller number of diffraction peaks yields relatively larger error ranges for normal tobermorite 11 Å. Furthermore, the ambient volume of Al-substituted normal tobermorite is larger than Al-free anomalous tobermorite. However, overall pressure behaviors are similar regardless of the different thermal behavior.

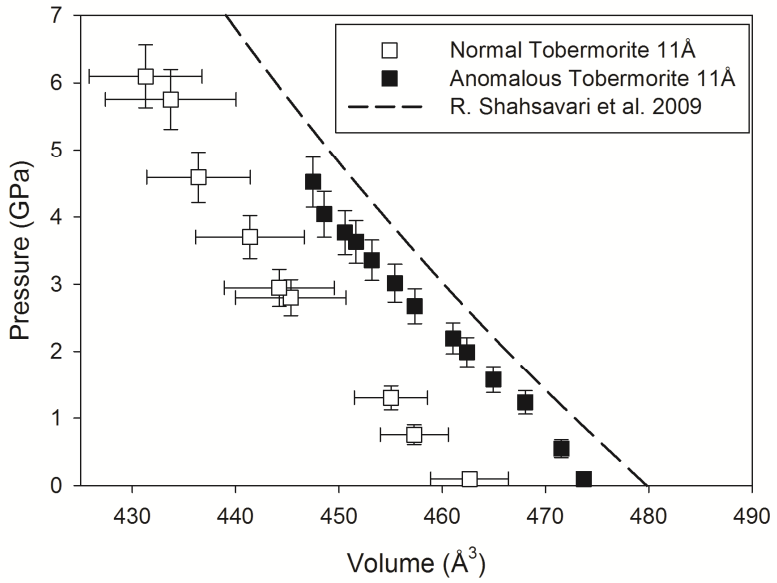

Figure 3.37 (Fig.3.10(b)) Pressure dependent behavior of normal and anomalous tobermorite 11 Å. First principles calculations result is reproduced from RVH bulk modulus of Shahsavari et al. [155].

Although calcium silicate hydrate crystals are the most important crystals in cement and concrete system, there has been no reported experimental bulk modulus except for tobermorite 14 Å [148]. Theoretically, a large number of studies using first-principles calculations and molecular dynamics have been applied to predict mechanical properties of calcium silicate hydrate crystals. The results have yielded various bulk modulus values depends on its crystal model and Ca/Si ratio [142, 171, 179]. Gmira et al. theoretically calculated the bulk modulus of tobermorite-like C-S-H gel (71.8 GPa) using both Hamid and Merlino models of tobermorite 11 Å [179]. However, Pellenq et al. predicted a value of 61.9 GPa for the tobermorite-like C-S-H structure [142]. Manzano et al. reported 46 GPa for tobermorite 14 Å, 74 GPa for tobermorite 11 Å, and 68 GPa for tobermorite 9 Å [171]. Recently, Shahsavari et al. used accurate first-principles calculation to determine mechanical properties of tobermorite phases considering varying Ca/Si ratios and jennite [155]. In the results, Merlino tobermorite 11 Å is stronger than Hamid tobermorite 11 Å due to double silicate tetrahedron chains (condensed wollastonite chains). Also, additional Ca cations with octahedral coordination make the crystal stronger as well [129]. About the Al incorporation on tobermorite like materials, the bulk modulus of Al substituted C-S-H from an alkaline activated slag experimentally gives a similar value with a synthesized C-S-H(I) as 33-35 GPa [40].

In the present study, high-pressure x-ray diffraction tests were performed to entire tobermorite family, which makes the systematic comparison possible. Figure 3.38 compares the experimentally measured pressure behaviors of tobermorite 14Å, normal 11 Å, anomalous 11 Å, and 9 Å. As expected from simulation [155], the compressibility is correlated with the interlayer distance of the principal layers of tobermorite. In all cases, the variations of ***a*** and ***b*** lattice parameters were negligible compared to that of ***c*** lattice parameter, suggesting that the incompressibility of layer direction determines the overall pressure behavior. The principal ***ab***-plane of a unit cell does not change but c-axis is mainly contracted under 'hydrostatic' pressure. Thus, larger interlayer spacing makes the crystal more compressible in tobermorite cases.

However, there is a difference in case of tobermorite 9 Å between simulation and experiment. Molecular dynamic (MD) simulation by Manzano et al. [171] predicted the bulk modulus of tobermorite 9 Å as 68 GPa while tobermorite 11Å as 74 GPa. It might be possible that interlayer water molecules are resistant against compression in tobermorite 11Å. Then, it could yield larger bulk modulus than that of tobermorite 9 Å. However, it was not the case in tobermorite system. The possible error sources in the MD simulation are the empirical force-fields they used in their research which were not designed for the tobermorite crystals. In addition, accurate equilibrium positions of interlayer waters are not obtainable through the MD simulation. On the other hand, the more accurate (but expensive) simulation method of first-principles calculation yields similar pressure behaviors with experiments. Detail comparison on each tobermorite family will be followed.

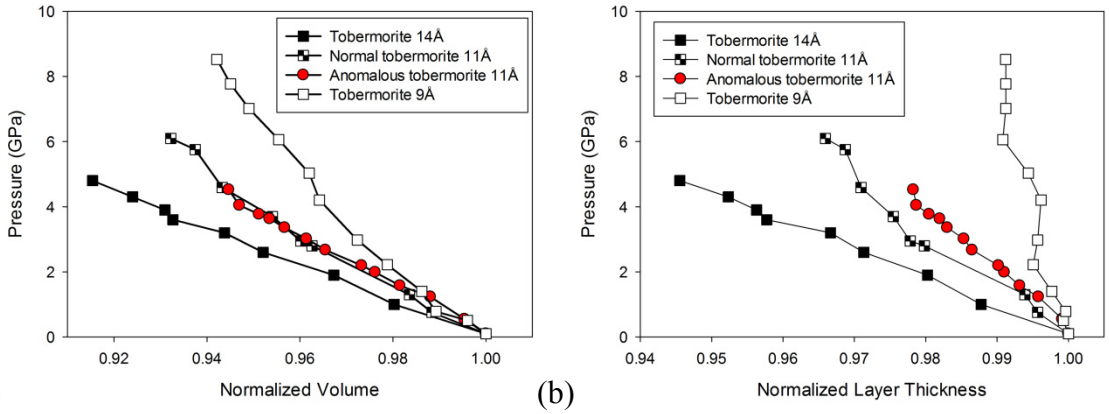

Figure 3.38 Comparison of experimentally measured pressure-volume (a) and pressure-layer thickness (b) behaviors of tobermorite series. Rectangular symbols indicate identical tobermorite source from Crestmore, CA with different thermal treatments.

Figure 3.38 shows an interesting behavior of normal and anomalous tobermorite 11 Å. Although they show exact same pressure-volume behavior (Fig. 3.38(a)), layer thickness of anomalous one is stiffer than one of normal case (Fig. 3.38(b)). If Merlino's hypothesis is correct [55, 115, 116], the normal tobermorite should have more incompressible layer because of the existence of abundant additional Ca atoms in their interlayers. It conflicts with experimentally observed pressure-layer thickness behavior as well as chemical compositions (normal tobermorite Ca/(Al+Si) = 0.68 in Table 3.3 and anomalous tobermorite Ca/Si = 1.05 in Table 3.5). It points out that additional explanation in terms of the crystal structure of tobermorite system may be required.

Recently, Oh et al. experimentally measured a bulk modulus of tobermorite 14 Å by high pressure x-ray diffraction method [148]. They refined unit cell volumes using different crystal systems of monoclinic and orthorhombic, but they produced identical bulk modulus of 47(4) GPa. On the other hand, first-principles calculation based on GGA pseudopotential were performed by Shahsavari et al. [155] and predicted RVH based bulk modulus as 36(6) GPa. In section 3.3.1, both LDA and GGA pseudopotentials were tested for monoclinic tobermorite 14 Å structure. Along with the RVH based elastic properties, isothermal bulk modulus could be directly computed by applying isotropic pressure on the crystal. The calculated bulk modulus can be used to verify the overall accuracy of the simulation by comparing with high pressure x-ray diffraction.

The calculated isothermal bulk modulus using LDA (44 GPa) agrees well with experimentally measured value of 47(4) GPa. In addition, GGA calculation yields similar values of elastic constants with previous simulation by Shahsavari et al.[155] (shown in Table 3.23). Although the first-principles calculation can predict material properties without any assumptions, the exchange-correlation potential is still unknown and can only be approximated as a functional of linearized electron density (LDA case) or gradient form of electron density (GGA case). As described in section 2.2, LDA pseudopotential usually tends to overbind atoms and overestimate the mechanical properties of material [82, 180, 181]. Therefore the large value of bulk modulus of tobermorite 14 Å from LDA calculation is acceptable. In addition, under pressure, the LDA calculation shows that it maintains the monoclinic crystal structure up to 7 GPa (Table 3.13). However, the monoclinic crystal structure breaks under pressure in case of the GGA calculation (Table 3.14). The broken symmetry definitely affects the overall crystal properties. The other error source could be van der Waals interaction. DFT used in this study may not yield accurate VdW dispersion forces due to its long-range electrostatic characteristics. Thus, the excellent agreement between the LDA calculation and experiment reported herein might be not just because LDA can well simulate the exchange-correlation energy in the system but because of a

result of complex undefined interactions between exchange-correlation energy and the VdW interaction. Furthermore, electron probe analysis verified Al substitution in tobermorite 14 Å (Al/Si = 0.14) as shown in Table 3.3. This also affects the mechanical properties of tobermorite 14 Å. Nevertheless, the LDA calculation predicts the pressure behavior quite well while the GGA calculation underestimates the bulk modulus.

Table 3.23 Summary of nanomechanical properties of tobermorite 14 Å.

Tobermorite 14 Å										
	LDA	**GGA**	**GGA [155]**			**LDA**	**GGA**	**GGA [155]**	**MD [171]**	**Exp. [148]**
c11	**125.5**	71.4	77.6		K_0	**39(1)**	33(2)	-	-	53(2)*
c12	**41.2**	18.5	35.9	**3rd EoS**	K_0'	**6.6**	4.7	-	-	0.8
c13	**35.3**	5.7	20.2		V_0	**1156**	1220	-	-	1156(1)**
c16	**-11.1**	6.5	3.1	**2nd EoS**	K_0	**44(1)**	34.9(9)	-	-	47(4)
c22	**121.7**	53.0	104.5		V_0	**1156**	1220	1213	-	1156(1)**
c23	**30.5**	26.6	26.3		**K**	**57(2)**	30(1)	36(6)	46	-
c26	**-4.9**	-6.1	-1.8	**RVH**	**G**	**41(2)**	22(3)	21(4)	39	-
c33	**73.5**	51.2	32.1		**E**	**99.5**	52.8	51.9	91	-
c36	**2.3**	-3.5	3.0		***v***	**0.2**	0.2	0.3	0.2	-
c44	**57.8**	39.6	24.5							
c45	**4.9**	-7.5	-9.4							
c55	**46.7**	16.6	14.7							
c66	**38.7**	24.8	38.1							

* Data was reproduced from [148]. ** Volume is refined using monoclinic (B11b) crystal structure of tobermorite 14Å [148]. Elastic constants and RVH bounds are computed based on X//a setting. Most reliable results are in bold.

In sections 3.2.1 and 3.2.2, high pressure x-ray diffraction experiments on normal and anomalous tobermorite 11 Å are discussed. Although overall pressure-normalized volume plots look almost identical (Fig. 3.38 (a)), the fitted isothermal bulk moduli are somewhat different: 71 GPa and 63 GPa for normal and anomalous tobermorite 11 Å, respectively. The reason of the difference is due to the unusual data points of normal tobermorite over 5 GPa (Fig. 3.15). At that pressure range, the pressure-induced amorphization makes difficult to identify the accurate x-ray diffraction positions which could lower the accuracy of the experiment (Fig. 3.9). Ignoring the two points over 5 GPa would lower the fitted bulk modulus significantly.

Table 3.24 summarizes experimentally and theoretically calculated elastic constants including bulk modulus of tobermorite 11 Å. Considering the fact that the GGA calculation tends to underestimate the mechanical properties of a material, the slightly smaller value of 67 GPa as a RVH based bulk modulus of

Merlino's tobermorite 11 Å looks reasonable. However, there is still no reliable crystal structure for normal and anomalous tobermorite 11 Å in terms of thermal behavior, pressure-induced amorphization, Al substitution, and different compressibility of layer thickness. It questions the results of theoretical calculation. Further studies on accurate crystallographic determination on various tobermorite 11 Å and computational simulations on the models are necessary.

Table 3.24 Summary of nanomechanical properties of tobermorite 11 Å.

Tobermorite 11Å							
	GGA [155]			GGA [155]	MD [171]	Exp. Normal	Exp. Anomalous
c11	117		K_0	-	-	62(4)	67(2)
c12	45.8	**3rd EoS**	K_0'	-	-	9.7	1.8
c13	27.9		V_0	-	-	463(3)	475.9(4)
c22	126.1		K_0	-	-	71(4)	63(2)
c23	46.2	**2nd EoS**	V_0	480.9*	-	463(3)	475.9(4)
c33	126.35		**K**	67(1)	74	-	-
c44	30.2	**RVH**	**G**	32(4)	29	-	-
c55	20.8		**E**	83.1	77	-	-
c66	44.4		***v***	0.3	0.3	-	-

* Volume is reproduced (i.e., divided by 2) for the comparison of I2mm symmetry of experimental tobermorite 11Å. Elastic constants and RVH bounds are computed based on X//a setting.

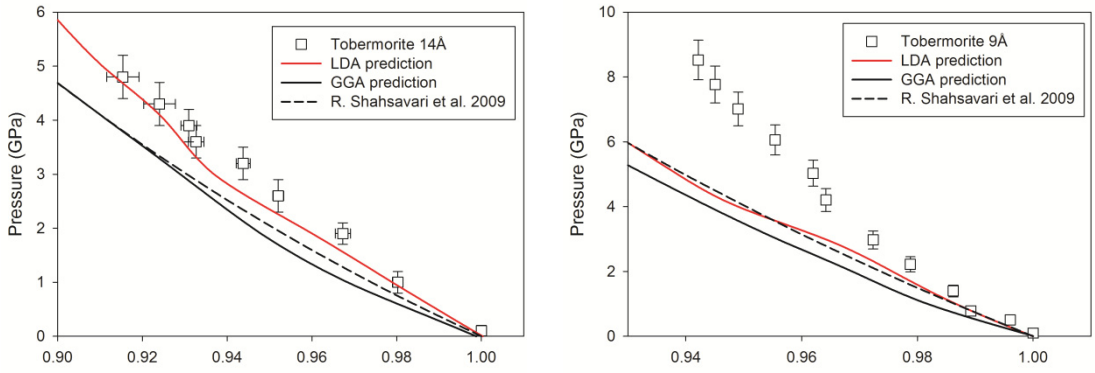

(a) (b)

Figure 3.39 Volumetric compressibilities of tobermorite 14 Å (a) and 9 Å (b) from high pressure experiment and LDA (red line) and GGA (black line) simulation. First principles calculations result is reproduced from RVH bulk modulus of Shahsavari et al. [155].

Despite of the good agreements of tobermorite 14 Å and 11 Å in experiments and simulations, there is a significant difference in case of tobermorite 9 Å as shown in Fig. 3.39(b). The result of first-principles calculation in section 3.3.2 predicts that the LDA computation is somewhat closer to the

experimental result up to 2 GPa. However, experimentally observed volume shows much stiffer behavior above 2 GPa. Thus the predictions from the first-principles calculation were not valid at high pressure. Possible error sources could be the infiltration of pressure-transmitting medium in high pressure x-ray experiment [182]. If there is a space in crystal structure, the solution might fill the space and affect the compressibility of crystal framework. The interlayer space in tobermorite 9 Å is smaller than those of 11 Å and 14 Å, suggesting that the infiltration does not affect the compressibility of crystal structure with larger cavities. In addition, the tobermorite 9 Å sample used in the experiment has Al-substitution (Al/Si = 0.14) while there is no Al in the crystal system in simulation. Further NMR and Rietveld studies are necessary for structural determination of Al substituted tobermorite 9 Å.

In Fig. 3.39 (b), the LDA computation in this study was rather similar with the GGA computation by Shahsavari et al. [155]. This is possible by setting different convergence criteria during the computation. The criteria such as energy cut-off and k-point sampling are critical in first-principles calculation because they will decide the accuracy of simulation and computational time. The higher convergence criteria were used in section 3.4 (but computationally more expensive) compared to the calculation of [155].

Figure 3.40 compares x-ray diffraction patterns of tobermorite 9Å in ambient condition (middle), with diamond anvil cell (top) and of ICSD database (bottom, #90037). Unlike the cases of tobermorite 11 Å and 14 Å, the intensity of basal peak is not strong, which means the layer character of this material is rather weak. Furthermore, the basal peak almost disappears with pressure-transmitting solution (methanol:ethanol=4:1) in diamond anvil cell (Fig. 3.40). Possible explanation is the size of crystal system in the solution. As discussed before, about 5-10 ordered lattice repeat is required for a clear Bragg reflection to be observed. Therefore, if the particle-cluster size of tobermorite 9 Å in the solution is less than 50 Å, the peak will be disappeared before being pressured. More fundamental study on the particle dispersion effect in high pressure x-ray experiment is necessary.

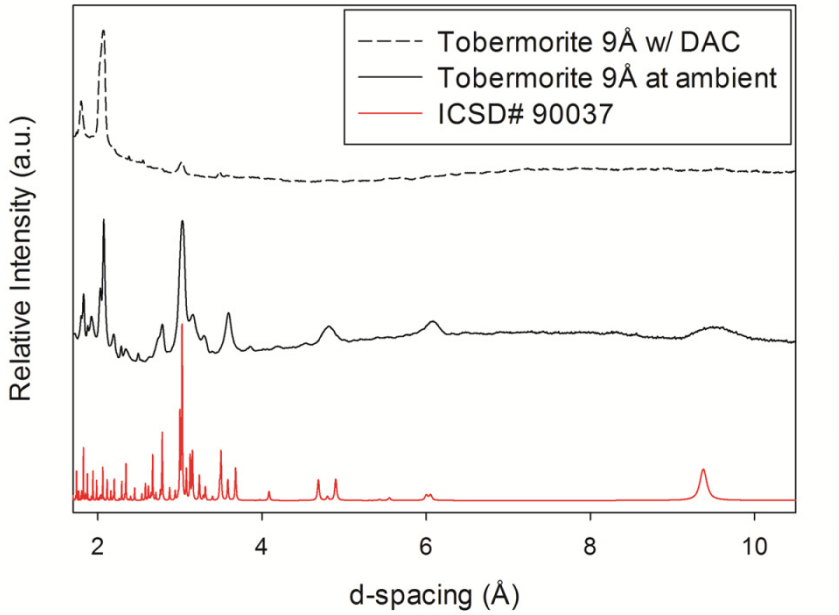

Figure 3.40 X-ray diffraction patterns of tobermorite 9 Å. Reference profile (red line) was reproduced from [116]. Tobermorite 9 Å was made from heating the tobermorite 14Å at 360 ºC for 24 hours. Black and dotted lines represent the x-ray profile at ambient condition and mixed with alcohol mixture in DAC, respectively.

Table 3.25 Summary of nanomechanical properties of tobermorite 9 Å.

Tobermorite 9 Å										
	LDA	GGA	GGA [155]			LDA	GGA	GGA [155]	MD [171]	Exp.
c11	180.2	179.1	169.2		K_0	70(3)	56(1)	-	-	86(6)
c12	79.3	51.0	54.5	**3rd EoS**	K_0'	4.6	6.8	-	-	20.9
c13	36.6	38.8	37.5		V_0	861	787	-	-	1472(1)*
c14	0.0	-0.4	-1.1	**2nd EoS**	K_0	71(4)	63(1)	-	-	115(14)
c15	-0.3	-2.1	-8.9		V_0	861	787	784.0	-	1472(1)*
c16	-6.3	-3.0	2.7		**K**	82(4)	74(4)	71(5)	68	-
c22	174.4	168.5	170.0	**RVH**	**G**	53(2)	50(2)	37(4)	67	-
c23	33.8	37.9	36.2		**E**	130.3	122.9	95.1	152	-
c24	-16.1	-12.1	3.6		***v***	0.2	0.2	0.3	0.13	-
c25	-9.4	-14.4	-11.8							
c26	-1.8	-0.1	-1.1							
c33	117.7	98.8	92.7							
c34	-6.3	-10.7	2.6							
c35	4.7	0.5	-3.5							
c36	-3.8	-1.1	0.6							
c44	52.7	53.1	40.6							
c45	-0.7	-0.3	0.4							
c46	-9.7	-10.7	-5.5							
c55	44.0	42.3	17.9							
c56	2.7	2.8	-1.9							
c66	69.8	59.9	45.7							

* In the high-pressure experiment, orthorhombic unit cell was used for refinement. On the other hand, triclinic (C-1) crystal structure is used for DFT simulation. Elastic constants and RVH bounds are computed based on X//a setting.

Table 3.26 summarizes the mechanical properties of jennite obtained from high pressure x-ray diffraction and first-principles calculation. First of all, the large K_0' value in 3rd order EoS is not realistic which is mainly due to the small number of data points. Therefore, the fitting result of 2nd order EoS is used to verify the simulation results. In general, LDA calculation accurately predicts the pressure-volume behavior while GGA slightly underestimates the values of the stiffness. In the case of oxide mineral, the LDA calculation usually tends to overestimate the mechanical properties while GGA is the opposite [82, 180, 183]. Not only in terms of the pressure-volume behavior, but the variation of lattice parameters of triclinic crystal system was also well predicted as an upper and lower bound (Fig. 3.33). Therefore, it can be safely suggested that the elastic tensor coefficient (Table 3.21) and anisotropic feature (Fig. 3.35) from the first-principle calculation are quite reliable.

Table 3.26 Summary of nanomechanical properties of jennite.

Jennite											
	LDA	**GGA**	**GGA [155]**			**LDA**	**GGA**	**GGA [155]**	**MD [171]**	**Exp. (M:E)**	**Exp. (SO)**
c11	**100.0**	110.4	100.1		K_0	**62(7)**	57(1)	-	-	45(5)	61(4)
c12	**49.0**	40.9	26.9	**3rd EoS**	K_0'	**5.1**	2.4	-	-	42.3	9.9
c13	**46.6**	41.1	32.0		V_0	**812**	765.2	-	-	754(2)	755(1)
c14	**-6.7**	1.5	1.3	**2nd EoS**	K_0	**63(1)**	54.2(8)	-	-	68(5)	64(2)
c15	**4.9**	5.1	1.5		V_0	**812**	765.2	775	-	754(2)	755(1)
c16	**-3.0**	1.9	3.3	**RVH**	**K**	**63(2)**	60(1)	32(5)	43	-	-
c22	**127.5**	126.9	45.7		**G**	**28(2)**	33(1)	22(1)	26	-	-
c23	**41.7**	33.9	4.4		**E**	**72.9**	83.3	53.6	66	-	-
c24	**3.0**	1.2	7.4		***v***	**0.3**	0.3	0.2	0.2	-	-
c25	**-4.9**	-5.7	-6.2								
c26	**-6.9**	-9.6	-3.2								
c33	**78.8**	78.4	59.2								
c34	**0.3**	-2.6	-1.3								
c35	**-6.0**	-1.5	1.4								
c36	**-1.4**	3.1	0.1								
c44	**23.3**	32.5	22.0								
c45	**-3.2**	-0.2	-1.7								
c46	**1.8**	-0.3	-1.6								
c55	**27.0**	30.3	21.0								
c56	**-0.6**	1.2	2.7								
c66	**41.1**	40.2	26.6								

* Most reliable results are in bold.

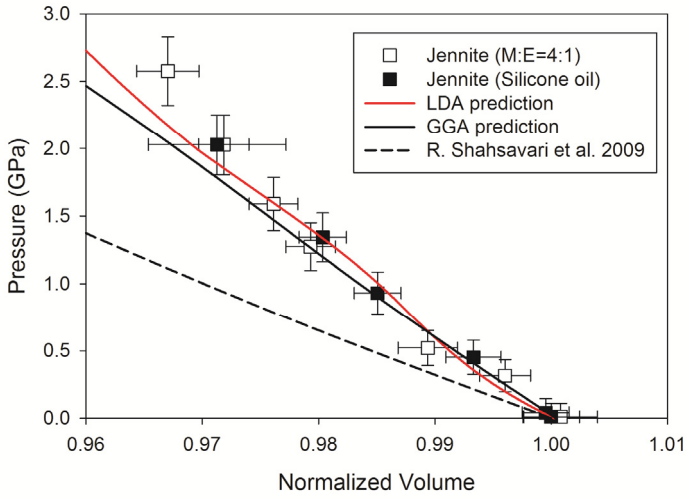

Figure 3.41 (Fig. 29) Comparison of volumetric compressibilities of jennite from high pressure experiment, LDA (red line), and GGA (black line) simulations. First-principles calculations result is reproduced from RVH bulk modulus of Shahsavari et al. [155].

However, there is a significant difference with the previous calculations using first-principle calculation and molecular dynamic simulation (Fig. 3.41 and Table 3.26). As discussed previously, MD simulation cannot be precise unless the empirical force fields are accurately designed for specific environment of a system. The force fields are typically designed based on accurate values of elastic constants and partial charges from first-principles calculation or experiments [184]. Therefore it is unfruitful to discuss the accuracy of MD simulation results at this stage. On the other hand, first-principles calculation does not depend on anything except exchange-correlation potential. In this study, the LDA and GGA calculation predict RVH based bulk modulus as 63 GPa and 60 GPa, respectively. The GGA calculation by Shahsavari et al.[155] predicted the bulk modulus as 32 GPa which is much lower than that from high pressure x-ray experiment (64 GPa, 2nd order EoS, SO). The RVH properties are determined from elastic tensor coefficient derived in Eqn. (2.39) to (2.44). Therefore, the lower values of C_{22} and C_{33} in their computations are responsible for the lower bulk modulus. Considering electron densities, the C_{22} should be the stiffest direction in the crystal system of jennite as shown in Fig. 3.42. The reason is C_{11} and C_{33} directions contain interlayer space but C_{22} is perpendicular direction to the interlayer. The possible error can be unrealistic starting structure especially with respect to water molecules and hydroxides. In addition, the convergence criteria are the important parameters in first-principles calculation (this study: 1900 eV for energy cut-off, 4 × 4 ×2 *k*-points sampling, and 0.001 eV/Å for force convergence). The criteria used in their simulation (i.e., 420 eV for energy cut-off, 2 × 2 ×1 k-points sampling, and 0.01 eV/Å for force convergence) may be too rough to get accurate simulation results. Further study may be necessary to verify this issue. Even so, this issue suggests high pressure x-ray diffraction can be the unique technique to validate the performance of first-principles calculations.

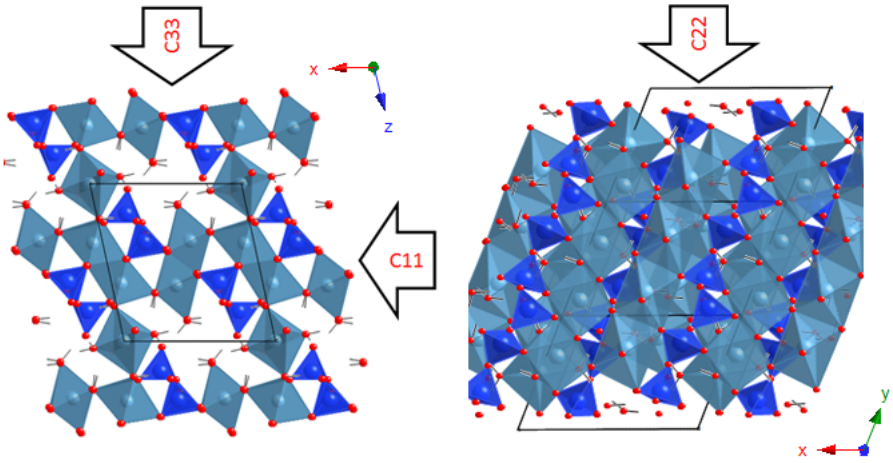

Figure 3.42 Standard directions of elastic constants in triclinic crystal system of jennite.

3.5 Chapter Summary

In chapter 3, the mechanical properties of calcium silicate hydrate phases were investigated. C-S-H gel in hydrated portland cement is poorly crystalline material with varying Ca/Si ratio. Systematic measurements of modulus of crystalline calcium silicate hydrate could give insights on the interpretations of structure at the small scale and on the deformation properties of C-S-H gel. High pressure x-ray diffraction and first-principles calculation are possible approaches. In addition, in order to investigate thermodynamic stability of a material, the first derivative of the energy should be calculated. Moreover, the second derivative of the energy also has to be considered to identity the relative thermodynamical stability of a material. The experimentally and theoretically calculated bulk moduli of materials which are the second derivative of the energy can be useful.

Up to the present time, there has been no reported experimentally measured bulk modulus of the tobermorites except for tobermorite 14 Å. In chapter 3, high pressure x-ray diffraction experiments were performed to study normal and anomalous tobermorite 11 Å, tobermorite 9 Å, and jennite. First-principle calculations of tobermorite 14 Å, 9 Å, and jennite support the experimental results and provides additional elastic properties of the materials. Overall, the compressibility of crystalline calcium silicate hydrate is related with the interlayer thickness of the materials. In the cases of tobermorite crystals, the layer thickness is a function of the number of contained water molecules in the interlayer. Under pressure, the variations of ***a*** and ***b*** lattice parameters were small compared to that of ***c*** lattice parameter. Furthermore, larger interlayer space makes the crystal more compressible, suggesting that the number of water molecules determines not only the interlayer space but overall compressibility of tobermorite. Since the C-S-H gel possesses single dreierketten chain, the phenomenon described above may not directly apply to C-S-H gel. Nevertheless, the mechanism proposed here suggests that the content of the interlayer space of calcium silicate hydrates can have an influence on both macroscopic mechanical properties of cement paste and thermodynamical stability.

However, there is a difference in case of tobermorite 9 Å between simulation and experiment. The result of first-principles calculation predicts well the initial pressure-volume behavior, but the experimentally observed volume transforms to much stiffer from 2 GPa. The difference can be due to the infiltration of pressure-transmitting medium in the high pressure x-ray experiment or the mechanical impact of Al substitution. Further NMR and Rietveld studies are required for structural determination of Al substituted tobermorite 9 Å in order to understand the computational results. Although the first-principles calculation is the most accurate method to predict the material properties, the calculation

result of jennite is significantly different with previous GGA calculation. The high pressure x-ray diffraction is the ideal method to validate the performance of different simulation results. Setting high convergence criteria in the first-principles calculation is a key to avoid some local minima of potential energy.

There is a slight difference in layer compressibility between normal and anomalous tobermorite 11 Å. According to Merlino's hypothesis, normal tobermorite has additional 'zeolitic' Ca cations in the interlayer of tobermorite 11 Å with a half occupancy, which results in thermal shrinkage to tobermorite 9 Å. However, measured chemical composition of normal and anomalous tobermorite used in this study are Ca/(Al+Si) = 0.68 and Ca/Si = 1.05, respectively. Opposite to the Merlino's hypothesis, anomalous tobermorite has more Ca atoms in structure, which might results in stiffer behavior of layer under pressure. However, overall pressure-volume behavior of normal and anomalous tobermorite 11 Å was almost identical. Further study on structural determination of tobermorite 11 Å is necessary to explain the pressure behavior and chemical composition.

4. High Pressure X-ray Diffraction and First-Principles Calculation Studies on Calcium Aluminate Oxides

4.1 Calcium Aluminate Hydrates in Concrete

During the hydration of portland cement, AFm (Al_2O_3-Fe_2O_3-mono) phases are formed when ions are brought together in appropriate concentrations in aqueous systems at room temperature or formed hydrothermally, i.e. in the presence of water under pressure above 100 ˚C. AFm phases have a layer structure derived from that of portlandite, $Ca(OH)_2$, whereby one third of Ca^{2+} ions is replaced by a trivalent ion, nominally Al^{3+} or Fe^{3+} ion. The principal layer has the chemical formula $[Ca_2(Al,Fe)(OH)_6]^+$. Between the principal layer it includes charge-balancing X anions and water molecules [185]. This interlayer region thus has the composition $[X_nH_2O]^-$. The X anion could be hydroxide, silicate, sulfate, chloride, or carbonate.

Carbonate sources in portland cement arise from numerous sources: from kiln dust, calcite, impurity in gypsum, or simply by reaction with the atmosphere to form carbonate- containing AFm phases, *e.g.* monocarboaluminate ($C_4A\overline{C}H_{11}$, triclinic, P1 or $P\bar{1}$) [186, 187] and hemicarboaluminate ($C_4A\overline{C}_{0.5}H_{12}$, trigonal, $R\bar{3}c$ or R3c) [188]. These varied sources of potential carbonate are sufficient to stabilize hemicarboaluminate or monocarboaluminate, or both in fresh and nominally uncarbonated cement. Monocarboaluminate is stable in contact with calcite, $CaCO_3$, but hemicarboaluminate is stable only over a limited range of CO_2 activities. Thus the hemicarboaluminate is not often observed in real concrete systems due to the difficulty of excluding CO_2 [189]. Damidot et al. showed that with rising carbonate activity, hydroxyl-AFm was replaced first by hemicarboaluminate and then by monocarboaluminate [190]. Thus small amounts of carbonate can influence the nature and stability of the AFm phase. Although hemicarboaluminate and monocarboaluminate contain only 3.8 and 7.7 wt.% CO_2, respectively, particular interest to the constitution of modern cement paste is the formation of ettringite as a consequence of carbonate additions to cement: sulfate displaced from AFm in the course of forming hemicarboaluminate and monocarboaluminate contributes to the formation of ettringite [188, 189]. In addition, carbon sequestration technique is being actively developed due to global carbon emission problem. In spite of concrete's remarkable mechanical properties and chemical durability as the world's premier construction material, the massive quantity of CO_2 emitted during the manufacturing of portland cement is responsible for roughly 7-10 % of global anthropogenic CO_2 emissions [1], making it problematic despite its widespread use. On the other hand, concrete has a great potential as a vast tank of carbon sequestration because of its enormous

global usage. Thus research related to AFm phases containing carbon can provide better understanding on the role of concrete as the carbon sequestration.

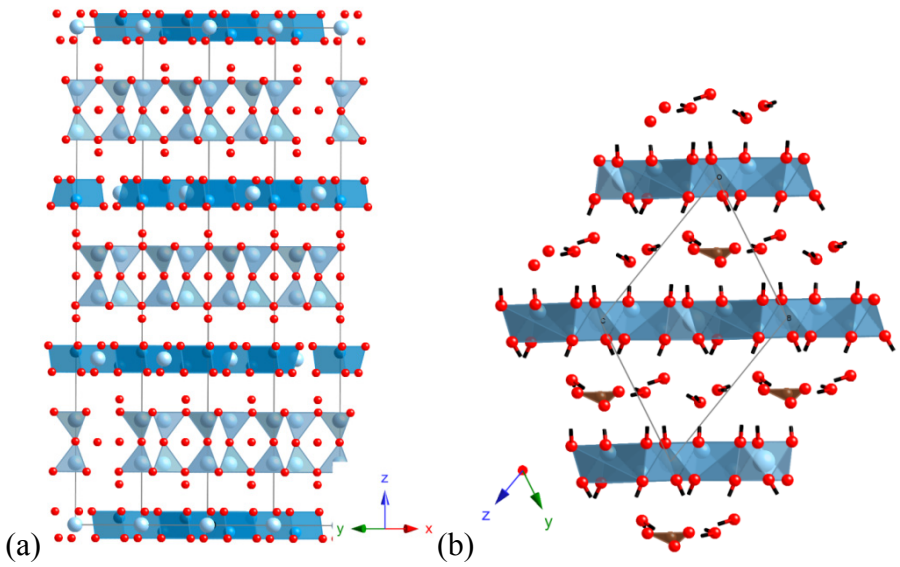

Figure 4.1 Crystal structure of (a) strätlingite [191] (b) monocarboaluminate [187]. Calcium-aluminate ions are shown as dark blue octahedral, silicate/aluminate ions in interlayers are shown as light blue tetrahedra, and oxygen ions are represented as red spheres. Water and hydroxyl groups in monocarboaluminate are denoted with red spheres and black sticks for oxygen and hydrogen atoms, respectively.

Crystal structures of AFm phases containing silicate and carbonate anion are shown in Fig. 4.1. The summary of crystallographic data of AFm phases is given in Table 4.1. The layer thickness depends on the nature of the X anion and the amount of interlayer water, which can be varied by stepwise dehydration at different temperature and humidity conditions [185, 192]. Changes in the water content associated with concomitant relaxation of the AFm framework have been observed in numerous variable-temperature studies, which explain why AFm phases undergo several dehydration stages at higher temperatures (see Table 4.1). However, the effects of pressure on the structure and the detailed crystal properties of dehydrated AFm phases are less well studies. Recently, Clark et al. calculated the bulk modulus of ettringite—one of AFt phases—using x-ray diffraction and infrared study [42]. But for AFm phases that are often less stable compared to the AFt phase, high pressure structural data are not yet available.

Table 4.1 Crystallographic data of calcium aluminate hydrates.

Mineral name	Chemical formula	Space group	Drying condition	Layer thickness (Å)	a (Å)	c (Å)	Vol. (Å^3)	Ref.
Strätlingite	$Ca_2Al_2SiO_7 \cdot 8H_2O$	R3, R-3	27ºC 37% RH	12.55	5.747	37.64	1076.6	[193]
			27ºC	-	5.737	37.59	1071.5	[194]
			27ºC	-	5.745	37.77	1079.6	[193]
			30ºC	-	5.747	37.64	1076.6	[195]
	$Ca_2Al_2SiO_7 \cdot 4H_2O$		> 135ºC	11.2	-	-	-	[193]
	$Ca_2Al_2SiO_7 \cdot 7.25H_2O$	R-3m	27ºC	-	5.745	37.77	1079.6	[191]
Hemicarbo aluminate	$Ca_4Al_2(CO_3)_{0.5}(OH)_{13} \cdot 5.5H_2O$	R3c, R-3c	22ºC 36% RH	8.193	5.770	49.16	1417.4	[196]
			30ºC	-	5.761	49.25	1415.6	[195]
	$Ca_4Al_2(CO_3)_{0.5}(OH)_{13} \cdot 4.75H_2O$		35ºC	7.63	-	-	-	[196]
	$Ca_4Al_2(CO_3)_{0.5}(OH)_{13} \cdot 4H_2O$		80ºC	7.26	-	-	-	[196]
	$Ca_4Al_2(CO_3)_{0.5}(OH)_{13}$		105ºC	6.6	-	-	-	[196]
Monocarbo aluminate	$Ca_4Al_2(CO_3)(OH)_{12} \cdot 5H_2O$	P1, P-1	27ºC	7.56	5.781	7.855	217.3	[196]
	$Ca_4Al_2(CO_3)(OH)_{12} \cdot 2H_2O$		95ºC	7.2	-	-	-	[196]
	$Ca_4Al_2(CO_3)(OH)_{12}$		130ºC	6.6	-	-	-	[196]
Hydrogarnet	$Ca_3Al_2O_6 \cdot 6H_2O$	IA-3D	25ºC	-	12.576	-	1988.7	[197]
			-	-	12.56	-	1981.4	[198]
			27ºC	-	12.57	-	1985.9	[199]

This chapter reports the behavior of strätlingite, hemicarboaluminate, hydrogarnet (with hemicarboaluminate as a minor phase), monocarboaluminate, and tricalcium aluminate under pressure from high-pressure x-ray diffraction experiments. In addition, first-principles calculation has been applied to monocarboaluminate hydrates and tricalcium aluminate. As discussed in chapter 3, two different exchange-correlation functionals have been tested for monocarboaluminate. The accuracy of the functional is investigated by comparing results with high pressure x-ray diffraction experiments. Furthermore, full elastic tensor coefficients, averaged mechanical properties, and static bulk moduli of the materials have been computed.

4.2 High Pressure X-ray Diffraction Experiments on Calcium Aluminate Oxides

4.2.1 Strätlingite

Dicalcium aluminate monosilicate-8-hydrate $Ca_2Al_2SiO_7 \cdot 8H_2O$, trigonal, $R\bar{3}$, R3 or $R\bar{3}m$ (also called gehlenite hydrate) occurs in nature as strätlingite [191, 200]. Its interlayer content is $[AlSi(OH)_8 \cdot H_2O]^-$ and the Al is tetrahedrally coordinated [201]. This phase also appears in the hydration of slag-containing portland cements or blended cements and contributes to compressive strength development in commercial high alumina cement [194].

The strätlingite used in the present study was synthesized following the methods of Matschei et al. [188]. High pressures were generated using a diamond anvil cell. Ambient condition phase identification and the high pressure powder x-ray diffraction experiment were carried out at beamline 12.2.2 of the Advanced Light Source [38], using a synchrotron monochromatic x-ray beam (λ = 0.6199 Å). All samples were finely ground and mixed with a pressure medium of silicone oil (a mixture composed of polysiloxane chains with methyl and phenyl groups) and a few chips of ruby in a glove box to avoid carbonation [188]. The sample was equilibrated for about 20 minutes at each pressure. Exposure times of 300 sec were sufficient to give adequate signals for powder diffraction patterns. The pressure was measured at off-line using the ruby fluorescence technique [150]. All two-dimensional x-ray data were radially integrated to give powder diffraction patterns using the fit2d program [151].

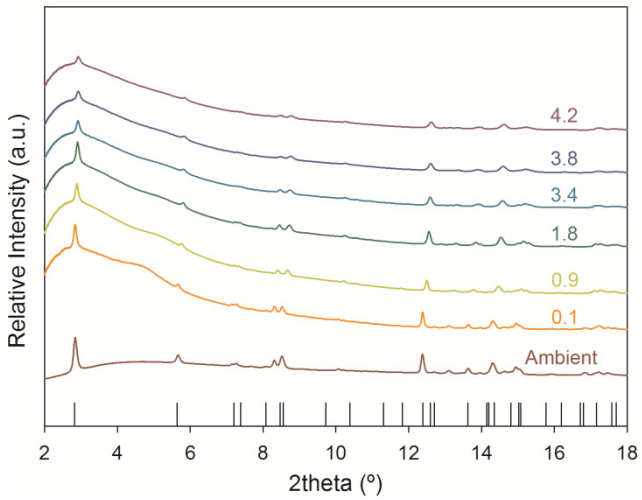

Figure 4.2 Measured x-ray diffraction patterns of strätlingite (λ = 0.6199Å). Bottom peaks indicate reference peak positions from [191]. The numbers indicate measured pressure (GPa) corresponding to each x-ray pattern.

The ambient x-ray diffraction pattern and high pressure patterns of strätlingite are shown in Fig. 4.2. The position and relative intensities of x-ray reflections of the strätlingite agree with the data of Kuzel [193] and Rinaldi et al. [191]. Diffraction peak positions of (003), (006), (009), (110), and (021) were used to calculate the unit cell volume of strätlingite. Changes in lattice parameters and a unit cell volume of the samples were calculated using the software XFit [152] and Celref program [153]. The calculated lattice parameters as a function of pressure are shown in Table 4.2 and Fig. 4.3.

Table 4.2 High pressure x-ray diffraction results of strätlingite (Silicone oil).

Strätlingite experiment (Silicone oil)			
P (GPa)	**a (Å)**	**c (Å)**	**V (Å^3)**
ambient	5.754(7)	37.56(1)	1077.30(2)
0.1(1)	5.75(1)	37.56(1)	1075.57(3)
0.8(2)	5.697(5)	36.887(4)	1036.96(1)
1.5(2)	5.669(5)	36.678(5)	1020.99(1)
2.2(2)	5.654(3)	36.603(3)	1013.43(1)
2.9(3)	5.646(4)	36.480(4)	1007.16(1)
3.4(3)	5.638(2)	36.456(3)	1003.72(1)

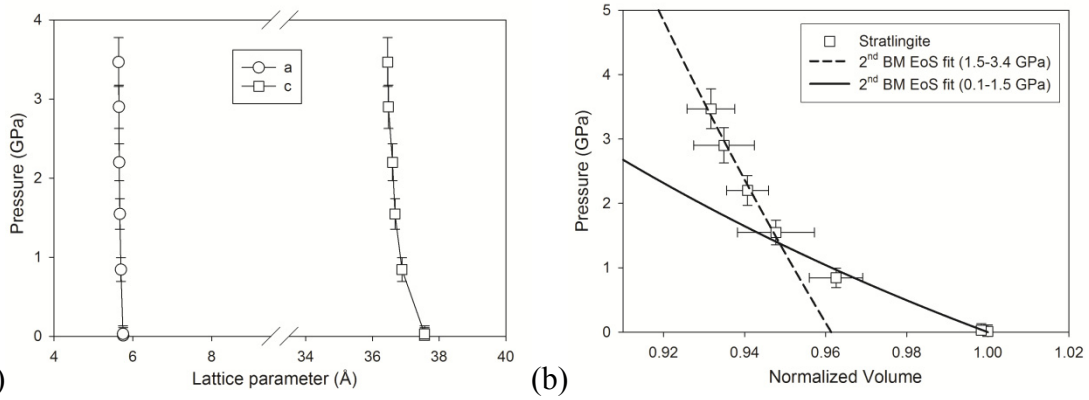

(a) (b)

Figure 4.3 (a) Variation of lattice parameters of strätlingite under pressure. (b) Refined unit cell volume of strätlingite under pressure. 2nd order BM EoS fitting gives the bulk modulus of 23(2) GPa at low pressure range and 100(3) GPa at higher pressure range.

The pressure-normalized volume data was fitted by a Birch-Murnaghan equation of state (BM EoS). In the relationship of F versus f in BM EoS, the y-intercept and slope of the weighted least-squares fit provide the bulk modulus K_0 and its derivative K_0', respectively [99]. A weighted linear least-squares fits with errors was applied to consider both pressure and volume error [154]. Due to its anomalous compressibility, the bulk modulus of strätlingite was calculated in two pressure ranges of 0.1-1.5 GPa and 1.5-3.4 GPa. In the second pressure range, the

initial volume for BM EoS at the point of the convergence was estimated at a value of 1035.67 $Å^3$ [202]. Based on the initial volume, the bulk modulus K_0 and its derivative K_0' were calculated with R^2=0.978 and 0.996 fitting convergence, shown in Fig. 4.3 (b). At the first pressure stage, because the number of volume-pressure points was too small to get a reasonable K_0' value, the value of K_0' was fixed at 4.0. The compressibility data for the BM EoS yielded a bulk modulus of K_0 = 23(2) and 100(3) GPa from 0.1 to 1.5 GPa and from 1.5 to 3.4 GPa, respectively.

4.2.2 Hemicarboaluminate

Tetracalcium aluminate hemicarbonate-12-hydrate (also called hemicarboaluminate), $Ca_4Al_2(CO_3)_{0.5}(OH)_{13}\cdot 5.5H_2O$, trigonal, $R\bar{3}c$ or R3c system [196] is another AFm phase that occurs during the hydration of ordinary portland cement with very low carbonate contents. There are two types of carbon-containing AFm phases: CO_3^{2-} anion monocarboaluminate ($C_4A\bar{C}H_{11}$, triclinic, $P\bar{1}$ system [187]) and hemicarboaluminate ($C_4A\bar{C}_{0.5}H_{12}$). At ambient conditions, monocarboaluminate and hemicarboaluminate have $[1/2(CO_3^{2-})\cdot 5/2H_2O]^-$ and $[1/4(CO_3^{2-})\cdot 1/2(OH^-)\cdot 11/4H_2O]^-$ as interlayer contents, respectively. The interlayer contents and layer thickness of hemicarboaluminate at varying hydration stages were studied by Fischer and Kuzel [196] are summarized in Table 4.1.

During the synthesis of the AFm phases, the low stability of hydroxyl AFm results in the appearance of other phases in the course of synthesis, notably hydrogarnet with hemicarboaluminate [203]. Hydrogarnet, $Ca_3Al_2(OH)_{12}$, cubic, Ia3d, whose structure is related to that of grossularite garnet [107], appears more readily in nominally sulfate-free cements. However, it is strongly destabilized by sulfate at low temperatures, (<50 ˚C) thus it does not generally appear during the hydration of portland cement unless the cement has been heat cured. Due to its importance in geophysics, the behavior of hydrogarnet under pressure has been well studied [204-206].

For strätlingite, silicone oil was used as the pressure medium. For hemicarboaluminate, a 4:1 mixture of methanol:ethanol was used in the first run (λ=0.4133 Å) and the silicone oil for the second run (λ=0.4959 Å). Diffraction patterns were collected with incremental rising and falling pressure for all experiments. Fig. 4.4 and 4.5 show the whole x-ray stack of hemicarboaluminate with different pressure-transmitting media. Newly emerging peaks observed in the post-compression sample were due to the steel gaskets and ruby chips which were present during the collection of the post-compression pattern while they were absent at ambient condition.

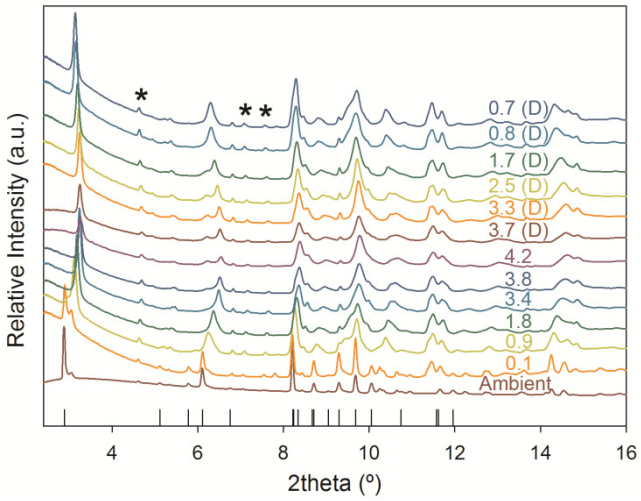

Figure 4.4 Measured x-ray diffraction patterns of hemicarboaluminate (λ = 0.4133 Å) with alcohol mixture (Methanol:ethanol=4:1). Hydrogarnet peaks are denoted as (*). Bottom peaks indicate reference peak positions from [196]. The numbers indicate measured pressure (GPa) corresponding to each x-ray pattern. The (D) means data collected in decompression.

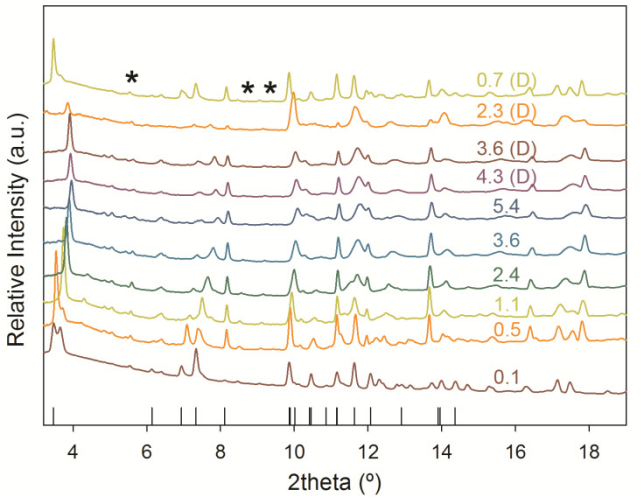

Figure 4.5 Measured x-ray diffraction patterns of hemicarboaluminate (λ = 0.4959 Å) with silicone oil. Hydrogarnet peaks are denoted as (*). Bottom peaks indicate reference peak positions from [196]. The numbers indicate measured pressure (GPa) corresponding to each x-ray pattern. The (D) means data collected in decompression.

The reflection data for hemicarboaluminate agreed with the data obtained by Fischer and Kuzel [196]. Matschei et al. suggested that monocarboaluminate and hydrogarnet could be found coexisting with hemicarboaluminate [188]. Also with rising temperature, the high temperature formation of portlandite in stoichiometric mixtures arises from the increasing destabilization of

hemicarboaluminate. However, some differences of basal reflections which are not consistent with those of monocarboaluminate or portlandite at ambient pressure can be explained by the different water contents in the interlayer of the hemicarboaluminate. In the hemicarboaluminate the dehydration is very likely to happen as indicated by relatively low temperature of dehydration (Table 4.1). The layer thickness of 8.193 Å of $C_4A\overline{C}_{0.5}H_{12}$ and 7.63Å of $C_4A\overline{C}_{0.5}H_{11.25}$ agree with those of the ambient diffraction patterns [196], indicating that both $C_4A\overline{C}_{0.5}H_{12}$ and $C_4A\overline{C}_{0.5}H_{11.25}$ coexist in the ambient sample. Figure 4.6 shows powder diffraction pattern corresponding to the basal reflections of the hemicarboaluminate contained in a diamond anvil cell with 4:1 methanol:ethanol pressure-transmitting medium. As pressure increased, however, those two basal reflections merged together to one intense peak.

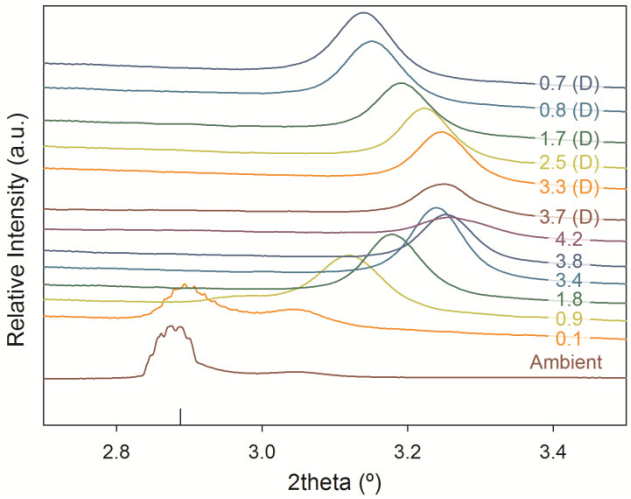

Figure 4.6 Variation of basal peak of hemicarboaluminate (λ = 0.4133 Å) with alcohol mixture (Methanol:ethanol=4:1). The numbers indicate measured pressure (GPa) corresponding to each x-ray pattern. The (D) means data collected in decompression.

To calculate the volume of hemicarboaluminate, the (006), (018), (110), (119), and (024) peaks were selected. Like the case of strätlingite, the XFit [152] and Celref programs [153] were used to define peak positions at each pressure point and compute unit cell volumes and corresponding volume errors. Similarly, the hemicarboaluminate also showed anomalous compressibility. To understand the relationship between this unusual compressibility and the pressure medium, the same experiment was performed again with different pressure transmitting medium. The results show that the nature of the pressure-transmitting medium itself does not significantly affect these unusual high-pressure phenomena (Table 4.3 and Fig. 4.7).

Table 4.3 High pressure x-ray diffraction results of hemicarboaluminate (Methanol:ethanol=4:1 and silicone oil).

Hemicarboaluminate experiment (Silicone oil)				Hemicarboaluminate experiment (M:E=4:1)			
P (GPa)	a (Å)	c (Å)	V (Å^3)	P (GPa)	a (Å)	c (Å)	V (Å^3)
ambient	5.770(2)	49.181(5)	1418.04(1)	ambient	5.765(8)	49.28(5)	1418.94(4)
0.1(1)	5.771(1)	49.222(9)	1419.98(1)	0.1(1)	5.774(6)	48.92(4)	1412.68(3)
0.5(1)	5.754(9)	48.29(4)	1385.1(3)	0.9(2)	5.750(1)	46.3(3)	1326.9(2)
1.1(2)	5.74(8)	46.3(3)	1323.8(2)	1.8(2)	5.71(8)	45.2(3)	1279.3(3)
2.4(2)	5.70(8)	45.0(3)	1270.7(3)	3.4(3)	5.69(9)	44.0(4)	1237.0(3)
3.6(3)	5.6(1)	43.9(4)	1232.3(3)	3.8(3)	5.6(1)	43.7(5)	1217.5(4)
5.4(4)	5.6(1)	43.3(4)	1205.0(3)	4.2(4)	5.6(1)	43.6(5)	1211.3(4)

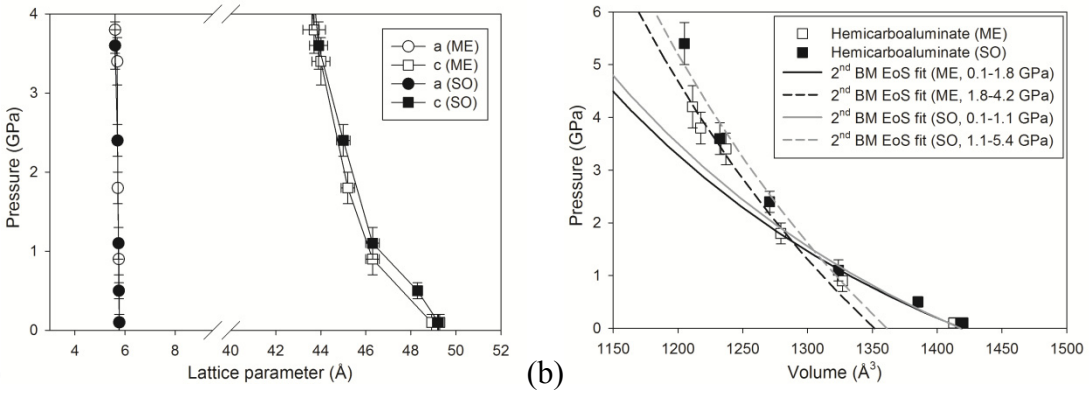

(a) (b)

Figure 4.7 (a) Variation of lattice parameters of hemicarboaluminate under pressure. (b) The refined unit cell volumes of hemicarboaluminate under pressure. Closed and open symbols correspond to pressure medium of alcohol mixture and silicone oil, respectively. Black and gray lines indicate BM EoS fitting results of alcohol mixture and silicone oil, respectively.

The calculated lattice parameters as a function of pressure are given in Table 4.3. Unlike strätlingite, hemicarboaluminate was found to reversibly transform to the initial volume phase with silicone oil as the pressure decreased to ambient. The compressibility of $\boldsymbol{a/a_0}$, $\boldsymbol{c/c_0}$, and volume decreased with increasing hydrostatic pressure as shown in Fig. 4.7 (a). Again, the pressure range could be divided into two regions. In the second pressure range, the initial volume for BM EoS calculation provided values of 1361.25 Å^3 and 1351.57 Å^3 for the silicone oil and the methanol and ethanol solution, respectively. Finally, the compressibility data for the BM EoS yielded a bulk modulus of K_0 = 15(2) and 14(1) GPa from 0.1 to 1.1 GPa with silicone oil and from 0.1 to 1.8 GPa with the methanol and ethanol solution, respectively (Fig. 4.7(b)). For the second phase, K_0 = 32(2) and 31(1) GPa from 1.1 to 5.4 GPa with silicone oil and from 1.8 to 4.2 GPa with the methanol and ethanol solution, respectively. The obtained bulk moduli are within error limits of standard deviations regardless its pressure medium.

Table 4.4 Measured lattice parameters of hydrogarnet in hemicarboaluminate (Methanol:ethanol=4:1 and silicone oil).

Hydrogarnet as an impurity (Silicone oil)			Hydrogarnet as an impurity (M:E=4:1)		
P (GPa)	a (Å)	V (Å^3)	P (GPa)	a (Å)	V (Å^3)
ambient	12.57(1)	1984.51(7)	ambient	12.57(1)	1987.11(1)
0.1(1)	12.561(8)	1982.38(1)	0.1(1)	12.51(7)	1959.01(7)
0.5(1)	12.53(5)	1968.62(5)	0.9(2)	12.50(6)	1956.03(7)
1.1(2)	12.50(1)	1954.48(1)	1.8(2)	12.46(2)	1935.65(3)
2.4(2)	12.44(2)	1928.98(2)	3.4(3)	12.38(3)	1898.42(3)
3.6(3)	12.37(7)	1896.45(7)	3.8(3)	12.377(8)	1896.13(1)
5.4(4)	12.2(1)	1851.0(1)			

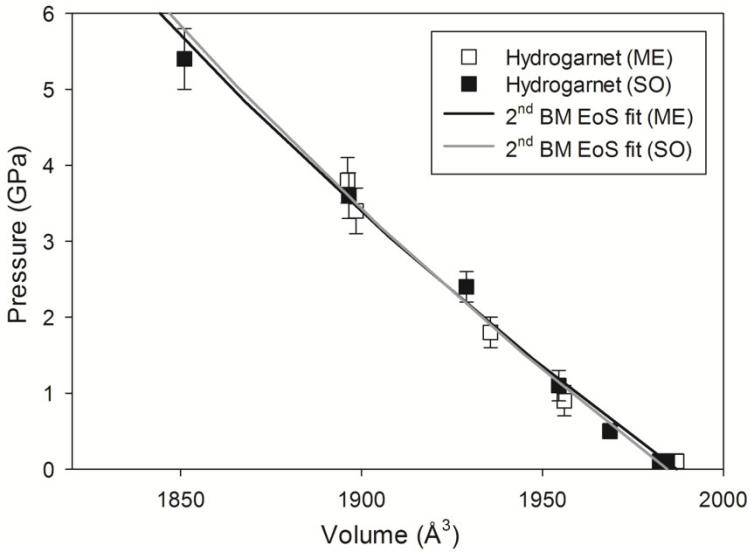

Figure 4.8 The refined unit cell volumes of hydrogarnet under pressure. Closed and open symbols correspond to pressure medium of alcohol mixture and silicone oil, respectively. Black and gray line indicate BM EoS fitting results of alcohol mixture and silicone oil, respectively.

A small amount of hydrogarnet was observed in the hemicarboaluminate sample (Fig. 4.4 and 4.5). Since the crystal structure of hydrogarnet is cubic, it is relatively easy to calculate its unit cell volume in spite of its small quantity. The (211), (321), and (400) peaks were selected for calculation. This volume-pressure result showed a perfect linear relationship over the entire pressure range in both pressure media (Fig. 4.8). The lattice parameters are summarized in Table 4.4. The BM EoS accounts well for the sets of data obtained with both silicone oil and methanol and ethanol solution pressure medium, and yielded a bulk modulus

K_0=69(4) and 72(4) with the pressure derivative K_0', fixed at 4.0. In addition, the sample was found to reversibly transform to its initial state.

4.2.3 Monocarboaluminate

As summarized in Table 4.1, the basic structures of carbon-containing AFm phases have been determined and refined for several subtypes using powder or single-crystal x-ray diffraction [186, 187, 195, 207-210]. The resulting charge imbalance gives the main layers a net positive charge, with the result that the interlayer spacing is much greater than in portlandite due to the need to intercalate charge-balancing anions. The layer thicknesses indicate that the CO_3^{2-} ions are oriented sub-parallel to the principal layers in monocarboaluminate but perpendicular to them in hemicarboaluminate. In all these CO_3^{2-} containing phases, some octahedral cavities contain a CO_3^{2-} ion while others contain varying combinations of H_2O molecules and OH^- ions. Francois et al. [186] reported detailed atomic structures of the ordered type of monocarboaluminate using single-crystal x-ray diffraction: among the five water molecules contained in the interlayer, two can be considered as only slightly bonded, and strong hydrogen bonds between O atoms in carbonate groups and water molecules provide cohesion of the interlayer (Fig. 4.9). In addition, the planar CO_3^{2-} groups are themselves tilted by 21.8(9) degree with respect to the planes formed by the principal calcium aluminate layers. The disordered monocarboaluminate structure, which has a pseudo-hexagonal symmetry, was also solved through single-crystal x-ray diffraction [187]. The main difference between these two modifications is the presence or absence of a center of symmetry and the order of stacking layers. When the structure is centrosymmetric, $P\bar{1}$, the compound is disordered and pseudo-hexagonal. When the structure is non-centrosymmetric P1, the structure is ordered but with a less pronounced pseudo-hexagonal nature. In the structure of Fe-containing monocarboaluminate, the carbonate location is different. While the carbonate bonds to the main layer in Al-containing monocarboaluminate, it is weakly bonded in the interlayer of Fe-containing monocarboaluminate [210].

The variable interlayer contents and layer thickness of monocarboaluminate at varying temperature were studied by Fischer and Kuzel [196] are shown in Table 4.1. In the temperature range 95-130 °C (i) the interlayer molecular water of the compound is released in two steps and (ii) the crystallinity degrades. As the crystallinity deteriorates, the corresponding diffraction peak of lamellar distance becomes diffuse. A lower hydrate with the approximate composition $C_4A\bar{C}H_8$ and a layer thickness of ***c'***=7.2 Å is formed at 100 °C, and at 130 °C a phase of composition $C_4A\bar{C}H_6$ with the interlamellar peak of 6.3 Å appears, which corresponds to the phase whereby all the interlayer water molecules have been lost. After that the x-ray reflections become progressively more diffuse until the phase is amorphous at 250 °C.

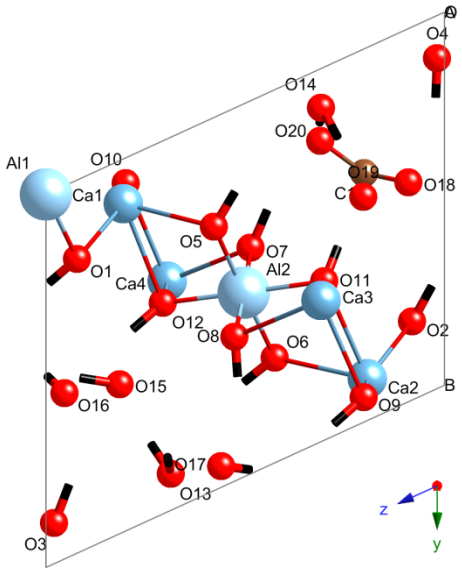

Figure 4.9 Crystal structure of monocarboaluminate [187]. Same graphical notation in Fig. 4.1 is used. Brown sphere indicates a carbon atom.

The stability of monocarboaluminate and hemicarboaluminate has an impact on the bulk chemistry of cements in terms of the formation of ettringite [188, 189, 211]. Sections 4.2.1 and 4.2.2 describe structural behavior of strätlingite and hemicarboalumiante under hydrostatic pressure where both AFm phases experienced pressure-induced dehydration, resulting in an abrupt volume contraction around 1.5 GPa. Reported in this section is a study of the behavior of the monocarboaluminate. In addition, the pressure-volume behavior and bulk modulus of the monocarboaluminate are computed and compared with those of hemicarboaluminate.

The monocarboaluminate was synthesized from calcium carbonate and tricalcium aluminate. Both materials were mixed in a 1:1 molar ratio and agitated in double distilled, CO_2 free water with water/solid ratio of 10 at 25 °C. After 14 days, the solid was filtered under nitrogen and subsequently dried in a desiccator over saturated calcium chloride [188]. Ambient condition phase identification were carried out at beamline 12.2.2 of the Advanced Light Source [38], using a synchrotron monochromatic x-ray beam with a 400.7570 mm sample to detector distance, x-ray wavelength of 0.6199 Å, and exposure time of 300 sec.

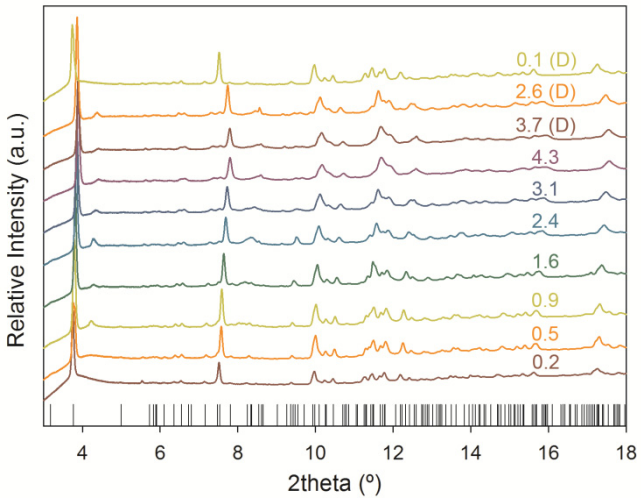

Figure 4.10 Measured x-ray diffraction patterns of monocarboaluminate (λ = 0.4965Å) with silicone oil. Bottom peaks indicate reference peak positions from [187]. The numbers indicate measured pressure (GPa) corresponding to each x-ray pattern. The (D) means data collected in decompression.

For this high-pressure experiment, a 357.1010 mm sample to detector distance and x-ray wavelength of 0.4965 Å were used. Exposure times of 600 sec were sufficient to give adequate signals for high-pressure powder diffraction patterns. The tested pressure range was 0.1-4.3 GPa, and diffraction patterns were collected with incremental rising and falling pressure. The MAR345 image plate detector was used in order to perfectly define the background, to observe very weak diffraction peaks, and to improve the accuracy of the integrated intensities by achieving a better powder average.

The ambient and high pressure x-ray diffraction pattern of monocarboaluminate is shown in Fig. 4.10. The positions and relative intensities of ambient x-ray reflections of the monocarboaluminate agree with the data of Francois et al. [186]. Thirty-six diffraction peaks were used to refine the unit-cell volume. Ambient crystallographic data of monocarboaluminate is shown in Table 4.5. The refined crystal structure is triclinic symmetry with parameters $\boldsymbol{a}$ = 5.77(2) Å, $\boldsymbol{b}$ = 8.47(5) Å, $\boldsymbol{c}$ = 9.93(4) Å, $\boldsymbol{\alpha}$ = 64.6(2) °, $\boldsymbol{\beta}$ = 82.8(3) °, $\boldsymbol{\gamma}$ = 81.4(4) °, and V = 433(3) Å^3. Because of the high-resolution synchrotron x-ray diffraction, more diffraction peaks than the one calibrated with Z=1/2 [195] appeared. Thus by using the O-$C_4A\bar{C}H_{11}$ data [186] (i.e., ordered-monocarboaluminate of triclinic crystal system, $P1/P\bar{1}$ space group, and Z=1) as a starting refinement structure, the lattice parameters and volume of ambient monocarboaluminate were successfully refined.

Table 4.5 High pressure x-ray diffraction results of monocarboaluminate (Silicone oil).

Monocarboaluminate experiment (Silicone oil)							
P (GPa)	**a (Å)**	**b (Å)**	**c (Å)**	**α (°)**	**β (°)**	**γ (°)**	**V (Å^3)**
ambient	5.77(2)	8.47(5)	9.93(4)	64.6(2)	82.8(3)	81.4(4)	433(3)
0.2(1)	5.76(2)	8.49(3)	9.92(3)	64.6(2)	82.4(3)	81.3(3)	433(3)
0.5(1)	5.73(1)	8.46(3)	9.89(3)	64.8(2)	82.4(3)	81.3(3)	428(2)
0.9(1)	5.72(1)	8.45(3)	9.87(3)	64.8(2)	82.4(3)	81.2(3)	426(2)
1.6(2)	5.71(2)	8.41(3)	9.83(4)	65.0(2)	82.2(3)	81.2(3)	422(3)
2.4(2)	5.69(2)	8.37(4)	9.78(4)	65.1(2)	82.3(3)	81.1(3)	416(3)
3.1(3)	5.66(3)	8.34(5)	9.74(5)	65.2(3)	82.3(4)	81.3(4)	412(4)
4.3(3)	5.64(5)	8.27(9)	9.66(9)	65.4(5)	82.7(8)	80.4(8)	403(7)
3.7(3)	5.64(5)	8.26(8)	9.68(8)	65.3(5)	82.7(8)	80.4(8)	404(7)
2.6(2)	5.64(3)	8.35(6)	9.73(6)	65.2(3)	82.4(5)	80.9(5)	410(5)
0.1(1)	5.77(2)	8.48(4)	9.93(4)	64.7(2)	82.4(3)	81.2(3)	434(3)

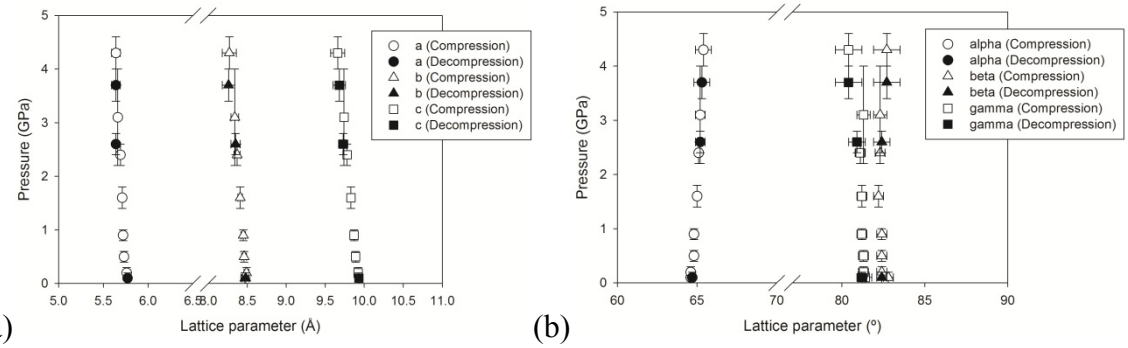

(a) (b)

Figure 4.11 Variation of (a) axial and (b) angular lattice parameters of mono-carboaluminate under pressure. Closed and open symbols correspond to refined parameters measured during compression and decompression, respectively.

The calculated lattice parameters of lengths and angles as a function of pressure are shown in Table 4.5 and Fig. 4.11. In the diamond anvil cell, the error ranges of calculated unit-cell volume increased at high pressure. This might be due to its lower symmetry of monocarboaluminate or to a peak broadening effect in the diamond anvil cell. Thus a weighted linear least-squares fit with errors was applied to the data to assess both pressure and volume errors [154] . The pressure-normalized volume data were fitted by the 2nd and 3rd order BM EoS [99].

In contrast with the hemicarboalumiante and strätlingite, the data did not show any abnormal compressibility or amorphization effect, thus the bulk modulus of monocarboaluminate could be calculated over the whole pressure range. However, since the unit-cell volume of the sample experienced some degree of unexpected volume contraction during the unloading process, only loading points were selected to compute the bulk modulus, K_0 and its first

derivative, K_0'. The initial volume for BM EoS at the point of a convergence was estimated at a value of 433(2) $Å^3$ [202], which is exactly same as the refined ambient volume. Finally, the 2nd and 3rd order BM EoS were fitted to the experimental points with R^2 = 0.991 and 0.990 fitting convergence, as shown in Fig. 4.12. In the 3rd order BM EoS the bulk modulus of 53(5) GPa with its derivative of 5.02 were obtained. When the first pressure derivative, K_0', is fixed at 4.0 (i.e., the 2nd order BM EoS), it yields a bulk modulus of 54(4) GPa.

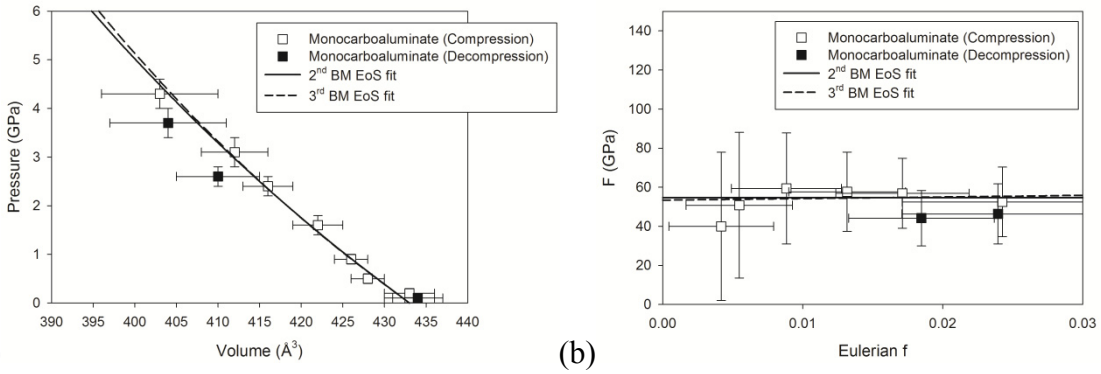

Figure 4.12 (a) Refined unit cell volumes of monocarboaluminate under pressure. (b) F-f plot of monocarboaluminate. The 2nd and 3rd order BM EoS fittings give the bulk modulus of 54(4) GPa and 53(5) GPa.

4.2.4 Tricalcium aluminate

Development of greener methods for the production of concrete requires determination of the physical properties and exact mechanism of clinker materials. Despite extensive research conducted to date, questions regarding these properties and mechanisms remain elusive. The third component in ordinary Portland cement clinker is tricalcium aluminate; $Ca_3Al_2O_6$ (C_3A in cement chemistry notation) with an amount ranging from 0-15 weight%. Because of the high heat it emits and rapid hydration, even a relatively small amount can lead to a significant effect on the early hydration characteristics of a cement paste and the long-term sulfate resistance of concrete. To control the immediate reaction of C_3A with water and its rapid hydration, gypsum is added to the clinker [1, 107]. Production clinkers contain cubic or orthorhombic forms of C_3A, alone or in combination. The orthorhombic modification is also known as the prismatic, dark interstitial material, which occurs if sufficient alkali is available. In addition, its formation appears to be favored also by rapid cooling and by bulk compositions potentially able to yield a relatively high proportion of aluminate [212].

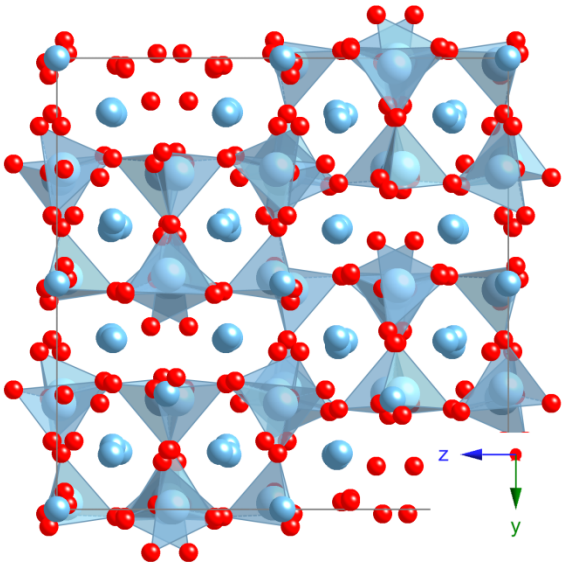

Figure 4.13 Crystal structure of tricalcium aluminate [213]. Light blue tetrahedra, dark blue spheres and red spheres indicate aluminates, calcium and oxygen atoms.

For the cubic form of C_3A, in 1967 Burdick and Day discovered the fourfold coordination of aluminum [214]. Later on, Mondal and Jeffery defined its detailed atomic structure using single-crystal x-ray diffraction [213]; ***a***=15.263 Å, space group *Pa*3 and *Z*=24; the structure is built from Ca^{+2} ions and eight rings of six AlO_4 tetrahedra of formula $Al_6O_{18}^{-18}$ in a unit cell (Fig. 4.13). The unit cell of C_3A contains 24 $Ca_3Al_2O_3$ units. The asymmetric unit contains 2 $Ca_3Al_2O_3$ units. The Ca atoms occupy 56 body-centering positions of (1/8,1/8,1/8) and its

symmetry-related positions. The presence of the holes in the structure facilitates the action of water in the hydration process [213, 215]. The 48 Al atoms and the remaining 16 Ca atoms occupy the corners of the pseudo-cells. The six AlO_4 tetrahedra in the Al_3O_{18} ring are tilted alternately to each side of the ring. Since some Ca coordinations to O atoms are rather irregular, the presence of short Ca-O bonds indicates a certain amount of strain to assist the break up of the structure under the action of water and the production of hydroxyl, hydroxylated aluminate, and calcium ions in solution.

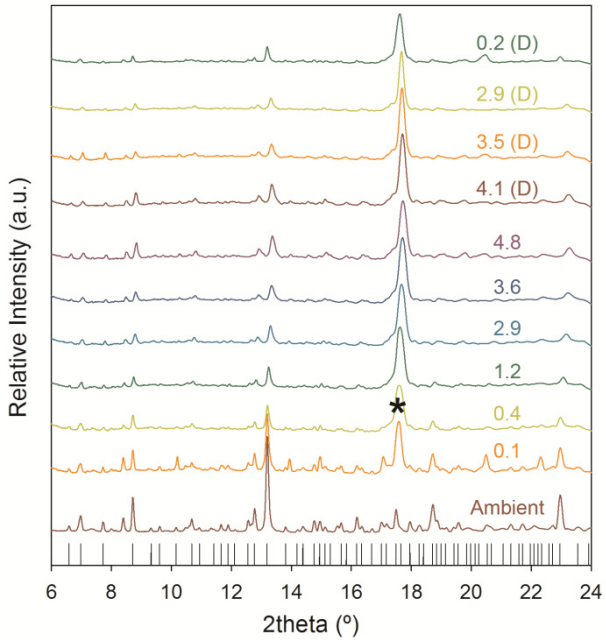

Figure 4.14 Measured x-ray diffraction patterns of tricalcium aluminate (λ = 0.6199Å) with silicone oil. Bottom peaks indicate reference peak positions from [213]. The numbers indicate measured pressure (GPa) corresponding to each x-ray pattern. The (D) means data collected in decompression.

With the increasing interest in the advanced applications of cementitous materials at the nano-scale, calculation of elastic constants is essential because many other parameters related to mechanical properties can be derived from them. In addition, C_3A agglomerates may be preserved unhydrated in mature cement pastes, and therefore affect to the global mechanical properties of the cement paste. Velez et al. found a value of the Young's modulus of C_3A; E = 145(10) GPa using the nanoindentation method and E = 190(10) GPa from resonance frequency technique [216]. Manzano et al. have computed the elastic constants and reactivity of C_3A by first-principles [171]. In this section, high pressure x-ray diffraction is used to investigate the crystal structure of the C_3A to pressures up to

4.8 GPa. In addition, the measurements are supported by first-principles calculations in later section.

The pure C_3A was purchased from CTL group (http://www.c-t-l.com). Ambient phase identification and the high pressure x-ray diffraction experiment were carried out at beamline 12.2.2 of the Advanced Light Source [38]. For ambient x-ray diffraction, a 350.8130 mm sample to detector distance, x-ray wavelength of 0.6199 Å, and exposure time of 300 sec were chosen. The ambient x-ray result is shown in the bottom diffraction pattern of Fig. 4.14. The peak positions and relative intensities of the pattern exactly matched with those determined by Mondal and Jeffery [213]. High pressures were generated using a two-screw DAC. Same sample-to-detector distance (350.8130 mm) and x-ray wavelength (0.6199 Å) were selected for the high-pressure experiments. Exposure times of 600 sec were sufficient to give adequate signals for high-pressure powder diffraction patterns. The tested pressure range was 0.1-4.8 GPa, and diffraction patterns were collected with incremental rising and falling pressure. The series of x-ray diffraction patterns taken at different pressures is shown in Fig. 4.14. The (*) peak indicates strong diffraction peak from the ruby in the DAC which is, of course, not shown in the ambient x-ray diffraction pattern. At ambient pressure, 25 diffraction peaks were used to refine the unit-cell volume. Although the weaker peaks of C_3A disappeared during increasing pressure, 14 peaks were used to calibrate its volume at 4.8 GPa, which is an adequate and this number of peaks is enough to calibrate the accurate unit-volume of simple cubic crystal system.

Table 4.6 High pressure x-ray diffraction results of tricalcium aluminate (Silicone oil).

Tricalcium aluminate experiment (Silicone oil)		
P (GPa)	a (Å)	V (Å^3)
ambient	15.259(6)	3552(1)
0.1(1)	15.258(6)	3552(1)
0.4(1)	15.256(6)	3551(1)
1.2(2)	15.202(9)	3513(2)
2.9(3)	15.135(9)	3467(2)
3.6(3)	15.11(2)	3447(3)
4.8(4)	15.06(1)	3415(2)
4.1(3)	15.09(2)	3435(3)
3.5(3)	15.12(2)	3454(3)
2.9(3)	15.14(3)	3468(5)
0.2(1)	15.27(3)	3559(5)

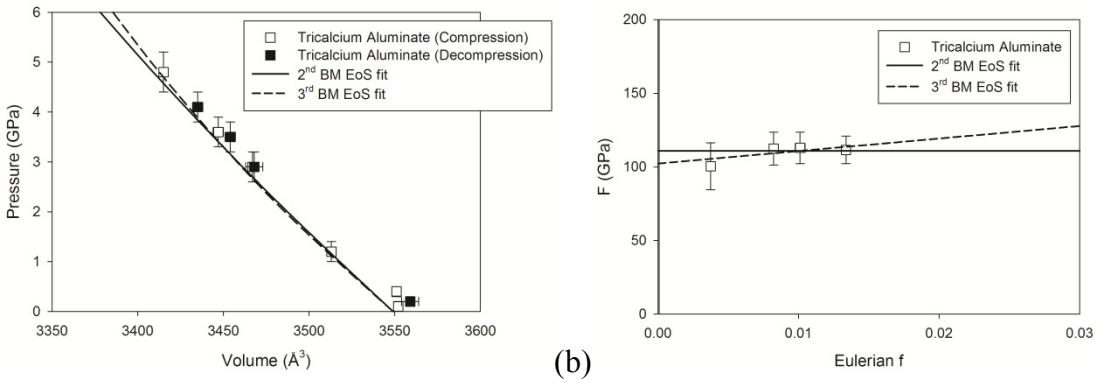

(a) (b)

Figure 4.15 (a) Refined unit cell volumes of tricalcium aluminate under pressure. (b) F-f plot of tricalcium aluminate. The 2nd and 3rd order BM EoS fittings give the bulk modulus of 110(3) GPa and 102(6) GPa.

Ambient and high pressure crystallographic data of C_3A are summarized in Table 4.6. At ambient pressure the refined crystal structure is a symmetry group of *Pa*3 with parameters ***a*** = 15.259(6) Å and V=3552(1) $Å^3$. There results agree well with those obtained by Mondal and Jeffery, which gives ***a*** = 15.263(3) Å and V=3556(2) $Å^3$. The refined lattice parameters at different pressures are shown in Table 4.6 and Fig. 4.15. In the DAC, the error ranges of calculated unit-cell volume increased at high pressure. This might be due to the peak broadening effect in the DAC as discusses in previous section. Again the weighted linear least-squares fit with errors was applied to the data to assess both pressure and volume errors [154]. The pressure-normalized volume data were fitted by the 2nd and 3rd order BM EoS. Since the crystal structure of C_3A is a simple cubic, the finite strain EoS is the ideal equation of state for C_3A under hydrostatic pressure. The initial volume, V_0, for finite strain EoS at the point of a convergence was estimated at a value of 3552.6 $Å^3$, which is the same as the refined ambient volume. Finally, the 2nd and 3rd order BM EoS were fitted to the experimental points with R^2 = 0.998 fitting convergence, as shown in Fig. 4.15. In the 3rd finite strain EoS, the bulk modulus of 110(3) GPa with its derivative of 9.5 were obtained. The 2nd order BM EoS gives a bulk modulus of 102(6) GPa.

4.3 First-principles Calculations on Calcium Aluminate Oxides

4.3.1 Monocarboaluminate

Previous x-ray diffraction experiments on hemicarboaluminate and strätlingite found that dehydration occurs under hydrostatic compression. This makes the crystal stiffer and yields larger isothermal bulk modulus at pressures above 1.5 GPa. However, this phenomenon was not found in monocarboaluminate. Its bulk modulus (K_0=54 GPa) is almost four times larger than that of hemicarboaluminate (K_0=14 GPa) and this stiffness seems to prevent dehydration. This can be one of the reasons of increase in mechanical performance of concrete attained by the use of limestone. Nevertheless, detailed atomic structure of monocarboaluminates could not be refined because of the extremely small sample sizes and complexity of the crystal structure. Thus the detailed atomic structure under high pressure remained undefined, especially the locations of the interlayer water molecules and orientation angle of anionic carbonation group under pressure. In this section, the crystal structures of two monocarboaluminate hydrates, with 5 interlayer waters (5 water MC) and 2 interlayer waters (2 water MC) are investigated using first-principles calculations. Like in the case of calcium silicate hydrates, two different exchange-correlation functionals were tested. The accuracy for these systems was investigated by comparing results with previous experimental crystallography data. The relation between crystallographic information and structural behavior under pressure has been resolved. Furthermore, full elastic tensor coefficients, averaged mechanical properties, and static bulk moduli of both monocarboaluminate hydrates have been computed.

Density functional theory (DFT) has been used to address the elasticity of both fully and partially hydrated monocarboaluminate phases. The identical DFT calculation with section 3.3 was performed using LDA and GGA [85] exchange-correlation functionals with a plane-wave energy cut-off of 1600 eV. The reference valence configurations and core radii for GGA and LDA pseudopotentials were chosen as $3s^2$, $3p^6$, $4s^2$, r_c = 1.2Å for Ca, $2s^2$, $2p^6$, $3s^2$, $3p^1$, r_c = 1.1Å for Al, $2s^2$, $2p^4$, r_c = 0.8Å for O, $2s^2$, $2p^2$, r_c = 0.8Å for C, and $1s^1$, for H. We have used a converged **k**-points grid of 4 × 2 × 2 [98].

Before calculating structural and elastic properties, structural optimizations were performed at zero pressure. As a starting crystal structure, the ordered monocarboaluminate was used for a 5-water monocarboaluminate hydrate (5 water MC) [186]. A previous study demonstrated that structures with 16 and 17 water molecules have weak hydrogen bonds [186] (Fig. 4.8). Therefore, the weakly bonded molecules are removed to generate a partially hydrated

monocarboaluminate (2 water MC). In addition, a water molecule of oxygen number of 14 is also removed to be consistent with the reported chemical formula of 2 water MC, $C_4A\bar{C}H_8$ [217]. Atomic positions and lattice parameters were optimized until atomic forces were smaller than 10^{-4} eV/Å and total energy converged within 10^{-6} eV. The final residual stress components of the optimized structure were less than 0.1 kbar. The relaxed lattice parameters and fractional atomic positions of both materials are summarized in appendix Table A4 and A5.

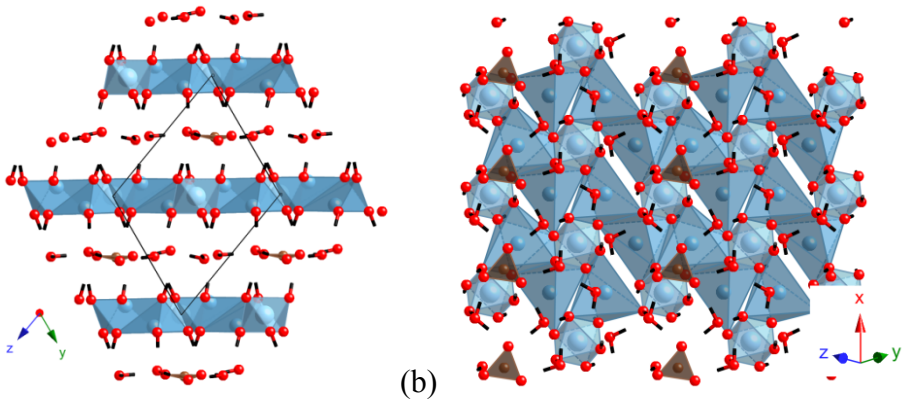

(a) (b)

Figure 4.16 (a) Geometrically optimized 5 water monocarboaluminate projected along [100]. (b) Water and hydroxyl group distribution in calcium aluminate principal layer. Calcium-aluminate ions are shown as dark blue octahedral, silicate/aluminate ions in interlayers are shown as light blue tetrahedra, and oxygen ions are represented as red spheres. Water and hydroxyl groups are denoted with red spheres and black sticks for oxygen and hydrogen atoms, respectively.

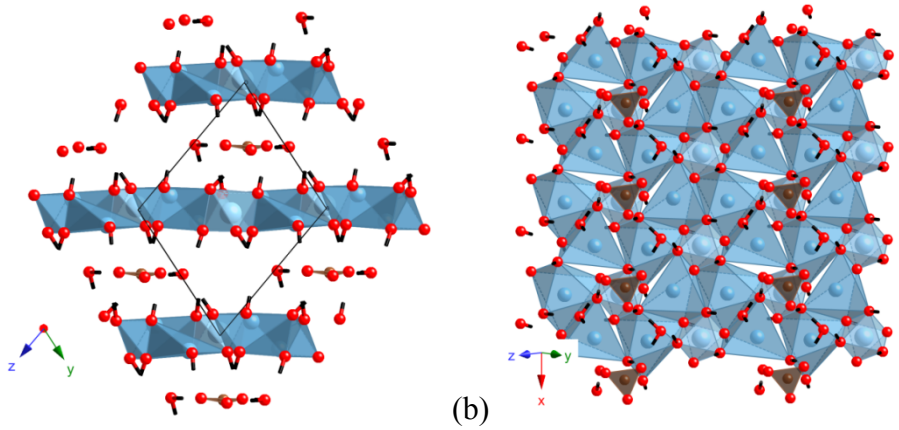

(a) (b)

Figure 4.17 (a) Geometrically optimized 2 water monocarboaluminate projected along [100]. (b) Water and hydroxyl group distribution in calcium aluminate principal layer. Same graphical notation in Fig. 4.15 is used.

The optimized crystal structures are shown in Figs. 4.16 and 4.17. Lattice parameters and unit cell volume from structures relaxed using the LDA functional compare more favorably with high pressure single-crystal [186] and ambient

pressure x-ray diffraction data. However, the LDA tilting angle between the carbonate group and the parallel layers is 9.6 °, which is quite smaller than the GGA angle, 19.1 ° and the experimental value, 21.8 °. Detailed crystallographic analysis of the 2 water MC does not exist for comparison. However, the experimentally observed interlayer spacing of 7.2 Å is only 3 % larger than the LDA result, 6.97 Å. Figure 4.18 shows experimental and simulated x-ray diffraction patterns for the 5 water MC and the 2 water MC structures. Because of the small unit cell volume and lattice parameters of the 2 water MC, the peak positions of x-ray diffraction pattern shifted. The weak (010) peak in optimized structures of 5 water and 2 water MC is overlapped with a strong (011) peak in x-ray spectra of Francois et al. Except that, overall x-ray profile of our crystal model is similar with the reference. The simulated x-ray profile of 2 water MC can be used in identifying the partially hydrated monocarboaluminate in concrete systems. In experiment, the x-ray pattern is more diffuse than simulated one. This might be due to the disorder of hydrogen or water molecules in real system. This will be discussed in more detail in discussion section.

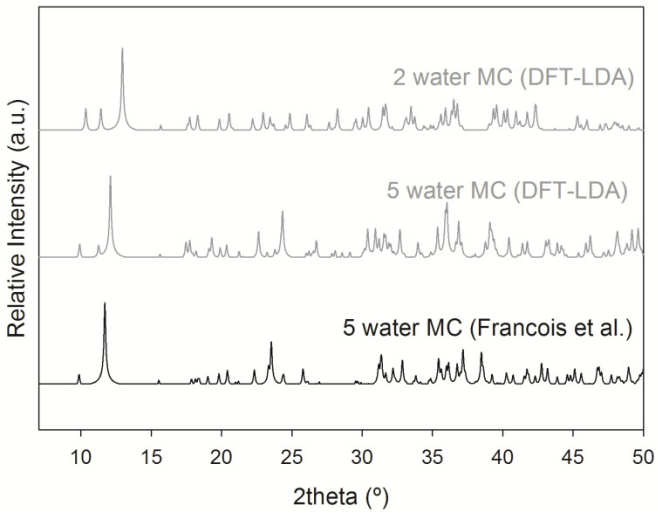

Figure 4.18 X-ray diffraction patterns of optimized monocarboaluminates and from the single-crystal x-ray experiment [218]. Weak (010) peak is overlapped with strong (011) peak in the reference x-ray profile of [218].

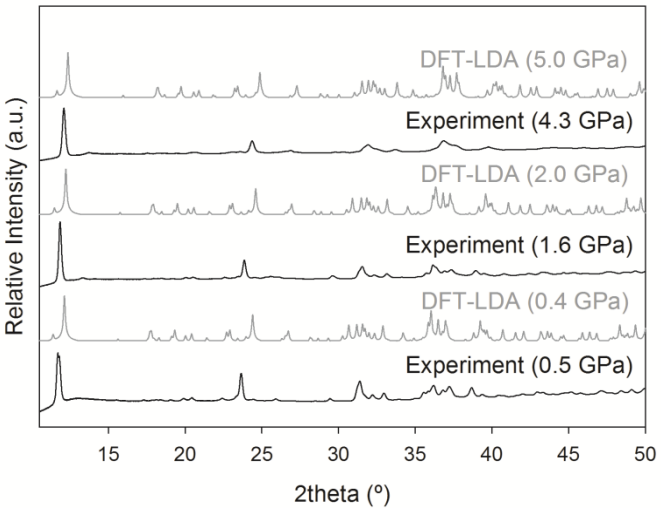

Figure 4.19 Comparison between high pressure x-ray diffraction patterns of monocarboaluminates and simulated patterns from first principles calculations. Hydrogen or water disorder makes experimental x-ray profile more diffuse.

Table 4.7 First-principles calculation results of monocarboaluminate containing 5 water molecules (LDA, GGA).

5 water monocarboaluminate LDA computation								
P (GPa)	**a (Å)**	**b (Å)**	**c (Å)**	**α (º)**	**β (º)**	**γ (º)**	**V (Å^3)**	**E (Ry)**
-1.8	5.954	8.558	9.762	67.86	82.03	80.75	453.13	-698.15
-1.4	5.933	8.529	9.714	67.90	82.01	80.86	448.04	-698.15
-0.8	5.909	8.495	9.675	67.90	81.98	80.84	442.57	-698.15
-0.3	5.894	8.463	9.650	67.90	81.86	80.90	438.60	-698.15
0.4	5.861	8.426	9.601	67.88	81.85	80.91	431.94	-698.15
1.3	5.827	8.390	9.547	67.88	81.93	80.99	425.38	-698.14
1.9	5.810	8.361	9.519	67.89	81.86	81.05	421.44	-698.14
2.7	5.783	8.335	9.475	67.82	81.95	81.09	416.16	-698.13
3.5	5.756	8.305	9.442	67.79	81.95	81.25	411.28	-698.12
5.0	5.722	8.269	9.375	67.53	81.99	80.77	403.11	-698.1
5 water monocarboaluminate GGA computation								
P (GPa)	**a (Å)**	**b (Å)**	**c (Å)**	**α (º)**	**β (º)**	**γ (º)**	**V (Å^3)**	**E (Ry)**
-0.6	5.850	8.607	10.110	64.66	82.50	80.87	453.13	-1300.5
-0.3	5.837	8.573	10.040	64.95	82.34	80.77	448.04	-1300.5
0.0	5.829	8.526	9.955	65.34	82.27	80.77	442.57	-1300.5
0.3	5.819	8.499	9.900	65.55	82.21	80.74	438.60	-1300.5
0.9	5.800	8.458	9.807	65.88	82.10	80.69	431.94	-1300.5
1.5	5.781	8.411	9.721	66.18	82.07	80.72	425.38	-1300.5
1.9	5.768	8.384	9.673	66.33	82.07	80.73	421.44	-1300.4
2.5	5.747	8.352	9.605	66.59	82.07	80.77	416.16	-1300.4
3.2	5.729	8.319	9.548	66.75	82.07	80.79	411.28	-1300.4
4.3	5.697	8.260	9.463	66.91	82.08	80.90	403.11	-1300.4

Table 4.8 First-principles calculation results of monocarboaluminate containing 2 water molecules (LDA, GGA).

2 water monocarboaluminate LDA computation								
P (GPa)	a (Å)	b (Å)	c (Å)	α (º)	β (º)	γ (º)	V (Å^3)	E (Ry)
-1.5	5.966	8.361	9.170	71.03	79.75	79.75	422.07	-594.7
-1.1	5.932	8.350	9.111	71.19	79.43	79.50	416.26	-594.7
-0.8	5.896	8.415	8.960	71.79	78.66	79.48	410.48	-594.7
-0.6	5.890	8.311	8.956	71.86	78.63	79.29	404.77	-594.7
0.1	5.918	8.530	8.672	71.97	75.82	77.68	399.09	-594.71
0.6	5.898	8.459	8.637	72.15	75.95	77.77	393.42	-594.71
1.2	5.868	8.398	8.618	72.29	75.86	77.68	387.83	-594.7
1.7	5.864	8.180	8.663	72.16	77.38	78.70	382.26	-594.69
2.2	5.826	8.092	8.684	72.14	77.47	78.81	376.78	-594.68
2 water monocarboaluminate GGA computation								
P (GPa)	a (Å)	b (Å)	c (Å)	α (º)	β (º)	γ (º)	V (Å^3)	E (Ry)
-1.0	5.864	8.565	10.140	64.86	80.92	79.49	451.49	-1196.9
-0.7	5.853	8.501	10.080	65.18	80.89	79.43	445.61	-1196.9
-0.5	5.843	8.436	10.014	65.50	80.96	79.45	439.78	-1196.9
-0.2	5.826	8.380	9.958	65.77	80.93	79.41	433.99	-1196.9
0.1	5.814	8.313	9.904	66.15	80.86	79.26	428.22	-1196.9
0.6	5.805	8.251	9.849	66.38	80.76	79.09	422.52	-1196.9
0.8	5.797	8.163	9.838	66.68	80.43	78.38	416.84	-1196.9
1.2	5.777	8.096	9.802	66.98	80.46	78.26	411.23	-1196.9
1.6	5.758	8.042	9.745	67.23	80.55	78.30	405.62	-1196.9
2.1	5.740	7.987	9.690	67.46	80.66	78.36	400.09	-1196.9

Static equilibrium structures at arbitrary pressures were obtained using damped variable cell shape molecular dynamics. Figure 4.19 shows three simulated x-ray diffraction patterns from LDA structures together with experimental x-ray patterns previously obtained at similar hydrostatic pressures. The overall shape and relative intensity of the main peaks are in good agreement, although calculated peaks are slightly shifted due to smaller d-spacings or different pressures. Computed lattice parameters for the same structure at different pressures are shown in Fig 4.20. As indicated in Fig. 4.21, LDA and GGA compression curves for the 5 water MC structure compare well with the experimental data, with the LDA giving a better agreement. GGA overestimates its volume at ambient. The general behaviors of calculated parameters are very similar to the experimental behaviors. LDA predicted the ***c*** parameter to be 5 % smaller but the angle ***α*** to be 3 % larger, showing a correlation between these parameters. They compensate for each other and produce volumes similar to the experimental volume, i.e., only 0.3 % smaller in the pressure range investigated.

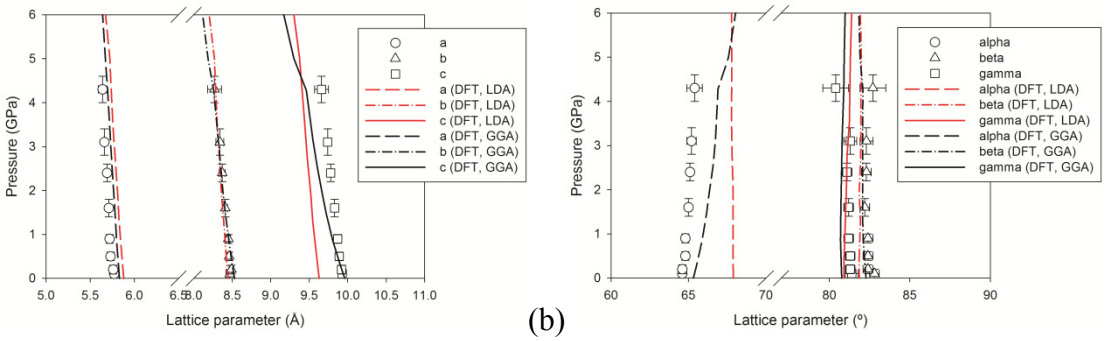

Figure 4.20 Comparison of (a) axial and (b) angular compressibilities of 5 water monocarboaluminate from high pressure experiment and LDA and GGA simulation.

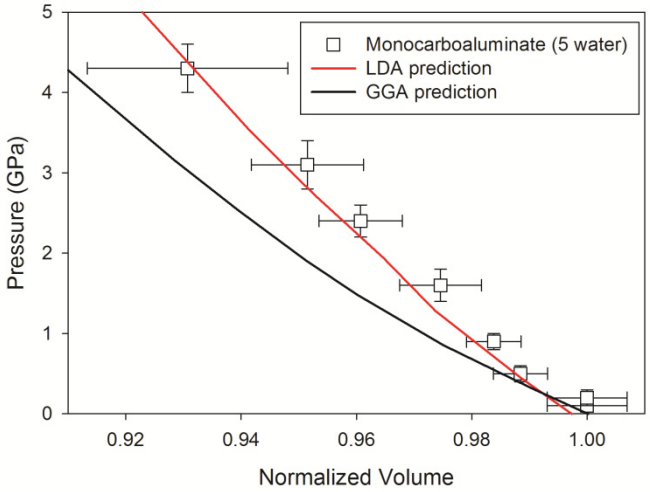

Figure 4.21 Variation of unit cell volume of 5 water monocarboaluminate from high pressure x-ray diffraction experiment and LDA and GGA calculation.

Then elastic coefficients for these structures were calculated based on a stress-strain relation as discussed in chapters 2 and 3. Strains of ± 0.5 % have been applied to get the coefficients. Due to the low symmetry, it has 21 independent elastic coefficients.

$$\sigma_i = \sum_{j=1}^{6} C_{ij}\varepsilon_j \qquad \text{- (4.1)}$$

$$C_{ij} = \begin{bmatrix} C_{11} & C_{12} & C_{13} & C_{14} & C_{15} & C_{16} \\ & C_{22} & C_{23} & C_{24} & C_{25} & C_{26} \\ & & C_{33} & C_{34} & C_{35} & C_{36} \\ & & & C_{44} & C_{45} & C_{46} \\ & & & & C_{55} & C_{56} \\ sym. & & & & & C_{66} \end{bmatrix} \qquad \text{- (4.2)}$$

This has been done by applying strains to the lattice vectors and calculating the resulting stress tensor [88, 219]. The atomic positions were re-optimized in each fixed strained configuration. The applied Lagrangian strains of $\vec{\varepsilon}_1$, $\vec{\varepsilon}_2$, $\vec{\varepsilon}_3$, $\vec{\varepsilon}_4$, $\vec{\varepsilon}_5$, and $\vec{\varepsilon}_6$ are

$$\varepsilon_1 = \begin{pmatrix} \delta & 0 & 0 \\ 0 & 0 & 0 \\ 0 & 0 & 0 \end{pmatrix},$$
$$\varepsilon_2 = \begin{pmatrix} 0 & 0 & 0 \\ 0 & \delta & 0 \\ 0 & 0 & 0 \end{pmatrix},$$
$$\varepsilon_3 = \begin{pmatrix} 0 & 0 & 0 \\ 0 & 0 & 0 \\ 0 & 0 & \delta \end{pmatrix} \qquad \text{- (4.3)}$$

$$\varepsilon_4 = \begin{pmatrix} 0 & 0 & 0 \\ 0 & 0 & \delta/2 \\ 0 & \delta/2 & 0 \end{pmatrix},$$
$$\varepsilon_5 = \begin{pmatrix} 0 & 0 & \delta/2 \\ 0 & 0 & 0 \\ \delta/2 & 0 & 0 \end{pmatrix},$$
$$\varepsilon_6 = \begin{pmatrix} 0 & \delta/2 & 0 \\ \delta/2 & 0 & 0 \\ 0 & 0 & 0 \end{pmatrix} \qquad \text{- (4.4)}$$

where the indices are given in Voigt notation. Sufficiently small strains of $\delta = \pm 0.5$ % were applied, so that the elastic coefficients could be obtained from taking averages of four and two values for off-diagonal and diagonal coefficients in Eqn.

(4.2), respectively. Table 4.9 compares computed elastic constants for 5 water and 2 water MC with LDA and GGA.

Table 4.9 summarizes the computed LDA and GGA elastic coefficients for 5 water and 2 water monocarboaluminates. The isothermal bulk modulus is obtained by fitting a finite strain expansion to the calculated free energy versus volume relation. The Helmholtz free energy versus volume relation is expanded in a power series in terms of the Eulerian strains. As discussed in previous chapter, the Helmholtz free energy, F, is identical with the internal energy, E (F=E-TS) since T = 0 K. The Birch-Murnaghan equation of state corresponds to a finite strain expansion to third power in the strain [99].

$$E(V) = E_0 + \frac{9V_0K_0}{16}\left\{\left[\left(\frac{V}{V_0}\right)^{-\frac{2}{3}} - 1\right]^3 K_0' + \left[\left(\frac{V}{V_0}\right)^{-\frac{2}{3}} - 1\right]^2 \left[6 - 4\left(\frac{V}{V_0}\right)^{-\frac{2}{3}}\right]\right\} \quad - (4.5),$$

The fitting gives the reference volume, isothermal bulk modulus at zero pressure, and its pressure derivative at 0 GPa. Then, the RVH and HS bound values were computed based on elastic coefficients, Cij, determined by first-principles calculations. The computed averaged mechanical properties for 5 water and 2 water MC structures are summarized in Table 4.9.

Table 4.9 Calculated elastic coefficients of monocarboaluminate.

Monocarboaluminate computation									
	5w MC		2w MC			5w MC		2w MC	
(GPa)	LDA	GGA	LDA	GGA	(GPa)	LDA	GGA	LDA	GGA
c11	94.2	107.3	84.3	83.2	**K_Voigt**	57.0	42.2	46.1	27.9
c12	36.6	27.3	30.7	14.8	**K_Reuss**	55.9	37.5	44.5	20.4
c13	38.0	27.6	31.5	13.9	**K_RVH**	56.5	39.8	45.3	24.1
c14	-7.2	-8.2	-8.8	-8.0	**G_Voigt**	32.7	34.8	29.6	24.9
c15	8.1	6.8	8.2	8.2	**G_Reuss**	30.6	31.0	25.3	17.9
c16	2.8	4.0	6.7	8.7	**G_RVH**	31.7	32.9	27.5	21.4
c22	83.8	70.8	63.5	44.6	**E_RVH**	80.1	77.4	68.5	49.6
c23	43.0	18.6	31.0	12.1	***v*_RVH**	0.3	0.2	0.2	0.2
c24	-2.6	-3.4	-8.6	-7.5					
c25	1.2	3.1	-1.6	5.2					
c26	-4.1	-4.3	-1.9	5.8					
c33	99.8	55.0	80.7	41.5					
c34	-1.6	-7.1	2.9	-7.1					
c35	-4.0	-4.8	1.7	2.9					
c36	-4.3	0.6	3.0	3.5					
c44	31.7	43.5	47.4	43.7					
c45	-2.1	-0.5	-2.9	-3.5					
c46	-2.8	-1.3	-5.0	-1.8					
c55	35.4	36.9	28.3	20.3					
c56	0.5	2.0	-2.2	-7.2					
c66	43.2	40.2	27.2	17.6					

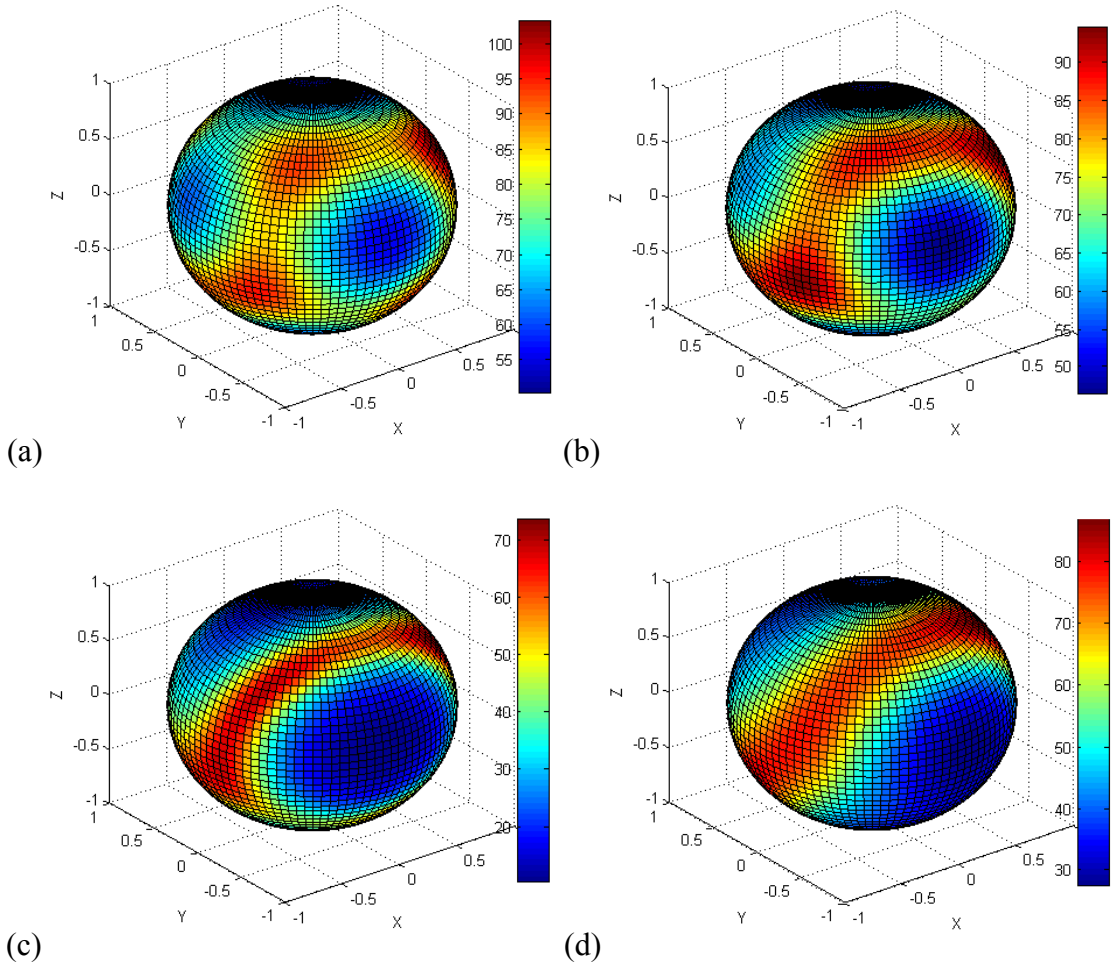

Figure 4.22 Directional Young's modulus of monocarboaluminates in conventional orthogonal coordinate system ($\vec{Z}\|\vec{c}$, $\vec{Y}\|\vec{c}\times\vec{a}$ and $\vec{X}\|\vec{Y}\times\vec{Z}$) : results for 5 water MC using (a) LDA and (b) GGA functionals and for 2 water MC using (c) LDA and (d) GGA functionals. Scale bars indicate Young's modulus in GPa. Anisotropy decreases by addition of water molecules in the interlayer region.

Last, the Young's modulus for uniaxial compression along arbitrary directions was computed like the cases of tobermorite 14 Å and 9 Å. The general definition of the directional Young's modulus in terms of unit vectors, $\hat{n}$ along the compression axis is:

$$E_{ani} = \frac{1}{\hat{n}^T \cdot [C^{-1} : (\hat{n}\cdot\hat{n})]\cdot\hat{n}} \qquad \text{- (4.6)}$$

Magnitudes of the LDA and GGA Young's modulus for monocarboaluminate hydrates are represented in colors on the surface of spheres (Fig. 4.22). X, Y, and Z directions are defined by the conventional setting of triclinic crystal system

($\vec{Z} \| \vec{c}$, $\vec{Y} \| \vec{c} \times \vec{a}$, and $\vec{X} \| \vec{Y} \times \vec{Z}$). The large structural anisotropy of mono-carboaluminate hydrates is evident in this figure. The softest direction of [011] was computed as the direction perpendicular to the principal layer.

4.3.2 Tricalcium aluminate

In this section, the results of first-principles calculation on tricalcium aluminate will be presented. Density Functional Theory (DFT) [86, 220] calculations were performed using GGA [85] for exchange-correlation energy. All pseudopotentials are generated by Vanderbilt Ultrasoft pseudopotential which allows a low-energy cutoff and high accuracy of large-scale calculations [166]. The configurations of reference and core radii for pseudopotentials have been taken as $3s^2$, $3p^6$, $4s^2$, and r_c = 1.2 Å for Ca, $2s^2$, $2p^6$, $3s^2$, $3p^1$, and r_c = 1.1 Å for Al, and $2s^2$, $2p^4$, and r_c = 0.8 Å for O, respectively.

Because the system size is large (264 atoms in a unit cell), a γ-point sampling of the Brillouin zone was selected for k-point integration. Calculations of elastic properties required precisely relaxed atomic positions and highly converged total energies, forces, and stresses. Therefore, a plane-wave cutoff energy of 1000 eV for the wave functions and geometry optimization convergence criterion of 10^{-5} eV for the total energy were used. The achieved residual stress components were less than 1 kbar.

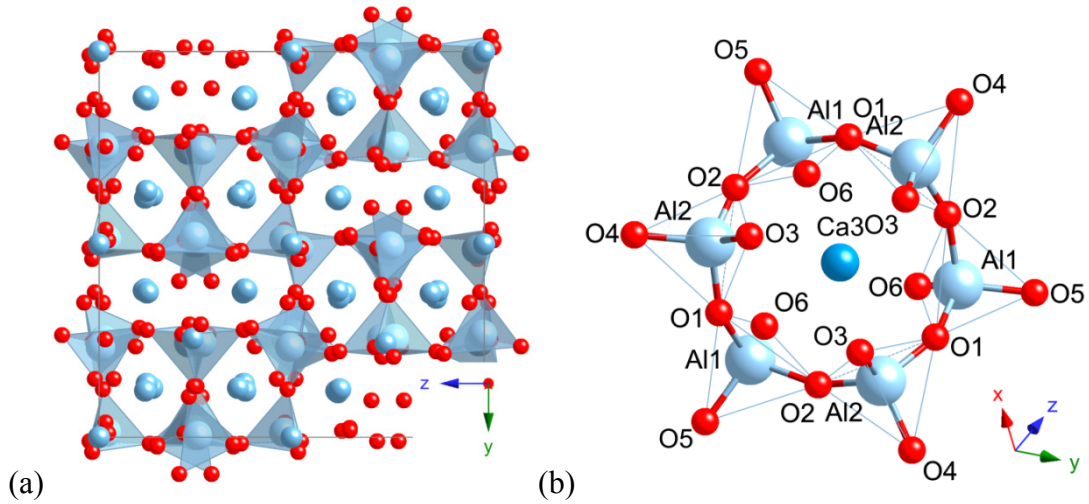

(a) (b)

Figure 4.23 (a) Geometrically optimized tricalcium aluminate projected along [100]. (b) Geometrically optimized structure of Al_6O_{18} ring. Light blue tetrahedra, dark blue spheres and red spheres indicate aluminates, calcium and oxygen atoms.

Before calculating structural and elastic properties, structural optimizations were performed to equilibrate the structure at zero pressure and arbitrary stress states. This optimization is computationally expensive but important to avoid possible metastable states and to ensure that the relaxed structure is in the region where linear elasticity holds. Thus, atomic positions and lattice parameters were fully relaxed. Although cubic symmetry was not enforced, unit-cell angles

remained equal to 90 ° and lattice parameters remained essentially equal, indicating that a simple cubic symmetry was always found after relaxation.

The relaxed lattice parameter, a, is 15.39 Å, which is 0.8 % larger than that obtained by Mondal and Jeffery [213]. This slight overestimation of the cell parameter is typical of the GGA functional [221, 222]. Fractional atomic positions of Mondal and Jeffery and the relaxed cell are summarized in appendix Table A6. Referred to its symmetry group of *Pa*3, the coordinations of only 14 atoms are summarized instead of 264 atoms. The calculations herein show an excellent agreement with the experimental data. The optimized crystal structure and six-member ring of AlO_4 tetrahedra are graphically shown in Fig. 4.23.

The components of the elastic constant tensor were calculated using stress vs strain relations where the Nielsen-Martin stresses were obtained after fully relaxing structures at a certain pressure [183, 223]. Starting from these pre-compressed states with lattice parameters $(\vec{a},\vec{b},\vec{c}) \equiv \vec{A}$, the lattice parameters of the strained unit cell $(\vec{a}',\vec{b}',\vec{c}') \equiv \vec{A}'$ are obtained from the relationship $\vec{A}'=\left(\vec{1}+\vec{\varepsilon}\right)\vec{A}$, where $\vec{1}$ is the unit matrix and $\vec{\varepsilon}$ is a Lagrangian strain tensor. Due to the cubic symmetry, C_3A has only three independent elastic moduli tensor coefficient: C_{11}, C_{12}, and C_{44}. Thus two different strains of $\vec{\varepsilon}_1$ and $\vec{\varepsilon}_4$ were applied [183, 224]:

$$\varepsilon_1 = \begin{pmatrix} \delta & 0 & 0 \\ 0 & 0 & 0 \\ 0 & 0 & 0 \end{pmatrix} \qquad \text{- (4.7)}$$

$$\varepsilon_4 = \begin{pmatrix} 0 & 0 & 0 \\ 0 & 0 & \delta/2 \\ 0 & \delta/2 & 0 \end{pmatrix} \qquad \text{- (4.8)}$$

where the indices are given in Voigt notation. Strains of different magnitude (δ = 0.5, 1, 1.5, and 2%) and pressure P was subtracted from calculated stresses σ_1, σ_2, and σ_3 before the components of the stress tensor were extracted from the following linear relationship:

$$\sigma_i = \sum_{j=1}^{6} C_{ij}\varepsilon_j \qquad \text{- (4.9)}$$

$$C_{ij} = \begin{bmatrix} C_{11} & C_{12} & C_{12} & 0 & 0 & 0 \\ & C_{11} & C_{12} & 0 & 0 & 0 \\ & & C_{33} & 0 & 0 & 0 \\ & & & C_{44} & 0 & 0 \\ & & & & C_{44} & 0 \\ sym. & & & & & C_{44} \end{bmatrix} \quad \text{- (4.10)}$$

Strains of different magnitude enabled us to extract the linear dependent of stress on strain. From the linear fitting of the computed points, the intercepts of each three lines give 169.8, 68.3, and 53.7 GPa for C_{11}, C_{12}, and C_{44}, respectively. The calculated elastic constants are summarized in Table 4.10.

Table 4.10 Calculated elastic coefficients of tricalcium aluminate.

Tricalcium aluminate GGA						
Applied strain	**0.50%**	**1.00%**	**1.50%**	**2.00%**	**at zero pressure**	**-3% to 3% [225]**
a (Å)			15.39			15.38
V (Å^3)			3645.2			3638.1
C11 (GPa)	168.3	168.7	167.9	165.7	169.8	172.1
C12 (GPa)	68.9	69.4	69.9	70.1	68.3	68.3
C44 (GPa)	53.4	53.1	53.1	52.6	53.7	56.1
K_RVH (GPa)	102	102.5	102.6	101.9	102.1	102.9
G_RVH (GPa)	51.99(1)	51.7(1)	51.4(1)	50.6(1)	52.5(1)	54.4
E_RVH (GPa)	133.1	132.7	132.2	130.3	134.4	138.7
***v*_RVH (GPa)**	0.28	0.28	0.29	0.29	0.28	0.28

Like in chapter 3, two different bulk moduli have been theoretically computed. The first uses calculated components of the elastic constant tensor to compute RVH averages. This method gives bounds on the bulk modulus (K) of isotropic poly-crystalline aggregates and shear (G) modulus. From the computed K and G, Young modulus (E) and Poisson ratio (η) are also calculated (Table 4.10). The second method is based on the analysis of the total energies of uniformly compressed states [99, 226]. In this case Eulerian strains are used and a finite strain equation of state is fit to the energy vs volume or pressure versus volume relation. Figure 4.24 shows GGA prediction line based on five computational data points up to 10 GPa and the fitting curve. This gives K_0 = 106.0 GPa, K_0' = 3.8, and V_0 = 3647.4 Å^3. Manzano et al. applied first method to compute elastic constants and mechanical properties of C_3A (Table 4.10). In this study, both methods have been applied to compare with high pressure experimental results and previous simulation by Manzano et al. [225].

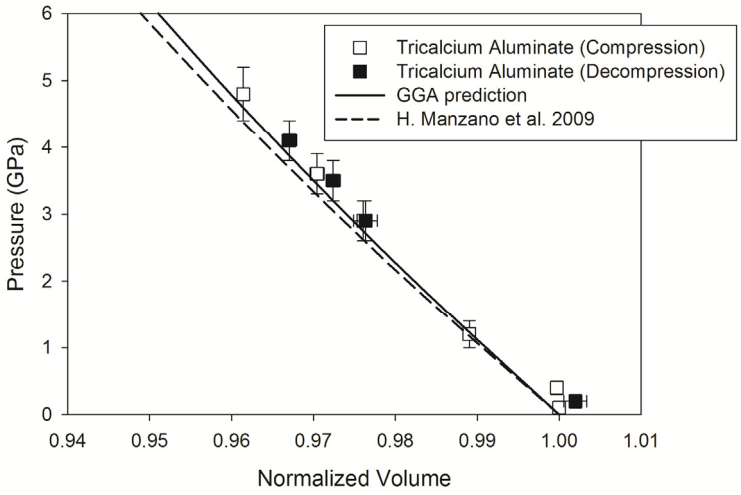

Figure 4.24 Variation of unit cell volume of tricalcium aluminate from high pressure x-ray diffraction experiment and GGA calculation. RVH bulk modulus from [225] is used for pressure-volume relation.

4.4 Discussion on Elastic Properties of Calcium Aluminate Oxides and Calcium Aluminate Hydrated Oxides

Calculated bulk modulus and its first derivative of all samples are summarized in Table 4.11. Under high pressure, both strätlingite and hemicarboaluminate show a sudden volume contraction around 1.5 GPa. Previous high pressure studies in materials containing large channels have shown that some pressure-transmitting medium can infiltrate into structural channels and cause a volume discontinuity [182, 227]. These studies have shown that the high pressure behavior is highly dependent on the molecular size of the pressure-transmitting medium. To determine the pressure medium effect on the abrupt volume contraction on AFm phases, the behavior of hemicarboaluminate was checked with two different pressure media and it was determined that the pressure medium does not affect the abnormal pressure behavior of AFm phases.

Table 4.11 Bulk modulus, its first derivative and ambient volume of calcium aluminate hydrates according to the Birch-Murnaghan equation of state.

		Strätlingite (Silicone oil)		Hemicarboaluminate (Silicone oil)		Hemicarboaluminate (M:E=4:1)		Monocarboaluminate (Silicone oil)
P range		0.1-1.5	1.5-3.4	0.1-1.1	1.1-5.4	0.1-1.8	1.8-4.2	0.1-4.3
3rd EoS	K_0 (GPa)	-	100(11)	-	32(7)	9(2)	30(3)	53(5)
	K_0'	-	3.8	-	4.19	13.6	4	5.02
	V_0 (Å^3)	-	1035.67	-	1361.25	1418.94	1351.57	433
2nd EoS	K_0 (GPa)	23(2)	100(3)	15(2)	32(2)	14(1)	31(1)	54(4)
	V_0 (Å^3)	1077.30	1035.67	1418.04	1361.25	1418.94	1351.57	433

Although the ambient sample began with two hydration stages of hemicarboaluminate, these two basal peaks, at 8.193 Å for $C_4A\overline{C}_{0.5}H_{12}$ and 7.63 Å for $C_4A\overline{C}_{0.5}H_{11.25}$, merge together into one intense peak under pressure (Fig. 4.6). This might be explained if the fully-hydrated hemicarboaluminate ($C_4A\overline{C}_{0.5}H_{12}$), initially mixed with $C_4A\overline{C}_{0.5}H_{11.25}$, moves towards $C_4A\overline{C}_{0.5}H_{11.25}$ once the pressure attains a certain level. Moreover, the basal reflection decreased stepwise to another hydration stage, i.e. 7.26 Å of $C_4A\overline{C}_{0.5}H_{10.5}$ (Table 4.1), indicating that this might reflect pressure-induced dehydration.

Another possibility is that, with changing pressure, the re-orientation of the carbonate groups can occur. The interchangeable ions in hemicarboaluminate include both OH and CO_3; the planar carbonate groups are assumed to be oriented normal to the plane of the calcium aluminate layer. Because of this orientation, which is not very economical in filling space, Balonis and Glasser noted that its physical density is lower than that of a hypothetical parallel arrangement of planar

carbonate groups [195]. In monocarboaluminate, the carbonated group is sub-parallel to the main layer (tilted by 21.8 ° from the main layers) [186, 187]. A pressure-induced change in the orientation of the carbonate group could explain the gradual discontinuity with rising pressure. Unlike strätlingite's perfect-bilinear pressure-volume behavior, hemicarboaluminate shows gradual abnormal pressure-volume behavior. Thus gradual abnormal compressibility of hemicarboaluminate could result from the re-orientation of carbonate groups or from an entirely different cause; pressure-induced dehydration.

To verify the two hypothesis, the hemicarboaluminate samples were measured in two different pressure transmitting media: hygroscopic 4:1 methanol:ethanol solution and non-hygroscopic silicone oil. If the reorientation of carbonate group of hemicarboaluminate is the dominant process, the type of pressure medium should not affect the final structure upon unloading. However, if pressure-induced dehydration is the dominant mechanism the chemical nature of the pressure medium must have a pronounced effect on the crystal structure at ambient pressure when the sample is unloaded because the hygroscopic medium will not allow water to return into the interlayer region while the non-hygroscopic medium would permit the recovery of the original crystal structure once the pressure is removed. Figure 4.4 show hysteresis of the hemicarboaluminate when a hygroscopic medium is used, while the results given in Fig. 4.5 indicate that the crystal structure returns to the original state once the sample is unloaded with the non-hygroscopic medium. These experimental results seem to favor the hypothesis that pressure-induced dehydration occurs. Considering the characteristic that the dehydration of hemicarboaluminate is likely happen at 35 °C [195], it can be assumed that the hygroscopic pressure medium could rapidly extract water molecules from the interlayer region. It could accelerate the pressure-induced dehydration especially at the low pressure range.

Per formula unit of strätlingite, the interlayer unit ($[AlSi(OH)_8 \cdot H_2O]^-$) contains only one water molecule. Considering the hypothesis of pressure-induced dehydration, the stiffness of the crystal should increase once water molecules move out from the calcium aluminosilicate framework. This phenomenon is confirmed by the experimental results shown in Fig. 4.2, where an increase in stiffness is observed for pressures greater than 1.5 GPa.

From a mechanical point of view, a noteworthy characteristic of this pressure-induced dehydration is that the frameworks of the crystals are preserved throughout the dehydration. The slight rearrangements of structural elements, even if several weak interlayer water bonds are broken, are not sufficient to destroy the crystal framework of the sample; which transforms from strätlingite to 'metasträtlingite'. It is possible, therefore, to calculate its bulk modulus at each

hydration stage. Based on this assumption, two stage bulk modulus of each hydration stage were calculated. Using the method developed by Jeanloz [202], the initial volume of the second stage at ambient pressure was estimated and regression curve at each stage gave excellent fit.

Table 4.12 The summary of high pressure x-ray diffraction and atomistic simulation results of hydrogarnet.

		Powder XRD	Powder neutron	Single-crystal XRD	Powder XRD (M:E=4:1)	Powder XRD (Silicone oil)	*Ab initio*	*Ab initio* Hartree-Fock	*Ab initio* B3-LYP
		[228]	[229]	[230]	This study		[231]	[232]	[232]
a (Å)		12.57	12.57	12.57	12.57(1)	12.57(7)	12.65	12.71	12.65
3rd EoS	K_0 (GPa)	66(4)	52(1)	58(1)	77(5)	58(5)	56(1)	67	68
	K_0'	4.1(5)	4	4.0(7)	1.4	13.5	3.6(1)	4.1	4
	V_0 (Å^3)	1985.9(3)	1985(3)	1987.6(1)	1984.51(7)	1987.11(1)	2021.8	2051.8	2024.2
2nd EoS	K_0 (GPa)	-	-	-	69(4)	72(4)	-	-	-
	V_0 (Å^3)	-	-	-	1987.11(1)	1984.51(7)	-	-	-

Although there is still some controversy about the effects of impurities on a high-pressure experiment, a comparison of the reported bulk modulus of hydrogarnet with the results obtained in this study showed agreement within an acceptable error range (Table 4.12) [204-206]. Given that the amount of hydrogarnet is very small compared to hemicarboaluminate, the bulk modulus obtained for hydrogarnet is less accurate than values obtained from single-crystal high-pressure experiment [204]. However, since the volume-pressure behavior of hydrogarnet does not show any anomalous compressibility, it is safe to assume that the abnormal compressibility of AFm phases is due to the existence of loosely bonded interlayer water molecules.

Interestingly monocarboaluminate has no significant dehydration effect. The interlamellar distance of 7.59 Å gradually decreased, however, a single diffraction peak was newly observed at 0.9 GPa (Fig. 4.10). The exact peak position is 6.7311 Å, which disappeared when it was fully relaxed. Considering the stepwise hydration of monocarboaluminate, this feature also might be due to the pressure-induced dehydration. Since very small amounts of monocarboaluminate dehydrated (i.e., the interlamellar distance is still remained same), the newly emerging peak was not included in calculating the bulk modulus. This minute amount of dehydration might be due to the movement of number 16 and 17 water molecules from the interlayer (Fig. 4.9). Based on the previous study on the refinement of atomic structure of the monocarboaluminate, these two waters are not directly connected to the calcium and aluminum oxide polyhedra [186]. On the other hand, the remaining 13, 14, 15 interlayer water molecules

form strong hydrogen bonds with an O atom of a carbonate group, which makes cohesion between the interlayer and principal layer (Fig. 4.9). Thus these two weakly bonded interlayer waters might be partly moved out from the interlayer of the samples causing an abrupt contraction of its interlamellar distance. Otherwise, considering the d-spacing data from the thermal dehydration of monocarboaluminate [196] (Table 4.1), the 6.6Å diffraction peak corresponds to that of $C_4A\bar{C}H_6$, which is similar in position to the newly emerging peak at 0.9 GPa. Because this dehydrated monocarboaluminate does not have any water molecules in its interlayer region, only a small portion of the samples might experience full dehydration. Note that the interlamellar distance cannot be directly compared with the experimental points because the peak itself is moving under pressure (i.e., the newly emerging peak should be compared with interlamellar distance of $C_4A\bar{C}H_6$ under 0.9 GPa, not under ambient pressure.).

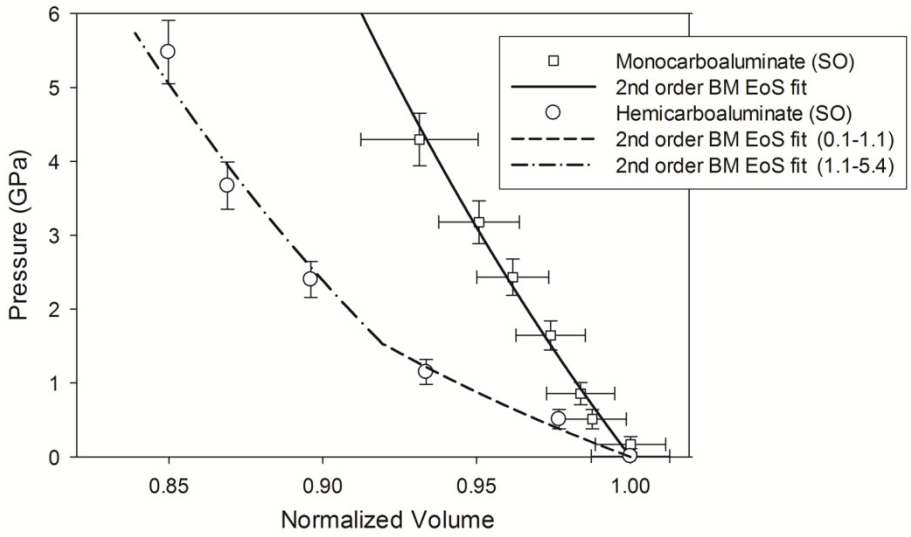

Figure 4.25 Pressure-volume behavior of monocarboaluminate and hemicarboaluminate. The lines show 2nd order BM EoS fitting results.

Comparison of the bulk modulus of monocarboaluminate with hemicarboaluminate is summarized in Table 4.11. According to the previous discussion, hemicarboaluminate might experience two complex pressure behaviors; pressure-induced dehydration at about 1.0 GPa and re-orientation of carbonate group. Thus, after the de-hydration of the hemicarboaluminate, it still shows a nonlinear pressure behavior due either to the re-orientation of carbonate groups or to additional dehydration. These effects make the abnormal value of pressure derivative, K_0', 13.6. In addition, the hydrogen bonds in hemicarboaluminate increase in strength as the interlayer space contracts, which yields an almost double bulk modulus relative to that of hemicarboaluminate at

ambient. One observation of note is that the pressure-volume curve of monocarboaluminate has a similar slope with that of dehydrated hemicarboaluminate (i.e., after some degree of dehydration of hemicarboaluminate; Fig. 4.25.). In this stage, although the exact atomic position of carbonate group in hemicarboaluminate has not been identified yet, the direction of the group can become parallel to the main layer due to the pressure effect. This re-orientation of carbonate group can contribute to the abnormal pressure behavior. Eventually it will make a similar structural framework with monocarboaluminate except the alternating existence of carbonate group. However, although the similar curve of dehydrated hemicarboaluminate and monocarboaluminate is particularly noteworthy above 1 GPa, the bulk moduli of the dehydration of hemicarboaluminate and monocarboaluminate are still quite different: 32(2) and 54(4) GPa, respectively. From this observation it can be concluded that the occupancy of carbon groups in the interlayer plays a key role in their bulk moduli of carbon containing AFm phases.

This difference can be also explained by an applied regression method on the hemicarboaluminate. The bulk modulus of second-phase hemicarboaluminate is a result of fitting the experimental points to the 'initial' point of 1.1 GPa, i.e., this yields the bulk modulus at 1.1 GPa with abnormal pressure derivative K_0'. Thus if it contains any interlayer water or perpendicular carbonate groups at 1.1 GPa, the actual bulk modulus at a higher pressure will be definitely greater than 32(2) GPa.

Figure 4.12 shows the difference between loading and unloading data points of monocarboaluminate. Differences might be due to experimental error (i.e., the relaxation time of silicone oil was not sufficient to equilibrate the solution) or additional dehydration induced by pressure during the unloading process. As shown, the dehydration effect is relatively weak for monocarboaluminate because of its intrinsically lower compressibility. In addition, although there can be some time-delayed dehydration effect during the unloading process, the dehydration effect is perfectly reversible. This is completely consistent with the previous research on strätlingite and hemicarboaluminate in a non-hygroscopic pressure medium.

An exceptionally high bulk modulus was computed for the monocarboaluminate. It is less compressible not only when compared to other AFm phases (strätlingite and hemicarboaluminate) but also to ettringite ($Ca_6Al_2(SO_4)_3(OH)_{12}.26(H_2O)$, trigonal, $\boldsymbol{a}$ = 11.23 Å, $\boldsymbol{c}$ = 21.44 Å, bulk modulus: 27(7) GPa, [42]), and portlandite ($Ca(OH)_2$, hexagonal, $\boldsymbol{a}$ = 3.5853(7) Å, $\boldsymbol{c}$ = 4.895(3) Å, bulk modulus: 37.8(1) GPa, [233]). In addition, the bulk modulus is still larger than that of dehydrated hemicarboaluminate. Therefore, the bulk

modulus of AFm phases is more dependent on its atomistic structural framework than the type of charge-balancing anion species in their interlayer region or the number of interlayer water molecules. This supports the fact that monocarboaluminate is stable not only thermodynamically but mechanically, because of its strong hydrogen bonds with sub-parallel carbonate groups in its interlayer.

Table 4.13 Computed elasticity of monocarboaluminate hydrates and tricalcium aluminate from first-principle calculations.

		5w MC			2w MC		C3A	
		LDA	**GGA**	**Exp.**	**LDA**	**GGA**	**GGA**	**Exp.**
3rd EoS	**K_0 (GPa)**	**55.9**	34.5	53(5)	25.0	23.1	106	102(6)
	K_0'	**4.2**	6.5	5.02	9.2	5.0	3.8	9.5
	V_0 (Å^3)	**435.1**	441.9	433	402.1	431.1	3647.4	3549(1)
2nd EoS	**K_0 (GPa)**	**56.2**	37.9	54(4)	29.0	23.8	108	110(3)
	V_0 (Å^3)	**435.1**	441.9	433	402.1	431.1	3647.4	3549(1)
RVH	**K (GPa)**	**56(1)**	39.8(2)	-	45(1)	24(4)	102	-
	G (GPa)	**32(1)**	33(2)	-	28(2)	21(3)	51.99	-
	E (GPa)	**80.1**	77.4	-	68.5	49.5	133.1	-
	v	**0.3**	0.2	-	0.22	0.2	0.28	-

Most reliable results of monocarboaluminate are in bold.

Table 4.7 and 4.13 summarizes DFT calculation on monocarboaluminate hydrates and tricalcium aluminate. For monocarboaluminate, although GGA lattice parameters differ by less than 1% from experimental values, the computed unit cell volume is 2 % larger. The LDA volume is more accurate, ~1 % larger. This better agreement happens despite differences in the structural details, such as smaller ***c*** lattice parameter, and larger alpha angles. The GGA and LDA predicted rather different structures for the 2 water MC system. Since there is no reported crystal structure for 2 water MC (except interlayer spacing), the accuracy of the LDA and GGA functionals is addressed for the 5 water MC system. The quality of results depends on the ability of the exchange-correlation functional to mimic many-body electronic interactions in a system. The LDA tends to overbind structures and underestimate lattice parameters and compressibility, while the GGA does the opposite [234-236].

Figure 4.18 and 4.19 show good agreement between experimental and simulated x-ray diffraction patterns. Not only peak positions but also relative peak intensities are well reproduced in the calculations. Experimental diffraction patterns have less small peaks, which suggest some hydrogen or water disorders. The overall, this agreement ensures that the atomic arrangement and structure are maintained at high pressures. The occurrence of diffused peaks in high-pressure

experiment can also be from pressure-transmitting medium (silicone oil was used in previous test to maintain the crystal in hydrostatic pressure), which can enter into the crystal structure and especially dissipate short-range diffraction peaks. This effect is well known in high-pressure experiments, especially for those crystals with complex layered structures with large interlayer spacing. Calculations do not show such pressure-medium effect.

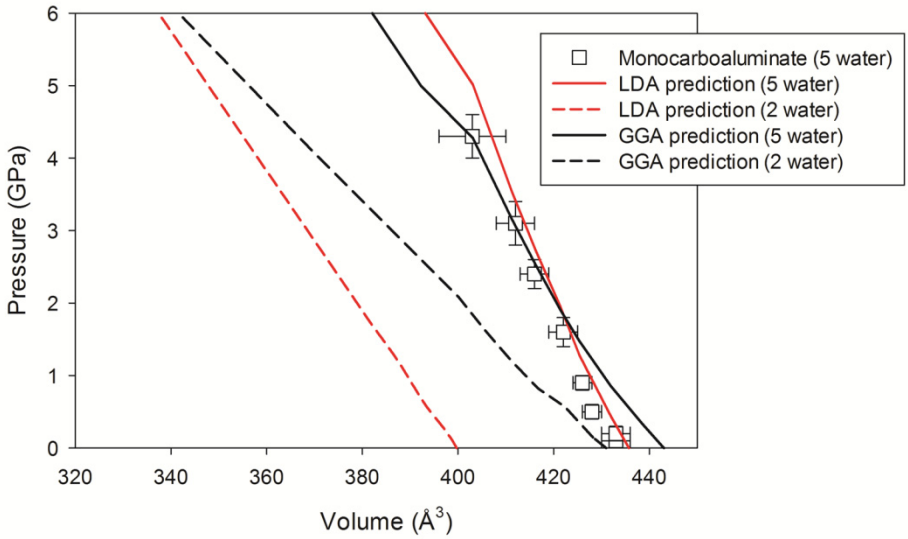

Figure 4.26 Variation of unit cell volume of 5 water and 2 water monocarboaluminates from LDA and GGA calculation.

As shown in Fig. 4.26, the LDA and GGA high-pressure behaviors of 5 water MC are similar with that from previous experiments. In general, the expanded GGA volume (~2 %) causes underestimation of the isothermal bulk modulus. In this case, the discrepancy is rather large producing an underestimation of ~29 % (37.9 GPa versus 54 GPa from experiments). The accuracy of LDA calculations is expected to improve upon introduction of vibrational effects by means of the quasi-harmonic approximation (QHA). Vibrational effects are particularly important in considering the water molecules in the interlayer region.

For hemicarboalumiante and strätlingite pressure-induced dehydration was observed irrespective of the type of pressure-transmitting medium. A contraction in volume and a significant increase on bulk modulus was observed as a result of a pressure-induced dehydration and re-orientation of anionic carbonate group (from perpendicular to parallel to the main layer). Although no significant change in behavior in 5 water MC was observed, partial dehydration might occur around 1 GPa; therefore, the variation of tilting angle of the carbonate group might provide

a clue to the anomalous behavior. In our simulation study, the LDA tilting angle varied from 9.6 ° to 8.9 ° while pressure changed 0 to 5 GPa. That indicates the carbonated group of the 5 water MC was slightly re-oriented to the parallel direction to the layers. However, since this angle change was not significant, it can be safely assumed that pressure-induced dehydration has more dominant effect on the anomalous behavior of hemicarboaluminate rather than the tilting of carbonate group.

LDA and GGA elastic coefficients computed by applying infinitesimal strains at 0 GPa (not at high pressure) display similar trends (see Table 4.9). The coefficient corresponding to longitudinal strains parallel to the axis with compact atomic arrangement C_{11}, is larger than those resulting from strains along the Y and Z axes. This is consistent with the expectation that layered structures are softer in the direction perpendicular to the layers. In addition, the difference between K_o, the bulk modulus derived by fitting equations of state to the compression curve, and K_{RVH}, the bulk modulus of the isotropic poly-crystalline aggregates, is negligible except the case of 2 water MC LDA computation (Table 4.13). Those from 2nd order finite strain EoS are larger than those from a 3rd order finite strain EoS. This is due to the smaller K_0' values (4.0) used in the fitting of the 2nd order EoS. As previously noted, LDA K_0 values using 2nd and 3rd order finite strain EoSs are quite accurate (less than 3%).

DFT calculations are powerful in predicting structural properties for systems where no data exists. Thus, the general trends on crystal structure under pressure for the 2 water MC system (Table 4.8) can be reliable. For both LDA and GGA calculations, the 2 water MC system is more compressible, and the cause of this smaller bulk modulus is the smaller number of water molecules in the interlayer region. The larger hydrogen bond-length in the 2 water MC results in a softer structure (Fig. 4.16 and 4.17). The water molecules in the 5 water MC structure are more packed in the interlayer region which makes this structure less compressive.

Figure 4.22 shows highly anisotropic LDA and GGA Young's modulus for both the 5 and 2 water MC. The significant anisotropy of the 2 water MC structure is partially lessened by addition of water in the interlayer region in 5 water MC. The soft elastic coefficient perpendicular to the layers of the 5 water MC system stiffens and becomes more similar to the other longitudinal strain coefficients, which decreases the anisotropy of this layered structure. The more anisotropic 2 water MC structure produces a wider range of Young's modulus as a function of direction (color bars in Fig. 4.22) and smaller mechanical properties such as K_{RVH}, G_{RVH}, and E.

In tricalcium aluminate experiment, isothermal bulk modulus was determined from the equation of state parameters. Thus, calculations were performed to simulate isotropic experimental conditions and direct comparison between experimental and computational pressure versus volume is possible as summarized in Table 4.13 and Fig. 4.24. Slightly larger value of K_0, 106 GPa, is obtained by fitting BM EoS, than by computing the RVH average of K_0, 102 GPa. This difference is expected, since VRH averages correspond to the bulk modulus of a isotropic poly-crystalline aggregate. The level of agreement between theory and experiments is precisely what is expected from GGA-PBE calculations: larger equilibrium volumes and smaller bulk modulus when compared with experiments. Consistent results were obtained for the relaxed structure and elastic constants determined by Manzano et al. (Table 4.10). Accordingly, computed mechanical properties agree well with those of Manzano et al. within 3% error range.

High pressure x-ray diffraction has the unique ability to directly observe the pressure-volume behavior of a unit crystal, making it possible to obtain the bulk modulus and its pressure derivative of the crystal. However, the diffraction resolution in DAC is not always sufficient to refine the structure, especially for such complex structure at high pressures. In addition, this pressure behavior in DAC depends on the type of pressure-transmitting medium and various pressure-induced reactions [237]. Thus atomic-level calculations will give us additional explanation on high-pressure experimental data.

The calculations were performed under 'static' conditions. This is not quite a 0 K calculation since vibrational zero-point energy, E_{zp}, is not included. Its effect on structural properties is sometimes significant. Finite temperature effects included according to the quasi-harmonic approximation are also important by less important than the zero-point motion effect. There is by now a substantial body of information showing that LDA plus finite temperatures calculations based on the quasiharmonic approximation (QHA) and first-principles phonons reproduce experimental data more accurately than GGA+QHA [181]. However, without the vibrational effects, LDA and GGA calculation reported in this section results in good agreement with experiments.

4.5 Chapter Summary

This chapter presented experimental and theoretical results on the following AFm phases that are often present in a hydrated cement paste: strätlingite, hemicarboaluminate, and monocarboaluminate. In hemicarboaluminate and strätlingite containing interlayer water molecules, major changes in the volume discontinuity take place at ~2.0 GPa hydrostatic pressure, regardless of the type of pressure-transmitting medium. The sudden changes of the c-lattice parameter are in good agreement with the previous studies of the layer thickness of different hydration stages caused by temperature variation. In the case of hemicarboaluminate, the re-orientation of perpendicular direction of planar carbonate group could influence its sudden volume contraction although the experimental results seem to indicate that the pressure-induced dehydration is the prevalent mechanism especially with a hygroscopic pressure medium. This pressure-induced dehydration caused significant changes in the bulk modulus so a two stage bulk modulus was calculated.

In contrast to strätlingite and hemicarboaluminate, monocarboaluminate did not show any significant dehydration or amorphization effect at elevated pressure. In comparing the calculated bulk modulus of monocarboaluminate, 54(4) GPa with that of hemicarboaluminate, 32(2) GPa, not only did the charge-balancing anion species and the number of interlayer water molecules play a key role in determining its mechanical properties, but its atomistic structural framework also contributed. The newly emerging diffraction peak and difference between some loading and unloading points indicate that there is a small degree of pressure-induced dehydration effect under hydrostatic pressure for both hemicarboaluminate and monocarboaluminate. But for monocarboaluminate, it had little effect on its bulk modulus because of its framework that consists of strong hydrogen bonds between interlayer waters and O atoms in carbonate groups.

Given the importance of monocarboaluminate for AFm phases, accurate knowledge of elastic properties of this phase is a central ingredient for understanding and modeling carbon uptaken concrete. Using first-principles calculations, the static elasticity of both fully and partially hydrated monocarboaluminate phases were calculated. The optimized static structures are in generally good agreement with experimental data at ambient conditions. Compressive behavior, elastic coefficients, isothermal bulk modulus, aggregate bulk and shear moduli, and Young's modulus for arbitrary directions were computed. Static LDA results agree better with high pressure experimental data than static GGA results. Irrespective of the exchange-correlation functional used, the more hydrated the structure the less compressible it becomes. Both monocarboaluminates have highly anisotropic Young's moduli because of the

layered nature of the structures. Adding more water can notably decrease this anisotropy and increase both bulk moduli computed from static compression curves and polycrystalline average.

This study did not include free energy contributions from zero-point motion or thermal excitations. Improved agreement between LDA results and experimental data is expected when these are included. Nevertheless, high pressure x-ray diffraction and static first-principle calculations proved to be an ideal combination of investigative tools for elasticity of cementitous materials. Overall, the mechanical properties of AFm phases are significantly different, dependent on the number of interlayer water molecules and the type of anion species. Especially the occupancy of carbonate group plays a key role in case of carbon containing AFm phases. Small additions of carbonate can significantly influence the stability and mechanical properties of the AFm phases.

In addition, the combination of experimental and theoretical studies shows a great performance on tricalcium aluminate, one of major clinker materials. Because the experimental bulk modulus agrees well with the computed one, it can be suggested that the other computed elastic properties are reliable as well. In addition, in Portland cement clinker various cations can be substituted in the large interstitial holes of the tricalcium aluminate structure. However, it is quite challenging for experiments to carry out these substitutions. The experimental and computational consistence reported herein can be applied to further computational approach to understanding effects of impurities on clinker properties at the atomic scale [238].

5. X-ray Absorption Experiments to Measure Pressure-induced Density Variation of Alkali-Silica Reaction Gel

5.1 Alkali-Silica Reaction Gel

The use of certain reactive aggregates containing amorphous or poorly crystalline silica in concrete can result in a chemical reaction in which silica from the aggregates reacts with alkali hydroxides dissolved in the pore solution of hydrated cement. The product of this reaction is known as alkali-silica reaction (ASR) gel. ASR gel is highly hygroscopic and is capable of irreversibly absorbing large amounts of water. This leads to volumetric expansion of the gel which can cause expansion and cracking of the concrete and eventual failure of the structure [134, 239, 240]. It is believed that ASR gel has a disordered atomic structure dominated by Q3 silicate tetrahedra in NMR spectrum [134, 239, 240]. It has been proposed that this structure is similar with that of the crystalline phases: hydrous Na kanemite ($NaHSi_2O_5 \cdot 3H_2O$) [239-241] and K kanemite ($KHSi_2O_5 \cdot 3H_2O$) [61] but with much greater overall disorder [61, 242].

Understanding of mechanical behaviors of ASR gel is a fundamental step to developing prevention and mitigation methods and to analyzing impact caused by a mismatch of elastic integrity of composite concrete. However, measuring the mechanical properties of ASR gel is difficult due to the amorphous nature of the gel. In addition, it is not easy to conduct a classical x-ray absorption experiment as the gel absorbs low amounts of x-ray. For example, as discussed in the previous chapters, synchrotron monochromatic x-ray allows a direct and accurate way to measure lattice volumes or densities of crystalline hydration products in cement. Also Brillouin spectroscopy was successfully applied to ettringite and portlandite to compute full elastic constants and averaged mechanical properties [243, 244] which yields consistent results with x-ray diffraction measurements [42]. In contrast, non-crystalline materials pose special challenges because of poorly defined atomic structure. Thus, the mechanical test on ASR gel has not been done yet and is still an experimental challenge.

The purpose of the research in this chapter is to take advantage of recent progress obtained in the characterization of amorphous materials using high energy x-ray absorption methods to analyze the ASR gel [46-48, 245]. As a result, isothermal bulk modulus of the gel will be measured. The pressure behavior of the gel gives some insights into its nanostructure and expansion mechanism.

5.2 High Pressure X-ray Absorption Experiment on Alkali-Silica Reaction Gel

5.2.1 Chemical Compositions and Density of Alkali-Silica Reaction Gel

Centimeter sized pieces of ASR gel were collected from the Furnas Dam located on the Rio Grande River in Minas Gerais, Brazil [246] shown in Fig. 5.1 (a). The portland cement used in the construction of the dam was manufactured close to the site of the dam and contained a total equivalent alkali content of 0.60%. Although this is quite a low equivalent alkali content, the locally mined quartzite used as the concrete aggregate slowly reacted with the alkali under the moist environmental conditions of the dam. In 1995, the symptoms of ASR, including map cracking, and staining, were first observed [247]. The ASR gel formed near the aggregates migrated through the porous hydrated cement matrix and created large macroscopic clusters which protruded out of cracks on the surface of the dam. The gel fragments used in this study were hand-picked from gallery walls in the dam. The fragment of ASR gel shown in Fig. 1 is semitransparent. It is identical to the sample used in the studies of Hou et al. [248] (sample FG1) and the Tambelli et al. [249] (bulk gel A).

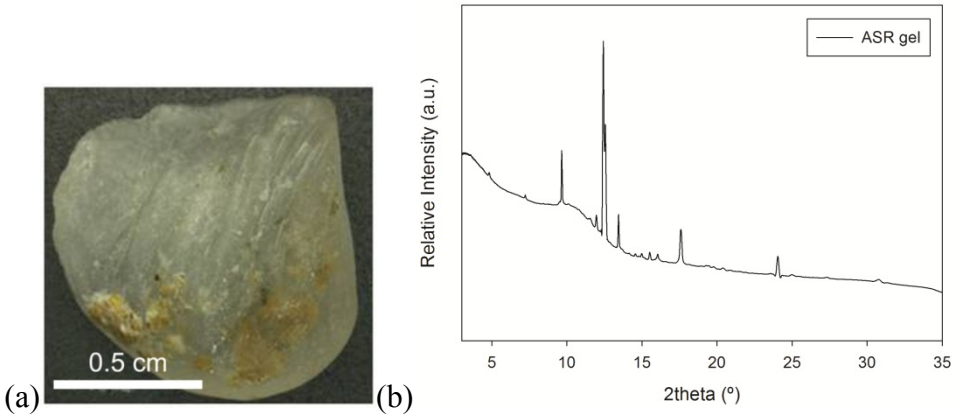

Figure 5.1 (a) ASR gel fragment collected from the Furnas dam. (b) Measured x-ray diffraction patterns of ASR gel at ambient condition ($\lambda = 0.6199$ Å). The broad hump of 8-14° indicates disordered crystal structure.

The density of 11 pieces of alkali-silica reaction gel was determined using the Archimedean method. The pieces had a weight ranging between 2.3 and 0.2 g and their average density was 2.06 ± 0.05 g/cm^3. The highly disordered nature of the ASR gel was confirmed by synchrotron x-ray diffraction as shown in Fig. 5.1(b). The pattern contains a weak basal peak with a d-spacing of about 10 Å and a broad peak with a d-spacing of about 1.7 Å due to the sample as well as several

weak sharper peaks indicating the presence of minor unidentified crystalline phases which is in agreement with the results of Hou et al. [248].

Table 5.1 Chemical composition of ASR gel (Major oxide weight %).

	SiO_2	K_2O	Na_2O	CaO	H_2O
ASR gel	69.2	12.2	2.7	0.9	15

The major oxide composition of the collected gel was found using a Philips PW2400 wavelength-dispersive x-ray fluorescence (XRF) spectrometer. 0.5 g of sample was finely ground and mixed with 3.5 g of lithium tetraborate as a flux. The mixture was then fused at high temperature (>1000°C) in a platinum crucible. The obtained melt was cooled to form a glass disc which was then used for the analysis. The result of the XRF measurement is contained in Table 5.1.

5.2.2 Application of X-ray Absorption Method

Since volume or density of crystalline materials can be measured by an x-ray diffraction method, this has become the method of choice for an extremely large number of materials including hydration products in cement [40, 42, 148]. On the other hand, using diffraction to determine the density of non-crystalline materials is not so straight forward due to the lack of translational symmetry in their structure. Lately a number of x-ray methods have been developed for the determination of density [47, 49, 250], primarily for the study of amorphous materials at high pressure. For example, the density of GeO_2 glass as a function of pressure inside a diamond anvil cell (DAC) using the x-ray absorption method [48]. However, it was not clear that this method would be sufficiently accurate for a low-Z, complex, non-crystalline material like ASR gel since the sample is very thin (about 20 μm) compared to the two diamond anvils (5 mm) making the vast majority of the absorption occur in the diamonds. Recently, however, it was demonstrated that combining x-ray diffraction and the absorption method using a two hole configuration of gasket with two reference materials can provide sufficiently accurate densities with SiO_2 glass which is also a low-Z noncrystalline material [245]. In following, the recently developed technique and its application to ASR gel will be introduced.

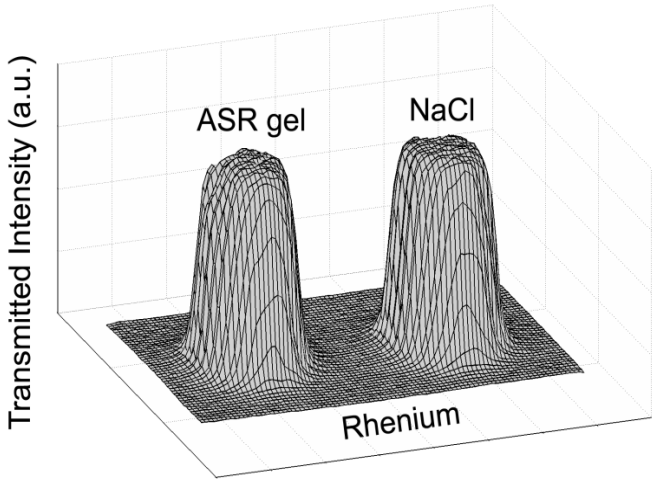

Figure 5.2 Transmitted x-ray contour profile measured by a diode with a monochromatic x-ray beam of 20 keV. The profile was measured by scanning in a step of 40 μm and 40 μm in x and y direction with x-ray beam size of 10 × 10 μm.

The x-ray absorption experiment has been performed at 12.2.2 beamline of Advanced Light Source [38]. An x-ray beam size of 10 × 10 μm was used for our measurements. The transmitted x-ray intensity after the DAC was monitored by a photodiode for the absorption measurements. Diffraction patterns were collected

using a MAR345 image plate detector for the diffraction measurements at a distance of 236.9 mm from the sample. A monochromatic x-ray beam with energy of 20 keV was selected. A rhenium gasket was indented to 22 μm thickness with 400 μm culet-size diamond anvils. Two holes of 80 μm diameter were drilled in the indentation at positions equidistant from the center as shown in Fig. 5.2. ASR gel was finely ground and loaded into one of the holes. The other hole was filled with NaCl that was used for thickness and absorption calibration. X-ray diffraction and absorption data were measured at pressures ranging from ambient to about 15.9 GPa (Fig 2 and 3). The pressure at each point was determined from the unit cell volumes of NaCl [99] and rhenium [251]. Figure 5.4 (a) and (b) show calibrated pressures of two reference materials. There is a slight discrepancy of applied pressures in two holes and the gap is significant in unloading process. The discrepancy will be discussed in more detail in later section.

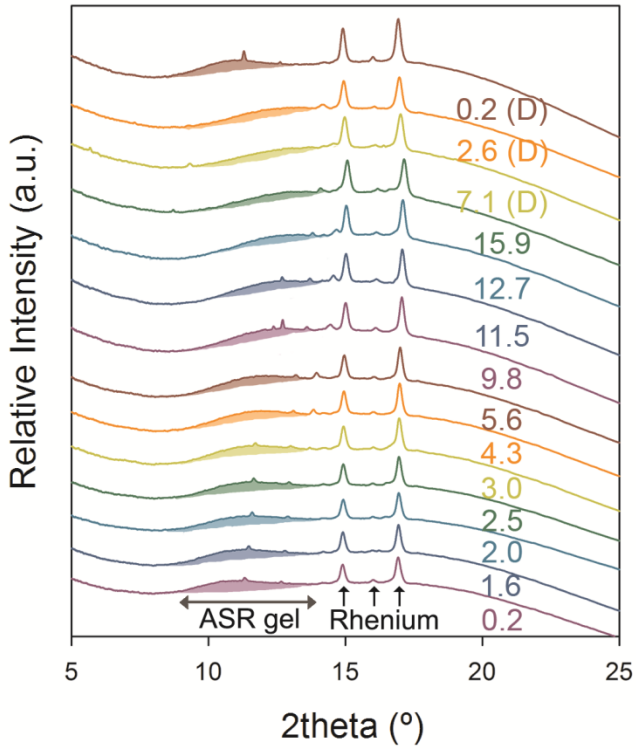

Figure 5.3 Measured x-ray diffraction patterns of ASR gel (λ = 0.6199 Å). The pressures were determined by x-ray diffraction peaks of Re at ASR gel sample hole. The wide range of hump was shifting as pressure increases. Top three patterns (D) were measured during decompression.

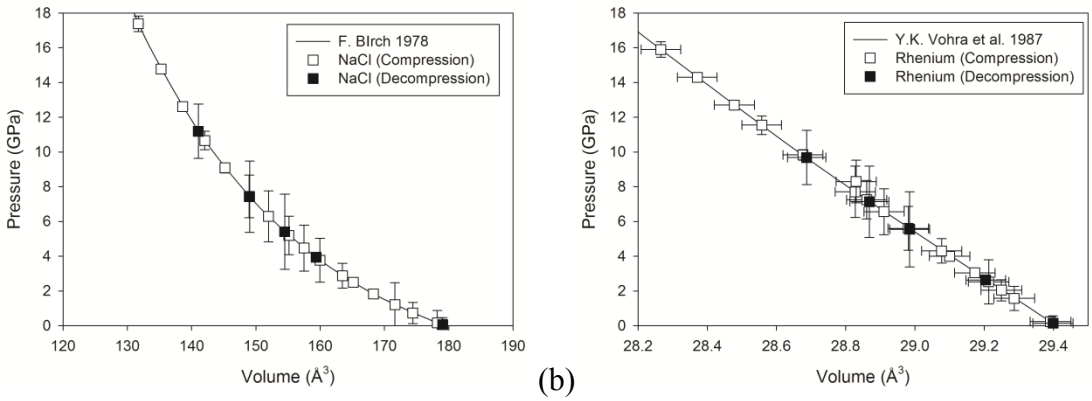

(a) (b)

Figure 5.4 Measured volumes of NaCl (a) and rhenium (b). Corresponding pressures are computed from the equation of state of NaCl [99] and rhenium [251].

As shown in Fig. 5.2, x-ray transmission intensities of the ASR, rhenium and NaCl were precisely determined by the photodiode. According to the absorption law, the transmission intensity can be expressed as below,

$$I_{ASR} = I_0 e^{-\mu_{Dia}\rho_{Dia}t_{Dia}} e^{-\mu_{ASR}\rho_{ASR}t_{ASR}} \quad \text{- (5.1)}$$

$$I_{NaCl} = I_0 e^{-\mu_{Dia}\rho_{Dia}t_{Dia}} e^{-\mu_{NaCl}\rho_{NaCl}t_{NaCl}} \quad \text{- (5.2)}$$

$$I_{\mathrm{Re}} = I_0 e^{-\mu_{Dia}\rho_{Dia}t_{Dia}} e^{-\mu_{\mathrm{Re}}\rho_{\mathrm{Re}}t_{\mathrm{Re}}} \quad \text{- (5.3)}$$

Here, I, μ, ρ, and t denote the intensity of x-rays, mass absorption coefficient, density, and thickness of sample, respectively. Subscripts 0, Dia, Re, and ASR represent incident x-rays, the two diamond anvils, rhenium, and the ASR gel, respectively. The mass absorption coefficients are considered to be known if the energy of monochromatic x-rays is far away from the absorption edges of a material. For example, total attenuation with coherent scattering of ASR gel is shown in Fig. 5.5 [252]. Also densities of two reference materials (rhenium and NaCl) can be measured from x-ray diffraction method as discussed before.

There are two assumptions for computing density of the gel. First one is the constant $I_0 e^{-\mu_{Dia}\rho_{Dia}t_{Dia}}$ term within the culet. And second one is same thickness across the gasket at each pressure (i.e. $t_{\mathrm{Re}} = t_{NaCl} = t_{ASR} = t$). Then the thickness of gasket can be computed from Eqn. (5.2) and (5.3),

$$t = \frac{\ln(I_{NaCl} / I_{\mathrm{Re}})}{\mu_{\mathrm{Re}}\rho_{\mathrm{Re}} - \mu_{NaCl}\rho_{NaCl}} \quad \text{- (5.4)}$$

The computed thickness variation is shown in Fig. 5.6 (a). The error of applied pressure was chosen from the difference of refined pressures in both holes (Fig. 5.6 (b)). Last, by substituting the computed thickness into Eqn. (5.1) and Eqn. (5.2), the density of ASR gel can be expressed as:

$$\rho_{ASR} = \frac{\ln(I_{NaCl} / I_{ASR}) + \mu_{NaCl}\rho_{NaCl}t}{\mu_{ASR}t} \qquad \text{- (5.5)}$$

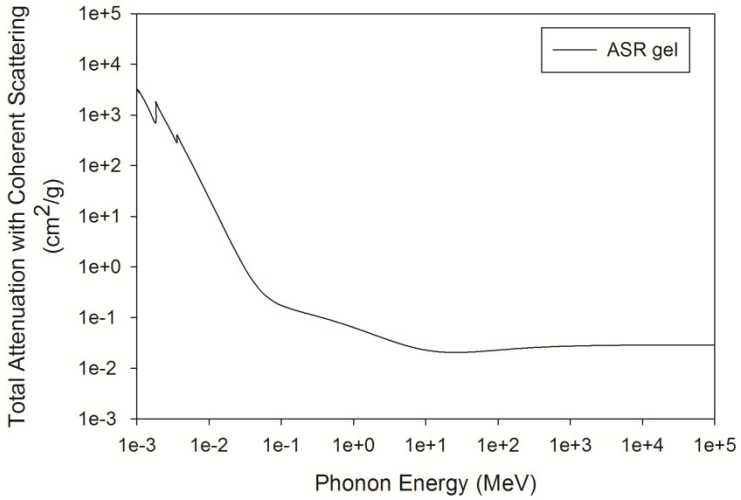

Figure 5.5 Total attenuation with coherent scattering of ASR gel as a function of phonon energy. Data was reproduced from NIST standard reference database [252].

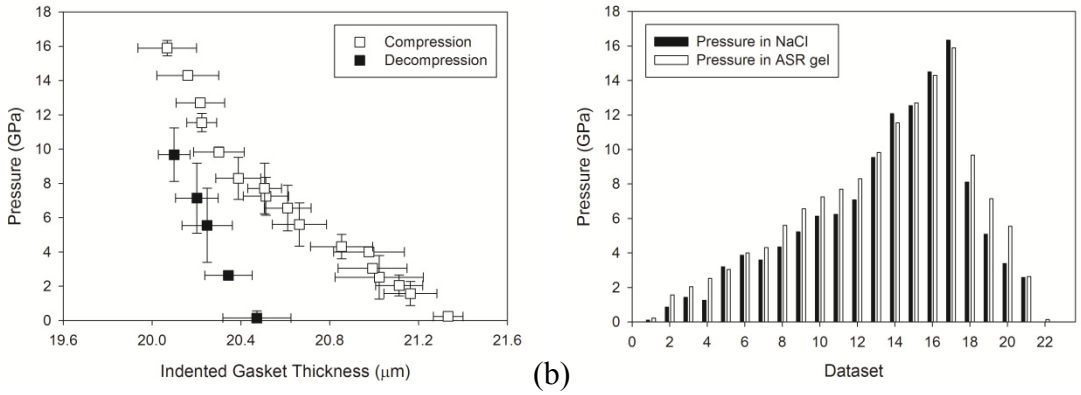

(a) (b)

Figure 5.6 (a) Thickness variation of the gasket as a function of pressure. (b) Applied pressures in two holes in DAC. The pressure was determined from Re and NaCl peaks of each holder.

Fig. 5.7 (a) shows the density determined using this method as a function of pressure up to 15.9 GPa. The error for the pressure was determined from the difference of the pressures determined in the two holes. The whole experimental

results are summarized in Table 5.2. The thickness of the gasket at 0.2 GPa was found to be 21.3(1) μm where the error is estimated from the variation of transmitted intensity. The measured densities at ambient pressure of NaCl and Re were found to be: 2.169(2), 21.04(4) g/cm^3. The density determined with this method for ASR gel is 2.93(7) g/cm^3. This value is sensibly higher than that obtained by the Archimedean method. In the analysis of the x-ray absorption data we fixed the starting (ambient) density of ASR gel to the value of 2.06(5) g/cm^3 from the Archimedean method which correspond to an effective mass absorption coefficient of 4.49 cm^2/g, where the standard deviations were estimated by the error propagation method [154].

Table 5.2 High pressure x-ray absorption results of ASR gel. The data of last five rows were collected during decompression.

ASR gel x-ray absorption experiment							
Pressure (GPa)	ρ_{NaCl} (g/cm^3)	ρ_{Re} (g/cm^3)	ρ_{ASR} (g/cm^3)	$v_{ASR}/v_{ASR,0}$	Thickness (μm)	μ_{NaCl}/μ_{Re}	μ_{ASR}/μ_{Re}
0.2 (1)	2.169 (2)	21.04 (4)	2.06 (4)	1.00 (3)	21.3 (1)	20.958 (1)	21.078 (1)
1.6 (7)	2.178 (2)	21.12 (4)	2.19 (6)	0.97 (3)	21.2 (1)	20.678 (5)	20.772 (5)
2.0 (6)	2.226 (2)	21.14 (4)	2.21 (7)	0.96 (4)	21.1 (1)	20.596 (4)	20.698 (4)
2.5 (12)	2.262 (2)	21.17 (4)	2.27 (8)	0.93 (4)	21.0 (2)	20.40 (1)	20.50 (1)
3.0 (1)	2.307 (2)	21.20 (4)	2.30 (7)	0.92 (4)	21.0 (2)	20.388 (9)	20.49 (1)
4.0 (1)	2.350 (2)	21.25 (4)	2.36 (7)	0.90 (4)	21.0 (2)	20.48 (1)	20.587 (1)
4.3 (7)	2.375 (2)	21.27 (4)	2.38 (7)	0.89 (3)	20.9 (1)	20.168 (7)	20.269 (8)
5.6 (12)	2.427 (3)	21.34 (4)	2.42 (8)	0.88 (4)	20.7 (1)	19.810 (5)	19.913 (6)
6.6 (13)	2.465 (3)	21.39 (4)	2.43 (8)	0.87 (4)	20.6 (1)	19.794 (4)	19.903 (4)
7.2 (11)	2.502 (3)	21.43 (4)	2.46 (5)	0.86 (3)	20.5 (1)	19.608 (4)	19.718 (4)
7.7 (14)	2.555 (3)	21.45 (4)	2.44 (9)	0.87 (3)	20.5 (1)	19.648 (2)	19.773 (2)
8.3 (12)	2.606 (3)	21.45 (4)	2.51 (9)	0.84 (4)	20.4 (1)	19.295 (4)	19.417 (4)
9.8 (2)	2.673 (3)	21.56 (4)	2.57 (9)	0.83 (4)	20.3 (1)	19.344 (5)	19.470 (5)
11.5 (5)	2.733 (3)	21.66 (4)	2.63 (8)	0.80 (3)	20.2 (1)	19.354 (1)	19.481 (1)
12.7 (1)	2.801 (3)	21.72 (4)	2.66 (6)	0.79 (3)	20.2 (1)	19.483 (4)	19.620 (5)
14.3 (1)	2.870 (3)	21.80 (4)	2.74 (5)	0.77 (2)	20.2 (1)	19.527 (8)	19.666 (8)
15.9 (4)	2.947 (3)	21.88 (4)	2.82 (6)	0.75 (2)	20.1 (1)	19.461 (7)	19.601 (7)
9.7 (15)	2.752 (2)	21.56 (4)	2.65 (8)	0.80 (3)	20.1 (1)	18.748 (1)	18.871 (2)
7.1 (20)	2.604 (2)	21.42 (4)	2.44 (9)	0.86 (4)	20.2 (1)	18.708 (3)	18.835 (3)
5.5 (21)	2.513 (2)	21.34 (4)	2.49 (6)	0.85 (3)	20.2 (1)	18.630 (4)	18.729 (4)
2.6 (1)	2.436 (2)	21.18 (4)	2.33 (5)	0.91 (3)	20.3 (1)	18.488 (4)	18.598 (4)
0.1 (4)	2.168 (2)	21.04 (4)	2.33 (8)	0.91 (4)	20.5 (2)	18.521 (8)	18.578)

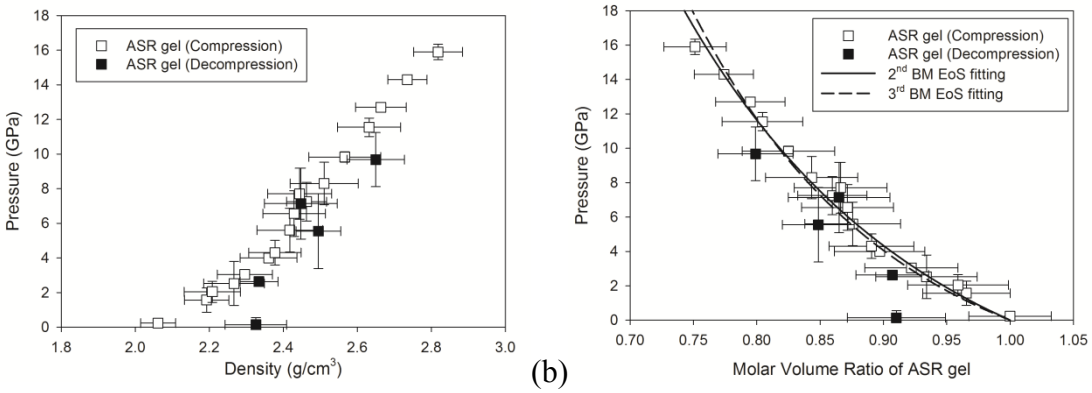

Figure 5.7 (a) Pressure dependence of the density of ASR gel. (b) Molar volume ratio of ASR gel as a function of pressure. The 2nd and 3rd BM EoS fitting results are shown in solid and dash line, respectively.

It should be noted that at high pressures, greater than about 30GPa, the accuracy of density determination from x-ray absorption measurements could deteriorate because the thickness of the gasket in a diamond anvil cell is not perfectly uniform due mainly to elastic deformation of the diamonds [46, 47]. In this study the maximum applied pressure was 15.9 GPa, and the anvil deformation or irregularity of the thickness of gasket was found to be negligible. However, during the unloading process, there was a significant pressure difference between the two holes. This is probably due to the rhenium, which has extruded to some extent, not relaxing elastically while the sample and NaCl do. This leads to an excess volume in the two holes which results in different pressures due to the NaCl and the sample having different compressibilities. Because of this the unloading data points were excluded in the calculation of the bulk modulus.

Molar volume ratio of amorphous material can be computed from the reciprocal value of the density. Figure 5.7 (b) represents the variation of molar volume ratio of ASR gel. It is revealed that the ratio decreases almost linearly from 0.2 to 15.9 GPa. Thus it can provide data points of P versus V/V_0 for calculating an isothermal bulk modulus. The converted molar volume variation is fitted using the third order isothermal Birch-Murnaghan equation of state (BM-EoS) in which $(\rho_{ASR,\ P=0}) / (\rho_{ASR,\ P\neq0})$ is used instead of $(V_{P\neq0}) / (V_{P=0})$ [99]. The modified equation of state is

$$P = \frac{3}{2} K_0 \left\{ \left(\frac{\rho}{\rho_0} \right)^{7/3} - \left(\frac{\rho}{\rho_0} \right)^{5/3} \right\} \left[1 + \frac{3}{4} \left(K_0^{'} - 4 \right) \left\{ \left(\frac{\rho}{\rho_0} \right)^{2/3} - 1 \right\} \right] \quad - (5.6)$$

where P is pressure, ρ is measured density, ρ_0 is density at zero pressure, K_0 is the isothermal bulk modulus at zero pressure, and K_0' is the first derivative of the bulk

modulus at zero pressure. Figure 5.7 (b) and 5.8 show fitting results. It gives K_0 = 33(2) GPa (fixed $K_0' = 4$, $R^2 = 0.986$) and K_0 = 34(2) GPa ($K_0' = 3.6$, $R^2 = 0.988$).

5.3 Discussion on Measured Bulk Modulus of Alkali-Silica Reaction Gel

In x-ray absorption measurement, $I_0 e^{-\mu_{Dia}\rho_{Dia}t_{Dia}}$ should be reasonably estimated to obtain density of a material. By applying the absorption law of two reference materials of NaCl and rhenium, the $I_0 e^{-\mu_{Dia}\rho_{Dia}t_{Dia}}$ term and thickness of gasket were accurately determined in our experiment. The applied pressure in ASR gel was calibrated by volume of rhenium using the equation of state of rhenium [251]. In addition, the pressure applied in reference material of NaCl was refined by volumes of NaCl [99]. Although there is a slight difference of applied pressure between the two holes as shown in Fig. 5.6 (b), it should be noted that pressures are not necessary to be the same for both holes, whereas the thicknesses should be the same as described in experimental principle. The thickness decreased almost linearly with pressure as shown in Fig. 5.6 (a). The average error in thickness is 0.1 μm, which was calculated from deviations in x-ray transmission intensities and in densities of crystalline materials by x-ray diffraction.

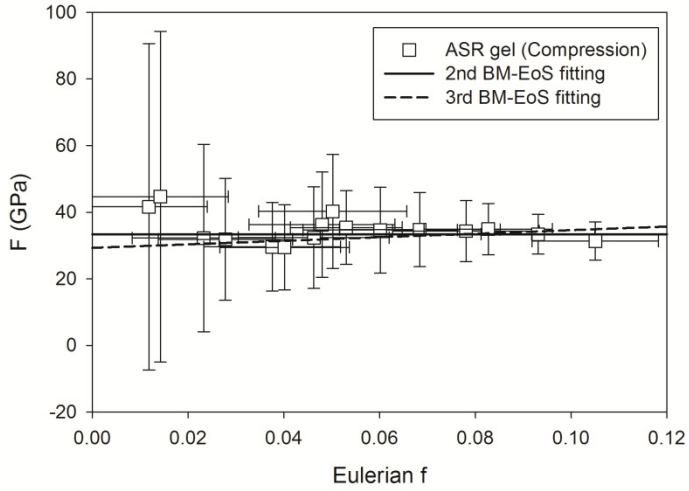

Figure 5.8 Normalized pressure F as a function of Eulerian strain f with 3rd and 2nd order BM EoS fitting results.

In addition, accurate chemical compositions and water contents should be known to compute the ideal value of mass absorption coefficient of a material. Based on the XRF data (Table 5.1), the mass absorption coefficient of our ASR gel is 3.157 cm^2/g and yields a density of 2.93(7) g/cm^3 from Eq. (5.5) for ASR gel at the pressure of 0.2 GPa. This does not agree well with the density that we measured at ambient pressure using the Archimedean method (2.06(5) g/cm^3). It might be due to variations in sample stoichiometry. An extremely small amount of powdered sample from the interior of the gel fragments was used for the x-ray

measurements to minimize the effect of externally attached impurities while a relatively large piece of sample was necessary for the XRF measurements. This may have resulted in the chemical composition determined from the XRF measurements being different to that of the samples used for the high-pressure measurements. An alternative explanation might be that the gel could have become compacted to some extent when it was loaded into the tiny sample chamber. However, this does not make a large difference to the elastic properties because of the fact that it is not density but density ratio that is used to determine the compressibility. That means the denominator in Eqn. (5.5) is cancelled out in the molar volume ratio. Thus modified mass absorption coefficient (4.490 cm^2/g) based on the density value from the Archimedean method was selected. The test results are summarized in Table 5.2.

The Birch-Murnaghan equation of state assumes that the sample is subjected to a hydrostatic stress. Any uniaxial stress generated by using two opposed anvils might cause additional error in the computation of the isothermal bulk modulus [253]. In order to try to quantify any uniaxial strain lattice parameter of NaCl independently from the (111), (200), and (220) reflections were calculated. Any uniaxial strain would be apparent from differences between these values. The calculated lattice parameters are virtually identical with less than 0.2% deviation. Therefore it can be safely assumed that the uniaxial stresses do not directly affect the absorption measurements and this could be due to a random orientation of compacted sample in a sample holder.

From the density variation measured from Archimedean method, it can be inferred that the gel is locally homogeneous and its variability at the meso/macroscale is probably due to heterogeneous composition of the aggregate material in the concrete. However, amorphous silica has a bulk modulus of 40(3) GPa with the density of 2.20(3) g/cm^3 [254]. It is larger than the bulk modulus of ASR gel determined by x-ray absorption (i.e., K_0 = 33(2) GPa when $K_0' = 4$). Thus it can be concluded that amorphous silica becomes compressible as it incorporates water molecules and alkali ions during ASR. On the other hand, the measured bulk modulus of ASR gel is larger than those determined by measuring synthetic alkaline-calcium silica gels with 0.8 M $Ca(OH)_2$ content [255]. However, it is important to note that the density of the gels from the dam is 80% higher than that of the synthetic gels analyzed by Phair et al. [255].

Although it contains 15% water, there is no pressure-induced instability which was observed in some soft calcium aluminate hydrates in cement system as discussed in chapter 4. In certain AFm phases, water molecules in interlayer regions become unstable under pressure and cause pressure-induced dehydration, especially in highly compressible hydrated materials. On the other hand, the

density of ASR gel increases significantly (about 40%) and nearly linearly up to 16 GPa. No discontinuous changes (e.g. phase transition) are observed. Thus the stable behavior under high pressure indirectly supports the idea of incorporation of water molecules not within interlayer but between nano-particles [241]. The probable reason is that water molecules within interlayer region tend to be unstable under pressure especially within highly compressible framework. Last, the amorphous material or melt is usually more compressible than the corresponding crystalline solid due to the large change in the intermediate-range structure and increment of coordination number at higher pressure [47]. But the lack of experimental or theoretical study on mechanical properties of Na/K kanemite makes a systematic comparison with ASR gel difficult.

5.4 Chapter Summary

Understanding of elastic properties of ASR gel is a key step in the development of science based prevention and mitigation procedures to combat the structural problems caused by the occurrence of the ASR in concrete structures. However, due to its amorphous structure, it is quite difficult to directly measure it. From x-ray absorption method, the mechanical properties of amorphous ASR gel have been successfully determined. Comparing with amorphous silica, lower density (2.06(5) g/cm^3) and higher compressibility (K_0=33(2) GPa) of the ASR gel suggest that incorporated water and alkali ions could cause volume growth and make the gel soft. The expanded volume with the higher compressibility would allow the gel migrating readily through the porous hydrated cement matrix. In addition, no pressure-induced instability supports the idea of incorporation of water between nano-particles, rather than within interlayer spacing of ASR gel.

It is not clear what the role of calcium ions or alkali content is in ASR expansion [256, 257]. A determination of the elastic properties of different compositional ASR gel will make an interesting subject for future study. The x-ray absorption method might also prove useful for the determination of the compressibility of many of the amorphous or poorly crystalline phases in concrete. For example: C-S-H gel and geopolymer gel which are main binders in conventional and green concrete.

6. Conclusions

The complexity of concrete research is from the lack of experimental data at a fundamental level. This study focuses on understanding of structural properties of materials which determines overall mechanical performance of concrete. Major findings in this work are given below:

Calcium silicate hydrates

C-S-H gel is poorly crystalline but similar to crystalline materials of tobermorite and jennite. From experimental and theoretical studies on tobermorite phases, structural mechanism under pressure was investigated. The most reliable mechanical properties of calcium silicate hydrates are as follows:

Experimental results (number in parenthesis indicates measured pressure range):

$Ca_4Al_6O_{15}(OH)_2 \cdot 5H_2O$ (Normal) : K_0 = 71(4) GPa (0.1-6.0 GPa)
$Ca_4Al_6O_{15}(OH)_2 \cdot 5H_2O$ (Anomalous) : K_0 = 63(2) GPa (0.1-4.5 GPa)
$Ca_5Al_6O_{16}(OH)_2$: K_0 = 115(14) GPa (0.1-8.5 GPa)
$Ca_9Al_6O_{18}(OH)_6 \cdot 8H_2O$: K_0 = 64(2) GPa (0.1-3.2 GPa)

First-principles calculations:

$Ca_5Al_6O_{16}(OH)_2 \cdot 7H_2O$: K = 57 GPa, G = 32 GPa, E = 80 GPa, ν = 0.3
$Ca_5Al_6O_{16}(OH)_2$: K = 57 GPa, G = 32 GPa, E = 80 GPa, ν = 0.3
$Ca_9Al_6O_{18}(OH)_6 \cdot 8H_2O$: K = 63 GPa, G = 28 GPa, E = 73 GPa, ν = 0.3

The incompressibility of layer direction, perpendicular to Ca-O layers, determines the overall bulk modulus of tobermorite phases. In the case of tobermorite 9Å, the gap between experiment and simulation can be explained by the infiltration of pressure-transmitting medium into the small interlayer space or the mechanical influence of Al substitution. Except the 9 Å case, there is excellent agreements in tobermorite 14 Å and 11 Å and jennite regarding pressure-volume behavior, especially with LDA approximation. This suggests that other elastic properties including elastic tensor coefficient, shear and Young's modulus, and Poisson's ratio from first-principle calculations are fairly reliable.

Calcium aluminate hydrates

Pressure-volume behavior of AFm phases was measured by high pressure x-ray diffraction. The hemicarboalumiante and strätlingite experience pressure-induced dehydration at low pressure (less than 2 GPa). However, monocarboaluminate which has a full occupancy of carbon oxide group in its interlayer has the largest bulk modulus among all crystalline minerals in concrete. The high incompressibility of monocarboaluminate indirectly suggests the high thermodynamical stability which is also confirmed by first-principles calculation.

As in the cases of tobermorite and jennite, LDA approximation accurately predicts the pressure-volume behavior of monocarboaluminate. The calculation also confirms that dehydrated monocarboaluminate is highly anisotropic thus mechanical properties are lower than those of fully hydrated monocarboaluminate. The full occupied water molecules in the monocarboaluminate tend to attenuate the anisotropic feature of the layer structure and make the crystal incompressible. As a clinker material, the mechanical characteristic of tricalcium aluminate is also investigated by high pressure x-ray experiment and first-principles calculation. The most reliable mechanical properties of calcium aluminate hydrates and calcium aluminate oxide are below.

Experimental results (number in parenthesis indicates measured pressure range):

$Ca_4Al_2(CO_3)(OH)_{12}\cdot 5H_2O$: K_0 = 54(4) GPa (0.1-4.3 GPa)

$Ca_4Al_2(CO_3)_{0.5}(OH)_{13}\cdot 5.5H_2O$: K_0 = 15(2) GPa (0.1-1.1 GPa)

: K_0 = 32(2) GPa (1.1-5.4 GPa)

$Ca_2Al_2SiO_7\cdot 8H_2O$: K_0 = 23(2) GPa (0.1-1.5 GPa)

:K_0 = 100(3) GPa (1.5-3.4 GPa)

$Ca_3Al_2O_6$: K_0 = 110(3) GPa (0.1-4.8 GPa)

First-principles calculations:

$Ca_4Al_2(CO_3)(OH)_{12}\cdot 5H_2O$: K = 57 GPa, G = 32 GPa, E = 80 GPa, ν = 0.3

$Ca_4Al_2(CO_3)(OH)_{12}\cdot 2H_2O$: K = 45 GPa, G = 28 GPa, E = 69 GPa, ν = 0.3

$Ca_3Al_2O_6$: K = 102 GPa, G = 52 GPa, E = 133 GPa, ν = 0.3

The confirmed experimental and computational consistence stimulates a future research on static and thermodynamic properties of other clinker materials such as alite and belite using first-principles calculation.

Alkali-Silica Reaction Gel

Compressibility of amorphous ASR gel was measured by combining x-ray diffraction and absorption methods. Indirectly measured densities at different pressures were fitted by the Birch-Murnaghan equation of states. The obtained bulk modulus of the gel is 33(2) GPa and 34(2) GPa (K_0'=3.6) from 2nd and 3rd BM EoS, respectively. The computed density and bulk modulus explain the expansion mechanism of transforming amorphous silica to ASR gel. Imbibing water and alkali ions into the silica make the gel softer and volumetric expanded. In addition, stable pressure behavior suggests the incorporated water molecules in the ASR gel may reside not inside its interlayer but between nano-particles.

Future research

Despite great mechanical performance and low price of ordinary concrete, the production of cement requires a considerable amount of energy and CO_2

emission which is responsible for up to 7-10% of anthropogenic CO_2 emissions worldwide. Along with the sustainable issue on cement, static and thermodynamic properties of clinker materials are the key material properties to understand the complex chemical process during the manufacture of cement. The material properties will be useful for not only understanding the chemical process but developing green cement with low environmental impact. However, it is quite challenging to carry out experiments on these.

The excellent agreement of experiment and theoretical calculation of tricalcium aluminate suggests a methodology to get accurate static properties. This can be also applied to compute thermodynamic properties. For instance, *ab initio* molecular dynamics simulation on cementitous crystals will allow investigating not only static properties but thermodynamic properties such as entropy variation and heat capacity. Furthermore, development of accurate empirical potentials for C-S-H and AFm phases can be used to study nano-particle cluster of C-S-H as well as large systems of material assemblies with thousands or millions of atoms with low computational cost. The accurately computed elastic constants in this research will be valuable parameters to assess the potential functions.

The most important material in concrete is unquestionably C-S-H. The combination of x-ray diffraction and absorption method as discussed in chapter 5 is also applicable to the density measurement of synthetic C-S-H at varying Ca/Si ratio. This will give an insight on the interpretations of the deformation properties of C-S-H with the effect of the length of silicate chain and/or abundance of Ca ions in C-S-H.

In concrete, strength of composite materials rests on the interactions between C-S-H and aggregates. The modification of the force by atomistic manipulation (e.g., ionic substitutions in C-S-H) can increase the mechanical performance of composite materials. In addition, understanding of the interaction of C-S-H with water is important for controlling time-dependent behavior of concrete (i.e., creep and shrinkage) of which is still unsettled problem in concrete design. As a new approach, molecular level study on the mechanism of the time-dependent behaviors of cement paste will be a stimulating research topic in future.

References

[1] P.K. Mehta, P.J.M. Monteiro, CONCRETE–Microstructure, Properties, and Materials, 3 (2006) 230-261.
[2] I. Richardson, The calcium silicate hydrates, Cement and Concrete Research, 38 (2008) 137-158.
[3] E. Bonaccorsi, S. Merlino, A.R. Kampf, The crystal structure of tobermorite 14 Å (Plombierite), a C–S–H phase, Journal of the American Ceramic Society, 88 (2005) 505-512.
[4] H.F.W. Taylor, Proposed structure for calcium silicate hydrate gel, Journal of the American Ceramic Society, 69 (2005) 464-467.
[5] H.M. Jennings, A model for the microstructure of calcium silicate hydrate in cement paste, Cement and Concrete Research, 30 (2000) 101-116.
[6] E. Gartner, K. Kurtis, P. Monteiro, Proposed mechanism of CSH growth tested by soft X-ray microscopy, Cement and Concrete Research, 30 (2000) 817-822.
[7] H. Jennings, B. Dalgleish, P.L. Pratt, Morphological development of hydrating tricalcium silicate as examined by electron microscopy techniques, Journal of the American Ceramic Society, 64 (1981) 567-572.
[8] I. Richardson, Tobermorite/jennite-and tobermorite/calcium hydroxide-based models for the structure of CSH: applicability to hardened pastes of tricalcium silicate, β-dicalcium silicate, Portland cement, and blends of Portland cement with blast-furnace slag, metakaolin, or silica fume, Cement and Concrete Research, 34 (2004) 1733-1777.
[9] M. Juenger, P. Monteiro, E. Gartner, G. Denbeaux, A soft x-ray microscope investigation into the effects of calcium chloride on tricalcium silicate hydration, Cement and Concrete Research, 35 (2005) 19-25.
[10] S. Goto, M. Daimon, G. Hosaka, R. Kondo, Composition and morphology of hydrated tricalcium silicate, Journal of the American Ceramic Society, 59 (1976) 281-284.
[11] H. Kurszhyk, H. Schwiete, Concerning the hydration products of C3S and β-C2S, Proceedings in 4th International Symposium on Chemistry of Cement, Washington, (1960) 349-358.
[12] E. Garboczi, D. Bentz, The effect of statistical fluctuation, finite size error, and digital resolution on the phase percolation and transport properties of the NIST cement hydration model, Cement and Concrete Research, 31 (2001) 1501-1514.
[13] H.M. Jennings, J.W. Bullard, J.J. Thomas, J.E. Andrade, J.J. Chen, G.W. Scherer, Characterization and modeling of pores and surfaces in cement paste: correlations to processing and properties, Journal of Advanced Concrete Technology, 6 (2008) 5-29.
[14] A.J. Allen, J.J. Thomas, H.M. Jennings, Composition and density of nanoscale calcium–silicate–hydrate in cement, Nature materials, 6 (2007) 311-316.
[15] X. Cong, R.J. Kirkpatrick, ^{29}Si MAS NMR study of the structure of calcium silicate hydrate, Advanced Cement Based Materials, 3 (1996) 144-156.
[16] I.G. Richardson, A.R. Brough, R. Brydson, G.W. Groves, C.M. Dobson, Location of aluminum in substituted calcium silicate hydrate (C-S-H) gels as determined by ^{29}Si and ^{27}Al NMR and EELS, Journal of the American Ceramic Society, 76 (1993) 2285-2288.
[17] X. Cong, R.J. Kirkpatrick, ^{17}O MAS NMR investigation of the structure of calcium silicate hydrate gel, Journal of the American Ceramic Society, 79 (1996) 1585-1592.

[18] M.D. Andersen, H.J. Jakobsen, J. Skibsted, Incorporation of aluminum in the calcium silicate hydrate (CSH) of hydrated Portland cements: A high-field ^{27}Al and ^{29}Si MAS NMR investigation, Inorganic Chemistry, 42 (2003) 2280-2287.
[19] J. Schneider, M. Cincotto, H. Panepucci, ^{29}Si and ^{27}Al high-resolution NMR characterization of calcium silicate hydrate phases in activated blast-furnace slag pastes, Cement and Concrete Research, 31 (2001) 993-1001.
[20] P. Yu, R. Kirkpatrick, Thermal dehydration of tobermorite and jennite, Concrete Science and Engineering, 1 (1999) 185-191.
[21] S. Mojumdar, L. Raki, Preparation, thermal, spectral and microscopic studies of calcium silicate hydrate–poly (acrylic acid) nanocomposite materials, Journal of Thermal Analysis and Calorimetry, 85 (2006) 99-105.
[22] C. Yip, G. Lukey, J. Van Deventer, The coexistence of geopolymeric gel and calcium silicate hydrate at the early stage of alkaline activation, Cement and Concrete Research, 35 (2005) 1688-1697.
[23] L. Skinner, S. Chae, C. Benmore, H. Wenk, P. Monteiro, Nanostructure of calcium silicate hydrates in cements, Physical Review Letters, 104 (2010) 195502.
[24] S. Soyer-Uzun, S.R. Chae, C.J. Benmore, H.R. Wenk, P.J.M. Monteiro, Compositional evolution of calcium silicate hydrate (C–S–H) structures by total x-ray scattering, Journal of the American Ceramic Society, (2012) 793-798.
[25] H. Taylor, J. Howison, Relationships between calcium silicates and clay minerals, Clay Minerals Bull, 3 (1956) 98-111.
[26] H. Taylor, The calcium silicate hydrates, The Chemistry of Cements, 1 (1964) 162-232.
[27] J. Gard, H. Taylor, Calcium silicate hydrate (II)("CSH (II)"), Cement and Concrete Research, 6 (1976) 667-677.
[28] I. Baur, C.A. Johnson, Sorption of selenite and selenate to cement minerals, Environmental Science & Technology, 37 (2003) 3442-3447.
[29] S.M. Leisinger, B. Lothenbach, G. Le Saout, R. Kägi, B. Wehrli, C.A. Johnson, Solid solutions between CrO_4- and SO_4-ettringite $Ca_6(Al(OH)_6)_2$-$[(CrO_4)_x(SO_4)_{1-x}]_3 \cdot 26$ H_2O, Environmental Science & Technology, 44 (2010) 8983-8988.
[30] L. Aimoz, E. Wieland, C. Taviot-Guého, R. Dähn, M. Vespa, S.V. Churakov, Structural insight into iodide uptake by AFm phases, Environmental Science & Technology, 46 (2012) 3874-3881.
[31] J. Stark, Recent advances in the field of cement hydration and microstructure analysis, Cement and Concrete Research, 41 (2011) 666-678.
[32] J.S.J. Van Deventer, J.L. Provis, P. Duxson, Technical and commercial progress in the adoption of geopolymer cement, Minerals Engineering, (2012) 89-104.
[33] R. Taylor, I. Richardson, R. Brydson, Composition and microstructure of 20-year-old ordinary portland cement–ground granulated blast-furnace slag blends containing 0 to 100% slag, Cement and Concrete Research, 40 (2010) 971-983.
[34] D. Silva, P. Monteiro, Hydration evolution of C_3S–EVA composites analyzed by soft x-ray microscopy, Cement and Concrete Research, 35 (2005) 351-357.
[35] P. Monteiro, M. Mancio, A. Kirchheim, R. Chae, J. Ha, P. Fischer, T. Tyliszczak, Soft x-ray microscopy of green cements, in: AIP Conference Proceedings, (2011) 351.

[36] J. Ha, S. Chae, K. Chou, T. Tyliszczak, P.J.M. Monteiro, Effect of polymers on the nanostructure and on the carbonation of calcium silicate hydrates: a scanning transmission x-ray microscopy study, Journal of Materials Science, 47 (2012) 976-989.
[37] J. Ha, S. Chae, K. Chou, T. Tyliszczak, P.J.M. Monteiro, Scanning transmission x-ray microscopic study of carbonated calcium silicate hydrate, Transportation Research Record: Journal of the Transportation Research Board, 2142 (2010) 83-88.
[38] M. Kunz, A.A. MacDowell, W.A. Caldwell, D. Cambie, R.S. Celestre, E.E. Domning, R.M. Duarte, A.E. Gleason, J.M. Glossinger, N. Kelez, A beamline for high-pressure studies at the Advanced Light Source with a superconducting bending magnet as the source, Journal of Synchrotron Radiation, 12 (2005) 650-658.
[39] J.E. Oh, P.J.M. Monteiro, S.S. Jun, S. Choi, S.M. Clark, The evolution of strength and crystalline phases for alkali-activated ground blast furnace slag and fly ash-based geopolymers, Cement and Concrete Research, 40 (2010) 189-196.
[40] J.E. Oh, S.M. Clark, P.J.M. Monteiro, Does the Al substitution in C-S-H (I) change its mechanical property?, Cement and Concrete Research, 41 (2011) 102-106.
[41] J.E. Oh, J. Moon, S.G. Oh, S.M. Clark, P.J.M. Monteiro, Microstructural and compositional change of NaOH-activated high calcium fly ash by incorporating Na-aluminate and co-existence of geopolymeric gel and C–S–H (I), Cement and Concrete Research, (2012) 673-685.
[42] S.M. Clark, B. Colas, M. Kunz, S. Speziale, P.J.M. Monteiro, Effect of pressure on the crystal structure of ettringite, Cement and Concrete Research, 38 (2008) 19-26.
[43] J.E. Oh, J. Moon, M. Mancio, S.M. Clark, P.J.M. Monteiro, Bulk modulus of basic sodalite, $Na_8[AlSiO_4]_6(OH)_2 \cdot 2H_2O$, a possible zeolitic precursor in coal-fly-ash-based geopolymers, Cement and Concrete Research, 41 (2011) 107-112.
[44] J.E. Oh, S.M. Clark, P.J.M. Monteiro, Determination of the bulk modulus of hydroxycancrinite, a possible zeolitic precursor in geopolymers, by high-pressure synchrotron X-ray diffraction, Cement and Concrete Composites, 33 (2011) 1014-1019.
[45] J. Yan, J. Knight, M. Kunz, S. Vennila Raju, B. Chen, A.E. Gleason, B.K. Godwal, Z. Geballe, R. Jeanloz, S.M. Clark, The resistive-heating characterization of laser heating system and LaB_6 characterization of x-ray diffraction of beamline 12.2. 2 at advanced light source, Journal of Physics and Chemistry of Solids, 71 (2010) 1179-1182.
[46] G. Shen, N. Sata, M. Newville, M.L. Rivers, S.R. Sutton, Molar volumes of molten indium at high pressures measured in a diamond anvil cell, Applied Physics Letters, 81 (2002) 1411-1413.
[47] G. Shen, N. Sata, N. Taberlet, M. Newville, M.L. Rivers, S.R. Sutton, Melting studies of indium: determination of the structure and density of melts at high pressures and high temperatures, Journal of Physics: Condensed Matter, 14 (2002) 10533-10540.
[48] X. Hong, G. Shen, V.B. Prakapenka, M.L. Rivers, S.R. Sutton, Density measurements of noncrystalline materials at high pressure with diamond anvil cell, Review of Scientific Instruments, 78 (2007) 103905-103905-103906.
[49] J.H. Eggert, G. Weck, P. Loubeyre, M. Mezouar, Quantitative structure factor and density measurements of high-pressure fluids in diamond anvil cells by x-ray diffraction: Argon and water, Physical Review B, 65 (2002) 174105.
[50] H.R. Wenk, P.J.M. Monteiro, M. Kunz, K. Chen, N. Tamura, L. Lutterotti, J. Del Arroz, Preferred orientation of ettringite in concrete fractures, Journal of Applied Crystallography, 42 (2009) 429-432.

[51] L. Miyagi, W. Kanitpanyacharoen, P. Kaercher, K.K.M. Lee, H.R. Wenk, Slip systems in MgSiO3 post-perovskite: implications for D´´ anisotropy, Science, 329 (2010) 1639-1641.
[52] H.R. Wenk, W. Kanitpanyacharoen, M. Voltolini, Preferred orientation of phyllosilicates: Comparison of fault gouge, shale and schist, Journal of Structural Geology, 32 (2010) 478-489.
[53] G.H. Stout, L.H. Jensen, X.S. Determination, A practical guide, MacMillan, New York, 1968.
[54] T. Egami, S.J.L. Billinge, Preface, Pergamon Materials Series, 7 (2003) vii-x.
[55] S. Merlino, E. Bonaccorsi, T. Armbruster, Tobermorites; their real structure and order-disorder (OD) character, American Mineralogist, 84 (1999) 1613-1621.
[56] F. Battocchio, P.J.M. Monteiro, H.R. Wenk, Rietveld refinement of the structures of 1.0 CSH and 1.5 CSH, Cement and Concrete Research, 42 (2012) 1534-1548.
[57] C.E. White, J.L. Provis, T. Proffen, J.S.J. Van Deventer, The effects of temperature on the local structure of metakaolin-based geopolymer binder: A neutron pair distribution function investigation, Journal of the American Ceramic Society, 93 (2010) 3486-3492.
[58] C.E. White, J.L. Provis, T. Proffen, D.P. Riley, J.S.J. van Deventer, Combining density functional theory (DFT) and pair distribution function (PDF) analysis to solve the structure of metastable materials: The case of metakaolin, Physical Chemistry Chemical Physics, 12 (2010) 3239-3245.
[59] C.E. White, J.L. Provis, A. Llobet, T. Proffen, J.S.J. van Deventer, Evolution of local structure in geopolymer gels: An in situ neutron pair distribution function analysis, Journal of the American Ceramic Society, 94 (2011) 3532-3539.
[60] C.E. White, K. Page, N.J. Henson, J.L. Provis, In situ synchrotron x-ray pair distribution function analysis of the early stages of gel formation in metakaolin-based geopolymers, Applied Clay Science, (2012) 17-25.
[61] C. Meral, C.J. Benmore, P.J.M. Monteiro, The study of disorder and nanocrystallinity in C-S-H, supplementary cementitious materials and geopolymers using pair distribution function analysis, Cement and Concrete Research, 41 (2011) 696-710.
[62] A. Leonard, Vortex methods for flow simulation, Journal of Computational Physics, 37 (1980) 289-335.
[63] A. Leonard, Computing three-dimensional incompressible flows with vortex elements, Annual Review of Fluid Mechanics, 17 (1985) 523-559.
[64] T. Liszka, An interpolation method for an irregular net of nodes, International Journal for Numerical Methods in Engineering, 20 (2005) 1599-1612.
[65] H. Feldmeier, J. Schnack, Molecular dynamics for fermions, arXiv preprint cond-mat/0001207, (2000).
[66] M.N. Kobrak, E.R. Bittner, Quantum molecular dynamics study of polaron recombination in conjugated polymers, Physical Review B, 62 (2000) 11473.
[67] C. Kilic, T. Yildirim, H. Mehrez, S. Ciraci, A first-principles study of the structure and dynamics of C_8H_8, Si_8H_8, and Ge_8H_8 molecules, The Journal of Physical Chemistry A, 104 (2000) 2724-2728.
[68] F. Hedman, A. Laaksonen, Parallel aspects of quantum molecular dynamics simulations of liquids, Computer Physics Communications, 128 (2000) 284-294.
[69] D.C. Rapaport, The art of molecular dynamics simulation, Cambridge University Press, (2004).

[70] M.P. Allen, D.J. Tildesley, J.R. Banavar, Computer simulation of liquids, Physics Today, 42 (1989) 105.
[71] M.P. Allen, D.J. Tildesley, Computer simulation in chemical physics, Springer, 1993.
[72] R. Catlow, S. Parker, M. Allen, Computer modelling of fluids polymers and solids, Springer, 1989.
[73] G. Ciccotti, W.G. Hoover, Molecular-dynamics simulation of statistical-mechanical systems: Proceedings of the International School of Physics "Enrico Fermi", Varenna on Lake Como, Villa Monastero, 25 July-2 August 1985: Course XCVII, North-Holland [for the Italian physical society], (1986).
[74] G. Ciccotti, D. Frenkel, I.R. Mc Donald, Simulation of Liquids and Solids, (1987).
[75] K. Ohno, K. Esfarjani, Y. Kawazoe, Computational materials science: From ab Initio to monte carlo methods, Springer, 2000.
[76] S. Li, W.K. Liu, Meshfree and particle methods and their applications, Applied Mechanics Reviews, 55 (2002) 1-34.
[77] A.R. Leach, Molecular modelling: principles and applications, Pearson College Division, (2001).
[78] D. Frenkel, B. Smit, M.A. Ratner, Understanding molecular simulation: from algorithms to applications, Physics Today, 50 (1997) 66.
[79] I.N. Levine, Quantum chemistry. 5th, New York, Prentice Hall, 1991.
[80] W. Kohn, L.J. Sham, Self-consistent equations including exchange and correlation effects, Physical Review, 140 (1965) A1133-A1138.
[81] M. Born, R. Oppenheimer, Zur Quantentheorie der Molekeln, Annalen der Physik, 389 (1927) 457-484.
[82] R. Wentzcovitch, L. Stixrude, J.J. Rosso, Theoretical and computational methods in mineral physics: geophysical applications, Mineralogical Society of America, (2010).
[83] D.M. Ceperley, B.J. Alder, Ground state of the electron gas by a stochastic method, Physical Review Letters, 45 (1980) 566-569.
[84] J.P. Perdew, A. Zunger, Self-interaction correction to density-functional approximations for many-electron systems, Physical Review B, 23 (1981) 5048-5079.
[85] J.P. Perdew, K. Burke, M. Ernzerhof, Generalized gradient approximation made simple, Physical Review Letters, 77 (1996) 3865-3868.
[86] P. Hohenberg, W. Kohn, Inhomogeneous electron gas, Physical Review, 136 (1964) B864.
[87] U. von Barth, L. Hedin, A local exchange-correlation potential for the spin polarized case. i, Journal of Physics C: Solid State Physics, 5 (2001) 1629.
[88] L.S. Bijaya B. Karki, Renata M. Wentzcovitch, High-pressure elastic properties of major materials of earth's mantle from first principles, Reviews of Geophysics, 39 (2001) 507-534.
[89] P. Antoniewicz, L. Kleinman, Kohn-Sham exchange potential exact to first order in $\rho(K\rightarrow)/\rho_0$, Physical Review B, 31 (1985) 6779.
[90] D.C. Langreth, S. Vosko, Response functions and nonlocal approximations, Advances in Quantum Chemistry, 21 (1990) 175-199.
[91] D.C. Langreth, M. Mehl, Beyond the local-density approximation in calculations of ground-state electronic properties, Physical Review B, 28 (1983) 1809.
[92] J.P. Perdew, Density-functional approximation for the correlation energy of the inhomogeneous electron gas, Physical Review B, 33 (1986) 8822.

[93] C. Lee, W. Yang, R.G. Parr, Development of the Colle-Salvetti correlation-energy formula into a functional of the electron density, Physical Review B, 37 (1988) 785.
[94] J.P. Perdew, Generalized gradient approximations for exchange and correlation: A look backward and forward, Physica B: Condensed Matter, 172 (1991) 1-6.
[95] J. Perdew, K. Burke, M. Ernzerhof, Perdew, Burke, and Ernzerhof Reply, Physical Review Letters, 80 (1998) 891-891.
[96] A.R. Oganov, P.I. Dorogokupets, All-electron and pseudopotential study of MgO: Equation of state, anharmonicity, and stability, Physical Review B, 67 (2003) 224110.
[97] J. Furthmuller, J. Hafner, G. Kresse, Ab initio calculation of the structural and electronic properties of carbon and boron nitride using ultrasoft pseudopotentials, Physical Review B, 50 (1994) 15606-15622.
[98] H.J. Monkhorst, J.D. Pack, Special points for Brillouin-zone integrations, Physical Review B, 13 (1976) 5188-5192.
[99] F. Birch, Finite strain isotherm and velocities for single-crystal and polycrystalline NaCl at high pressures and 300 K, Journal of Geophysical Research, 83 (1978) 1257-1268.
[100] O.H. Nielsen, R.M. Martin, First-principles calculation of stress, Physical Review Letters, 50 (1983) 697.
[101] R. Hill, The elastic behaviour of a crystalline aggregate, Proceedings of the Physical Society Section A, 65 (1952).
[102] J.P. Watt, G.F. Davies, R.J. O'Connell, The elastic properties of composite materials, Reviews of Geophysics, 14 (1976).
[103] W. Voigt, Lehrbuchder Kristallphysik, Teubner, Leipzig, (1928).
[104] A. Reuss, Z. Angnew, A calculation of the bulk modulus of polycrystalline materials, Mathmatical Methods, 9 (1929) 55.
[105] J.J. Thomas, H.M. Jennings, A.J. Allen, The surface area of cement paste as measured by neutron scattering: evidence for two CSH morphologies, Cement and Concrete Research, 28 (1998) 897-905.
[106] J.J. Thomas, S.A. FitzGerald, D.A. Neumann, R.A. Livingston, State of water in hydrating tricalcium silicate and portland cement pastes as measured by quasi-elastic neutron scattering, Journal of the American Ceramic Society, 84 (2001) 1811-1816.
[107] H.F.W. Taylor, Cement Chemistry, Thomas Telford, 1997.
[108] H.F.W. Taylor, 726. Hydrated calcium silicates. Part I. Compound formation at ordinary temperatures, Journal of the Chemical Society (Resumed), (1950) 3682-3690.
[109] S. Brunauer, S. Greenberg, The hydration of tricalcium silicate and dicalcium silicate at room temperature, Chemistry of Cement, Proceedings 4th International Symposium, Washington DC, (1960) 429-468.
[110] L. Heller, H.F.W. Taylor, Hydrated calcium silicates. Part IV. Hydrothermal reactions: lime: silica ratios 2:1 and 3:1, Journal of the Chemical Society (Resumed), (1952) 2535-2541.
[111] G. Claringbull, M. Hey, A re-examination of tobermorite, Mineralogical Magazine, 29 (1952) 960-962.
[112] L. Heller, H. Taylor, Hydrated calcium silicates. Part II. Hydrothermal reactions: lime: silica ratio 1: 1, Journal of the Chemical Society (Resumed), (1951) 2397-2401.
[113] L. Heller, The stucture of dicalcium silicate-hydrate, Acta Crystallographica, 5 (1952) 724-728.

[114] H.D. Megaw, C. Kelsey, Crystal structure of tobermorite, Nature, 177 (1956) 390-391.
[115] E. Bonaccorsi, S. Merlino, Modular microporous minerals: cancrinite-davyne group and CSH phases, Reviews in Mineralogy and Geochemistry, 57 (2005) 241-290.
[116] S. Merlino, E. Bonaccorsi, T. Armbruster, The real structures of clinotobermorite and tobermorite 9 Å OD character, polytypes, and structural relationships, European Journal of Mineralogy, 12 (2000) 411-429.
[117] J. McConnell, The hydrated calcium silicates riversideite, tobermorite, and plombierite, Mineralogical Magazine, 30 (1954) 293-305.
[118] E. Bonaccorsi, S. Merlino, H. Taylor, The crystal structure of jennite, $Ca_9Si_6O_{18}(OH)_6 \cdot 8H_2O$, Cement and Concrete Research, 34 (2004) 1481-1488.
[119] C. Hejny, T. Armbruster, Polytypism in xonotlite $Ca_6Si_6O_{17}(OH)_2$, Zeitschrift für Kristallographie / International Journal for Structural, Physical, and Chemical Aspects of Crystalline Materials, 216 (2001) 396-408.
[120] H.D. Megaw, The structure of afwillite, $Ca_3(SiO_3OH)2.2H_2O$, Acta Crystallographica, 5 (1952) 477-491.
[121] S. Merlino, Gyrolite: its crystal structure and crystal chemistry, Mineralogical Magazine, 52 (1988) 377-387.
[122] H. Taylor, D. Roy, Structure and composition of hydrates, 7th International Congress on the Chemistry of Cement, (1980) 1-13.
[123] S. Shaw, S. Clark, C. Hendersona, Hydrothermal formation of the calcium silicate hydrates, tobermorite ($Ca_5Si_6O_{16}(OH)_2 \cdot 4H_2O$) and xonotlite ($Ca_6Si_6O_{17}(OH)_2$): an in situ synchrotron study, Chemical Geology, 167 (2000) 129-140.
[124] H. Taylor, Tobermorite, jennite, and cement gel, Zeitschrift für Kristallographie, 202 (1992) 41-50.
[125] H. Taylor, 33. Hydrated calcium silicates. Part V. The water content of calcium silicate hydrate (I), Journal of the Chemical Society (Resumed), (1953) 163-171.
[126] T. Mitsuda, H. Taylor, Normal and anomalous tobermorites, Mineralogical Magazine, 42 (1978) 229-235.
[127] C. Henmi, I. Kusachi, Monoclinic tobermorite from Fuka, Bitchu-cho, Okayama Prefecture, Japan, Journal of the Japanese Association of Mineralogist, Petrlogist and Economic Geologists, 84 (1989) 374-379.
[128] C. Henmi, I. Kusachi, Clinotobermorite, $Ca_5Si_6(O,OH)_{18} \cdot 5H_2O$, a new mineral from Fuka, Okayama Prefecture, Japan, Mineralogical Magazine, 56 (1992) 353-358.
[129] S. Hamid, The crystal structure of the 11Å natural tobermorite $Ca_{2.25}[Si_3O_{7.5}(OH)_{1.5}] \cdot 1H_2O$, Zeitschrift für Kristallographie, 154 (1981) 189-198.
[130] W. Wieker, A.R. Grimmer, A. Winkler, M. Mägi, M. Tarmak, E. Lippmaa, Solid-state high-resolution ^{29}Si NMR spectroscopy of synthetic 14 Å, 11 Å and 9 Å tobermorites, Cement and Concrete Research, 12 (1982) 333-339.
[131] E. Lippmaa, M. Mägi, M. Tarmak, W. Wieker, A. Grimmer, A high resolution ^{29}Si NMR study of the hydration of tricalciumsilicate, Cement and Concrete Research, 12 (1982) 597-602.
[132] S. Komarneni, D.M. Roy, C.A. Fyfe, G. Kennedy, Naturally occurring 1.4 nm tobermorite and synthetic jennite: Characterization by ^{27}Al and ^{29}Si MASNMR spectroscopy and cation exchange properties, Cement and Concrete Research, 17 (1987) 891-895.

[133] M. Tsuji, S. Komarneni, P. Malla, Substituted tobermorites: ^{27}Al and ^{29}Si MASNMR, cation exchange, and water sorption studies, Journal of the American Ceramic Society, 74 (1991) 274-279.
[134] A.R. Brough, C.M. Dobson, I.G. Richardson, G.W. Groves, Alkali activation of reactive silicas in cements: in situ ^{29}Si MAS NMR studies of the kinetics of silicate polymerization, Journal of Materials Science, 31 (1996) 3365-3373.
[135] I. Richardson, G. Groves, Models for the composition and structure of calcium silicate hydrate (CSH) gel in hardened tricalcium silicate pastes, Cement and Concrete Research, 22 (1992) 1001-1010.
[136] K. Dornberger-Schiff, F. Liebau, E. Thilo, Zur Struktur des-Wollastonits des Maddrellschen Salzes und des Natriumpolyarsenats, Acta Crystallographica, 8 (1955) 752-754.
[137] K. Dornberger-Schiff, On order-disorder structures (OD-structures), Acta Crystallographica, 9 (1956) 593-601.
[138] K. Dornberger-Schiff, H. Grell-Niemann, On the theory of order-disorder (OD) structures, Acta Crystallographica, 14 (1961) 167-177.
[139] K. Dornberger-Schiff, Reinterpretation of pseudo-orthorhombic diffraction patterns, Acta Crystallographica, 21 (1966) 311-322.
[140] G. Ferraris, E. Makovicky, S. Merlino, Crystallography of modular materials, Oxford University Press, (2008).
[141] S. Merlino, E. Bonaccorsi, T. Armbruster, The real structure of tobermorite 11Å: Normal and anomalous forms, OD character and polytypic modifications, European Journal of Mineralogy, 13 (2001) 577-590.
[142] R.J.M. Pellenq, A. Kushima, R. Shahsavari, K.J. Van Vliet, M.J. Buehler, S. Yip, F.J. Ulm, A realistic molecular model of cement hydrates, Proceedings of the National Academy of Sciences, 106 (2009) 16102-16107.
[143] D. Viehland, J.F. Li, L.J. Yuan, Z. Xu, Mesostructure of calcium silicate hydrate (C-S-H) gels in portland cement paste: short-range ordering, nanocrystallinity, and local compositional order, Journal of the American Ceramic Society, 79 (1996) 1731-1744.
[144] K. Fujii, W. Kondo, Heterogeneous equilibrium of calcium silicate hydrate in water at 30ºC, Journal of the Chemical Society, Dalton Transactions, (1981) 645-651.
[145] H. Taylor, Nanostructure of CSH: Current status, Advanced Cement Based Materials, 1 (1993) 38-46.
[146] M. Sakiyama, T. Maeshima, T. Mitsuda, Synthesis and crystal chemistry of Al-substituted 11Å tobermorite, Journal of the Society of Inorganic Materials, Japan, 7 (2000) 413-419.
[147] S. Yamazaki, H. Toraya, Determination of positions of zeolitic calcium atoms and water molecules in hydrothermally formed aluminum-substiqtuted tobermorite-1.1 nm using synchrotron radiation powder diffraction data, Journal of the American Ceramic Society, 84 (2004) 2685-2690.
[148] J.E. Oh, S.M. Clark, H.R. Wenk, P.J.M. Monteiro, Experimental determination of bulk modulus of 14Å tobermorite using high pressure synchrotron X-ray diffraction, Cement and Concrete Research, 42 (2012) 397-403.
[149] V. Farmer, J. Jeevartnam, K. Speakman, Thermal decomposition of 14 Å tobermorite from Crestmore, Highway Research Board Special Report, (1966).

[150] H.K. Mao, J. Xu, P.M. Bell, Calibration of the ruby pressure gauge to 800 kbar under quasi-hydrostatic conditions, Journal of Geophysical Research, 91 (1986) 4673-4676.
[151] A.P. Hammersley, S.O. Svensson, M. Hanfland, A.N. Fitch, D. Hcousermann, Two-dimensional detector software: From real detector to idealised image or two-theta scan, High Pressure Research, 14 (1996) 235-248.
[152] R.W. Cheary, A.A. Coelho, Programs XFIT and FOURYA, deposited in CCP14 Powder Diffraction Library, Engineering and Physical Sciences Research Council, Daresbury Laboratory, Warrington, England, (http://wwwccp14acuk/tutorial/xfit-95/xfithtm), (1996).
[153] J. Laugier, B. Bochu, CELREF. Version 3. Cell parameter refinement program from powder diffraction diagram, Laboratoire des Matériaux et du Génie Physique, Ecole Nationale Supérieure de Physique de Grenoble (INPG), France (2002).
[154] B.C. Reed, Linear least-squares fits with errors in both coordinates, American Journal of Physics, 57 (1989) 642-646.
[155] R. Shahsavari, M.J. Buehler, R.J.M. Pellenq, F.J. Ulm, First-principles study of elastic constants and interlayer interactions of complex hydrated oxides: Case study of tobermorite and jennite, Journal of the American Ceramic Society, 92 (2009) 2323-2330.
[156] D.L. Carpenter, Whistler studies of the plasmapause in the magnetosphere 1. Temporal variations in the position of the knee and some evidence on plasma motions near the knee, Journal of Geophysical Research, 71 (1966) 693-709.
[157] R.J. Kirkpatrick, J. Yarger, P.F. McMillan, Y. Ping, X. Cong, Raman spectroscopy of CSH, tobermorite, and jennite, Advanced Cement Based Materials, 5 (1997) 93-99.
[158] P. Yu, R.J. Kirkpatrick, B. Poe, P.F. McMillan, X. Cong, Structure of calcium silicate hydrate (C-S-H): Near-, Mid-, and Far-infrared spectroscopy, Journal of the American Ceramic Society, 82 (1999) 742-748.
[159] N. Hara, N. Inoue, Formation of jennite from fumed silica, Cement and Concrete Research, 10 (1980) 677-682.
[160] N. Hara, N. Inoue, H. Noma, Formation of jennite and tobermorite and their relationship with C–S–H gel in hydrated cement paste, Proceedings of the Professor Sidney Diamond Symposium, Honolulu, Hawaii Edited by M Cohen, S Mindess, and J Skalny, The American Ceramic Society, Westerville, OH, (1998) 71-80.
[161] J. Neter, M.H. Kutner, C.J. Nachtsheim, W. Wasseman, Applied linear statistical models, (1996).
[162] J. Gard, H. Taylor, G. Cliff, G. Lorimer, A reexamination of jennite, American Mineralogist, 62 (1977) 365-368.
[163] D. Viehland, L.J. Yuan, Z. Xu, X.D. Cong, R.J. Kirkpatrick, Structural studies of jennite and 1.4 nm tobermorite: Disordered layering along the [100] of jennite, Journal of the American Ceramic Society, 80 (1997) 3021-3028.
[164] T. Maeshima, H. Noma, M. Sakiyama, T. Mitsuda, Natural 1.1 and 1.4 nm tobermorites from Fuka, Okayama, Japan: Chemical analysis, cell dimensions, ^{29}Si NMR and thermal behavior, Cement and Concrete Research, 33 (2003) 1515-1523.
[165] G. Paolo, et al., QUANTUM ESPRESSO: a modular and open-source software project for quantum simulations of materials, Journal of Physics: Condensed Matter, 21 (2009) 395502.

[166] D. Vanderbilt, Soft self-consistent pseudopotentials in a generalized eigenvalue formalism, Physical Review B, 41 (1990) 7892.
[167] P. Giannozzi, S. Baroni, N. Bonini, M. Calandra, R. Car, C. Cavazzoni, D. Ceresoli, G.L. Chiarotti, M. Cococcioni, I. Dabo, QUANTUM ESPRESSO: a modular and open-source software project for quantum simulations of materials, Journal of Physics: Condensed Matter, 21 (2009) 395502.
[168] S. Matthies, H.-R. Wenk, Transformations for monoclinic crystal symmetry in texture analysis, Journal of Applied Crystallography, 42 (2009) 564-571.
[169] J.F. Nye, Physical properties of crystals: Their representation by tensors and matrices, Clarendon Press, (1957).
[170] S.V. Churakov, Hydrogen bond connectivity in jennite from ab initio simulations, Cement and Concrete Research, 38 (2008) 1359-1364.
[171] H. Manzano, J. Dolado, A. Guerrero, A. Ayuela, Mechanical properties of crystalline calcium-silicate-hydrates: comparison with cementitious C-S-H gels, Physica Status Solidi (a), 204 (2007) 1775-1780.
[172] T. Mitsuda, K. Sasaki, H. Ishida, Phase evolution during autoclaving process of aerated concrete, Journal of the American Ceramic Society, 75 (2005) 1858-1863.
[173] T. Mitsuda, H. Toraya, Y. Okada, M. Shimoda, Synthesis of tobermorite: NMR spectroscopy and analytical electron microscopy, Advanced Characterisation Techniques for Ceramics Proceeding 41st Pacific Coast Regional Meeting American Ceramic Society, San Francisco, 24-26 October, (1988) 206-213.
[174] M. Miyake, S. Komarneni, R. Roy, Kinetics, equilibria and thermodynamics of ion exchange in substituted tobermorites, Materials Research Bulletin, 24 (1989) 311-320.
[175] K. Sasaki, T. Masuda, H. Ishida, T. Mitsuda, Structural degradation of tobermorite during vibratory milling, Journal of the American Ceramic Society, 79 (2005) 1569-1574.
[176] S. Komarneni, R. Roy, D.M. Roy, C.A. Fyfe, G.J. Kennedy, A.A. Bothner-By, J. Dadok, A.S. Chesnick, ^{27}Al and ^{29}Si magic angle spinning nuclear magnetic resonance spectroscopy of Al-substituted tobermorites, Journal of Materials Science, 20 (1985) 4209-4214.
[177] H. Manzano, J. Dolado, A. Ayuela, Aluminum incorporation to dreierketten silicate chains, The Journal of Physical Chemistry B, 113 (2009) 2832-2839.
[178] H.F.W. Taylor, The dehydration of tobermorite, Sixth National Conference on Clays and Clay Minerals, (1959) 101-109.
[179] A. Gmira, M. Zabat, R. Pellenq, H. Van Damme, Microscopic physical basis of the poromechanical behavior of cement-based materials, Materials and Structures, 37 (2004) 3-14.
[180] R.M. Wentzcovitch, Z. Wu, P. Carrier, First principles quasiharmonic thermoelasticity of mantle minerals, Reviews in Mineralogy and Geochemistry, 71 (2010) 99-128.
[181] B. Karki, R. Wentzcovitch, S. De Gironcoli, S. Baroni, High-pressure lattice dynamics and thermoelasticity of MgO, Physical Review B, 61 (2000) 8793.
[182] Y. Lee, T. Vogt, J.A. Hriljac, J.B. Parise, J.C. Hanson, S.J. Kim, Non-framework cation migration and irreversible pressure-induced hydration in a zeolite, Nature, 420 (2002) 485-489.
[183] B.B. Karki, L. Stixrude, R.M. Wentzcovitch, High-pressure elastic properties of major oxide, Reviews of Geophysics, 39 (2001) 507-534.

[184] D. Fincham, B. Ralston, Molecular dynamics simulation using the CRAY-1 vector processing computer, Computer physics communications, 23 (1981) 127-134.
[185] H.F.W. Taylor, Crystal structures of some double hydroxide minerals, Mineralogical Magazine, 39 (1973) 377-389.
[186] M. François, G. Renaudin, O. Evrard, A cementitious compound with composition $3CaO.Al_2O_3.CaCO_3.11H_2O$, Acta Crystallographica Section C, 54 (1998) 1214-1217.
[187] G. Renaudin, M. François, O. Evrard, Order and disorder in the lamellar hydrated tetracalcium monocarboaluminate compound, Cement and Concrete Research, 29 (1999) 63-69.
[188] T. Matschei, B. Lothenbach, F.P. Glasser, The AFm phase in portland cement, Cement and Concrete Research, 37 (2007) 118-130.
[189] T. Matschei, B. Lothenbach, F.P. Glasser, The role of calcium carbonate in cement hydration, Cement and Concrete Research, 37 (2007) 551-558.
[190] D. Damidot, S. Stronach, A. Kindness, M. Atkins, F.P. Glasser, Thermodynamic investigation of the $CaO-Al_2O_3-CaCO_3-H_2O$ closed system at 25°C and the influence of Na_2O, Cement and Concrete Research, 24 (1994) 563-572.
[191] R. Rinaldi, M. Sacerdoti, E. Passaglia, Stratlingite: crystal structure, chemistry, and a reexamination of its polytype vertumnite, European Journal of Mineralogy, 2 (1990) 841-849.
[192] R. Allman, Chimica, 24 (1970).
[193] H. Kuzel, Crystallographic data and thermal decomposition of synthetic gehlenite hydrate $2CaO.Al_2O_3.SiO_2.8H_2O$, Neues Jahrb Mineral, Monatsh, (1976) 319-325.
[194] H. Midgley, P. Bhaskara Rao, Formation of stratlingite, $2CaO.SiO_2.Al_2O_3.8H_2O$, in relation to the hydration of high alumina cement, Cement and Concrete Research, 8 (1978) 169-172.
[195] M. Balonis, F.P. Glasser, The density of cement phases, Cement and Concrete Research, 39 (2009) 733-739.
[196] R. Fischer, H.J. Kuzel, Reinvestigation of the system $C_4A.nH_2O-C_4A.CO_2.nH_2O$, Cement and Concrete Research, 12 (1982) 517-526.
[197] H. Kuzel, Ubre die orientierte Entwässerung von Tricalciumaluminath ydrate C3AH6, Neues Jahrbuch fuer Mineralogie, Monatshefte, 9 (1969) 397-403.
[198] E. Brandenberger, Kristallstrukturelle Untersuchungen an Ca-Aluminathydraten, Schweizerische Mineralogische und Petrographische Mitteilingen, 13 (1933) 569-570.
[199] G. Lager, T. Armbruster, J. Faber, Neutron and X-ray diffraction study of hydrogarnet $Ca_3Al_2(O_4H_4)_3$, American Mineralogist, 72 (1987) 756-765.
[200] G. Hentschel, H.J. Kuzel, Strätlingite, $2CaO–Al_2O_3–SiO_2.8H_2O$, ein neues Mineral, Neues Jahrbuch für Mineralogie Monatshefte, (1976) 326-330.
[201] S. Kwan, J. LaRosa, M.W. Grutzeck, ^{29}Si and ^{27}Al MASNMR Study of Stratlingite, Journal of the American Ceramic Society, 78 (1995) 1921-1926.
[202] R. Jeanloz, Finite-strain equation of state for high-pressure phases, Geophysical Reserach Letters, 8 (1981) 1219-1222.
[203] F.P. Glasser, A. Kindness, S.A. Stronach, Stability and solubility relationships in AFm phases: Part 1. Chloride, sulfate and hydroxide, Cement and Concrete Research 29 (1999) 861-866.

[204] G.A. Lager, R.T. Downs, M. Origlieri, R. Garoutte, High-pressure single-crystal X-ray diffraction study of katoite hydrogarnet: Evidence for a phase transition from *Ia*3*d*-*I*43*d* symmetry at 5 GPa, American Mineralogist, 86 (2002) 642-647.
[205] R.H. Nobes, E.V. Akahmatskaya, V. Milman, J.A. White, B. Winkler, C.J. Pickard, An ab initio study of hydrogarnets, American Mineralogist, 85 (2000) 1706-1715.
[206] F. Pascale, P. Ugliengo, B. Civalleri, R. Orlando, P. D'Arco, R. Dovesi, The katoite hydrogarnet Si-free $Ca_3Al_2([OH]_4)_3$: A periodic Hatree-Fock and B3-LYP study, Journal of Chemical Physics, 121 (2004) 1005-1013.
[207] R. Allmann, Die Doppelschichtstruktur der plaettchenfoermigen Calcium-Aluminium–Hydroxysalze am Beispiel des $3CaO{\cdot}Al_2O_3{\cdot}CaSO_4{\cdot}12H_2O$, Neues Jahrbuch für Mineralogie - Monatshefte, (1968) 140-144.
[208] F.G. Buttler, L.S.D. Glasser, H.F.W. Taylor, Studies on $4CaO{\cdot}Al_2O_3{\cdot}13H_2O$ and the related natural mineral hydrocaluminate, Journal of the American Ceramic Society, 42 (1959) 121-126.
[209] R. Allmann, Refinement of the hybrid layer structure $[Ca_2Al(OH)_6]^{+}{\cdot}[1/2SO_4{\cdot}3H_2O]^{-}$, Neues Jahrbuch für Mineralogie - Monatshefte, (1977) 136-144.
[210] B.Z. Dilnesa, B. Lothenbach, G. Le Saout, G. Renaudin, A. Mesbah, Y. Filinchuk, A. Wichser, E. Wieland, Iron in carbonate containing AFm phases, Cement and Concrete Research, 41 (2011) 311-323.
[211] B. Lothenbach, G. Le Saout, E. Gallucci, K. Scrivener, Influence of limestone on the hydration of portland cements, Cement and Concrete Research, 38 (2008) 848-860.
[212] I. Maki, Nature of the prismatic dark interstitial material in portland cement clinker, Cement and Concrete Research, 3 (1973) 295-313.
[213] P. Mondal, J. Jeffery, The crystal structure of tricalcium aluminate, $Ca_3Al_2O_6$, Acta Crystallographica Section B: Structural Crystallography and Crystal Chemistry, 31 (1975) 689-697.
[214] V.L. Burdick, D.E. Day, Coordination of aluminum ions in tricalcium aluminate, Journal of the American Ceramic Society, 50 (2006) 97-101.
[215] M. Collepardi, G. Baldini, M. Pauri, M. Corradi, Tricalcium aluminate hydration in the presence of lime, gypsum or sodium sulfate, Cement and Concrete Research, 8 (1978) 571-580.
[216] K. Velez, S. Maximilien, D. Damidot, G. Fantozzi, F. Sorrentino, Determination by nanoindentation of elastic modulus and hardness of pure constituents of portland cement clinker, Cement and Concrete Research, 31 (2001) 555-561.
[217] H.F.W. Taylor, The chemistry of cements, Vol. 1. Academic Press (1964).
[218] M. Francois, G. Renaudin, O. Evrard, A cementitious compound with composition $3CaO.Al_2O_3.CaCO_3.11H_2O$, Acta Crystallographica Section C: Crystal Structure Communications, 54 (1998) 1214-1217.
[219] B B Karki, G.J. Ackland, J. Crain, Elastic instabilities in crystals from ab initio stress-strain relations, Journal of Physics: Condensed Matter, 9 (1997).
[220] G. Kresse, J. Furthmuller, Efficiency of ab-initio total energy calculationa for metals and semicunductors using a plane-wave basis set, Computational Materials Science, 6 (1996) 15-50.
[221] H. Yao, L. Ouyang, W.Y. Ching, Ab initio calculation of elastic constants of ceramic crystals, Journal of the American Ceramic Society, 90 (2007) 3194-3204.

[222] T. Demuth, Y. Jeanvoine, J. Hafner, J. Angyan, Polymorphism in silica studied in the local density and generalized-gradient approximations, Journal of Physics: Condensed Matter, 11 (1999) 3833.
[223] R.M. Wentzcovitch, N.L. Ross, G. Price, Ab initio study of $MgSiO_3$ and $CaSiO_3$ perovskites at lower-mantle pressures, Physics of the Earth and Planetary Interiors, 90 (1995) 101-112.
[224] B. Karki, G. Ackland, J. Crain, Elastic instabilities in crystals from ab initio stress-strain relations, Journal of Physics: Condensed Matter, 9 (1999) 8579.
[225] H. Manzano, J.S. Dolado, A. Ayuela, Structural, mechanical, and reactivity properties of tricalcium aluminate using first-principles calculations, Journal of the American Ceramic Society, 92 (2009) 897-902.
[226] J.P. Poirier, Introduction to the physics of the earth's interior, Cambridge University Press, 2000.
[227] R.M. Hazen, Zeolite molecular sieve 4Å: Anomalous compressibility and volume discontinuities at high pressure, Science, 219 (1983) 1065-1067.
[228] H. Olijnyk, E. Paris, C. Geiger, G. Lager, Compressional study of katoite [$Ca_3Al_2(O_4H_4)_3$] and grossular garnet, Journal of Geophysical Research, 96 (1991) 14313-14318.
[229] G.A. Lager, R.B. Von Dreele, Neutron powder diffraction study of hydrogarnet to 9.0 GPa, American Mineralogist, 81 (1996) 1097-1104.
[230] G.A. Lager, R.T. Downs, M. Origlieri, R. Garoutte, High-pressure single-crystal X-ray diffraction study of katoite hydrogarnet: Evidence for a phase transition from Ia3d $\rightarrow I\bar{4}3d$ symmetry at 5 GPa, American Mineralogist, 87 (2002) 642-647.
[231] R.H. Nobes, E.V. Akhmatskaya, V. Milman, B. Winkler, C.J. Pickard, Structure and properties of aluminosilicate garnets and katoite: an ab initio study, Computational Materials Science, 17 (2000), 141-145.
[232] R. Orlando, F.J. Torres, F. Pascale, P. Ugliengo, C. Zicovich-Wilson, R. Dovesi, Vibrational spectrum of katoite $Ca_3Al_2[(OH)_4]_3$: A periodic ab Initio study, The Journal of Physical Chemistry B 110.2 (206), 692-701.
[233] H.E. Petch, The hydrogen positions in portlandite, $Ca(OH)_2$, as indicated by the electron distribution, Acta Crystallographica, 14 (1961) 950-957.
[234] A.R. Oganov, M.J. Gillan, G.D. Price, Ab initio lattice dynamics and structural stability of MgO, The Journal of Chemical Physics, 118 (2003) 10174.
[235] P. Carrier, R. Wentzcovitch, J. Tsuchiya, First-principles prediction of crystal structures at high temperatures using the quasiharmonic approximation, Physical Review B, 76 (2007) 064116.
[236] R.M. Wentzcovitch, G.Y. Yonggang, Z. Wu, Thermodynamic properties and phase relations in mantle minerals investigated by first priniciples quasiharmonic theory, Reviews in Mineralogy & Geochemistry, 71 (2010) 59-98.
[237] M. Colligan, P.M. Forster, A.K. Cheetham, Y. Lee, T. Vogt, J.A. Hriljac, Synchrotron X-ray powder diffraction and computational investigation of purely siliceous zeolite Y under pressure, Journal of the American Chemical Society, 126 (2004) 12015-12022.
[238] H. Manzano, E. Durgun, M.J. Abdolhosseine Qomi, F.J. Ulm, R.J.M. Pellenq, J.C. Grossman, Impact of chemical impurities on the crystalline cement clinker phases determined by atomistic simulations, Crystal Growth & Design, 11 (2011) 2964-2972.

[239] W. Wieker, C. Hubert, D. Heidemann, R. Ebert, Alkali-silica reaction-a problem of the insufficient fundamental knowledge of its chemical base, Material Science Concrete, Special Volume (Sidney Diamond Symposium), (1998) 395-408.
[240] W. Wieker, C. Hubert, D. Heidemann, R. Ebert, Some experiences in chemical modelling of the alkali-silica reaction, 11th International Conference on Alkali-aggregate Reactions, Quebec, (2000) 119-128.
[241] R.J. Kirkpatrick, A.G. Kalinichev, X. Hou, L. Struble, Experimental and molecular dynamics modeling studies of interlayer swelling: water incorporation in kanemite and ASR gel, Materials and Structures, 38 (2005) 449-458.
[242] C.J. Benmore, P.J.M. Monteiro, The structure of alkali silicate gel by total scattering methods, Cement and Concrete Research, 40 (2010) 892-897.
[243] S. Speziale, F. Jiang, Z. Mao, P.J.M. Monteiro, H.R. Wenk, T.S. Duffy, F.R. Schilling, Single-crystal elastic constants of natural ettringite, Cement and Concrete Research, 38 (2008) 885-889.
[244] S. Speziale, H.J. Reichmann, F.R. Schilling, H.R. Wenk, P.J.M. Monteiro, Determination of the elastic constants of portlandite by Brillouin spectroscopy, Cement and Concrete Research, 38 (2008) 1148-1153.
[245] T. Sato, N. Funamori, High-pressure in situ density measurement of low-Z noncrystalline materials with a diamond-anvil cell by an x-ray absorption method, Review of Scientific Instruments, 79 (2008) 073906.
[246] N.P. Hasparyk, P.J.M. Monteiro, D.C.C. Dal Molin, AAR in Furnas dam, Brazil, residual expansion and the effect of lithium, Proceedings of the 13th ICAAR (Broekmans MATH and Wigum BJ (eds)), Trondheim, Norway (2008) 16-19.
[247] K.E. Kurtis, P.J.M. Monteiro, J.T. Brown, W. Meyer-Ilse, Imaging of ASR gel by soft x-ray microscopy, Cement and Concrete Research, 28 (1998) 411-421.
[248] X. Hou, R.J. Kirkpatrick, L.J. Struble, P.J.M. Monteiro, Structural investigations of alkali silicate gels, Journal of the American Ceramic Society, 88 (2005) 943-949.
[249] C.E. Tambelli, J.F. Schneider, N.P. Hasparyk, P.J.M. Monteiro, Study of the structure of alkali-silica reaction gel by high-resolution NMR spectroscopy, Journal of Non-Crystalline Solids, 352 (2006) 3429-3436.
[250] X. Xiao, H. Liu, L. Wang, F. De Carlo, Density measurement of samples under high pressure using synchrotron microtomography and diamond anvil cell techniques, Journal of Synchrotron Radiation, 17 (2010) 360-366.
[251] Y.K. Vohra, S.J. Duclos, A.L. Ruoff, High-pressure x-ray diffraction studies on rhenium up to 216 GPa (2.16 Mbar), Physical Review B, 36 (1987) 9790.
[252] M. Berger, J. Hubbell, S. Seltzer, J. Chang, J. Coursey, R. Sukumar, D. Zucker, XCOM: Photon cross sections database, NIST standard reference database 8 (XGAM), Available on URL www physics nist gov/PhysRefData/Xcom/Text/XCOM html (17 November 2005), (2005).
[253] N. Funamori, T. Yagi, T. Uchida, Deviatoric stress measurement under uniaxial compression by a powder x-ray diffraction method, Journal of Applied Physics, 75 (1994) 4327-4331.
[254] O.B. Tsiok, V.V. Brazhkin, A.G. Lyapin, L.G. Khvostantsev, Logarithmic kinetics of the amorphous-amorphous transformations in SiO_2 and GeO_2 glasses under high pressure, Physical Review Letters, 80 (1998) 999-1002.

[255] J.W. Phair, S.N. Tkachev, M.H. Manghnani, R.A. Livingston, Elastic and structural properties of alkaline-calcium silica hydrogels, Journal of Materials Research, 20 (2005) 344-349.
[256] S. Diamond, Chemistry and other characteristics of ASR gels, Proceedings of the 11th International Conference on Alkali-Aggregate Reaction in Concrete, (2000) 31-40.
[257] M. Kawamura, K. Iwahori, ASR gel composition and expansive pressure in mortars under restraint, Cement and Concrete Composites, 26 (2004) 47-56.

Appendix: Geometrically optimized atomic coordinates of crystals in concrete

Table A1. Relaxed atomic coordinates of tobermorite 14 Å.

Tobermorite 14 Å LDA						Tobermorite 14 Å GGA					
a (Å)	b (Å)	c (Å)	α (º)	β (º)	γ (º)	a (Å)	b (Å)	c (Å)	α (º)	β (º)	γ (º)
7.115	7.703	25.28	90.00	90.00	123.56	6.789	7.507	28.650	90.26	89.76	123.32
	Fractional coordinates						Fractional coordinates				
	X		Y		Z		X		Y		Z
Ca	0.778		0.417		0.304	Ca	0.732		0.432		0.284
Ca	0.213		0.470		0.796	Ca	0.241		0.420		0.786
Ca	0.713		0.970		0.704	Ca	0.741		0.919		0.714
Ca	0.278		0.917		0.196	Ca	0.232		0.932		0.216
Ca	0.806		0.883		-0.029	Ca	0.947		1.016		0.001
Ca	0.306		0.382		0.529	Ca	0.479		0.525		0.501
Ca	0.345		0.446		0.206	Ca	0.247		0.438		0.219
Ca	0.749		0.493		0.710	Ca	0.762		0.431		0.718
Ca	0.249		0.993		0.790	Ca	0.262		0.931		0.781
Ca	0.845		0.946		0.294	Ca	0.746		0.938		0.281
O	0.889		0.624		0.143	O	0.739		0.519		0.128
O	0.212		0.550		0.612	O	0.236		0.510		0.633
O	0.712		0.050		0.888	O	0.736		0.011		0.867
O	0.389		0.124		0.357	O	0.237		0.018		0.372
O	0.844		0.239		0.140	O	0.736		0.188		0.157
O	0.233		0.237		0.638	O	0.240		0.177		0.655
O	0.733		0.737		0.863	O	0.739		0.678		0.845
O	0.344		0.739		0.360	O	0.235		0.688		0.343
O	1.042		0.511		0.219	O	0.972		0.549		0.209
O	0.452		0.577		0.701	O	0.482		0.530		0.710
O	0.952		0.077		0.800	O	0.983		0.031		0.790
O	0.541		0.011		0.281	O	0.471		0.049		0.291
O	0.591		0.311		0.204	O	0.504		0.315		0.207
O	0.006		0.355		0.701	O	0.014		0.297		0.711
O	0.506		0.855		0.799	O	0.514		0.799		0.789
O	0.091		0.811		0.296	O	0.004		0.815		0.293
O	0.815		0.248		0.977	O	0.868		0.211		0.949
O	0.254		0.116		0.455	O	0.390		0.265		0.450
O	0.754		0.616		0.045	O	0.900		0.765		0.050
O	0.315		0.748		0.523	O	0.361		0.697		0.550
O	0.903		0.954		0.099	O	0.758		0.876		0.126
O	0.254		0.921		0.607	O	0.285		0.881		0.623
O	0.754		0.421		0.893	O	0.786		0.383		0.876
O	0.403		0.454		0.402	O	0.255		0.376		0.374
O	0.571		0.833		0.166	O	0.502		0.822		0.204

O	0.011	0.883	0.695	O	0.017	0.810	0.702
O	0.511	0.383	0.805	O	0.517	0.310	0.798
O	0.071	0.333	0.334	O	0.001	0.321	0.296
O	1.009	0.061	0.201	O	0.968	0.058	0.210
O	0.456	0.108	0.698	O	0.483	0.053	0.708
O	0.956	0.608	0.802	O	0.983	0.555	0.792
O	0.509	0.561	0.299	O	0.468	0.558	0.290
O	0.217	0.881	0.086	O	0.159	0.885	0.130
O	0.623	0.903	0.603	O	0.665	0.856	0.625
O	0.123	0.403	0.897	O	0.168	0.362	0.874
O	0.717	0.381	0.414	O	0.656	0.384	0.370
O	1.068	0.752	0.966	O	0.899	0.778	0.939
O	0.658	0.886	0.471	O	0.529	0.779	0.446
O	1.158	0.386	0.029	O	1.031	0.287	0.054
O	0.568	0.252	0.535	O	0.407	0.278	0.561
O	0.427	0.773	1.001	O	0.517	0.876	0.995
O	0.927	0.273	0.499	O	0.944	0.363	0.513
O	0.223	0.196	-0.049	O	0.342	0.296	-0.017
O	0.722	0.696	0.549	O	0.855	0.803	0.519
O	0.487	0.206	0.027	O	0.745	0.385	0.016
O	-0.013	0.706	0.473	O	0.249	0.888	0.484
O	0.415	0.532	0.106	O	0.299	0.458	0.132
O	0.790	0.477	0.610	O	0.783	0.432	0.631
O	0.290	0.977	0.890	O	0.284	0.931	0.870
O	0.915	1.032	0.394	O	0.797	0.958	0.368
Si	0.836	0.414	0.177	Si	0.742	0.397	0.177
Si	0.228	0.431	0.667	Si	0.248	0.383	0.679
Si	0.728	0.931	0.833	Si	0.747	0.884	0.821
Si	0.336	0.914	0.323	Si	0.241	0.897	0.323
Si	0.941	0.761	0.089	Si	0.889	0.762	0.106
Si	0.358	0.791	0.586	Si	0.387	0.739	0.605
Si	0.858	0.291	0.914	Si	0.890	0.245	0.894
Si	0.441	0.261	0.411	Si	0.384	0.262	0.394
Si	0.839	1.027	0.153	Si	0.743	0.984	0.176
Si	0.237	1.033	0.662	Si	0.257	0.975	0.674
Si	0.737	0.533	0.838	Si	0.757	0.476	0.826
Si	0.339	0.527	0.347	Si	0.242	0.484	0.324
H	0.323	1.008	0.062	H	0.291	0.952	0.109
H	0.696	0.835	0.581	H	0.792	0.918	0.602
H	0.196	0.335	0.919	H	0.292	0.413	0.897
H	0.823	0.508	0.438	H	0.789	0.453	0.392
H	0.969	0.599	0.968	H	1.016	0.742	0.936
H	0.782	0.964	0.422	H	0.607	0.831	0.415
H	1.282	0.464	0.078	H	1.109	0.335	0.085

H	0.469	0.099	0.532	H	0.527	0.245	0.564
H	0.325	0.623	1.013	H	0.448	0.733	0.983
H	0.825	0.123	0.487	H	0.969	0.250	0.505
H	0.340	0.210	-0.023	H	0.497	0.323	-0.005
H	0.840	0.710	0.523	H	1.009	0.829	0.505
H	0.611	0.200	0.006	H	0.821	0.365	-0.012
H	0.111	0.700	0.494	H	0.325	0.867	0.511
H	0.549	0.562	0.082	H	0.441	0.452	0.128
H	0.944	0.504	0.608	H	0.939	0.451	0.627
H	0.444	1.004	0.893	H	0.442	0.954	0.872
H	1.049	1.062	0.418	H	0.940	0.952	0.372
H	1.144	0.805	0.929	H	0.834	0.752	0.907
H	0.500	0.839	0.487	H	0.409	0.816	0.449
H	1.000	0.339	0.013	H	0.909	0.322	0.052
H	0.644	0.305	0.571	H	0.337	0.251	0.593
H	0.311	0.801	0.990	H	0.585	0.974	0.968
H	0.811	0.301	0.510	H	1.085	0.473	0.531
H	0.204	0.318	0.002	H	0.317	0.390	0.002
H	0.704	0.818	0.498	H	0.835	0.907	0.503
H	0.581	0.356	0.039	H	0.825	0.541	0.026
H	0.082	0.856	0.461	H	0.328	1.043	0.474
H	0.502	0.723	0.133	H	0.360	0.610	0.128
H	0.779	0.587	0.587	H	0.807	0.567	0.621
H	0.279	1.087	0.913	H	0.306	1.066	0.879
H	1.002	1.223	0.367	H	0.858	1.109	0.372

Table A2. Relaxed atomic coordinates of tobermorite 9 Å.

Tobermorite 9 Å LDA						Tobermorite 9 Å GGA					
a (Å)	b (Å)	c (Å)	α (º)	β (º)	γ (º)	a (Å)	b (Å)	c (Å)	α (º)	β (º)	γ (º)
11.901	7.544	9.668	97.03	91.33	90.93	11.247	7.364	9.620	98.54	91.87	90.52
	Fractional coordinates						Fractional coordinates				
	X		Y	Z			X		Y	Z	
Ca	0.378		0.101	0.878		Ca	0.374		0.104	0.902	
Ca	0.878		0.602	0.881		Ca	0.873		0.603	0.903	
Ca	0.622		0.898	0.119		Ca	0.627		0.897	0.097	
Ca	0.122		0.399	0.122		Ca	0.126		0.396	0.098	
Ca	0.493		0.463	0.504		Ca	0.495		0.442	0.504	
Ca	0.007		0.037	0.496		Ca	0.005		0.058	0.496	
Ca	0.368		0.609	0.885		Ca	0.366		0.604	0.884	
Ca	0.868		0.107	0.884		Ca	0.867		0.100	0.881	
Ca	0.632		0.393	0.116		Ca	0.633		0.400	0.119	
Ca	0.132		0.891	0.115		Ca	0.134		0.896	0.116	
O	0.374		0.128	0.384		O	0.378		0.155	0.388	
O	0.869		0.626	0.383		O	0.872		0.642	0.385	
O	0.631		0.874	0.617		O	0.628		0.858	0.615	
O	0.126		0.372	0.616		O	0.122		0.345	0.612	
O	0.491		0.641	0.125		O	0.501		0.658	0.115	
O	0.991		0.141	0.128		O	1.002		0.152	0.115	
O	0.509		0.359	0.872		O	0.498		0.348	0.885	
O	0.009		0.859	0.875		O	-0.001		0.842	0.885	
O	0.268		0.642	0.126		O	0.266		0.640	0.118	
O	0.768		0.142	0.125		O	0.766		0.143	0.119	
O	0.732		0.358	0.875		O	0.734		0.357	0.881	
O	0.232		0.858	0.874		O	0.234		0.860	0.882	
O	0.387		0.424	0.278		O	0.407		0.441	0.277	
O	0.888		0.927	0.283		O	0.905		0.937	0.278	
O	0.612		0.573	0.717		O	0.595		0.563	0.722	
O	0.113		0.076	0.722		O	0.093		0.059	0.723	
O	0.187		0.911	0.381		O	0.175		0.946	0.378	
O	0.685		0.401	0.381		O	0.676		0.416	0.378	
O	0.815		0.099	0.619		O	0.824		0.084	0.622	
O	0.313		0.589	0.619		O	0.325		0.554	0.622	
O	0.393		0.766	0.362		O	0.391		0.790	0.356	
O	0.893		0.269	0.361		O	0.898		0.279	0.360	
O	0.607		0.231	0.639		O	0.602		0.221	0.640	
O	0.107		0.734	0.638		O	0.109		0.710	0.644	
O	0.486		0.146	0.138		O	0.498		0.142	0.137	
O	-0.014		0.648	0.143		O	-0.001		0.640	0.142	
O	0.514		0.852	0.857		O	0.501		0.860	0.858	
O	1.014		0.354	0.862		O	1.002		0.358	0.863	

O	0.263	0.156	0.134	O	0.264	0.164	0.132
O	0.765	0.659	0.134	O	0.765	0.664	0.131
O	0.735	0.841	0.866	O	0.735	0.836	0.869
O	0.237	0.344	0.866	O	0.236	0.336	0.868
O	0.158	0.556	0.399	O	0.161	0.524	0.398
O	0.660	1.057	0.399	O	0.660	1.035	0.397
O	0.840	0.443	0.601	O	0.840	0.465	0.603
O	0.342	-0.056	0.601	O	0.339	-0.024	0.602
H	0.165	0.687	0.380	H	0.153	0.649	0.374
H	0.669	1.188	0.379	H	0.665	1.162	0.372
H	0.831	0.312	0.621	H	0.835	0.338	0.628
H	0.335	-0.187	0.620	H	0.347	-0.149	0.626
Si	0.375	0.203	0.225	Si	0.384	0.214	0.226
Si	0.876	0.706	0.230	Si	0.883	0.710	0.230
Si	0.624	0.794	0.770	Si	0.617	0.790	0.770
Si	0.125	0.297	0.775	Si	0.116	0.286	0.774
Si	0.318	0.940	0.430	Si	0.313	0.966	0.429
Si	0.815	0.441	0.431	Si	0.814	0.455	0.431
Si	0.685	0.059	0.569	Si	0.686	0.045	0.569
Si	0.182	0.560	0.570	Si	0.187	0.534	0.571
Si	0.381	0.624	0.217	Si	0.388	0.639	0.211
Si	0.880	0.124	0.216	Si	0.888	0.133	0.209
Si	0.620	0.376	0.784	Si	0.612	0.367	0.791
Si	0.119	0.876	0.783	Si	0.112	0.861	0.789

Table A3. Relaxed atomic coordinates of Jennite.

Jennite LDA						Jennite GGA					
a (Å)	b (Å)	c (Å)	α (º)	β (º)	γ (º)	a (Å)	b (Å)	c (Å)	α (º)	β (º)	γ (º)
10.762	7.584	11.046	102.14	96.38	109.94	10.626	7.292	10.912	100.98	97.71	109.35
	Fractional coordinates						Fractional coordinates				
	X	Y	Z				X	Y	Z		
Ca	0.058	0.356	0.353			Ca	0.061	0.361	0.364		
Ca	0.942	0.644	0.647			Ca	0.939	0.639	0.636		
Ca	0.430	0.795	0.343			Ca	0.417	0.799	0.365		
Ca	0.570	0.205	0.657			Ca	0.583	0.201	0.635		
Ca	0.067	0.861	0.374			Ca	0.067	0.864	0.380		
Ca	0.933	0.139	0.626			Ca	0.933	0.137	0.620		
Ca	0.428	0.288	0.335			Ca	0.425	0.291	0.351		
Ca	0.572	0.712	0.665			Ca	0.575	0.709	0.649		
Ca	0.000	0.500	0.000			Ca	0.000	0.500	0.000		
O	0.953	0.001	0.223			O	0.964	0.015	0.246		
O	0.047	0.999	0.777			O	0.036	0.985	0.754		
O	0.269	0.940	0.276			O	0.272	0.960	0.311		
O	0.731	0.060	0.724			O	0.728	0.040	0.689		
O	0.593	0.143	0.421			O	0.588	0.130	0.417		
O	0.407	0.857	0.579			O	0.412	0.870	0.583		
O	0.865	0.318	0.477			O	0.867	0.318	0.479		
O	0.135	0.682	0.523			O	0.133	0.682	0.521		
O	0.742	0.112	0.241			O	0.745	0.123	0.236		
O	0.258	0.888	0.759			O	0.255	0.877	0.764		
O	0.716	0.751	0.252			O	0.709	0.753	0.245		
O	0.284	0.249	0.748			O	0.291	0.247	0.755		
O	0.710	0.436	0.324			O	0.700	0.437	0.327		
O	0.290	0.564	0.676			O	0.300	0.563	0.673		
O	0.729	0.849	0.037			O	0.757	0.866	0.034		
O	0.271	0.151	0.963			O	0.243	0.134	0.966		
O	0.587	0.651	0.432			O	0.580	0.662	0.432		
O	0.413	0.349	0.568			O	0.420	0.338	0.568		
O	0.862	0.794	0.480			O	0.864	0.801	0.477		
O	0.138	0.206	0.520			O	0.136	0.199	0.523		
O	0.273	0.445	0.275			O	0.275	0.454	0.306		
O	0.727	0.555	0.725			O	0.725	0.546	0.694		
O	0.960	0.527	0.221			O	0.986	0.537	0.226		
O	0.040	0.473	0.779			O	0.014	0.463	0.774		
O	0.450	0.125	0.110			O	0.447	0.162	0.129		
O	0.550	0.875	0.890			O	0.553	0.838	0.871		
O	0.546	0.211	0.893			O	0.550	0.208	0.859		
O	0.454	0.789	0.107			O	0.450	0.792	0.141		
O	0.913	0.116	0.939			O	0.909	0.139	0.933		

O	0.087	0.884	0.061	O	0.091	0.861	0.066
O	0.769	0.531	0.964	O	0.786	0.530	0.956
O	0.231	0.469	0.036	O	0.214	0.470	0.044
Si	0.791	0.930	0.189	Si	0.801	0.940	0.189
Si	0.209	0.070	0.811	Si	0.199	0.060	0.811
Si	0.729	0.249	0.373	Si	0.726	0.247	0.372
Si	0.271	0.751	0.627	Si	0.274	0.753	0.628
Si	0.723	0.666	0.379	Si	0.717	0.675	0.378
Si	0.277	0.333	0.621	Si	0.283	0.325	0.622
H	0.218	0.914	0.190	H	0.228	0.919	0.219
H	0.782	0.086	0.810	H	0.772	0.081	0.781
H	0.248	0.439	0.184	H	0.243	0.439	0.214
H	0.752	0.561	0.816	H	0.757	0.561	0.786
H	0.863	0.481	0.219	H	0.887	0.485	0.216
H	0.137	0.519	0.781	H	0.113	0.515	0.784
H	0.369	0.129	0.042	H	0.368	0.151	0.055
H	0.534	0.194	0.084	H	0.534	0.244	0.113
H	0.456	0.207	0.906	H	0.459	0.217	0.850
H	0.549	0.074	0.893	H	0.541	0.071	0.869
H	0.968	0.058	0.883	H	0.960	0.075	0.879
H	0.857	0.015	0.977	H	0.856	0.033	0.975
H	0.682	0.416	0.951	H	0.697	0.417	0.938
H	0.750	0.657	0.996	H	0.772	0.662	0.990
H	0.631	0.871	0.958	H	0.632	0.849	0.945
H	0.466	0.806	0.916	H	0.466	0.756	0.887
H	0.544	0.793	0.094	H	0.541	0.783	0.149
H	0.451	0.926	0.107	H	0.459	0.929	0.131
H	0.032	0.942	0.117	H	0.040	0.925	0.121
H	0.143	0.985	0.023	H	0.144	0.966	0.025
H	0.318	0.584	0.049	H	0.303	0.582	0.062
H	0.250	0.343	0.004	H	0.228	0.338	0.010

Table A4. Relaxed atomic coordinates of monocarboaluminate containing 5 water.

5 water monocarboaluminate LDA						5 water monocarboaluminate GGA					
a (Å)	b (Å)	c (Å)	α (º)	β (º)	γ (º)	a (Å)	b (Å)	c (Å)	α (º)	β (º)	γ (º)
5.766	8.504	9.628	68.42	81.72	80.728	5.766	8.538	9.984	65.135	82.336	80.805
	Fractional coordinates						Fractional coordinates				
	X	Y	Z				X	Y	Z		
Al	0.005	-0.002	0.998			Al	0.003	-0.004	1.001		
Al	0.496	0.504	0.504			Al	0.494	0.503	0.506		
C	0.861	0.324	0.188			C	0.880	0.327	0.199		
Ca	0.528	0.108	0.787			Ca	0.522	0.114	0.807		
Ca	0.479	0.892	0.205			Ca	0.479	0.885	0.195		
Ca	0.018	0.618	0.300			Ca	0.014	0.623	0.314		
Ca	0.978	0.385	0.709			Ca	0.979	0.377	0.696		
H	0.177	0.231	1.029			H	0.175	0.261	0.987		
H	0.842	0.766	-0.032			H	0.833	0.726	0.023		
H	0.298	0.767	0.968			H	0.323	0.775	0.971		
H	0.701	0.227	0.031			H	0.688	0.214	0.039		
H	0.346	0.262	0.471			H	0.344	0.237	0.512		
H	0.659	0.749	0.526			H	0.650	0.771	0.494		
H	0.788	0.291	0.446			H	0.814	0.298	0.452		
H	0.211	0.726	0.545			H	0.170	0.720	0.541		
H	-0.050	1.018	0.253			H	-0.019	1.005	0.252		
H	0.071	0.004	0.730			H	0.023	0.006	0.739		
H	0.544	0.510	0.229			H	0.511	0.511	0.245		
H	0.440	0.488	0.780			H	0.475	0.482	0.771		
H	0.718	0.762	0.743			H	0.703	0.785	0.738		
H	0.467	0.835	0.674			H	0.450	0.863	0.683		
H	0.255	0.224	0.275			H	0.287	0.213	0.270		
H	0.538	0.170	0.313			H	0.558	0.146	0.312		
H	0.064	0.633	0.851			H	0.061	0.628	0.820		
H	0.841	0.538	0.951			H	0.858	0.524	0.927		
H	0.474	0.504	0.999			H	0.485	0.504	1.000		
H	0.210	0.479	0.039			H	0.220	0.500	0.042		
H	1.013	0.939	0.561			H	0.986	0.984	0.527		
H	0.255	1.012	0.481			H	0.249	0.998	0.472		
O	0.156	0.191	0.948			O	0.152	0.209	0.920		
O	0.856	0.805	0.052			O	0.852	0.784	0.085		
O	0.295	0.880	0.975			O	0.312	0.887	0.979		
O	0.712	0.118	0.016			O	0.693	0.109	0.021		
O	0.349	0.310	0.550			O	0.351	0.288	0.581		
O	0.643	0.698	0.451			O	0.639	0.718	0.427		
O	0.785	0.386	0.482			O	0.804	0.394	0.482		
O	0.209	0.618	0.530			O	0.185	0.608	0.531		
O	0.038	0.940	0.205			O	0.069	0.933	0.204		

O	0.967	0.060	0.794	O	0.931	0.062	0.800
O	0.455	0.568	0.296	O	0.423	0.572	0.303
O	0.539	0.437	0.711	O	0.569	0.430	0.708
O	0.627	0.861	0.670	O	0.604	0.896	0.684
O	0.373	0.132	0.334	O	0.400	0.106	0.314
O	0.902	0.618	0.844	O	0.905	0.599	0.819
O	0.321	0.552	0.958	O	0.334	0.559	0.956
O	0.180	0.924	0.574	O	0.142	0.934	0.561
O	0.727	0.418	0.085	O	0.750	0.407	0.087
O	0.069	0.362	0.180	O	0.076	0.385	0.197
O	0.790	0.199	0.297	O	0.815	0.192	0.312

Table A5. Relaxed atomic coordinates of monocarboaluminate containing 2 water.

2 water monocarboaluminate LDA						2 water monocarboaluminate GGA					
a (Å)	b (Å)	c (Å)	α (º)	β (º)	γ (º)	a (Å)	b (Å)	c (Å)	α (º)	β (º)	γ (º)
5.766	8.213	9.065	71.628	80.564	80.661	5.766	8.365	9.945	65.807	80.909	79.391
	Fractional coordinates						Fractional coordinates				
	X		Y	Z			X		Y	Z	
Al	0.017		-0.027	0.997		Al	-0.005		-0.011	0.995	
Al	0.484		0.505	0.526		Al	0.478		0.512	0.512	
C	0.833		0.318	0.185		C	0.926		0.318	0.208	
Ca	0.545		0.098	0.776		Ca	0.501		0.141	0.821	
Ca	0.464		0.904	0.225		Ca	0.479		0.864	0.180	
Ca	0.028		0.598	0.311		Ca	0.008		0.617	0.313	
Ca	0.951		0.371	0.746		Ca	0.967		0.369	0.693	
H	0.153		0.211	1.047		H	0.057		0.284	0.979	
H	0.863		0.720	-0.019		H	0.872		0.694	0.026	
H	0.321		0.734	0.973		H	0.341		0.773	0.953	
H	0.692		0.211	0.047		H	0.694		0.200	0.062	
H	0.447		0.287	0.432		H	0.338		0.239	0.518	
H	0.619		0.733	0.581		H	0.656		0.780	0.487	
H	0.788		0.288	0.444		H	0.806		0.303	0.451	
H	0.165		0.731	0.568		H	0.135		0.731	0.543	
H	-0.087		1.007	0.272		H	-0.019		1.003	0.247	
H	0.086		-0.013	0.694		H	-0.006		0.004	0.729	
H	0.567		0.536	0.222		H	0.489		0.475	0.271	
H	0.409		0.478	0.826		H	0.469		0.506	0.779	
H	0.489		0.468	1.039		H	0.548		0.487	1.012	
H	0.216		0.433	0.075		H	0.275		0.488	0.052	
H	1.121		1.146	0.360		H	1.026		1.058	0.451	
H	0.253		1.140	0.495		H	0.282		0.967	0.497	
O	0.166		0.163	0.957		O	0.123		0.213	0.919	
O	0.864		0.783	0.057		O	0.856		0.773	0.079	
O	0.316		0.857	0.966		O	0.313		0.891	0.960	
O	0.718		0.108	0.012		O	0.682		0.102	0.033	
O	0.349		0.300	0.535		O	0.348		0.287	0.590	
O	0.619		0.701	0.484		O	0.605		0.736	0.421	
O	0.777		0.373	0.502		O	0.791		0.397	0.489	
O	0.175		0.613	0.565		O	0.158		0.613	0.540	
O	0.020		0.926	0.219		O	0.070		0.926	0.198	
O	0.986		0.035	0.777		O	0.906		0.057	0.797	
O	0.465		0.578	0.308		O	0.420		0.563	0.311	
O	0.507		0.431	0.739		O	0.557		0.454	0.710	
O	0.327		0.518	1.010		O	0.395		0.545	0.970	
O	0.211		1.060	0.443		O	0.117		0.966	0.536	
O	0.760		0.423	0.057		O	0.827		0.376	0.085	
O	0.047		0.315	0.205		O	0.098		0.392	0.216	
O	0.704		0.217	0.293		O	0.853		0.184	0.323	

Table A6. Relaxed atomic coordinates of tricalcium aluminate.

	Mondal and Jeffery [213]			Tricalcium aluminate GGA			
	Pa3, a = 15.263 Å				Pa3, a = 15.39 Å		
	Fractional coordinates				Fractional coordinates		
	x	y	z		x	y	z
Ca1	0	0	0	Ca1	0	0	0
Ca2	0.5	0	0	Ca2	0.5	0	0
Ca3	0.2561(1)	0.2561(1)	0.2561(1)	Ca3	0.2516	0.2516	0.2516
Ca4	0.3750(1)	0.3750(1)	0.3750(1)	Ca4	0.3686	0.3688	0.3688
Ca5	0.1386(1)	0.3763(1)	0.1272(1)	Ca5	0.1421	0.3814	0.1271
Ca6	0.3800(1)	0.3838(1)	0.1209(1)	Ca6	0.3803	0.3764	0.1204
Al1	0.2526(1)	0.0133(1)	0.0197(1)	Al1	0.2517	0.0133	0.0192
Al2	0.2444(1)	0.2335(1)	0.0046(1)	Al2	0.2435	0.2298	0.0045
O1	0.2777(2)	0.1241(2)	0.0103(2)	O1	0.2878	0.1227	0.0103
O2	0.4835(2)	0.1315(2)	0.2536(2)	O2	0.4825	0.13	0.2649
O3	0.2664(2)	0.2841(2)	0.1049(2)	O3	0.2627	0.2823	0.1042
O4	0.2350(2)	0.4047(2)	0.2921(2)	O4	0.2357	0.4027	0.2872
O5	0.3491(2)	-0.0385(2)	-0.0174(2)	O5	0.3467	-0.0463	-0.0098
O6	0.1509(2)	-0.0104(2)	-0.0242(2)	O6	0.1515	-0.003	-0.0333